Research Topics

Live cell imaging: Cell and developmental research bridging education, optical engineering, industry, software, shared facilities

Edited by
Michelle S. Itano, Paul Maddox and Abhishek Kumar

Published in
Frontiers in Cell and Developmental Biology

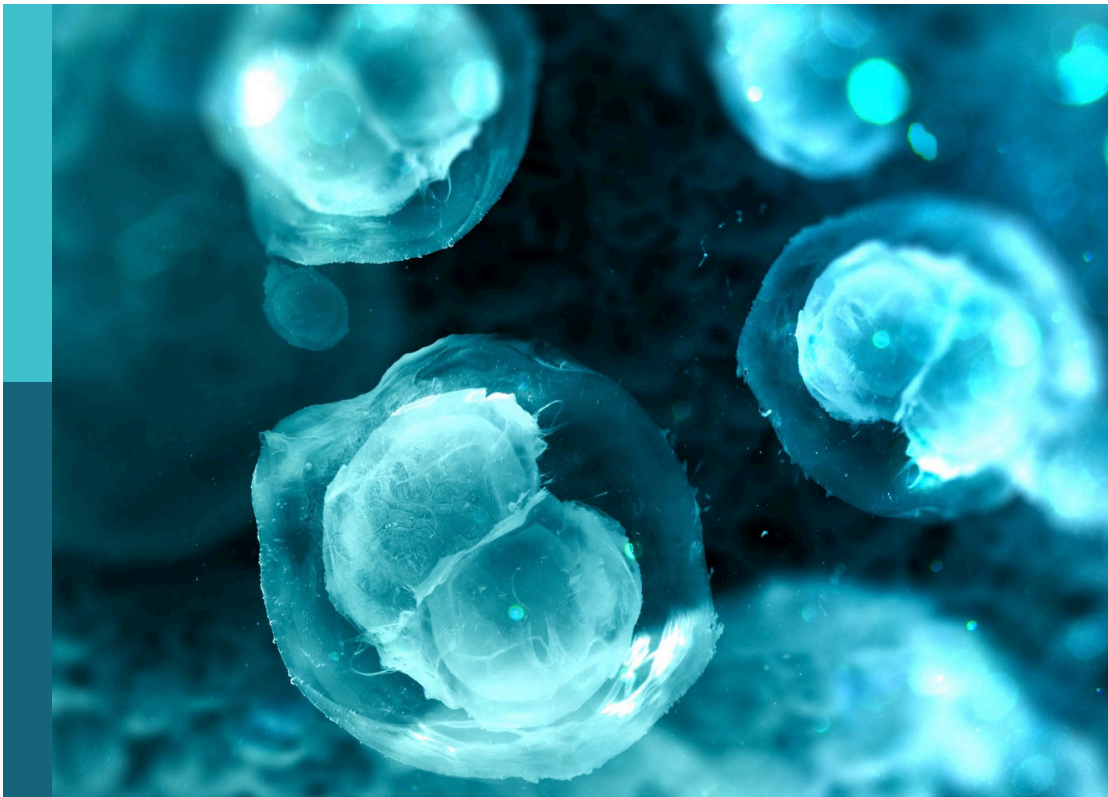

ISSN 1664-8714
ISBN 978-2-8325-2212-7
DOI 10.3389/978-2-8325-2212-7

About Frontiers

Frontiers is more than just an open access publisher of scholarly articles: it is a pioneering approach to the world of academia, radically improving the way scholarly research is managed. The grand vision of Frontiers is a world where all people have an equal opportunity to seek, share and generate knowledge. Frontiers provides immediate and permanent online open access to all its publications, but this alone is not enough to realize our grand goals.

Frontiers journal series

The Frontiers journal series is a multi-tier and interdisciplinary set of open-access, online journals, promising a paradigm shift from the current review, selection and dissemination processes in academic publishing. All Frontiers journals are driven by researchers for researchers; therefore, they constitute a service to the scholarly community. At the same time, the *Frontiers journal series* operates on a revolutionary invention, the tiered publishing system, initially addressing specific communities of scholars, and gradually climbing up to broader public understanding, thus serving the interests of the lay society, too.

Dedication to quality

Each Frontiers article is a landmark of the highest quality, thanks to genuinely collaborative interactions between authors and review editors, who include some of the world's best academicians. Research must be certified by peers before entering a stream of knowledge that may eventually reach the public - and shape society; therefore, Frontiers only applies the most rigorous and unbiased reviews. Frontiers revolutionizes research publishing by freely delivering the most outstanding research, evaluated with no bias from both the academic and social point of view. By applying the most advanced information technologies, Frontiers is catapulting scholarly publishing into a new generation.

What are Frontiers Research Topics?

Frontiers Research Topics are very popular trademarks of the *Frontiers journals series*: they are collections of at least ten articles, all centered on a particular subject. With their unique mix of varied contributions from Original Research to Review Articles, Frontiers Research Topics unify the most influential researchers, the latest key findings and historical advances in a hot research area.

Find out more on how to host your own Frontiers Research Topic or contribute to one as an author by contacting the Frontiers editorial office: frontiersin.org/about/contact

Live cell imaging: Cell and developmental research bridging education, optical engineering, industry, software, shared facilities

Topic editors
Michelle S. Itano — University of North Carolina at Chapel Hill, United States
Paul Maddox — University of North Carolina at Chapel Hill, United States
Abhishek Kumar — Marine Biological Laboratory (MBL), United States

Citation
Itano, M. S., Maddox, P., Kumar, A., eds. (2023). *Live cell imaging: Cell and developmental research bridging education, optical engineering, industry, software, shared facilities*. Lausanne: Frontiers Media SA. doi: 10.3389/978-2-8325-2212-7

Table of contents

frontiers | Frontiers in Cell and Developmental Biology

TYPE Editorial
PUBLISHED 15 June 2023
DOI 10.3389/fcell.2023.1191235

OPEN ACCESS

EDITED AND REVIEWED BY
Philipp Kaldis,
Lund University, Sweden

*CORRESPONDENCE
Michelle S. Itano,
✉ itano@unc.edu

RECEIVED 21 March 2023
ACCEPTED 30 May 2023
PUBLISHED 15 June 2023

CITATION
Itano MS, Kumar A and Maddox PS (2023), Editorial: Live cell imaging: Cell and developmental research bridging education, optical engineering, industry, software, shared facilities.
Front. Cell Dev. Biol. 11:1191235.
doi: 10.3389/fcell.2023.1191235

Editorial: Live cell imaging: Cell and developmental research bridging education, optical engineering, industry, software, shared facilities

Michelle S. Itano[1]*, Abhishek Kumar[2] and Paul S. Maddox[1]

[1]University of North Carolina at Chapel Hill, Chapel Hill, NC, United States, [2]Marine Biological Laboratory (MBL), Woods Hole, MA, United States

KEYWORDS

imaging, optics and imaging, collaboration, technology development, fluorescence

Editorial on the Research Topic
Live cell imaging: Cell and developmental research bridging education, optical engineering, industry, software, shared facilities

Optical imaging is one of the original technological pillars of biomedical research, spanning centuries of discovery. Drive for biological understanding has fueled significant progress in imaging tool development, ranging from illumination sources, detectors, and mechanical stages, to novel optical components and analysis strategies. The number and variety of optical imaging tools is now so vast that in some cases cutting-edge technologies require specialized training across a wide set of skills. Considering the exponential growth in imaging tools, fruitful and conducive partnerships between academic researchers, commercial vendors, and instrument facilitators, such as core facility managers and staff, are more important than ever.

Advancement: Optical imaging has advanced at an unprecedented speed in the past decade fueled by innovation on multiple fronts. This spur in tool availability has generated multiple choices for researchers from a wide range of specialized, customized techniques to turnkey commercial systems (Weber and Huisken, Gibbs et al., Hobson et al., Varady and Distel). Microscope startup companies play an important role in this ecosystem and facilitate researchers' rapid ability to design a system or range of systems best suited to their specific experimental needs and preferences. Additionally, many laboratories, researchers, and companies developing such technologies are sharing their results and their processes openly and helping advance the science of the broader imaging community (Weber and Huisken, Smith et al., Katunin et al., Alghamdi et al., Marston et al., Bostock et al.). We anticipate that tool development will keep advancing and cross-disciplinary collaboration will increasingly become a necessity, which is a positive sign for the biomedical sciences and scientific community (Chandris et al.).

Access: Although the scientific community has made tremendous advances on all fronts of optical imaging, the Frontier is moving ever forward and translating this technology to the general, non-technical, biomedical community is ever challenging. Many researchers, universities, and research funders are taking an active interest in opening the door to enable the translation of these technologies for all to use. Innovation on the "distribution" side is also ongoing with microscope companies setting up centers where researchers can access advanced tools at a moderate cost. This approach circumnavigates the requirement to hire expert trainers and to make a permanent, significant capital investment. Making advanced tools along with expert help accessible is still a challenge and it requires investment from federal organizations, private foundations, and an active effort from universities and scientists. Additionally, various professional and community-building societies such as BINA (BioImaging North America), Global Bioimaging, Association of Biomolecular Resource Facilities (ABRF), etc., are advancing and advocating access for researchers. Optical microscopy training courses and workshops (e.g., those offered by the Marine Biological Laboratory, Janelia Research Campus, and Cold Spring Harbor Laboratory) are critical in training scientists across all levels of the research collective who share common interests in using imaging science in their research. These courses serve as the backbone of the training ecosystems required to best use advanced imaging tools in the future.

Avenues: The field of optical imaging offers avenues for collaboration, contribution, and complementation. Three broad areas that can benefit from interdisciplinary collaborations, for example, are a) data handling and image processing/analysis, b) information and protocols for sample preparation and mounting and c) sharing microscope parts and design details for advanced tools so that scientists can adopt such technologies during the pre-commercialization phase. There is a growing need to foster collaborations more efficiently and provide avenues to further enhance resource sharing for optimal use of optical microscopy and associated image analysis approaches. Effective collaborations require investment from a broad range of individuals representing perspectives from institutional administrators, trainers, developers, investors, and those actively collecting and analyzing data, including those who may be new to the imaging field. In order for these initiatives that foster increased collaboration to be successful, they will require multiple years (4–5 years, similar to the length of most research program grants) of commitment from a dedicated group of individuals and financial investment in order to support the prioritization of these activities. Currently, the main limitation to growth in this arena is the lack of funding opportunities for a time period that would allow for broad and sustainable impact.

We hope you enjoy and utilize this special edition of research articles, tutorial perspectives and methodological protocols that are advancing the field of imaging science. It is our intent to be a step toward embracing the complexities as we move into a new era accelerating both innovation and access in biomedical imaging.

Author contributions

All authors listed have made a substantial, direct, and intellectual contribution to the work and approved it for publication.

Conflict of interest

PM is William Burwell Harrison scholar and founder and president of Mizar Imaging, LLC.

The remaining authors declare that the research was conducted in the absence of any commercial or financial relationships that could be construed as a potential conflict of interest.

Publisher's note

frontiers in Cell and Developmental Biology

MINI REVIEW
published: 03 June 2020
doi: 10.3389/fcell.2020.00418

Non-neuromodulatory Optogenetic Tools in Zebrafish

*Adam Varady and Martin Distel**

St. Anna Children's Cancer Research Institute, Innovative Cancer Models, Vienna, Austria

The zebrafish (*Danio rerio*) is a popular vertebrate model organism to investigate molecular mechanisms driving development and disease. Due to its transparency at embryonic and larval stages, investigations in the living organism are possible with subcellular resolution using intravital microscopy. The beneficial optical characteristics of zebrafish not only allow for passive observation, but also active manipulation of proteins and cells by light using optogenetic tools. Initially, photosensitive ion channels have been applied for neurobiological studies in zebrafish to dissect complex behaviors on a cellular level. More recently, exciting non-neural optogenetic tools have been established to control gene expression or protein localization and activity, allowing for unprecedented non-invasive and precise manipulation of various aspects of cellular physiology. Zebrafish will likely be a vertebrate model organism at the forefront of *in vivo* application of non-neural optogenetic tools and pioneering work has already been performed. In this review, we provide an overview of non-neuromodulatory optogenetic tools successfully applied in zebrafish to control gene expression, protein localization, cell signaling, migration and cell ablation.

Keywords: zebrafish, optogenetics, non-neural optogenetics, synthetic biology, gene expression, protein localization, cell signaling

OPEN ACCESS

Edited by:
Maria Caterina Mione,
University of Trento, Italy

Reviewed by:
Stephan C. F. Neuhauss,
University of Zurich, Switzerland
Gerald Radziwill,
University of Freiburg, Germany

****Correspondence:***
Martin Distel
martin.distel@ccri.at

Specialty section:
This article was submitted to Cell Growth and Division, a section of the journal Frontiers in Cell and Developmental Biology

Received: *19 February 2020*
Accepted: *05 May 2020*
Published: *03 June 2020*

Citation:
Varady A and Distel M (2020) Non-neuromodulatory Optogenetic Tools in Zebrafish. Front. Cell Dev. Biol. 8:418. doi: 10.3389/fcell.2020.00418

INTRODUCTION

Experimental control over protein function is an invaluable asset to dissect cellular processes on the molecular level. Conventional means of conditionally inducing protein activity, e.g., by small molecules or by heatshock, provide temporal control, but are typically limited in their spatial resolution. Optogenetic techniques emerged as a highly precise way to establish spatiotemporal control over protein activity by light.

Optogenetics was initially applied in neurobiology by ectopic expression of channelrhodopsins (ChRs), light-sensitive ion-channels, in neuronal cells (Boyden et al., 2005). ChRs depolarize neurons upon illumination and thereby modulate neuronal activity. Since then, the field has evolved to include non-neural applications. At the core of the new toolkit are light-sensitive proteins or protein-domains of bacterial, fungal and plant origin, such as phytochromes (e.g., PHYB-PIF), blue light using flavin (BLUF) domain proteins, cryptochromes (e.g., CRY2-CIB1) and light oxygen voltage (LOV) domains (**Figure 1**) (Ni et al., 1999; Harper et al., 2003; Liu et al., 2008; Yuan and Bauer, 2008). Irradiation with light of an appropriate wavelength causes conformational changes, commonly resulting in dimerization or oligomerization of the proteins. Careful engineering of photosensitive domains into enzymes, transcription factors or other proteins of interest endowed light-mediated control over the conformation of these proteins and resulted in light-activatable genetic tools for a variety of applications such as control over gene expression, genome editing, and protein relocalization (Beyer et al., 2015; Buckley et al., 2016; Polesskaya et al., 2018).

Zebrafish are an excellent model for optogenetic *in vivo* applications, since they are transparent at embryonic and larval stages and develop extra-uterine, providing light accessibility to the entire organism (Simmich et al., 2012). This optical clarity has been exploited to directly monitor fluorescently tagged cells and proteins in the living organism, hereby gaining great insights into cellular and subcellular processes during development and disease. In addition to this passive observation, novel optogenetic tools now enable manipulation of biological processes *in vivo* with the possibility of a direct readout of the effects. In this review, we summarize non-neuromodulatory optogenetic tools, which have recently been applied in zebrafish to control gene expression, cell migration, protein localization, signaling pathway activity and cell death (**Table 1**). Many of them can be readily combined with existing genetic systems like Gal4/UAS and established transgenic strains, making them a powerful addition to the genetic toolbox in zebrafish.

GENE EXPRESSION

Control over gene expression is beneficial to interrogate gene function and to model diseases including neurodegeneration and cancer. Temporal control is typically achieved in zebrafish by using either compound-activated systems like tamoxifen for estrogen receptor fusions or heatshock promoters (Mayrhofer and Mione, 2016). Optogenetic gene expression systems additionally offer spatial control and here we present their current applications in zebrafish.

Cryptochrome 2 (CRY2-CIB1)

The *Arabidopsis thaliana* photoreceptor protein cryptochrome 2 (CRY2) heterodimerizes with the CRY-interacting basic-helix-loop-helix (bHLH) transcription factor 1 (CIB1) upon blue light illumination (Liu et al., 2008). This heterodimerization was exploited to create a light-inducible Gal4 system by fusing the Gal4 DNA binding domain to CRY2 and the Gal4 activation domain containing VP16 to CIB1. A luciferase-based readout revealed that blue-light illumination for 2 h, but not red light, induced luciferase expression in zebrafish with this system (Liu et al., 2012).

LOV Domains

EL222/C120 and TAEL

EL222 is a LOV domain-containing light-inducible transcription factor from *Erythrobacter litoralis*. Blue light induces homodimerization of EL222 and subsequent binding to its regulatory element C120 activates transcription of downstream genes. EL222 was adapted for eukaryotic use by adding a nuclear localization sequence and the *herpes simplex* virus-derived VP16 transcriptional activation domain resulting in VP-EL222 (Motta-Mena et al., 2014). Injection of VP-EL222 mRNA together with a C120:mCherry reporter into zebrafish demonstrated that blue light effectively mediates gene expression in this system. As some toxicity was observed with VP-EL222 it was further optimized for applications in zebrafish by exchanging the VP16 transcriptional activation domain with TA4, which is better tolerated in zebrafish, resulting in TA4-EL222 (TAEL) (Distel et al., 2009; Reade et al., 2017).

The TAEL system was used to control the expression of several genes, including *sox32* to convert ectoderm to endoderm, *lefty* to modulate Nodal signaling and Cas9 for light-induced mosaic gene knock out. Importantly, selective illumination using either an epifluorescene, a confocal or light sheet microscope or a digital mirror device (DMD) demonstrated that TAEL endows temporal and spatial control over gene expression in zebrafish (Reade et al., 2017).

LightOn/GAVPO

The LightOn gene expression system is based on a synthetic protein termed GAVPO (Wang et al., 2012). GAVPO contains a Gal4 DNA binding domain, a p65 transactivation domain and the small fungal protein Vivid including its LOV domain for light-mediated dimerization (Schwerdtfeger and Linden, 2003). As Gal4 binds to UAS sites as a homodimer, its transcriptional activity can be controlled by light using the LightOn system (Wang et al., 2012). Illumination with blue light triggers homodimerization of GAVPO. The dimer then binds to UAS sites to induce expression of a gene of interest. The LightOn system was applied in zebrafish to gain spatiotemporal control over expression of two cell ablation systems, nitroreductase and the cytotoxic viral ion channel M2H37A (Mruk et al., 2019). GAVPO-mediated nitroreductase expression induced apoptosis in embryos when treated with metronidazole and irradiated with blue light. In addition, blue-light induced GAVPO-triggered expression of M2H37A leading to necrotic cell death and developmental defects in zebrafish embryos, which could be rescued by addition of the antiviral channel blocker rimantadine. Furthermore, a transgenic GAVPO strain (*elavl3:GAVPO*) was successfully established, demonstrating that GAVPO expression can be tolerated in zebrafish, although a previous study reported toxicity of GAVPO (Reade et al., 2017).

PICCORO

The BLUF domain-based "PixD complex dependent control of transcription" (PICCORO) system was engineered to directly control transcription factor activity by protein localization (Masuda et al., 2013). PixD is a bacterial blue-light photoreceptor that interacts with the response regulator-like protein PixE

Abbreviations: ActA, actin assembly inducing protein; AdoCbl, 5′-deoxyadenosylcobalamin; AMBRA1, autophagy and beclin-1 regulator 1; BLUF, blue light using flavin; bHLH, basic-helix-loop-helix transcription factor; CBD, cobalamin binding domain; ChR, Channel rhodopsin; CIB1, cryptochrome interacting bHLH 1; CRY2, cryptochrome 2; DMD, digital mirror device; FAD, flavin adenine dinucleotide; FMN, flavin mononucleotide; Fz(7), frizzled (7); iLID, improved light-inducible dimer; KR, KillerRed; LOV, light oxygen voltage; MxCBD, *M. xanthus* CBD; Ntl, No Tail; PA-Rac, photo-activatable Rac; PCB, phycocyanobilin; PCP, planar cell polarity; PHYB, phytochrome B; PI3K, phosphoinositide 3-kinase; PICCORO, PixD complex dependent control of transcription; PIF, phytochrome interacting factor; RFP, red fluorescent protein; ROS, reactive oxygen species; TAEL, TA4-EL222; TDP-43, transactivation response element DNA-binding protein 43; TetR, tetracycline repressor; UAS, upstream activating sequence.

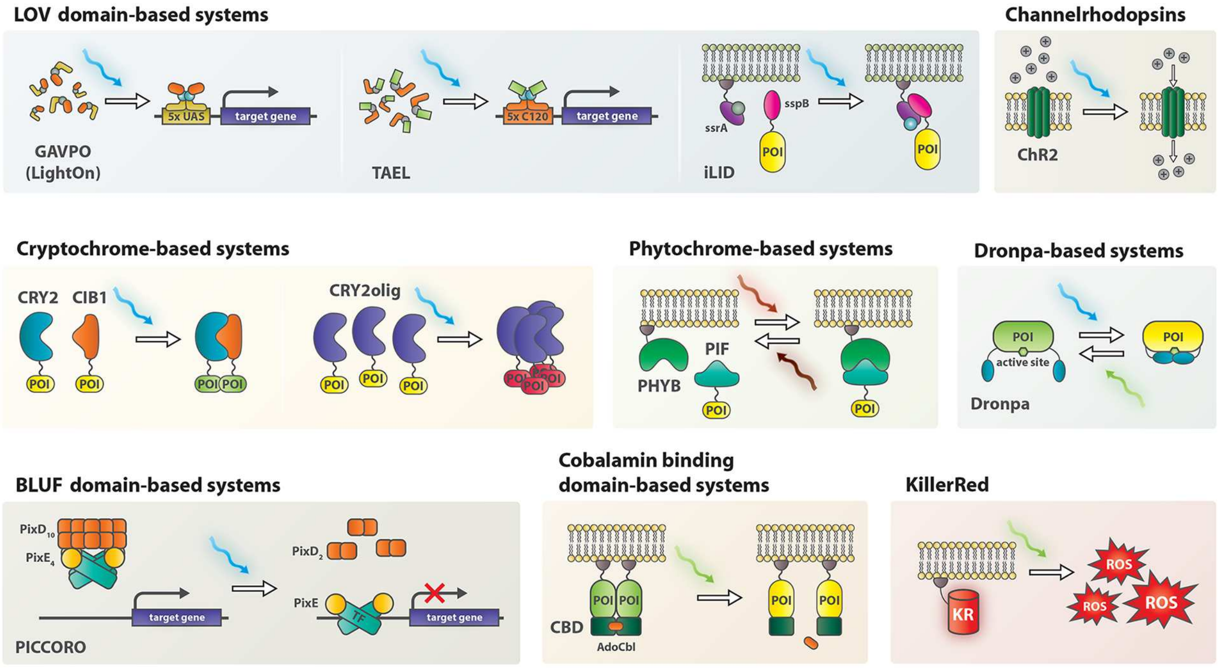

FIGURE 1 | Schematic representation of non-neuromodulatory optogenetic systems applied in zebrafish. AdoCbl, 5′-deoxyadenosylcobalamin; CBD, cobalamin binding domain; ChR2, channelrhodopsin 2; CIB1, cryptochrome interacting bHLH 1; CRY2, cryptochrome 2; KR, KillerRed; PHYB, Phytochrome B; PIF, phytochrome interacting factor; POI, protein of interest; ROS, reactive oxygen species; TF, transcription factor.

and forms PixD$_{10}$-PixE$_4$ oligomers in the dark (Masuda and Tanaka, 2016). Illumination with blue light dissociates the large oligomeric complexes into PixD dimers and PixE monomers, triggered by changes in protein conformation (Yuan and Bauer, 2008) (**Figure 1**).

The PICCORO system was applied in zebrafish for light-mediated control of an engineered transcriptionally repressive version of the transcription factor No Tail (Ntl), which is important for tail tissue formation (Masuda et al., 2013). For this, the DNA binding domain of Ntl and the repressor domain of Engrailed were fused, resulting in the transcriptional repressor Ntl-EnR. When expressed in zebrafish, Ntl-EnR led to the typical “ntl” phenotype with missing tail tissues. To achieve light-dependent transcriptional repression, the N-terminus of PixE was fused to Ntl-EnR and the construct was named NtlPixE. When NtlPixE was expressed in a transgenic strain also ubiquitously expressing PixD (tg(EF1α:PixD)), transcriptional repression and the resulting “ntl” phenotype was ameliorated in the dark, as PixD$_{10}$-NtlPixE$_4$ oligomers would form and sequester NtlPixE away from its DNA binding site. Blue light illumination could restore the “ntl” phenotype, revealing direct light-mediated control of a chimeric transcription factor in zebrafish.

CELL MIGRATION

The cytoskeleton is a major contributor to cell migration and morphology changes. Several optogenetic tools have been established to control cytoskeleton dynamics in a precise manner, offering possibilities to investigate the mechanisms underlying migration.

Photoactivatable Rac

In an effort to investigate phosphoinositide 3-kinase (PI3K)-dependent movement of neutrophils in zebrafish, photo-activatable Rac (PA-Rac) was employed (Yoo et al., 2010). PA-Rac was engineered by fusion of a phototropin-derived LOV domain to Rac1 to sterically inhibit Rac function. Illumination with blue-light restores Rac activity and induces directed cell movement *in vitro* (Wu et al., 2009). In zebrafish embryos expressing PA-Rac in neutrophils, precise regulation of directional neutrophil migration was demonstrated using laser illumination. By this means, neutrophils could even be diverted away from wounds, opening up new possibilities to investigate cellular functions in inflammation (Yoo et al., 2010).

Channelrhodopsin (ChR)

In addition to controlling neuronal activity, ChRs were also applied in modulating cell migration. Through tissue-specific expression of ChR2, a blue-light-reactive cation channel protein, zebrafish pigmentation patterns were temporarily disarranged by illumination due to induced migration of pigment melanophores (Aramaki and Kondo, 2019).

TABLE 1 | Overview of non-neural optogenetic tools used in zebrafish.

Protein/ dimer system	Co-factors/ chromophores	Reported activation wavelength (nm)	Binding/ activation time	Unbinding/ deactivation time	Mechanism of action	Applications in Zebrafish	References
CRY2-CIB1	FAD	450-488	<1 s	12 min	Light-induced heterodimer (or CRY2 homo-oligomer), disruption in dark-state	Gal4-UAS-mediated gene expression in luciferase reporter assay	Liu et al., 2008, 2012
TAEL, EL222	FMN	460-470	<10 s (EL222)	<50 s (EL222)	Light-induced homodimer, disruption in dark-state	C120-promoter-mediated gene expression; induction of Cas9 expression for mosaic gene knockout	Motta-Mena et al., 2014; Reade et al., 2017
LightOn (GAVPO)	FAD, FMN	450-470 (<500)	Seconds**	2 h	Light-induced homodimer, disruption in dark-state	UAS-promoter-mediated gene expression for inducible cell ablation systems	Schwerdtfeger and Linden, 2003; Wang et al., 2012; Mruk et al., 2019
PICCORO (PixD/PixE)	FAD, FMN	472* (320–500)	Seconds**	Minutes**	Dark-state heterooligomerization, light-induced oligomer-dissociation into homodimers	Light-mediated control over the activity of a dominant negative transcription factor	Yuan and Bauer, 2008; Masuda et al., 2013; Masuda and Tanaka, 2016
PA-Rac (LOV)	FMN	458–473*	Seconds**	Tens of seconds**	Light-induced Ras-GTPase-activity	Control over neutrophil movement	Wu et al., 2009; Yoo et al., 2010
ChR2	all-trans-Retinal	450–490	-	-	Cation-channel, modulation of cellular ion concentrations	Perturbation of pigment migration	Boyden et al., 2005; Aramaki and Kondo, 2019
PHYB-PIF	PCB	630-664	6.5 s	> 2 h (dark); 46.9 s (> 740 nm)	Light-induced heterodimer, stable in dark-state, disruption upon >740 nm light illumination	Gene expression in a luciferase assay, subcellular protein relocalization	Ni et al., 1999; Beyer et al., 2015; Buckley et al., 2016
CRY2olig	FAD	473*	15-75 s (t 1/2)	23 min (t 1/2)	Light-induced homooligomerization	Localized clustering of TDP-43 protein in neuronal cells	Bugaj et al., 2013; Lee et al., 2014; Asakawa et al., 2019
iLID	FMN	488*	<1 min	< 2 min	Light-induced heterodimer, disruption in dark-state	Induction of mitophagy by protein relocalization	Guntas et al., 2015; D'Acunzo et al., 2019
Opto-Fz7	Rhodopsin	488*	N.A.	N.A.	Light-induced Fz7 activity	Direction of cell migration during gastrulation	Capek et al., 2019
Opto-Acvr1b/2b (LOV)	FMN	458*	Seconds**	Minutes**	Light-induced dimerization, leading to smad 2/3 phosphorylation and target gene expression	Control over Nodal signaling in zebrafish embryos during gastrulation	Sako et al., 2016
CBD	AdoCbl	540-550	N.A.	N.A.	Dark-state assembled heterodimer, disruption upon activating illumination	Disruption of constitutively active mFGFR1	Jost et al., 2015; Kainrath et al., 2017
psMEK (Dronpa)	-	400	Seonds**	500 nm; Seconds**	Homodimerization upon 400 nm illumination, dissociation upon 500 nm illumination	Modulation of MEK activity	Zhou et al., 2017; Patel et al., 2019
KillerRed	-	520–590	-	-	Photosensitizer, chromophore generating high amounts of ROS upon activating illumination	Directed cell ablation in heart, kidney and spinal cord	Bulina et al., 2006; Teh et al., 2010; Buckley et al., 2017; Formella et al., 2018

AdoCbl, 5′-deoxyadenosylcobalamin; CBD, cobalamin binding domain; ChR, Channel rhodopsin; CIB1, cryptochrome interacting bHLH 1; CRY2, cryptochrome 2; FAD, flavin adenine dinucleotide; FMN, flavin mononucleotide; Fz7, frizzled 7; iLID, improved light-inducible dimer; LOV, light oxygen voltage; PA-Rac, photo-activatable Rac; PCB, phycocyanobilin; PhyB, phytochrome B; PICCORO, PixD complex dependent control of transcription; PIF, phytochrome interacting factor; ROS, reactive oxygen species; TAEL, TA4-EL222; TDP-43, transactivation response element DNA-binding protein 43.

**Single wavelength used in experiments, full range not tested in cited literature. **Approximate activation times taken from Optobase (https://www.optobase.org/switches/)* Kolar et al., 2018.

PROTEIN LOCALIZATION

Tight regulation of protein localization in cellular compartments is crucial for many biological processes, and its dysregulation can lead to disease. Studying these processes by manipulation of protein localization requires tools, which act rapidly and with high spatial resolution. Several optogenetic systems have been developed to shuttle proteins between specific subcellular compartments or to form clusters among each other.

Phytochrome B (PHYB-PIF)

The photoreactive *Arabidopsis* proteins phytochrome B (PHYB) and the bHLH transcription factor phytochrome interaction partner (PIF) heterodimerize upon red light illumination in the presence of the chromophore phycocyanobilin (PCB) (Ni et al., 1999). The interaction remains stable in the dark for hours after activation. Furthermore, illumination with far-red light dissociates the dimers.

In an elegant study, PHYB-PIF was applied to control nuclear localization of a synthetic transcription factor. Here, PHYB was fused to a VP16 activation domain and a heterodimerizing antiparallel leucine zipper. The tetracycline repressor (TetR) DNA binding protein was attached to PHYB-VP16 via a corresponding leucine zipper. PIF3, which possesses a nuclear localization signal, was used to translocate this chimeric transcription factor into the nucleus in zebrafish upon red-light illumination, hereby controlling the expression of luciferase. PCB was added to the medium in this study (Beyer et al., 2015). The PHYB-PIF system was further optimized for application in zebrafish by truncation of PHYB for efficient expression and injection of PCB to deliver the chromophore into cells beyond the first layer of tissue (Buckley et al., 2016). After these adjustments, PHYB was linked to CAAX for cell-membrane binding, while PIF6 was fused to enhanced green fluorescent protein (EGFP) or Pard3 (Buckley et al., 2016). Red light illumination of a region of interest triggered protein shuttling of PIF6-EGFP or PIF6-Pard3 to the cell membrane, respectively. Activation and binding of the association partners were reported to occur in a matter of seconds, with unbinding kinetics of less than a minute after far-red light illumination.

CRY2olig

CRY2 self-clusters when illuminated, which is an undesirable feature for its function in the CRY2/CIB1 heterodimer but was found useful to induce protein relocalization, leading to the development of the CRY2olig protein clustering system (Bugaj et al., 2013; Lee et al., 2014). Functionality of this system in zebrafish was demonstrated by expression of mRFP1-tagged CRY2olig, which clustered *in vivo* upon blue-light stimulation (Asakawa et al., 2019). To study the effects of transactivation response element DNA-binding protein 43 (TDP-43) oligomerization in amyotrophic lateral sclerosis in zebrafish, the zebrafish *tardp* gene was inserted into the mRFP1-CRY2olig construct and named opTDP-43z. Physiological function of opTDP-43z was unaffected by the CRY2olig-fusion compared to wildtype *tardp*. In dark-state, opTDP-43z was detected mainly in cell nuclei, but started relocalizing to and aggregating in the cytosol after a blue-light stimulus. Light-induced clustering of opTDP-43z expressed in neurons perturbed axonal outgrowth, increased myofiber denervation frequency and seeded non-optogenetically induced delocalization of TDP-43 (Asakawa et al., 2019).

CRY2olig promises to be a general tool to investigate protein-clustering related diseases or to control protein activity by delocalization.

Improved Light-Inducible Dimer (iLID)

The improved light-inducible dimer (iLID) system consisting of the *E.coli* peptides SspB and SsrA fused to the *Avena sativa* LOV2 domain was engineered for a high change in affinity for their respective binding partner upon blue light stimulation (Guntas et al., 2015). The iLID system offers rapid activation and deactivation kinetics and lacks homo-monomerization. iLID was applied in zebrafish to regulate mitophagy (D'Acunzo et al., 2019). To achieve this, SsrA was fused to Venus and actin assembly inducing protein (ActA). SspB was fused to RFP and autophagy and beclin-1 regulator 1 (AMBRA1). Venus-ssrA-ActA was tethered to mitochondrial outer membranes while AMBRA1-RFP-sspB was present in the cytosol in the dark. Blue-light illumination triggered association of the two proteins, resulting in relocalization of AMBRA1 to the mitochondrial membrane, inducing mitophagy and leading to a loss of mitochondrial mass (D'Acunzo et al., 2019).

CONTROLLING CELL SIGNALING AND PROTEIN ACTIVITY

Precise spatiotemporal control over signaling pathway activity allows for detailed investigation of their role in cellular processes. In contrast to studying the function of proteins and pathways by transient or permanent changes in gene expression, manipulation of protein activity results in an immediate effect. Light is an ideal activator for fast-acting interference in signaling and multiple optogenetic proteins have been engineered to modulate major pathways like Wnt, Nodal or FGF in zebrafish.

Rhodopsin-Based Opto-Fz7 to Study Non-canonical Wnt-Fz/PCP Signaling

The non-canonical Wnt receptor frizzled 7 (Fz7) was engineered to be activated by light independent of ligand binding. To achieve this, the intracellular loop 3 and the C-terminus of the light sensitive receptor rhodopsin were replaced by the corresponding intracellular domains of Fz7 to create Opto-Fz7 (Capek et al., 2019). Applying Opto-Fz7 revealed that non-canonical Wnt-Frizzled(Fz)/planar cell polarity (PCP) signaling provides a permissive signal for directed migration of mesenchymal cells during zebrafish gastrulation.

LOV-Domain-Mediated Optogenetic Control Over Nodal Signaling

In order to control Nodal signaling and study its temporal role in mesendoderm induction in zebrafish, light-sensitive Nodal receptors were engineered by fusing the LOV domain of aureochrome 1 from *Vaucheria frigida* with the C-terminal intracellular domains of Nodal receptors Acvr1b and Acvr2b (Sako et al., 2016). Blue light controlled the dimerization of Opto-Acvr1b and 2b, upon which Nodal signaling was activated resulting in phosphorylation of Smad2 and expression of downstream target genes like goosecoid (Sako et al., 2016).

Cobalamin Binding Domains (CBDs) to Interrogate FGF Signaling

In contrast to the LOV domain based Nodal receptors Opto-Acvr1b and 2b, which dimerize upon blue light illumination, a green light-mediated de-dimerization system was used to inactivate FGF signaling. This system is based on cobalamin binding domains (CBDs) of bacterial CarH transcription factors, which are present as dimers in the dark but dissociate upon illumination with green light (Jost et al., 2015). For CBD-dimer assembly in the dark, 5′-deoxyadenosylcobalamin (AdoCbl) is required, which is cleaved from the protein upon green light illumination. A constitutively active FGF receptor, which can be inactivated by green light, was created by fusing murine mFGFR1 to the CBD from *M. xanthus* (MxCBD) (Kainrath et al., 2017). Injection of mFGFR1-MxCBD into zebrafish embryos together with AdoCbl led to severe malformations when kept in the dark consistent with hyperactive FGF signaling. However, green light illumination after injection of mFGFR1-MxCBD and AdoCbl completely rescued the phenotype, demonstrating that excessive FGF signaling could be inactivated *in vivo* (Kainrath et al., 2017).

DRONPA-Caged MEK1 to Control ERK Activity

In order to render MEK1 light-inducible, photo-dimerizable Dronpa (pdDronpa) was used to cage MEK1's active site in a single chain construct termed psMEK1tight (Zhou et al., 2017). Upon illumination with 500 nm Dronpa de-dimerizes and allows psMEK1 to bind ERK, whereas 400 nm light re-establishes the caged conformation. When applied in zebrafish psMEK1tight showed surprisingly no effect during early development (Patel et al., 2019). However, once optimized by introduction of an activating mutation found in cancer (E203K), a non-leaky light-controlled MEK1 ($\text{psMEK}^{\text{E203K}}$) for *in vivo* investigation of MAPK signaling in zebrafish could be generated.

OPTICAL CELL ABLATION SYSTEMS

Methods to ablate distinct cells are beneficial to study cell function or regeneration. Current chemical/genetically encoded systems are limited in their spatial resolution, but optogenetic tools offer unique selectivity of target cells.

KillerRed

KillerRed (KR) is a fluorescent protein, which produces large doses of reactive oxygen species (ROS) upon green light illumination, leading to apoptosis (Bulina et al., 2006). KR has been implemented in zebrafish for ROS-induced cell ablation *in vivo*. Transgenic fish lines with membrane-tethered KR expressed either in the heart or kidney were generated (Teh et al., 2010; Buckley et al., 2017). ROS levels could be controlled to inflict damage to cell membranes or cause death of illuminated KR-positive cells. Additionally, KR-activation in the heart closely resembled heart failure in humans (Teh et al., 2010). For studying neurodegeneration, a transgenic zebrafish model expressing KR in spinal cord neurons was generated, providing single cell control over cell ablation (Formella et al., 2018).

The possibility to control area, intensity and duration of ROS expression makes KR transgenic models a useful tool, not only for directed cell ablation, but also to study effects of free radicals on different tissues.

CONCLUSION AND PERSPECTIVES

Applying optogenetics in zebrafish offers unprecedented spatiotemporal control over protein function in a living vertebrate model organism. We have summarized recent studies using chimeric proteins engineered to endow light-mediated control over their activity in biological processes ranging from gene expression, cell migration, mitophagy and signaling pathways to cell ablation.

So far, LOV and BLUF domain-, pdDronpa-, CRY2-CIB-, PHYB-PIF-, and CBD-based systems have been successfully applied in zebrafish, revealing that zebrafish are generally permissive for various optogenetic systems (**Table 1**). Some of the systems needed zebrafish-specific optimization to ensure proper expression (e.g., truncation of the PHYB-PIF system Buckley et al., 2016) or to reduce toxicity (e.g., replacement of the transactivation domain of VP-EL222 to generate TAEL Reade et al., 2017).

LOV and BLUF domain-based systems as well as CRY-CIB are activated by blue light, CBD by green light and PHYB-PIF by red light, offering potential orthogonal applications, which have not been realized in zebrafish to date.

An important aspect to be considered is the availability of the co-factor for the respective optogenetic system in zebrafish. Blue-light activated systems typically rely on Flavin mononucleotides (FMN) or Flavin adenine dinucleotides (FAD), which are readily available in zebrafish cells (**Table 1**). However, cobalamins needed for CBD or PCB for PHYB-PIF have to be supplemented and as absorption from the medium is limited, these cofactors are ideally injected. Injection at the one cell-stage will result in dilution of the cofactor while cells are dividing and will thus limit the application of the system to early developmental stages. Possible ways to apply these systems at later stages are to engineer transgenic zebrafish strains, expressing the enzymes needed to produce the cofactor (e.g., mitochondria-localized cyanobacterial heme oxygenase 1 and PCB:ferredoxin oxidoreductase for PCB). This would greatly enhance the applicability of the PHYB-PIF system with its unique and elegant far-red light off-switch.

Some of the systems like LightOn (GAVPO) can be combined with available UAS strains for light-mediated control of a plethora of transgenes promising widespread use. The ideal optogenetic system for zebrafish still needs to be determined and further rounds of optimization of expression levels, toxicity and increased activity change will likely be required for their easy application. Nevertheless, the possibility to manipulate a biological process and to image the effects using real time reporters as readout, puts zebrafish in a prime position to take full advantage of the optogenetic toolkit and shine light on many biological processes.

AUTHOR CONTRIBUTIONS

AV and MD wrote the manuscript.

ACKNOWLEDGMENTS

We would like to thank Benjamin Natha and Michael Grusch for proofreading the manuscript.

REFERENCES

Aramaki, T., and Kondo, S. (2019). Method for disarranging the pigment pattern of zebrafish by optogenetics. *Dev. Biol.* 460, 12–19. doi: 10.1016/j.ydbio.2018.12.019

Asakawa, K., Handa, H., and Kawakami, K. (2019). Optogenetic modulation of TDP-43 oligomerization fast-forwards ALS-related pathologies in the spinal motor neurons. *Nat Commun.* 11:1004. doi: 10.1101/789057

Beyer, H. M., Juillot, S., Herbst, K., Samodelov, S. L., Müller, K., Schamel, W. W., et al. (2015). Red light-regulated reversible nuclear localization of proteins in mammalian cells and zebrafish. *ACS Synth. Biol.* 4, 951–958. doi: 10.1021/acssynbio.5b00004

Boyden, E. S., Zhang, F., Bamberg, E., Nagel, G., and Deisseroth, K. (2005). Millisecond-timescale, genetically targeted optical control of neural activity. *Nat. Neurosci.* 8, 1263–1268. doi: 10.1038/nn1525

Buckley, C., Carvalho, M. T., Young, L. K., Rider, S. A., McFadden, C., Berlage, C., et al. (2017). Precise spatio-temporal control of rapid optogenetic cell ablation with mem-killerred in zebrafish. *Sci. Rep.* 7:5096. doi: 10.1038/s41598-017-05028-2

Buckley, C. E., Moore, R. E., Reade, A., Goldberg, A. R., Weiner, O. D., and Clarke, J. D. W. (2016). Reversible optogenetic control of subcellular protein localization in a live vertebrate embryo. *Dev. Cell* 36, 117–126. doi: 10.1016/j.devcel.2015.12.011

Bugaj, L. J., Choksi, A. T., Mesuda, C. K., Kane, R. S., and Schaffer, D. V. (2013). Optogenetic protein clustering and signaling activation in mammalian cells. *Nat. Methods* 10, 249–252. doi: 10.1038/nmeth.2360

Bulina, M. E., Chudakov, D. M., Britanova, O. V., Yanushevich, Y. G., Staroverov, D. B., Chepurnykh, T. V., et al. (2006). A genetically encoded photosensitizer. *Nat. Biotechnol.* 24, 95–99. doi: 10.1038/nbt1175

Capek, D., Smutny, M., Tichy, A. M., Morri, M., Janovjak, H., and Heisenberg, C. P. (2019). Light-activated frizzled7 reveals a permissive role of non-canonical wnt signaling in mesendoderm cell migration. *Elife* 8:e42093. doi: 10.7554/eLife.42093

D'Acunzo, P., Strappazzon, F., Caruana, I., Meneghetti, G., Di Rita, A., Simula, L., et al. (2019). Reversible induction of mitophagy by an optogenetic bimodular system. *Nat. Commun.* 10:1533. doi: 10.1038/s41467-019-09487-1

Distel, M., Wullimann, M. F., and Köster, R. W. (2009). Optimized Gal4 genetics for permanent gene expression mapping in zebrafish. *Proc. Natl. Acad. Sci. U.S.A.* 106, 13365–13370. doi: 10.1073/pnas.0903060106

Formella, I., Svahn, A. J., Radford, R. A. W., Don, E. K., Cole, N. J., Hogan, A., et al. (2018). Real-time visualization of oxidative stress-mediated neurodegeneration of individual spinal motor neurons *in vivo*. *Redox Biol.* 19, 226–234. doi: 10.1016/j.redox.2018.08.011

Guntas, G., Hallett, R. A., Zimmerman, S. P., Williams, T., Yumerefendi, H., Bear, J. E., et al. (2015). Engineering an improved light-induced dimer (ILID) for controlling the localization and activity of signaling proteins. *Proc. Natl. Acad. Sci. U.S.A.* 112, 112–117. doi: 10.1073/pnas.1417910112

Harper, S. M., Neil, L. C., and Gardner, K. H. (2003). Structural basis of a phototropin light switch. *Science* 301, 1541–1544. doi: 10.1126/science.1086810

Jost, M., Fernández-Zapata, J., Polanco, M. C., Ortiz-Guerrero, J. M., Chen, P. Y., Kang, G., et al. (2015). Structural basis for gene regulation by a B12-dependent photoreceptor. *Nature* 526, 536–541. doi: 10.1038/nature14950

Kainrath, S., Stadler, M., Reichhart, E., Distel, M., and Janovjak, H. (2017). Green-light-induced inactivation of receptor signaling using cobalamin-binding domains. *Angew. Chem. Int. Ed.* 56, 4608–4611. doi: 10.1002/anie.201611998

Kolar, K., Knobloch, C., Stork, H., Žnidarič, M., and Weber, W. (2018). OptoBase: a web platform for molecular optogenetics. *ACS Synth. Biol.* 7, 1825–1828. doi: 10.1021/acssynbio.8b00120

Lee, S., Park, H., Kyung, T., Kim, N. Y., Kim, S., Kim, J., et al. (2014). Reversible protein inactivation by optogenetic trapping in cells. *Nat. Methods* 11, 633–636. doi: 10.1038/nmeth.2940

Liu, H., Gomez, G., Lin, S., Lin, S., and Lin, C. (2012). Optogenetic control of transcription in zebrafish. *PLoS ONE* 7:e50738. doi: 10.1371/journal.pone.0050738

Liu, H., Yu, X., Li, K., Klejnot, J., Yang, H., Lisiero, D., et al. (2008). Photoexcited CRY2 interacts with CIB1 to regulate transcription and floral initiation in arabidopsis. *Science* 322, 1535–1539. doi: 10.1126/science.1163927

Masuda, S., Nakatani, Y., Ren, S., and Tanaka, M. (2013). Blue light-mediated manipulation of transcription factor activity *in vivo*. *ACS Chem. Biol.* 8, 2649–2653. doi: 10.1021/cb400174d

Masuda, S., and Tanaka, M. (2016). PICCORO: a technique for manipulating the activity of transcription factors with blue light. *Methods Cell Biol*. 135, 289–295. doi: 10.1016/bs.mcb.2016.03.009

Mayrhofer, M., and Mione, M. (2016). The toolbox for conditional zebrafish cancer models. *Adv. Exp. Med. Biol.* 916, 21–59. doi: 10.1007/978-3-319-30654-4_2

Motta-Mena, L. B., Reade, A., Mallory, M. J., Glantz, S., Weiner, O. D., Lynch, K. W., et al. (2014). An optogenetic gene expression system with rapid activation and deactivation kinetics. *Nat. Chem. Biol.* 10, 196–202. doi: 10.1038/nchembio.1430

Mruk, K., Ciepla, P., Piza, P. A., Alnaqib, M., and Chen, J. K. (2019). Targeted cell ablation in zebrafish using optogenetic transcriptional control. *bioRxiv [Preprint].* doi: 10.1101/730507

Ni, M., Tepperman, J. M., and Quail, P. H. (1999). Binding of phytochrome B to its nuclear signalling partner PIF3 is reversibly induced by light. *Nature* 400, 781–784. doi: 10.1038/23500

Patel, A. L., Yeung, E., McGuire, S. E., Wu, A. Y., Toettcher, J. E., Burdine, R. D., et al. (2019). Optimizing photoswitchable MEK. *Proc. Natl. Acad. Sci. U.S.A.* 116, 25756–25763. doi: 10.1073/pnas.1912320116

Polesskaya, O., Baranova, A., Bui, S., Kondratev, N., Kananykhina, E., Nazarenko, O., et al. (2018). Optogenetic regulation of transcription. *BMC Neurosci.* 19(Suppl. 1):12. doi: 10.1186/s12868-018-0411-6

Reade, A., Motta-Mena, L. B., Gardner, K. H., Stainier, D. Y., Weiner, O. D., and Woo, S. (2017). TAEL: a zebrafish-optimized optogenetic gene expression system with fine spatial and temporal control. *Development* 144, 345–355. doi: 10.1242/dev.139238

Sako, K., Pradhan, S. J., Barone, V., Inglés-Prieto, Á., Müller, P., Ruprecht, V., et al. (2016). Optogenetic control of nodal signaling reveals a temporal pattern of nodal signaling regulating cell fate specification during gastrulation. *Cell Rep.* 16, 866–877. doi: 10.1016/j.celrep.2016.06.036

Schwerdtfeger, C., and Linden, H. (2003). VIVID is a flavoprotein and serves as a fungal blue light photoreceptor for photoadaptation. *EMBO J.* 22, 4846–4855. doi: 10.1093/emboj/cdg451

Simmich, J., Staykov, E., and Scott, E. (2012). Zebrafish as an appealing model for optogenetic studies. *Prog. Brain Res.* 196, 145–162. doi: 10.1016/B978-0-444-59426-6.00008-2

Teh, C., Chudakov, D. M., Poon, K. L., Mamedov, I. Z., Sek, J. Y., Shidlovsky, K., et al. (2010). Optogenetic *in vivo* cell manipulation in killerred-expressing zebrafish transgenics. *BMC Dev. Biol.* 10:110. doi: 10.1186/1471-213X-10-110

Wang, X., Chen, X., and Yang, Y. (2012). Spatiotemporal control of gene expression by a light-switchable transgene system. *Nat. Methods* 9, 266–269. doi: 10.1038/nmeth.1892

Wu, Y. I., Frey, D., Lungu, O. I., Jaehrig, A., Schlichting, I., Kuhlman, B., et al. (2009). A genetically-encoded photoactivatable rac controls the motility of living cells. *Nature* 461, 104–108. doi: 10.1038/nature08241

Yoo, S. K., Deng, Q., Cavnar, P. J., Wu, Y. I., Hahn, K. M., and Huttenlocher, A. (2010). Differential regulation of protrusion and polarity by PI(3)K during neutrophil motility in live zebrafish. *Dev. Cell* 18, 226–236. doi: 10.1016/j.devcel.2009.11.015

Yuan, H., and Bauer, C. E. (2008). PixE promotes dark oligomerization of the BLUF photoreceptor PixD. *Proc. Natl. Acad. Sci. U.S.A.* 105, 11715–11719. doi: 10.1073/pnas.0802149105

Zhou, X. X., Fan, L. Z., Li, P., Shen, K., and Lin, M. Z. (2017). Optical control of cell signaling by single-chain photoswitchable kinases. *Science* 355, 836–842. doi: 10.1126/science.aah3605

Conflict of Interest: The authors declare that the research was conducted in the absence of any commercial or financial relationships that could be construed as a potential conflict of interest.

frontiers in Cell and Developmental Biology

METHODS
published: 06 October 2020
doi: 10.3389/fcell.2020.590094

An Immobilization Technique for Long-Term Time-Lapse Imaging of Explanted *Drosophila* Tissues

Matthew P. Bostock[1]†, Anadika R. Prasad[1]†, Rita Chaouni[2], Alice C. Yuen[1], Rita Sousa-Nunes[2], Marc Amoyel[1] and Vilaiwan M. Fernandes[1]*

[1] Department of Cell and Developmental Biology, University College London, London, United Kingdom, [2] Centre for Developmental Neurobiology, King's College London, London, United Kingdom

Time-lapse imaging is an essential tool to study dynamic biological processes that cannot be discerned from fixed samples alone. However, imaging cell- and tissue-level processes in intact animals poses numerous challenges if the organism is opaque and/or motile. Explant cultures of intact tissues circumvent some of these challenges, but sample drift remains a considerable obstacle. We employed a simple yet effective technique to immobilize tissues in medium-bathed agarose. We applied this technique to study multiple *Drosophila* tissues from first-instar larvae to adult stages in various orientations and with no evidence of anisotropic pressure or stress damage. Using this method, we were able to image fine features for up to 18 h and make novel observations. Specifically, we report that fibers characteristic of quiescent neuroblasts are inherited by their basal daughters during reactivation; that the lamina in the developing visual system is assembled roughly 2–3 columns at a time; that lamina glia positions are dynamic during development; and that the nuclear envelopes of adult testis cyst stem cells do not break down completely during mitosis. In all, we demonstrate that our protocol is well-suited for tissue immobilization and long-term live imaging, enabling new insights into tissue and cell dynamics in *Drosophila*.

Keywords: *Drosophila*, live imaging, neuroblasts, adult stem cells, cell migration, cell proliferation, optic lobe, explant culturing

Edited by:
Hongyan Wang,
Duke-NUS Medical School,
Singapore

Reviewed by:
Sonal Nagarkar Jaiswal,
Centre for Cellular & Molecular Biology (CCMB), India
Rajprasad Loganathan,
Johns Hopkins University,
United States
Cédric Maurange,
Centre National de la Recherche Scientifique (CNRS), France

Correspondence:
Vilaiwan M. Fernandes
vilaiwan.fernandes@ucl.ac.uk

† These authors have contributed equally to this work

Specialty section:
This article was submitted to Cell Growth and Division, a section of the journal Frontiers in Cell and Developmental Biology

Received: *31 July 2020*
Accepted: *15 September 2020*
Published: *06 October 2020*

Citation:
Bostock MP, Prasad AR, Chaouni R, Yuen AC, Sousa-Nunes R, Amoyel M and Fernandes VM (2020) An Immobilization Technique for Long-Term Time-Lapse Imaging of Explanted Drosophila Tissues. Front. Cell Dev. Biol. 8:590094. doi: 10.3389/fcell.2020.590094

INTRODUCTION

Live imaging is a powerful tool to elucidate mechanistic and temporal aspects of intricate biological processes. Dynamic processes such as cell migration, protein localization, axon pathfinding and branching morphogenesis are described poorly in fixed tissue, whereas live imaging can reveal features within these processes with exquisite temporal resolution (Besson et al., 2015; Rabinovich et al., 2015; Chen et al., 2016). This approach has seen dramatic improvements with 2-photon and light sheet microscopy due to the increased depth of access and diminished phototoxicity (Huisken and Stainier, 2009; Nickerson et al., 2013; Ichikawa et al., 2014). Furthermore, developments in sample preparation for *in vivo* and *ex vivo* imaging as well as in advanced computational analyses have increased accessibility to investigations of dynamic processes (Ritsma et al., 2014; Speder and Brand, 2014; Rabinovich et al., 2015; Martin et al., 2018). Notwithstanding, a major obstacle with live imaging is sample drift, which results in a structure of interest moving out of focus. This can pose challenges to image analysis of dynamic processes.

Sample drift has been combatted by using coverslips or glass slides coated with adhesive extracellular matrix proteins such as fibronectin or collagen to physically immobilize the tissue of interest. However, these steps may exert extraneous anisotropic physical stress on the sample and affect developmental mechanisms, cause injuries to fragile tissues and therefore significantly reduce imaging time (Savoian and Rieder, 2002; Siller et al., 2005; Lerit et al., 2014; Rabinovich et al., 2015). Solutions to these problems have included placing explants in agarose wells (Rabinovich et al., 2015) but without being held in place, they still move. Although there are computational algorithms that can account for sample drift, they are often slow and can result in discontinuities between frames thus decreasing confidence in the image (Parslow et al., 2014).

Live imaging has been applied to many systems but here we focus on *Drosophila melanogaster,* whose genetic tractability makes it an outstanding model to image dynamic cellular processes. The *Drosophila* embryo was one of the earliest animal systems imaged live, due to being translucent and immobile up to late stages. Dechorionated live embryos can be imaged by gluing to a coverslip and covering with halocarbon oil to minimize dehydration (Cavey and Lecuit, 2008; Parton et al., 2010). Live imaging of the *Drosophila* embryo has been used widely to elucidate nuclear and cytoplasmic behaviors in the preblastodermal embryo (Foe and Alberts, 1983; Baker et al., 1993), epithelial adhesion during dorsal closure (Jacinto et al., 2000; Kiehart et al., 2000), germ cell migration (Sano et al., 2005), neuroblast divisions (Kaltschmidt et al., 2000) and mechanisms of salivary gland formation (Sanchez-Corrales et al., 2018) among many others. Beyond the embryo, *in vivo* live imaging becomes challenging since larvae and adults move continuously and have opaque cuticles which scatter light (Aldaz et al., 2010; Rabinovich et al., 2015; Bell, 2017). Calcium oscillations across the blood-brain barrier have been imaged through the thinner cuticle of very young larvae, reasonably steadied between coverslip and culture dish (Speder and Brand, 2014). Notwithstanding, while this methodology was apt for capturing relatively large-scale inter-cellular calcium wave propagation, the considerable drift remaining is not suited to visualize finer (sub)cellular events. Similarly, although larvae and pupae have been imaged live, the need to strike a balance between phototoxicity and image-acquisition rates often mean that some dynamic processes are hard to capture (Bosveld et al., 2012; Ghannad-Rezaie et al., 2012; Heemskerk et al., 2014; Tsao et al., 2016; Dye et al., 2017). In adults, live imaging can be performed through windows cut out of the cuticles of immobilized animals (Fiala et al., 2002; Seelig et al., 2010; Martin et al., 2018; Aimon et al., 2019) but feasibility of this approach depends on the accessibility of the tissue of interest.

An alternative to *in vivo* imaging is to image tissues in culture. Initially, explanted tissues were imaged to study processes over short periods of time (i.e., minutes to hours) such as cell cycle progression and oriented cell divisions, epithelial cell packing, intracellular protein movements and secretion (Siller et al., 2005; Farhadifar et al., 2007; Siller and Doe, 2008; Aldaz et al., 2010; Mao et al., 2011; Lerit et al., 2014). More recently, live imaging of cultured explants has been extended to processes that unfold over several hours such as morphogenesis of pigment cells during pupal eye development (Hellerman et al., 2015), cell migration (Prasad et al., 2015; Chen et al., 2016; Barlan et al., 2017), neuronal remodeling (Rabinovich et al., 2015), growth cone dynamics (Ozel et al., 2015; Akin and Zipursky, 2016), and spermatogonial stem cell dynamics in their niche (Sheng and Matunis, 2011; Lenhart and DiNardo, 2015).

Different culture media compositions have been applied to long-term live imaging of explanted *Drosophila* tissues. The most commonly used is Schneider's Insect medium (Echalier, 1997). Echalier's D-22 medium (Siller et al., 2005; Lee et al., 2006), Shield's and Sang's M3 medium (Aldaz et al., 2010) and Grace's Insect Culture medium have also been employed (Dye et al., 2017). These media are often supplemented with exogenous growth supporting components such as insulin, fetal bovine serum, fly extract, larval fat bodies, ascorbic acid and/or 20-hydroxy-ecdysone (20E) to optimize culture conditions. Supplement requirements vary with the tissues being imaged (Parton et al., 2010) and there are conflicting opinions regarding supplements for the same tissue. For example, some studies report that the addition of fly extract is essential to support imaginal disc growth *ex vivo* (Wyss, 1982; Zartman et al., 2013; Restrepo et al., 2016) whereas others demonstrated that fly extract had no effect on disc growth and in fact caused aberrant calcium oscillations in cultured wing discs (Tsao et al., 2016; Balaji et al., 2017). Similarly, larval fat bodies were found to be vital to maintain neuroblast divisions *ex vivo* (Siller et al., 2005; Cabernard and Doe, 2013) but others either found them dispensable for neural proliferation in the young larval central nervous system (CNS) or inhibitory of early pupal CNS development (Sousa-Nunes et al., 2011; Rabinovich et al., 2015). Lastly, addition of 20E and insulin to culture medium aimed at supporting imaginal disc growth has also been debated. Absence of insulin and presence of 20E has been reported to enable disc growth *ex vivo* (Aldaz et al., 2010; Dye et al., 2017) although other studies suggest that insulin is necessary (Restrepo et al., 2016; Tsao et al., 2016) but that 20E impairs disc development (Tsao et al., 2016). Differences in tissue responses to these supplements might be attributed to the specific stage and/or basal medium being used. For example, Zartman et al. (2013) demonstrated that cells derived from wing discs proliferated to a greater extent when insulin was added to Schneider's Insect Medium but not M3 medium (Zartman et al., 2013).

Here, we present a simple protocol for culturing and imaging *Drosophila* larval and adult tissues *ex vivo*. We use Schneider's Insect Medium along with relatively few growth supplements and immobilize samples in low gelling temperature agarose, an adaptation of the method commonly used to immobilize zebrafish embryos or larvae for live imaging (Distel and Koster, 2007). In this way, the explanted tissue is held in place without imposing anisotropic physical stress on it. Moreover, this technique allows tissues to be held in any orientation, independent of shape and center of gravity, rendering imaging of fine features readily accessible. A similar agarose-based immobilization technique was recently described for short-term imaging of larval neuroblast divisions (Miszczak and Egger, 2020). We have used this approach successfully to image the migration of glial cells and neurons in the *Drosophila* brain during the third larval instar over long developmental periods (Chen et al., 2016; Rossi and Fernandes, 2018). Here, we validate our protocol in multiple tissues from multiple developmental stages and report new biological observations for the first time. Specifically, we followed neuroblast divisions not only in the commonly-imaged wandering third larval instar (wL3) brain but also as they reactivate from quiescence during the first and second larval instars (L1 and L2); we captured glial and neuronal migration in the optic lobe, assembly of lamina columns and eye-antennal disc eversion; and we imaged cyst stem cell mitoses in adult testes. Overall, this is an inexpensive and simple method to carry out live imaging experiments to broaden understanding of cell and tissue dynamics in *Drosophila*.

MATERIALS AND METHODS

See supplementary material for a detailed step-by-step protocol with suggested volumes.

Fly Husbandry and Stocks

Fly strains and crosses were raised on standard cornmeal food at 25°C, except for the sparse labeling of epithelial and marginal glia (*dpp* > *FlexAmp*), which was raised at 29°C.

The Following genotypes were used in this study: *{yw; gcm-GAL4/CyO;}* Bloomington Drosophila Stock Center (BDSC) #3554, *{;; UAS-CD8::GFP/TM6B}* BDSC #5130, *{;; UAS-nls::GFP/TM6B}* BDSC #4776, *{; 13xLexAop-6xmcherry/CyO;}* BDSC #52271, *{yw, UAS-FLP; GAL80*^{ts}*/CyO; Act > y+ > lexA, lexAop-myr::GFP /TM6B} (FlexAmp)* (Bertet et al., 2014), *{;; dpp-GAL4/TM6B}* BDSC #7007, *{; E-Cad-E-Cad::GFP;}* (Huang et al., 2009), *{;; R27G05-LexA/TM6C}* (Tan et al., 2015), *{; ubi-GFP::CAAX;}* Drosophila Genomics Resource Center (DGRC) *#109830, {; His2av::EGFP/SM6a;}* BDSC #24163, *{; Tj-GAL4;}* DGRC #104055, *{; grh-GAL4;}* (Chell and Brand, 2010), *{;; UAS-syn21-GFP-p10}* (Pfeiffer et al., 2012), *{;; UAS-CD4-tdTomato}* a gift from D, Williams.

Explant Culture Medium

Explant culture medium consisted of Schneider's Insect medium (Sigma #S0146) supplemented with 2.5 μL/mL human insulin (Sigma #I9278), 1 % Penicillin-Streptomycin (Sigma #P4333) and 10 % Fetal Bovine Serum (Sigma #F2442) stored at 4°C and used within a month of preparation.

Preparation of Low Gelling Temperature Agarose

A total 2% low-gelling temperature agarose (Sigma #A9414) was prepared in sterile water. These were cut into ∼0.5 cm^3 pieces and stored in distilled water at 4°C. The agarose was deionized by changing the water each day for 5 days before use.

Dissections

Forceps, dissection pads, pipettes, falcon tubes and working areas were wiped down with 70% ethanol before use. Dissection of L1, L3 and adult tissues was carried out in cold culture medium. Dissections of L1 CNSs were performed using forceps to hold down the posterior end of the larva and a tungsten needle to slowly rip open the larval cuticle, and then lightly pull on the mouth hooks to extract the CNS. CNSs were left attached to mouth hooks via the esophagus, as well as to surrounding fat tissue and imaginal discs to avoid damage. Dissections of L3 CNSs were performed with a pair of forceps, used to rip and remove the larval cuticle, and sever the CNS from the midgut. Fat tissue and imaginal discs were removed, leaving only mouth hooks attached to the CNS via the esophagus. For L1–L3 CNS imaging esophageal muscles were crushed to cease unwanted contractions. For adult testes, flies were dissected 0–3 days post-eclosion with careful removal of the ejaculatory duct and accessory glands of the male gonad leaving each testis intact with its connecting seminal vesicle.

Tissue Immobilization in Agarose

Deionized agarose (see above) was melted in a microwave for approximately 20–30 s (per 0.5 cm^3 cube of 2% low-gelling temperature agarose) and diluted to 0.4% in culture medium heated to 42°C using a programmable heating block. The temperature was then lowered to 34°C before being added to coat the bottom of untreated 35 × 10 mm petri dishes (Thermo #171099). A single explant was placed in each dish and maneuvered to the center to be oriented using forceps. To maneuver the tissue, forceps were used to move the viscous agarose rather than the tissue itself. Once the desired orientation was achieved, the forceps were gently withdrawn from the agarose, which held the tissue in place due to its viscosity. All movements and orientations of the tissue were achieved within 5 min of placing the brain in the agarose so as not to disrupt its setting. The agarose was left to solidify for 10 min after which cold culture medium was added.

Imaging and Image Processing

We used an upright microscope set-up (Olympus FV1000MPE multi-photon laser scanning microscope or Zeiss 880, both with Spectra-Physics Mai Tai DeepSee 2-photon lasers) with water-immersion lens (Olympus XLPLN 25X WMP2 or Zeiss Plan-Apochromat 20X). The objective was immersed directly in the culture medium for imaging. The fluorophores used were all GFP or RFP derivatives, therefore the excitation wavelength was tuned between 925 and 935 nm. Laser power never exceeded 15%. Zen Blue (Zeiss) and ImageJ software was used to analyze movies. The Bleach Correction and Manual Tracking plugins were used to correct photobleaching and to track cells. The Correct 3D Drift plugin was used to correct for movements caused by tissue contraction. Adobe Photoshop (v21.1.3) and Adobe Premiere Pro (v14.2) were used to annotate and edit movies. Figures were generated using Adobe Illustrator (v24.1.3).

RESULTS

Neuroblast Divisions in the L3 Central Brain

The late larval CNS has been used extensively to study the biology of neural stem cells, called neuroblasts in *Drosophila*. Neuroblasts generate a vast number of diverse neuronal and

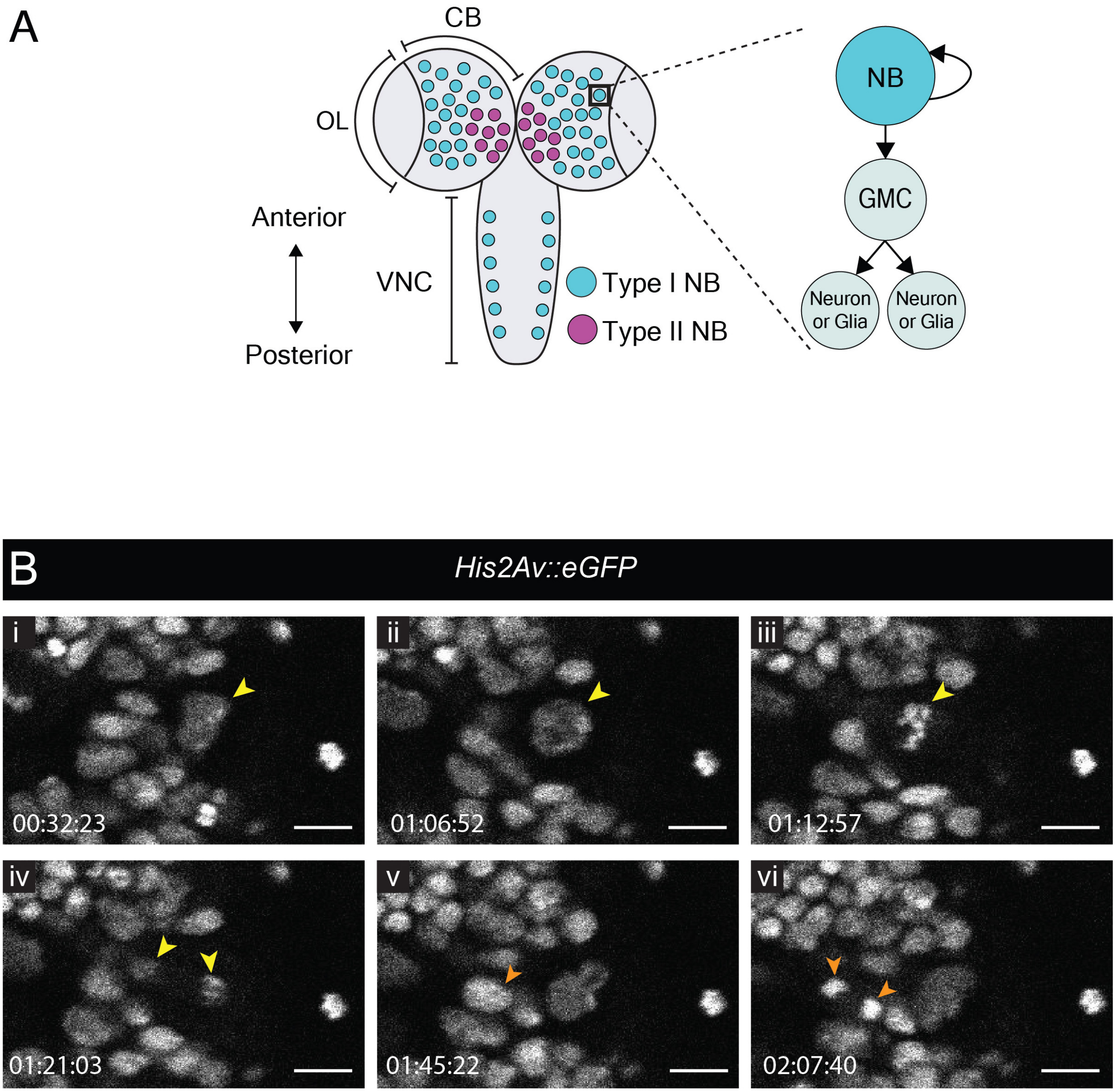

FIGURE 1 | Neuroblast and GMC divisions in the central brain during L3. **(A)** A schematic of the dorsal view of an L3 CNS, which is made up of the optic lobes (OL), the central brain (CB) and the ventral nerve cord (VNC) (Sousa-Nunes and Hirth, 2016). Type I neuroblasts (blue), which divide to self-renew and generate a GMC, are most abundant and are present throughout the CNS. GMCs divide symmetrically in size to generate two differentiating neuronal or glial progeny. Type II neuroblasts (magenta), defined by generation of two types of transit-amplifying progenitors (intermediate neural precursors and GMCs) consist of eight paired lineages found in the dorsoposterior regions of the CB. The black box indicates the region selected for live imaging, which contains only type I neuroblasts. **(B)** A time-series extracted from Movie 1 showing a cultured *His2aV::eGFP* brain (wL3) with a Type I neuroblast nucleus (yellow arrowhead) and a GMC nucleus (orange arrowhead) undergoing cell divisions. Timescale displayed as hh:mm:ss, scale bar = 10 μm.

glial cell subtypes which are critical for neural function. So-called type I neuroblasts are the most abundant and are found throughout the CNS (**Figure 1A**). They divide asymmetrically to self-renew and generate a transit-amplifying progenitor called ganglion mother cell (GMC) [reviewed by Sousa-Nunes and Hirth (2016)]. The GMC then undergoes a terminal division to produce two neuronal and/or glial progeny whereas the self-renewed neuroblast continues to proliferate. To compare our protocol to existing strategies for visualizing neuroblast dynamics, we imaged divisions in the central brain from animals dissected at the wL3 stage (**Figure 1**). To visualize chromatin we used *His2Av::eGFP*, a histone variant fused to an enhanced green fluorescent protein (eGFP); larval neuroblasts were identified as large (∼10–15 μm diameter) superficial cells (Truman and Bate, 1988). As expected, these cells underwent a self-renewing division to generate a neuroblast and a GMC (**Figure 1B** and Movie 1).

Between divisions, neuroblasts grew in size and their cell-cycle time was ~90 min, consistent with other reports (Cabernard and Doe, 2013; Homem et al., 2013). We also observed GMC divisions (**Figure 1B** and Movie 1). Although it has been reported that larval fat bodies are essential for sustaining neuroblast divisions *ex vivo* (Siller et al., 2005; Cabernard and Doe, 2013), we found them to be dispensable here. In summary, neural progenitor divisions proceeded as expected, demonstrating that our culture medium and immobilization technique can support them.

Neuroblast Reactivation

In contrast to many studies employing live imaging of neuroblasts from L3 CNSs, none as yet report imaging of neuroblast divisions in the more fragile first or second larval instars (L1/L2). Nonetheless, these earlier stages include specific processes of interest. By the end of embryogenesis, most neuroblasts enter a state of reversible cell cycle arrest termed quiescence (Truman and Bate, 1988; Valcourt et al., 2012). Following larval hatching and feeding, neuroblasts exit quiescence (reactivate) in an anteroposterior order (Truman and Bate, 1988; Britton and Edgar, 1998; Chell and Brand, 2010; Sousa-Nunes et al., 2011). Neuroblasts are relatively large when actively proliferating (10–15 μm diameter) (Chell and Brand, 2010; Sousa-Nunes et al., 2011) and are devoid of morphological polarity despite extensive molecular asymmetries during mitosis. In contrast, quiescent neuroblasts are much smaller (~4 μm diameter) and morphologically polarized, projecting a basal fiber into the neuropil (**Figure 2A**). This morphology is reminiscent of that of vertebrate radial glia (Weissman et al., 2003) and renders quiescent neuroblasts morphologically indistinguishable from adjacent neurons (**Figure 2A**). As they reactivate, neuroblasts enlarge and lose their fiber. We wondered whether fibers would be severed or retracted during neuroblast reactivation and endeavored to image this process live.

Young larval CNSs are more susceptible to mechanical stress than later ones, including to forces exerted by laminin or poly-L-lysine-coated surfaces (our own observations). Immobilizing L1 or L2 brains in this way invariably resulted in CNS rupture. While L1 and L2 CNSs did not rupture when immobilized under a fibrin clot (Lerit et al., 2014), we were unable to orient them at will to visualize neuroblasts clearly using this method (data not shown). The agarose-based immobilization approach described here proved sufficiently gentle and allowed for the desired orientation, enabling documentation of neuroblast reactivation for the first time.

To reactivate, neuroblasts require a fat body signal or downstream glial-derived Insulin-like peptides, produced in response to larval feeding (Britton and Edgar, 1998; Chell and Brand, 2010; Sousa-Nunes et al., 2011). Therefore, we imaged neuroblast reactivation in the ventral nerve cord of CNSs dissected at 22–24 h after larval hatching (late L1/early L2), in which nutritional-dependent signals are already present (reported by soma enlargement and EdU incorporation in the brain lobes (Britton and Edgar, 1998; Chell and Brand, 2010; Sousa-Nunes et al., 2011). *grainyhead (grh)-GAL4*, expressed in a subset of neuroblasts (Chell and Brand, 2010) was used to drive expression of *UAS-Syn21-GFP-p10*, a translationally enhanced GFP reporter (Pfeiffer et al., 2012). Several ventral nerve cord neuroblasts were observed reactivating and undergoing mitosis over the course of 17 h (**Figure 2B** and Movie 2). Mitoses were clearly recognizable by cells rounding prior to dividing into one larger apical daughter (renewed neuroblast) and one smaller basal daughter (the GMC). Neuroblast and GMC divisions

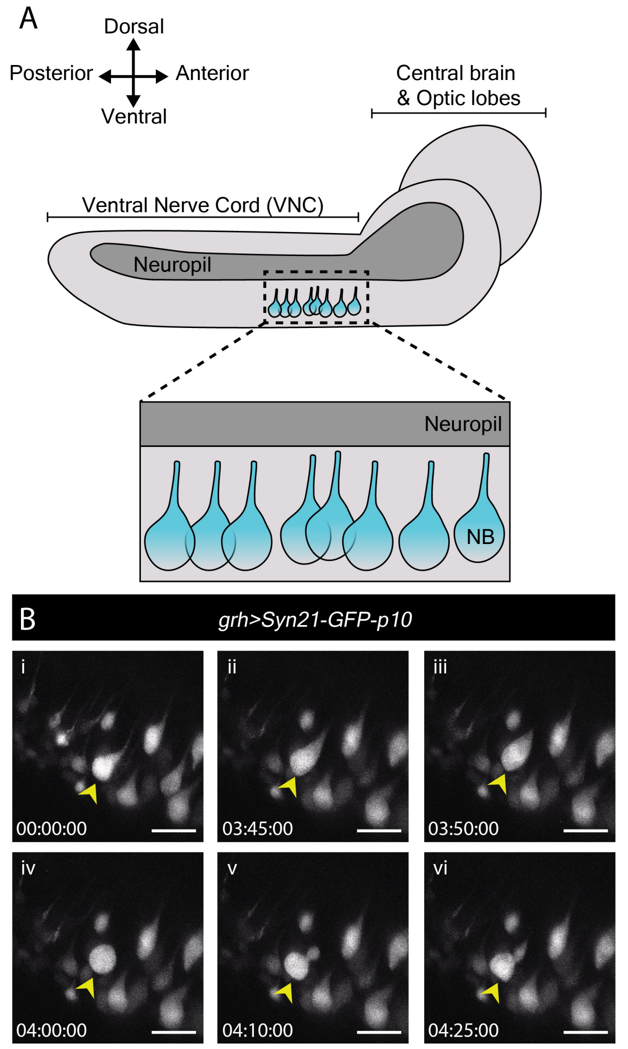

FIGURE 2 | Reactivation of quiescent neuroblasts in the L1/L2 CNS. **(A)** A schematic of the lateral view of an L1/L2 CNS. Neuroblasts, depicted in blue, are shown within the thoracic region of the ventral nerve chord (VNC, dashed box), the region selected for live imaging. Neuroblast (NB) cell bodies are situated on the ventral side of the VNC. During quiescence, they extend a fiber toward the neuropil. Upon reactivation, which occurs roughly 24 h after larval hatching for neuroblasts in the thoracic VNC, neuroblasts lose their fiber, which marks a relatively early morphogenetic event we sought to capture through our live imaging protocol. **(B)** A time-series extracted from Movie 2 of a cultured *grh > Syn21-GFP-p10* brain (L1/L2) showing an example neuroblast in the VNC (yellow arrowhead), which reactivates first by moving dorsally, then rounding before undergoing an asymmetric division to produce a dorsally positioned GMC. Timescale displayed as hh:mm:ss, scale bar = 10 μm.

continued after reactivation in a few cases ($n = 6$) indicating favorable conditions.

To our surprise, we found that neuroblasts retained their fiber throughout the first post-reactivation division and that the fiber was inherited by the first post-reactivation GMC (Movie 3, Part 1; $n = 19$). Asymmetric basal fiber inheritance has been described for zebrafish, rodent and human embryonic/fetal neural progenitors. Intriguingly, in contrast to what we observed in *Drosophila*, in those models it was generally the self-renewing progenitor that inherited the fiber (Weissman et al., 2003; Konno et al., 2008; Alexandre et al., 2010; Hansen et al., 2010; Shitamukai et al., 2011) although, on occasion, asymmetric inheritance by neuronal progeny was observed (Miyata et al., 2001; Konno et al., 2008), as was fiber splitting and seemingly symmetric inheritance by both daughter cells (Konno et al., 2008). In the few cases where we were able to follow the basal fiber throughout a GMC division ($n = 5$), the fiber appeared to be inherited by GMC progeny (Movie 3, Part 2). Further work is necessary to assess the generality of this finding, but we speculate that fiber inheritance by GMCs and then neuronal progeny could be a mechanism to develop neurites quickly, especially important for a fast-developing organism like *Drosophila*.

The above demonstrates that our protocol is well-suited to immobilize early larval brains even in the generally unstable side orientation for long-term neuroblast imaging, including observation of the first post-reactivation division and GMC fiber inheritance from quiescent neuroblasts, which has not been reported before.

Lamina Development in the L3 Optic Lobes

Next, we turned our attention to the developing L3 optic lobe, specifically focusing on the developing lamina. The lamina arises from a crescent-shaped neuroepithelium called the outer proliferation center (OPC), which is located at the surface of the optic lobe. The lateral edge of the OPC folds to form a structure called the lamina furrow (LF), from which lamina precursor cells (LPCs) are generated (**Figures 3A,B**). Photoreceptors from the eye disc grow their axons through the optic stalk and into the optic lobe where they defasciculate and contact the LF along the dorsoventral length of the OPC crescent. R1–R6 photoreceptors terminate their growth cones at the level of the LF (**Figure 3B**). Photoreceptors deliver Hedgehog through their axons and induce LPC formation from LF neuroepithelial cells (**Figure 3A**; Huang and Kunes, 1996; Huang et al., 1998). LPCs then associate with photoreceptor axons to form columns before differentiating into lamina neurons (Huang and Kunes, 1996; Huang et al., 1998; Umetsu et al., 2006; Fernandes et al., 2017).

To visualize lamina development we used *E-Cadherin::GFP* (*E-Cad::GFP*), which localizes to epithelial adherens junctions, together with the lamina-specific *(R27G05-GAL4)* expression of cytoplasmic *mCherry* (**Figure 3C** and Movie 4). Photoreceptor axons and the lamina furrow showed enriched *E-Cad::GFP* expression (**Figure 3C** and Movie 4). The lamina grew dramatically over the course of ∼18 h (**Figure 3C** and Movie 4). Interestingly, throughout this growth the lamina furrow remained relatively stable (**Figure 3C** and Movie 4 – asterisk), with lamina growth displacing older lamina columns posteriorly (Movie 4). This is in contrast to previous assumptions based on fixed images that the lamina furrow moved similarly to the morphogenetic furrow in the eye imaginal disc (Selleck and Steller, 1991; Huang and Kunes, 1998) and implies a different process by which LPCs are generated from the neuroepithelium.

The use of cytoplasmic mCherry prevented us from distinguishing individual LPCs and their incorporation into columns. We therefore switched to nuclear GFP (*UAS-nlsGFP*) driven by *glial cells missing (gcm)-GAL4,* which marks LPCs and lamina glia (**Figures 3A,B** and Movie 5). We manually tracked LPCs as they exited the LF through to incorporation into columns. Rather than column assembly progressing one column at a time, we observed that LPCs incorporated into the first 2–3 columns simultaneously, suggesting that multiple young columns are assembled together (Movie 5). This was surprising since it was generally assumed that the lamina is built one row of columns at a time (Umetsu et al., 2006; Sugie et al., 2010; Sato et al., 2013).

Glial and Neuronal Migration in the L3 Optic Lobes

In addition to LPCs, the developing lamina is also populated by glia. Epithelial and marginal glia are positioned above and below photoreceptor growth cones (**Figure 3A**). These glia originate from glial precursor cell domains at the dorsal and ventral tips of the lamina and migrate tangentially into the developing lamina (**Figure 3A**; Dearborn, 2004; Yoshida et al., 2005; Chen et al., 2016). When viewed in cross-section (Movie 5), we noticed that epithelial glia, situated above the photoreceptor growth cones (**Figure 3A**), were very motile and moved across photoreceptor growth cones and sometimes below to the level of marginal glia (Movie 5). Though they originate from the same domains, epithelial and marginal glia are distinct cell types (Chotard and Salecker, 2007; Edwards and Meinertzhagen, 2010; Edwards et al., 2012). While they express different molecular markers at later developmental stages, at L3 they have been distinguished solely by their by their relative positions on either side of photoreceptor growth cones (in fixed samples) (Chotard and Salecker, 2007; Edwards et al., 2012). In our L3 live imaging, lamina glial positions were not as stable as expected from previous descriptions (Movie 5). We also observed glial migration toward the anterior side of the lamina from posterior positions (Movie 5), most likely a consequence of glial incorporation into young lamina columns.

Epithelial and marginal glia have neuronal siblings, which develop into two neuron subtypes called lamina wide-field neurons 1 and 2 (Lawfs) (Chen et al., 2016; Suzuki et al., 2016). Lawfs are also born in the glial precursor cell domains and migrate tangentially but below the level of glia to incorporate into the deepest layers of the medulla (Chen et al., 2016). Since *gcm-GAL4* labels Lawfs as well as LPCs and lamina glia, we used it to express membrane-tagged GFP *(UAS-CD8::GFP)* to visualize glial and Lawf neuronal migration (Movie 6). Lawf migration was readily captured as described (Chen et al., 2016). However, the dense packing of labeled glia proved challenging

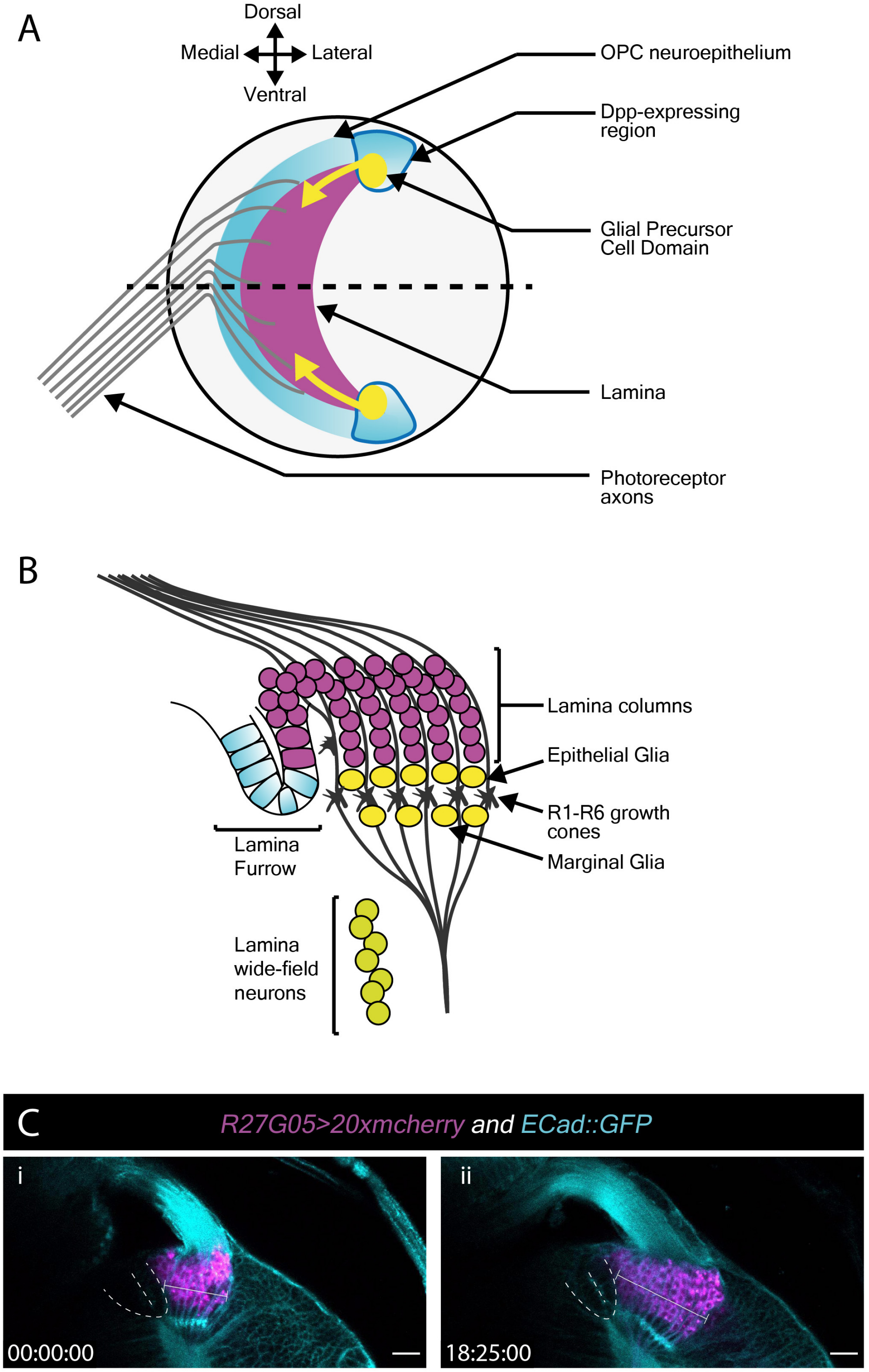

FIGURE 3 | Lamina development including the migration of epithelial and marginal glia, and lamina wide-field neurons (Lawf)**.** **(A)** Schematic of the lateral view of the third larval instar optic lobe. Developing photoreceptors project to a fold in the outer proliferation center neuroepithelium called the lamina furrow and induce lamina formation. **(B)** Diagram of a cross-section along the dotted line in A. The developing lamina forms in characteristic columns. Seven lamina precursor cells are incorporated into each column. Epithelial and marginal glia migrate above and below photoreceptor growth cones. Lawf neurons share the same progenitors as epithelial and marginal glia; they migrate from their point of origin at the tips of the lamina to the medulla, where they stop immediately adjacent to the neuropil. **(C)** Two timepoints extracted from Movie 3 of a cultured *R27G05* > *20xmcherry* (magenta) and *Ecad::GFP* (cyan) brain (wL3) showing the lamina, photoreceptor axons and surrounding tissue. The lamina furrow is marked by a dashed line. The lamina grows considerably over ~18 h as indicated by the bracket. Timescale displayed as hh:mm:ss, scale bar = 20 μm.

for tracking these cells (**Figure 3A** and Movie 6). We therefore switched to a sparse labeling technique, called FlexAmp (Bertet et al., 2014) to induce stochastic and permanent expression of *myristoylated-GFP (myr-GFP)* in the glial precursor cell domains and thus progeny originating therein. Using *dpp-GAL4* to induce sparse labeling, GFP-positive cells were observed at the dorsal and ventral tips of the lamina and in the lobula plug, where *dpp-GAL4* is expressed (**Figure 3A** and Movie 7). Furthermore, we could clearly track the migration of several glia originating from these domains into the lamina. These glia displayed many dynamic membrane protrusions (Movie 7), as inferred by others from fixed tissue (Poeck et al., 2001; Yoshida et al., 2005). Overall, we show that our live imaging protocol can be used to capture dynamic processes involved in cell migration during lamina development. We revealed cell behaviors that were not apparent from fixed tissue, including membrane protrusion dynamics during glial migration and epithelial and marginal glial incorporation into lamina columns, suggesting that these two glial cell types are not strictly separate until later in development.

Eye Disc Eversion

During wL3 stage, the eye-antennal discs (EADs) undergo complex remodeling to give rise to several adult head structures and the head epidermis (reviewed by Kumar, 2018). One of the most prominent metamorphic events that primes the EADs to generate their corresponding adult appendages is disc evagination, which is subdivided into two discrete processes – elongation and eversion (reviewed by Gibson and Schubiger, 2001). The EADs are comprised of two epithelial layers, the columnar disc proper and a squamous epithelium called peripodial membrane. The peripodial membrane sits atop and is continuous with the disc proper (**Figure 4**), with interaction between the two described as vital for disc eversion (Milner et al., 1983). To date, studies focused on this dynamic event have been limited to fixed tissues (Gibson and Schubiger, 2001), largely attributed to absence of appropriate culturing and immobilization systems given anisotropic forces exerted by biological glues that likely affect morphogenesis (Kumar, 2018).

We tested whether our culture system and immobilization technique could be used to capture EAD eversion. We dissected late L3 CNSs ubiquitously expressing a membrane-bound GFP (*ubi-GFP-CAAX*) with attached EADs. These explanted EADs immobilized in agarose underwent disc eversion within a period of 5 h (**Figure 4C** and Movie 8). The peripodial membrane appeared to contract and pull the eye disc proper toward the larval epidermis. The eye disc curled anteriorly taking on an oval shape, at the same time the antennal disc was molded into a circular shape. This morphological change of the antennal discs is important to drive their movement outside the larval epidermis and then fusion to form the adult head epidermis (Milner et al., 1984). Since our culture system and immobilization technique recapitulated disc eversion events as observed in histological studies of cultured EADs carried out by others (Milner et al., 1983), it can be used to study and visualize in real time how the peripodial membrane affects disc eversion. For example, EADs in which the peripodial membrane is genetically or physically ablated can be imaged live to further analyze the mechanics of disc eversion.

Stem Cell Maintenance in the Adult Testis

Ex vivo imaging can bypass many of the technical challenges associated with imaging adult tissues such as opaque cuticle and animal movement. To test whether our *ex vivo* imaging setup could be applied to adult tissue we focused on the *Drosophila* testis, a well-characterized model to study homeostatic mechanisms regulating stem cell behaviors in their intact microenvironment. The testis stem cell niche is composed of a cluster of quiescent stromal cells collectively known as the hub (Hardy et al., 1979). The hub is anchored at the apex of a blunt-ended coiled tube that forms the testis (**Figure 5A**). Hub cells support two stem cell populations, germline stem cells (GSCs) and somatic cyst stem cells (CySCs). GSCs and CySCs are physically attached to the hub, and their self-renewal is maintained by hub-derived signals (**Figure 5A**) (reviewed by Greenspan et al., 2015). The two stem cell populations are easily distinguishable by morphology and position. GSCs are large and round cells that tightly associate with the hub whereas CySC have smaller nuclei located behind GSCs and extend a thin membrane projection between GSCs to contact the hub (Hardy et al., 1979; **Figure 5A**).

Previous efforts to image the testis typically involved weighing down the tissue onto the culture dish using cellulose membranes, teflon sheets or coverslips (Cheng and Hunt, 2009; Sheng and Matunis, 2011; Inaba et al., 2015) or adhering the tissue to poly-L-lysine-coated coverslips (Lenhart and DiNardo, 2015; Greenspan and Matunis, 2017). These methods exert physical stress on the tissue during imaging. Here, we used our immobilization strategy to eliminate any non-specific effects of anisotropic forces exerted on the tissue. We used the somatic lineage-specific driver, *traffic jam (tj)-GAL4* to drive membrane targeted GFP (*UAS-CD8::GFP*), thus labeling the entire lineage including the CySCs and their progeny. As documented by others previously, the muscle sheath encasing the testis can cause contractility. Testes vary in contractility, and only testes with mild movements were chosen for imaging (Sheng and Matunis, 2011; Inaba et al., 2015). Post-acquisition computational drift correction (Correct 3D Drift Plugin, ImageJ – see Methods) was sufficient to generate a stable movie for analysis for testes that displayed minor contractility. We observed multiple CySC divisions (**Figure 5B** and Movie 9), during which CySC nuclei moved closer to the hub and rounded up. Unexpectedly, nuclear membrane labeling by CD8::GFP was apparent and persisted throughout CySC divisions, and we observed that this nuclear labeling could be reliably used to identify dividing CySCs (**Figure 5B**, and Movies 9, 10). This observation suggests that CySCs divide with a closed or semi-closed nuclear division as has been reported in other *Drosophila* cells including embryos, neuroblasts and germ cell meiosis (Church and Lin, 1982; Stafstrom and Staehelin, 1984; Debec and Marcaillou, 1997; Cheng et al., 2011; Boettcher and Barral, 2013; Roubinet et al., 2020). Recent work in neuroblasts implicates asymmetric nuclear division in the control of daughter

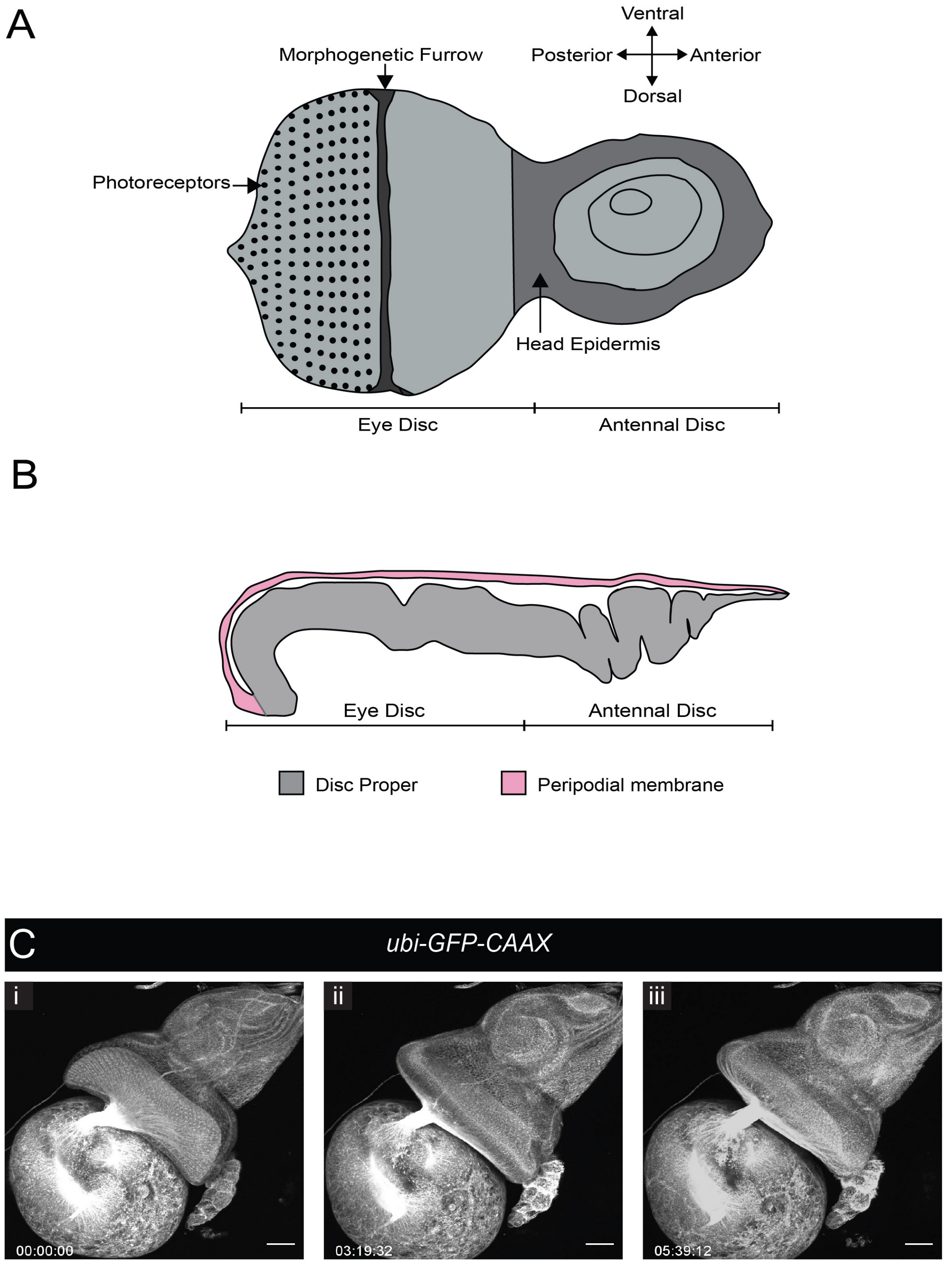

FIGURE 4 | Eye-antennal disc structure and disc eversion. **(A)** Schematic of an L3 eye-antennal disc. **(B)** Cross-section of the eye-antennal disc. The columnar epithelium of the disc proper at the anterior end (antennal side) is folded whereas that of the eye disc is stretched and convex in shape. The thin peripodial membrane sits above and is continuous with the disc proper which constitutes the eye disc and the antennal disc. **(C)** A time-series extracted from Movie 8 (maximum intensity projection) of a cultured *ubi-GFP-CAAX* eye-antennal disc-brain complex (wL3) showing the eye-antennal disc undergoing eversion. Timescale displayed as hr:mm:ss, scale bar = 40 μm.

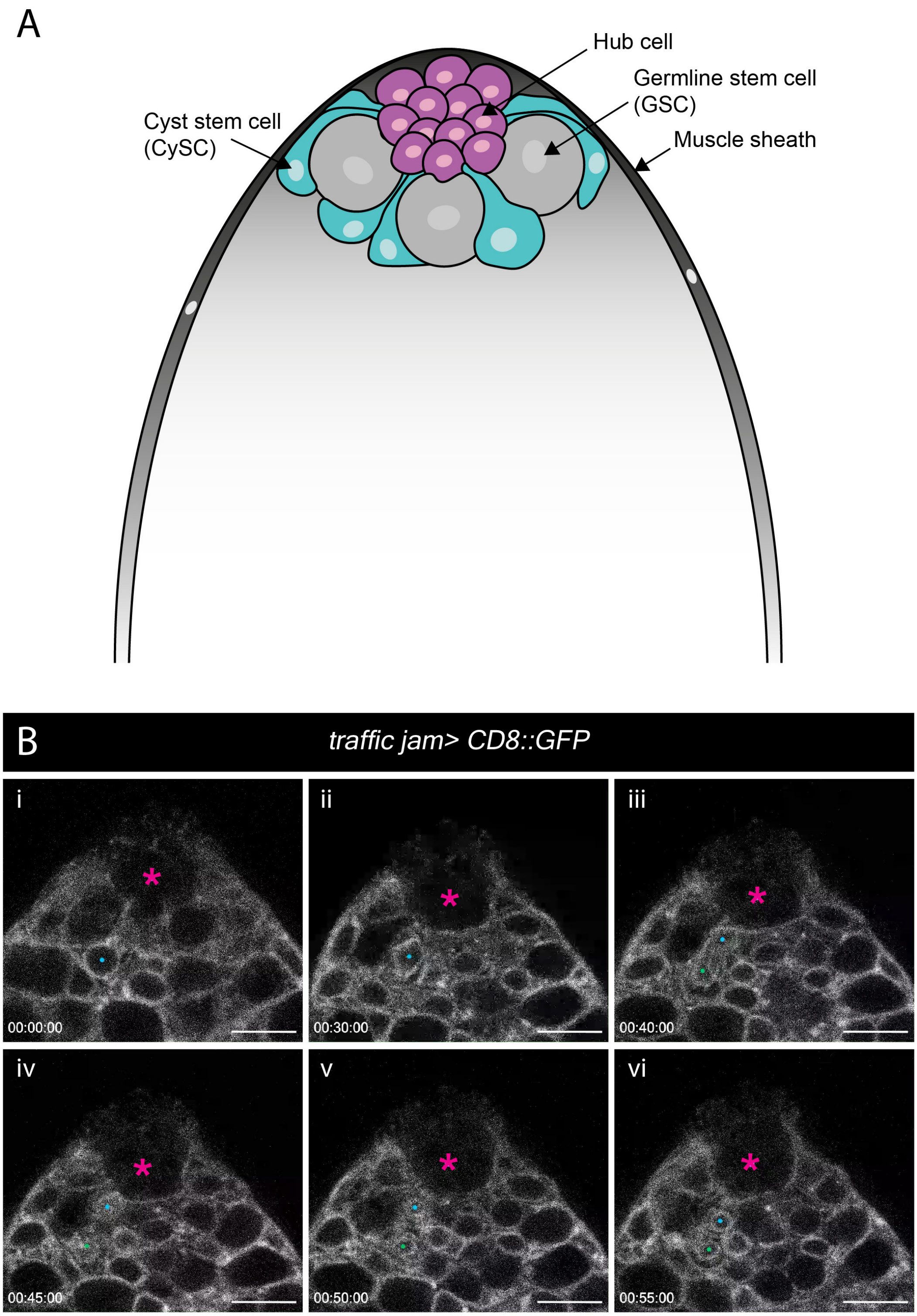

FIGURE 5 | Spatial organization of stem and niche cells in the adult testis and mitosis in the CySCs. **(A)** Schematic of the adult testis, which is encased in a muscle sheath (dark gray). Anchored at the apical tip of the tissue is a cluster of small post-mitotic cells known as the hub (magenta), which constitutes the stem cell niche. Two stem cell populations are in direct contact with the hub – germline stem cells (GSCs, gray) and cyst stem cells (CySCs, cyan). GSCs are large, round cells that closely associate with the hub. CySCs are located behind GSCs and extend thin membrane protrusions between GSCs to contact the hub. **(B)** A time-series extracted from Movie 9 of a cultured *traffic jam > CD8::GFP* adult testis. The hub is marked with a magenta asterisk. A CySC that undergoes a division is marked with a blue dot (i, ii). The nuclear membrane is visible during the division and takes on a characteristic diamond shape (ii) before the two daughter cells (blue and green dots; iii, vi) pull apart. Timescale displayed as hr:mm:ss, scale bar = 10 μm.

cell fates (Roubinet et al., 2020), raising the question of whether a similar mechanism may control cell fates in the testis. This work demonstrates that our protocol can be adjusted to track cellular behaviors in adult tissues.

CONCLUSION

Live imaging enables novel insights into dynamic biological processes of different scales, from the subcellular to the multicellular. Here we detail a simple and inexpensive protocol for immobilizing explanted tissues in any precise orientation desired, which supports long-term live imaging with minimal physical stress. We validated our approach by visualizing dynamic processes previously described for L3 brains and adult testes and applied it to make novel observations: (1) multiple lamina columns undergo assembly together, (2) dynamic membrane protrusions and extensions of epithelial and marginal glia during migration, (3) fibers of quiescent neuroblasts are inherited by the GMC upon reactivation, and (4) the nuclear membrane of adult CySCs does not break down completely during mitosis.

Our protocol is amenable to customization with minimal effort and could be used for experimental approaches requiring temperature shifts (e.g., 29°C for temperature-sensitive mutants or increased GAL4 activity), for approaches requiring acute drug treatment by combination with a flow perfusion apparatus (Williamson and Hiesinger, 2010), and to other species.

We note that this protocol is optimized for upright microscopes using a water-dipping objective. The upright set-up is useful for certain tissue orientations, but the protocol could be used with an inverted microscope using a glass-bottomed petri dish or a live cell chamber (Miszczak and Egger, 2020). When working with an inverted microscope set-up, users should consider the objective working distance and the volume of agarose for immobilization, however. While we have not tested our protocol with an inverted set-up, the volume of agarose used to immobilize the tissue may need to be reduced or the sample pushed closer to bottom to ensure close proximity to the glass bottom for imaging.

Overall, this protocol offers a simple, inexpensive and versatile method to immobilize explanted tissues for long-term live imaging.

DATA AVAILABILITY STATEMENT

All datasets presented in this study are included in the article/**Supplementary Material**.

AUTHOR CONTRIBUTIONS

MB and AP designed and performed L3 experiments with *gcm-GAL4* and *dpp-GAL4* (MB), and *ubi-GFP-CAAX* (AP). MB analyzed the data, prepared the figures and movies, and wrote the majority of the manuscript together with AP. RC performed the L1 experiments, analyzed the data, and prepared the figures and movies. RC and RS-N wrote the corresponding text. AY performed experiments related to the adult testis, analyzed the data, prepared the figures and movies, and wrote the corresponding text. RS-N and MA contributed to writing and editing the manuscript. VF designed and performed the experiments with *His2av::EGFP* and dual-fluorophore labelling of the lamina, supervised the project, and contributed to writing and editing the manuscript. All authors contributed to the article and approved the submitted version.

FUNDING

This project was funded by a Wellcome Trust and Royal Society Sir Henry Dale Research Fellowship (210472/Z/18/A) to VF, a Medical Research Council Career Development Award (MR/P009646/2) to MA, and a Cancer Research UK Career Development Fellowship (C45046/A14958) to RS-N.

ACKNOWLEDGMENTS

We are grateful to members of the Fernandes, Amoyel, and Sousa-Nunes lab for critical comments on the manuscript.

SUPPLEMENTARY MATERIAL

The Supplementary Material for this article can be found online at: https://www.frontiersin.org/articles/10.3389/fcell.2020.590094/full#supplementary-material

Supplementary Movie 1 | Neuroblast divisions in the third instar brain lobe. Time-lapse 2-photon imaging of wandering L3 (wL3) larval brain lobes. Example neuroblast and GMC divisions are highlighted; neuroblasts were identified by their large cell size. His2Av::eGFP marks chromosomes. Timescale displayed as hh:mm:ss, scale bar = 10 μm.

Supplementary Movie 2 | Neuroblasts reactivating from quiescence. Time lapse 2-photon imaging of *grh > syn21-GFP-p10* labeled neuroblasts in late L1 VNC. Explants oriented laterally to best visualize the neuroblast fibers, present during quiescence. The movie starts 24 h after larval hatching, a time when most VNC neuroblasts are quiescent. Reactivation divisions were first observed at movie time 1 h 40 min. Compared with membrane-localized GFP, cytoplasmic GFP requires higher levels of expression to achieve similar brightness in fine cellular processes due to unfavorable surface area-to-volume ratios (Pfeiffer et al., 2012). Timescale displayed as hh:mm:ss, scale bar = 20 μm.

Supplementary Movie 3 | Basal fiber inheritance upon neuroblast reactivation. (Part 1) Time lapse imaging of *grh > CD4::tdTomato* neuroblast in late L1 VNC undergoing first post-reactivation division. Movie captures fiber inheritance by the firstborn GMC. Timescale displayed as hh:mm:ss, scale bar = 10 μm. (Part 2) Time lapse imaging of a neuroblast and GMC labeled with *grh > CD8::GFP, syn21-GFP-p10*. The GMC which has inherited the fiber divides, and the fiber is inherited by one of the daughter cells. Time scale displayed as hh:mm:ss, scale bar = 5 μm.

Supplementary Movie 4 | Growth of the larval lamina. Time-lapse 2-photon imaging of *E-Cad::GFP* (cyan), *27G05 > mCherry* (magenta) demonstrating lamina growth. Brains were oriented to visualize the lamina in a lateral view. The lamina furrow, photoreceptors, and lamina columns were easily distinguishable using *E-Cad::GFP*; lamina precursors and neurons were labeled with *27G05 > mCherry*. We observed that whilst the lamina increased in width during the course of the movie (∼18 h) the position of the lamina furrow (asterisk) did not move significantly. Timescale displayed as hh:mm:ss, scale bar = 20 μm.

Supplementary Movie 5 | Incorporation of lamina precursor cells into lamina columns. Time-lapse 2-photon imaging of gcm > nlsGFP. We saw multiple LPCs from the lamina assembly domain incorporate into columns. The positions of the lamina furrow, lamina pre-assembly domain, photoreceptor axon entry point, lamina columns and epithelial and marginal glia are marked. In the first half of the movie LPCs were tracked (colored dots) and seen to incorporate into multiple columns simultaneously. In the second half, epithelial and marginal glia were tracked (colored dots) with several re-locating to different positions. Note: Dots remain in the last observed position of a cell if we could not track it due to movement out of plane. We also observed the incorporation of an epithelial glia into the youngest lamina column. Timescale displayed as hh:mm:ss, scale bar = 20 μm.

Supplementary Movie 6 | Migration of lamina wide-field neurons and epithelial and marginal glia. Time-lapse 2-photon imaging of *gcm > CD8::GFP* (expressed in Lawfs, epithelial and marginal glia and lamina precursors) captured the migration of Lawfs, and epithelial and marginal glia. The explant was oriented such that a cross-section of the lamina could be seen together with the dorsal arm of the lamina crescent. A maximum intensity projection is presented to account for movement in the z dimension. The video starts with Lawf migration marked by colored dots and the second half of the video shows epithelial and marginal glial migration, also marked by colored dots. Note: Dots remain in the last observed position of a cell if we could not track it due to movement out of plane. Timescale displayed as hh:mm:ss, scale bar = 20 μm.

Supplementary Movie 7 | Migration of epithelial and marginal glia. Using *dpp > flexamp* to induce stochastic expression of myristoylated-GFP, time-lapse 2-photon imaging was employed to capture eg/mg migration. The brains were oriented such that a lateral view of the lamina could be seen. A maximum intensity projection is presented to account for movement in the z dimension. The lobula plug and glial progenitor domains of the OPC can be seen. Epithelial and marginal glia migrate toward the central region of the lamina (marked with arrows). Epithelial and marginal glia migrating are labeled on the right-hand side of the lamina and their migration path is indicated. A cropped zoom clearly shows filopodia-like projections in migrating epithelial and marginal glia. Timescale displayed as hh:mm:ss, scale bar = 20 μm.

Supplementary Movie 8 | Eye-antennal disc eversion in third instar larva. Wandering L3 eye discs (attached to the underlying CNS) ubiquitously expressing membrane bound GFP (*ubi-GFP-CAAX*) to visualize eye-antennal disc eversion. As eversion begins, the peripodial epithelium is seen to contract (indicated by arrows) and pull the eye disc toward the antennal disc which becomes circular in shape. Disc eversion is completed within 5 h. Timescale displayed as hh:mm:ss, scale bar = 40 μm.

Supplementary Movie 9 | Cyst stem cell (CySC) division in the adult testis stem cell niche. A time-lapse movie of *tj > CD8::GFP*, which labels the somatic lineage. The hub is indicated by a magenta dot. CySCs are the first row of labeled cells around the hub. The CySC labeled with a blue dot undergoes a division to produce two daughter cells (blue and green dots). The nuclear membrane remains visible throughout mitosis of the CySC. Timescale displayed as hh:mm:ss, scale bar = 10 μm.

Supplementary Movie 10 | Nuclear envelope retention during CySC division. A time-lapse movie of *tj > CD8::GFP*, which labels the somatic lineage. The hub is marked by a blue dot, a dividing CySC is marked by a green dot. During mitosis, the labeled CySC rounded up. Once again, the nuclear membrane could be clearly observed during mitosis and adopted a distinctive diamond shape. Note that the division occurs out of plane such that only one daughter is visible after the division. Timescale displayed as hh:mm:ss, scale bar = 20 μm.

REFERENCES

Aimon, S., Katsuki, T., Jia, T., Grosenick, L., Broxton, M., Deisseroth, K., et al. (2019). Fast near-whole-brain imaging in adult Drosophila during responses to stimuli and behavior. *PLoS Biol.* 17:e2006732. doi: 10.1371/journal.pbio.2006732

Akin, O., and Zipursky, S. L. (2016). Frazzled promotes growth cone attachment at the source of a Netrin gradient in the *Drosophila* visual system. *eLife* 5:e20762. doi: 10.7554/eLife.20762

Aldaz, S., Escudero, L. M., and Freeman, M. (2010). Live imaging of *Drosophila* imaginal disc development. *Proc. Natl. Acad. Sci. U.S.A.* 107, 14217–14222. doi: 10.1073/pnas.1008623107

Alexandre, P., Reugels, A. M., Barker, D., Blanc, E., and Clarke, J. D. W. (2010). Neurons derive from the more apical daughter in asymmetric divisions in the zebrafish neural tube. *Nat. Neurosci.* 13, 673–679. doi: 10.1038/nn.2547

Baker, J., Theurkauf, W. E., and Schubiger, G. (1993). Dynamic changes in microtubule configuration correlate with nuclear migration in the preblastoderm Drosophila embryo. *J. Cell Biol.* 122, 113–121. doi: 10.1083/jcb.122.1.113

Balaji, R., Bielmeier, C., Harz, H., Bates, J., Stadler, C., Hildebrand, A., et al. (2017). Calcium spikes, waves and oscillations in a large, patterned epithelial tissue. *Sci. Rep.* 7:42786. doi: 10.1038/srep42786

Barlan, K., Cetera, M., and Horne-Badovinac, S. (2017). Fat2 and Lar define a basally localized planar signaling system controlling collective cell migration. *Dev. Cell* 40, 467–477.e5. doi: 10.1016/j.devcel.2017.02.003

Bell, D. M. (2017). Imaging morphogenesis. *Philos. Trans. R. Soc. B Biol. Sci.* 372:20150511. doi: 10.1098/rstb.2015.0511

Bertet, C., Li, X., Erclik, T., Cavey, M., Wells, B., and Desplan, C. (2014). Temporal patterning of neuroblasts controls notch-mediated cell survival through regulation of hid or reaper. *Cell* 158, 1173–1186. doi: 10.1016/j.cell.2014.07.045

Besson, C., Bernard, F., Corson, F., Rouault, H., Reynaud, E., Keder, A., et al. (2015). Planar cell polarity breaks the symmetry of PAR protein distribution prior to mitosis in *Drosophila* sensory organ precursor cells. *Curr. Biol.* 25, 1104–1110. doi: 10.1016/j.cub.2015.02.073

Boettcher, B., and Barral, Y. (2013). The cell biology of open and closed mitosis. *Nucleus* 4, 160–165. doi: 10.4161/nucl.24676

Bosveld, F., Bonnet, I., Guirao, B., Tlili, S., Wang, Z., Ambre, P., et al. (2012). Mechanical control of morphogenesis by fat/dachsous/four-jointed planar cell polarity pathway. *Science* 336, 724–727. doi: 10.1126/science.1221071

Britton, J. S., and Edgar, B. A. (1998). Environmental control of the cell cycle in Drosophila: nutrition activates mitotic and endoreplicative cells by distinct mechanisms. *Development* 125, 2149–2158.

Cabernard, C., and Doe, C. Q. (2013). Live imaging of neuroblast lineages within intact larval brains in *Drosophila*. *Cold Spring Harb. Protoc.* 2013, 970–977. doi: 10.1101/pdb.prot078162

Cavey, M., and Lecuit, T. (2008). Imaging cellular and molecular dynamics in live embryos using fluorescent proteins. *Methods Mol. Biol.* 420, 219–238. doi: 10.1007/978-1-59745-583-1_13

Chell, J. M., and Brand, A. H. (2010). Nutrition-responsive glia control exit of neural stem cells from quiescence. *Cell* 143, 1161–1173. doi: 10.1016/j.cell.2010.12.007

Chen, Z., Del Valle Rodriguez, A., Li, X., Erclik, T., Fernandes, V. M., and Desplan, C. (2016). A unique class of neural progenitors in the *Drosophila* optic lobe generates both migrating neurons and glia. *Cell Rep.* 15, 774–786. doi: 10.1016/j.celrep.2016.03.061

Cheng, J., and Hunt, A. J. (2009). Time-lapse live imaging of stem cells in drosophila testis. *Curr. Protoc. Stem Cell Biol.* 11, 2E.2.1–2E.2.8.

Cheng, J., Tiyaboonchai, A., Yamashita, Y. M., and Hunt, A. J. (2011). Asymmetric division of cyst stem cells in *Drosophila* testis is ensured by anaphase spindle repositioning. *Development* 138, 831–837. doi: 10.1242/dev.057901

Chotard, C., and Salecker, I. (2007). Glial cell development and function in the *Drosophila* visual system. *Neuron Glia Biol.* 3, 17–25. doi: 10.1017/S1740925X07000592

Church, K., and Lin, H. P. (1982). Meiosis in *Drosophila melanogaster*. II. The prometaphase-I kinetochore microtubule bundle and kinetochore orientation in males. *J. Cell Biol.* 93, 365–373. doi: 10.1083/jcb.93.2.365

Dearborn, R. (2004). An axon scaffold induced by retinal axons directs glia to destinations in the *Drosophila* optic lobe. *Development* 131, 2291–2303. doi: 10.1242/dev.01111

Debec, A., and Marcaillou, C. (1997). Structural alterations of the mitotic apparatus induced by the heat shock response in *Drosophila* cells. *Biol. Cell* 89, 67–78. doi: 10.1016/s0248-4900(99)80082-3

Distel, M., and Koster, R. W. (2007). In vivo time-lapse imaging of zebrafish embryonic development. *Cold Spring Harb. Protoc.* 2007:db.rot4816. doi: 10.1101/pdb.prot4816

Dye, N. A., Popoviæ, M., Spannl, S., Etournay, R., Kainmüller, D., Ghosh, S., et al. (2017). Cell dynamics underlying oriented growth of the drosophila wing imaginal disc. *Development* 144, 4406–4421. doi: 10.1242/dev.155069

Echalier, G. (ed.). (1997). "Composition of the body fluid of *Drosophila* and the design of culture media for *Drosophila* cells," in *Drosophila Cells in Culture*, (Cambridge, MA: Academic Press), 1–67. doi: 10.1016/b978-012229460-0/50002-6

Edwards, T. N., and Meinertzhagen, I. A. (2010). The functional organisation of glia in the adult brain of *Drosophila* and other insects. *Prog. Neurobiol.* 90, 471–497. doi: 10.1016/j.pneurobio.2010.01.001

Edwards, T. N., Nuschke, A. C., Nern, A., and Meinertzhagen, I. A. (2012). Organization and metamorphosis of glia in the *Drosophila* visual system. *J. Comp. Neurol.* 2085, 2067–2085. doi: 10.1002/cne.23071

Farhadifar, R., Ro, J., Aigouy, B., and Eaton, S. (2007). The influence of cell mechanics, cell-cell interactions, and proliferation on epithelial packing. *Curr. Biol.* 17, 2095–2104. doi: 10.1016/j.cub.2007.11.049

Fernandes, V. M., Chen, Z., Rossi, A. M., Zipfel, J., and Desplan, C. (2017). Glia relay differentiation cues to coordinate neuronal development in *Drosophila*. *Science* 891, 886–891. doi: 10.1126/science.aan3174

Fiala, A., Spall, T., Eisermann, B., Sachse, S., Devaud, J., Buchner, E., et al. (2002). Genetically expressed cameleon in *Drosophila melanogaster* is used to visualize olfactory information in projection neurons. *Curr. Biol.* 12, 1877–1884. doi: 10.1016/s0960-9822(02)01239-3

Foe, V. E., and Alberts, B. M. (1983). Studies of nuclear and cytoplasmic behaviour during the five mitotic cycles that precede gastrulation in Drosophila embryogenesis. *J. Cell Sci.* 61, 31–70.

Ghannad-Rezaie, M., Wang, X., Mishra, B., Collins, C., and Chronis, N. (2012). Microfluidic chips for *in vivo* imaging of cellular responses to neural injury in *Drosophila* larvae. *PLoS One* 7:e29869. doi: 10.1371/journal.pone.0029869

Gibson, M. C., and Schubiger, G. (2001). *Drosophila* peripodial cells, more than meets the eye? *BioEssays* 23, 691–697. doi: 10.1002/bies.1098

Greenspan, L. J., de Cuevas, M., and Matunis, E. (2015). Genetics of gonadal stem cell renewal. *Annu. Rev. Cell Dev. Biol.* 31, 291–315. doi: 10.1146/annurev-cellbio-100913-013344

Greenspan, L. J., and Matunis, E. L. (2017). "Live imaging of the drosophila testis stem cell niche," in *Methods in Molecular Biology*, ed. M. Buszczak (New York, NY: Humana Press), 63–74. doi: 10.1007/978-1-4939-4017-2_4

Hansen, D. V., Lui, J. H., Parker, P. R. L., and Kriegstein, A. R. (2010). Neurogenic radial glia in the outer subventricular zone of human neocortex. *Nature* 464, 554–561. doi: 10.1038/nature08845

Hardy, R. W., Tokuyasu, K. T., Lindsley, D. L., and Garavito, M. (1979). The germinal proliferation center in the testis of *Drosophila melanogaster*. *J. Ultrasruct. Res.* 69, 180–190. doi: 10.1016/s0022-5320(79)90108-4

Heemskerk, I., Lecuit, T., and LeGoff, L. (2014). Dynamic clonal analysis based on chronic *in vivo* imaging allows multiscale quantification of growth in the *Drosophila* wing disc. *Development* 141, 2339–2348. doi: 10.1242/dev.109264

Hellerman, M. B., Choe, R. H., and Johnson, R. I. (2015). Live-imaging of the *Drosophila* pupal eye. *J. Vis. Exp.* 95:52120. doi: 10.3791/52120

Homem, C. C. F., Reichardt, I., Berger, C., Lendl, T., and Knoblich, J. A. (2013). Long-term live cell imaging and automated 4D analysis of *Drosophila* neuroblast lineages. *PLoS One* 8:e79588. doi: 10.1371/journal.pone.0079588

Huang, J., Zhou, W., Dong, W., Watson, A. M., and Hong, Y. (2009). Directed, efficient, and versatile modifications of the *Drosophila* genome by genomic engineering. *Proc. Natl. Acad. Sci. U.S.A.* 106, 8284–8289. doi: 10.1073/pnas.0900641106

Huang, Z., and Kunes, S. (1996). Hedgehog, transmitted along retinal axons, triggers neurogenesis in the developing visual centers of the Drosophila brain. *Cell* 86, 411–422. doi: 10.1016/s0092-8674(00)80114-2

Huang, Z., and Kunes, S. (1998). Signals transmitted along retinal axons in Drosophila: hedgehog signal reception and the cell circuitry of lamina cartridge assembly. *Development* 125, 3753–3764.

Huang, Z., Shilo, B., and Kunes, S. (1998). A retinal axon fascicle uses spitz, an EGF receptor ligand, to construct a synaptic cartridge in the brain of *Drosophila*. *Cell* 95, 693–703. doi: 10.1016/s0092-8674(00)81639-6

Huisken, J., and Stainier, D. Y. R. (2009). Selective plane illumination microscopy techniques in developmental biology. *Development* 136, 1963–1975. doi: 10.1242/dev.022426

Ichikawa, T., Nakazato, K., Keller, P. J., Kajiura-Kobayashi, H., Stelzer, E. H. K., Mochizuki, A., et al. (2014). Live imaging and quantitative analysis of gastrulation in mouse embryos using light-sheet microscopy and 3D tracking tools. *Nat. Protoc.* 9, 575–585. doi: 10.1038/nprot.2014.035

Inaba, M., Buszczak, M., and Yamashita, Y. M. (2015). Nanotubes mediate niche-stem-cell signalling in the *Drosophila* testis. *Nature* 523, 329–332. doi: 10.1038/nature14602

Jacinto, A., Wood, W., Balayo, T., Turmaine, M., Martinez-arias, A., and Martin, P. (2000). Dynamic actin-based epithelial adhesion and cell matching during *Drosophila* dorsal closure. *Curr. Biol.* 10, 1420–1426. doi: 10.1016/s0960-9822(00)00796-x

Kaltschmidt, J. A., Davidson, C. M., Brown, N. H., and Brand, A. H. (2000). Rotation and asymmetry of the mitotic spindle direct asymmetric cell division in the developing central nervous system. *Nat. Cell Biol.* 2, 7–12. doi: 10.1038/71323

Kiehart, D. P., Galbraith, C. G., Edwards, K. A., Rickoll, W. L., and Montague, R. A. (2000). Multiple forces contribute to cell sheet morphogenesis for dorsal closure. *J. Cell Biol.* 149, 471–490. doi: 10.1083/jcb.149.2.47

Konno, D., Shioi, G., Shitamukai, A., Mori, A., Kiyonari, H., Miyata, T., et al. (2008). Neuroepithelial progenitors undergo LGN-dependent planar divisions to maintain self-renewability during mammalian neurogenesis. *Nat. Cell Biol.* 10, 93–101. doi: 10.1038/ncb1673

Kumar, J. P. (2018). The fly eye?: through the looking glass. *Dev. Dyn.* 247, 111–123. doi: 10.1002/dvdy.24585

Lee, C., Andersen, R. O., Cabernard, C., Manning, L., Tran, K. D., Lanskey, M. J., et al. (2006). *Drosophila* Aurora-A kinase inhibits neuroblast self-renewal by regulating aPKC/Numb cortical polarity and spindle orientation. *Genes Dev.* 20, 3464–3474. doi: 10.1101/gad.1489406

Lenhart, K. F., and DiNardo, S. (2015). Somatic cell encystment promotes abscission in germline stem cells following a regulated block in cytokinesis. *Dev. Cell* 34, 192–205. doi: 10.1016/j.devcel.2015.05.003

Lerit, D. A., Plevock, K. M., and Rusan, N. M. (2014). Live imaging of *Drosophila* larval neuroblasts. *J. Vis. Exp.* 89:51756. doi: 10.3791/51756

Mao, Y., Tournier, A. L., Bates, P. A., Gale, J. E., Tapon, N., and Thompson, B. J. (2011). Planar polarization of the atypical myosin Dachs orients cell divisions in *Drosophila*. *Genes Dev.* 25, 131–136. doi: 10.1101/gad.610511

Martin, J. L., Sanders, E. N., Moreno-roman, P., Ann, L., Koyama, J., Balachandra, S., et al. (2018). Long-term live imaging of the *Drosophila* adult midgut reveals real-time dynamics of division, differentiation and loss. *eLife* 7:e36248. doi: 10.7554/eLife.36248

Milner, M. J., Bleasby, A. J., and Pyott, A. (1983). The role of the peripodial membrane in the morphogenesis of the eye-antennal disc of *Drosophila melanogaster*. *Rouxs Arch. Dev. Biol.* 192, 164–170. doi: 10.1007/bf00848686

Milner, M. J., Bleasby, A. J., and Pyott, A. (1984). Cell interactions during the fusion *in vitro* of *Drosophila* eye-antennal imaginal discs. *Rouxs Arch. Dev. Biol.* 193, 406–413. doi: 10.1007/bf00848232

Miszczak, K., and Egger, B. (2020). "Live cell imaging of neural stem cells in the Drosophila larval brain," in *Brain Development: Methods and Protocols, Methods in Molecular Biology*, ed. S. G. Sprecher (Berlin: Springer Science+Business Media), 153–160. doi: 10.1007/978-1-4939-9732-9_9

Miyata, T., Kawaguchi, A., Okano, H., and Ogawa, M. (2001). Asymmetric inheritance of radial glial fibers by cortical neurons. *Neuron* 31, 727–741. doi: 10.1016/s0896-6273(01)00420-2

Nickerson, P. E., Ronellenfitch, K. M., Csuzdi, N. F., Boyd, J. D., Howard, P. L., Delaney, K. R., et al. (2013). Live imaging and analysis of postnatal mouse retinal development. *BMC Dev. Biol.* 13:24. doi: 10.1186/1471-213X-13-24

Ozel, M. N., Langen, M., Hassan, B. A., and Hiesenger, R. P. (2015). Filopodial dynamics and growth cone stabilization in *Drosophila* visual circuit development. *eLife* 4:e10721. doi: 10.7554/eLife.10721

Parslow, A., Cardona, A., and Bryson-Richardson, R. J. (2014). Sample drift correction following 4D confocal time-lapse imaging. *J. Vis. Exp.* 86:51086. doi: 10.3791/51086

Parton, R. M., Vallés, A. M., Dobbie, I. M., and Davi, I. (2010). Live cell imaging in *Drosophila melanogaster*. *Cold Spring Harb. Protoc.* 5:db.to75. doi: 10.1101/pdb.top75

Pfeiffer, B. D., Truman, J. W., and Rubin, G. M. (2012). Using translational enhancers to increase transgene expression in *Drosophila*. *Proc. Natl. Acad. Sci. U.S.A.* 109, 6626–6631. doi: 10.1073/pnas.1204520109

Poeck, B., Fischer, S., Gunning, D., Zipursky, S. L., and Salecker, I. (2001). Glial cells mediate target layer selection of retinal axons in the developing visual system of *Drosophila*. *Neuron* 29, 99–113. doi: 10.1016/s0896-6273(01)00183-0

Prasad, M., Wang, X., He, L., Cai, D., and Montell, D. J. (2015). Border cell migration: a model system for live imaging and genetic analysis of collective cell movement. *Methods Mol. Biol.* 1328, 89–97. doi: 10.1007/978-1-4939-2851-4_6

Rabinovich, D., Mayseless, O., and Schuldiner, O. (2015). Long term *ex vivo* culturing of *Drosophila* brain as a method to live image pupal brains: insights into the cellular mechanisms of neuronal remodeling. *Front. Cell. Neurosci.* 9:327. doi: 10.3389/fncel.2015.00327

Restrepo, S., Zartman, J. J., and Basler, K. (2016). "Cultivation and live imaging of *Drosophila* imaginal discs," in *Drosophila: Methods and Protocols, Methods in Molecular Biology*, ed. C. Dahmann (New York, NY: Springer Science+Business Media), 203–213. doi: 10.1007/978-1-4939-6371-3_11

Ritsma, L., Ellenbroek, S. I. J., Zomer, A., Snippert, H. J., De Sauvage, F. J., Simons, B. D., et al. (2014). Intestinal crypt homeostasis revealed at single-stem-cell level by in vivo live imaging. *Nature* 507, 362–365. doi: 10.1038/nature12972

Rossi, A. M., and Fernandes, V. M. (2018). Wrapping glial morphogenesis and signaling control the timing and pattern of neuronal differentiation in the *Drosophila* lamina. *J. Exp. Neurosci.* 12:1179069518759294. doi: 10.1177/1179069518759294

Roubinet, C., White, I. J., and Baum, B. (2020). Asymmetric nuclear division of neural stem cells contributes to the formation of sibling nuclei with different identities. *bioRxiv [Preprint]* doi: 10.1101/2020.08.29.272724

Sanchez-Corrales, Y. E., Blanchard, G. B., and Röper, K. (2018). Radially patterned cell behaviours during tube budding from an epithelium. *eLife* 7:e35717. doi: 10.7554/eLife.35717

Sano, H., Renault, A. D., and Lehmann, R. (2005). Control of lateral migration and germ cell elimination by the *Drosophila melanogaster* lipid phosphate phosphatases Wunen and Wunen 2. *J. Cell Biol.* 171, 675–683. doi: 10.1083/jcb.200506038

Sato, M., Suzuki, T., and Nakai, Y. (2013). Waves of differentiation in the fly visual system. *Dev. Biol.* 380, 1–11. doi: 10.1016/j.ydbio.2013.04.007

Savoian, M. S., and Rieder, C. L. (2002). Mitosis in primary cultures of *Drosophila melanogaster* larval neuroblasts. *J. Cell Sci.* 115, 3061–3072.

Seelig, J. D., Chiappe, M. E., Lott, G. K., Dutta, A., Osborne, J. E., Reiser, M. B., et al. (2010). Two-photon calcium imaging from head-fixed *Drosophila* during optomotor walking behavior. *Nat. Methods* 7, 535–540. doi: 10.1038/nmeth.1468

Selleck, S. B., and Steller, H. (1991). The Influence of retinal innervation on neurogenesis in the first optic ganglion of Drosophila. *Neuron* 6, 83–99. doi: 10.1016/0896-6273(91)90124-i

Sheng, X. R., and Matunis, E. (2011). Live imaging of the *Drosophila* spermatogonial stem cell niche reveals novel mechanisms regulating germline stem cell output. *Development* 138, 3367–3376. doi: 10.1242/dev.065797

Shitamukai, A., Konno, D., and Matsuzaki, F. (2011). Oblique radial glial divisions in the developing mouse neocortex induce self-renewing progenitors outside the germinal zone that resemble primate outer subventricular zone progenitors. *J. Neurosci.* 31, 3683–3695. doi: 10.1523/JNEUROSCI.4773-10.2011

Siller, K. H., and Doe, C. Q. (2008). Lis1/dynactin regulates metaphase spindle orientation in *Drosophila* neuroblasts. *Dev. Biol.* 319, 1–9. doi: 10.1016/j.ydbio.2008.03.018

Siller, K. H., Serr, M., Steward, R., Hays, T. S., and Doe, C. Q. (2005). Live imaging of Drosophila brain neuroblasts reveals a role for Lis1/dynactin in spindle assembly and mitotic checkpoint control. *Mol. Biol. Cell* 16, 5127–5140. doi: 10.1091/mbc.E05

Sousa-Nunes, R., and Hirth, F. (2016). "Stem cells and asymmetric cell division," in *Regenerative Medicine - from Protocol to Patient: 1. Biology of Tissue Regeneration*, ed. G. Steinhoff (Cham: Springer International Publishing), 87–121. doi: 10.1007/978-3-319-27583-3_3

Sousa-Nunes, R., Yee, L. L., and Gould, A. P. (2011). Fat cells reactivate quiescent neuroblasts via TOR and glial insulin relays in *Drosophila*. *Nature* 471, 508–513. doi: 10.1038/nature09867

Speder, P., and Brand, A. H. (2014). Gap junction proteins in the blood-brain barrier control nutrient-dependent reactivation of *Drosophila* neural stem cells. *Dev. Cell* 30, 309–321. doi: 10.1016/j.devcel.2014.05.021

Stafstrom, J. P., and Staehelin, L. A. (1984). Dynamics of the nuclear envelope and of nuclear pore complexes during mitosis in the *Drosophila* embryo. *Eur. J. Cell Biol.* 34, 179–189.

Sugie, A., Umetsu, D., Yasugi, T., Fischbach, K. F., and Tabata, T. (2010). Recognition of pre- and postsynaptic neurons via nephrin/NEPH1 homologs is a basis for the formation of the *Drosophila* retinotopic map. *Development* 137, 3303–3313. doi: 10.1242/dev.047332

Suzuki, T., Hasegawa, E., Nakai, Y., Kaido, M., Takayama, R., and Sato, M. (2016). Formation of neuronal circuits by interactions between neuronal populations derived from different origins in the *Drosophila* visual center. *Cell Rep.* 15, 499–509. doi: 10.1016/j.celrep.2016.03.056

Tan, L., Zhang, K. X., Pecot, M. Y., Nagarkar-Jaiswal, S., Lee, P. T., Takemura, S. Y., et al. (2015). Ig superfamily ligand and receptor pairs expressed in synaptic partners in *Drosophila*. *Cell* 163, 1756–1769. doi: 10.1016/j.cell.2015.11.021

Truman, J. W., and Bate, M. (1988). Spatial and temporal patterns of neurogenesis in the central nervous system of *Drosophila melanogaster*. *Dev. Biol.* 125, 145–157. doi: 10.1016/0012-1606(88)90067-X

Tsao, C. K., Ku, H. Y., Lee, Y. M., Huang, Y. F., and Sun, Y. H. (2016). Long term *ex vivo* culture and live imaging of *Drosophila* larval imaginal discs. *PLoS One* 11:e0163744. doi: 10.1371/journal.pone.0163744

Umetsu, D., Murakami, S., Sato, M., and Tabata, T. (2006). The highly ordered assembly of retinal axons and their synaptic partners is regulated by Hedgehog / Single-minded in the *Drosophila* visual system. *Development* 133, 791–800. doi: 10.1242/dev.02253

Valcourt, J. R., Lemons, J. M. S., Haley, E. M., Kojima, M., Demuren, O. O., and Coller, H. A. (2012). Staying alive: metabolic adaptations to quiescence. *Cell Cycle* 11, 1680–1696. doi: 10.4161/cc.19879

Weissman, T., Noctor, S. C., Clinton, B. K., Honig, L. S., and Kriegstein, A. R. (2003). Neurogenic radial glial cells in reptile, rodent and human: from mitosis to migration. *Cereb. Cortex* 13, 550–559. doi: 10.1093/cercor/13.6.550

Williamson, W. R., and Hiesinger, P. R. (2010). Preparation of developing and adult *Drosophila* brains and retinae for live imaging. *J. Vis. Exp.* 37:e1936. doi: 10.3791/1936

Wyss, C. (1982). Ecdysterone, insulin and fly extract needed for the proliferation of normal *Drosophila* cells in defined medium. *Exp. Cell Res.* 139, 297–307. doi: 10.1016/0014-4827(82)90254-3

Yoshida, S., Soustelle, L., Giangrande, A., Umetsu, D., Murakami, S., Yasugi, T., et al. (2005). DPP signaling controls development of the lamina glia required forretinal axon targeting in the visual system of *Drosophila*. *Development* 132, 4587–4598. doi: 10.1242/dev.02040

Zartman, J., Restrepo, S., Basler, K., Zartman, J., Restrepo, S., and Basler, K. (2013). A high-throughput template for optimizing *Drosophila* organ culture with response-surface methods. *Development* 2848, 667–674. doi: 10.1242/dev.098921

Conflict of Interest: The authors declare that the research was conducted in the absence of any commercial or financial relationships that could be construed as a potential conflict of interest.

frontiers
in Cell and Developmental Biology

METHODS
published: 20 August 2021
doi: 10.3389/fcell.2021.685825

Correcting Artifacts in Ratiometric Biosensor Imaging; an Improved Approach for Dividing Noisy Signals

Daniel J. Marston[1], Scott D. Slattery[1], Klaus M. Hahn[1,2]* and Denis Tsygankov[3]*

[1] Department of Pharmacology, University of North Carolina at Chapel Hill, Chapel Hill, NC, United States, [2] Lineberger Comprehensive Cancer Center, University of North Carolina at Chapel Hill, Chapel Hill, NC, United States, [3] Wallace H. Coulter Department of Biomedical Engineering, Georgia Institute of Technology and Emory University School of Medicine, Atlanta, GA, United States

Edited by:
Abhishek Kumar,
Marine Biological Laboratory (MBL),
United States

Reviewed by:
Matthew Anderson,
National Cancer Institute at Frederick,
United States
Ariz Mohammad,
Washington University in St. Louis,
United States

***Correspondence:**
Klaus M. Hahn
khahn@med.unc.edu
Denis Tsygankov
denis.tsygankov@bme.gatech.edu

Specialty section:
This article was submitted to
Cell Growth and Division,
a section of the journal
Frontiers in Cell and Developmental
Biology

Received: *25 March 2021*
Accepted: *02 August 2021*
Published: *20 August 2021*

Citation:
Marston DJ, Slattery SD,
Hahn KM and Tsygankov D (2021)
Correcting Artifacts in Ratiometric
Biosensor Imaging; an Improved
Approach for Dividing Noisy Signals.
Front. Cell Dev. Biol. 9:685825.
doi: 10.3389/fcell.2021.685825

The accuracy of biosensor ratio imaging is limited by signal/noise. Signals can be weak when biosensor concentrations must be limited to avoid cell perturbation. This can be especially problematic in imaging of low volume regions, e.g., along the cell edge. The cell edge is an important imaging target in studies of cell motility. We show how the division of fluorescence intensities with low signal-to-noise at the cell edge creates specific artifacts due to background subtraction and division by small numbers, and that simply improving the accuracy of background subtraction cannot address these issues. We propose a new approach where, rather than simply subtracting background from the numerator and denominator, we subtract a noise correction factor (NCF) from the numerator only. This NCF can be derived from the analysis of noise distribution in the background near the cell edge or from ratio measurements in the cell regions where signal-to-noise is high. We test the performance of the method first by examining two noninteracting fluorophores distributed evenly in cells. This generated a uniform ratio that could provide a ground truth. We then analyzed actual protein activities reported by a single chain biosensor for the guanine exchange factor (GEF) Asef, and a dual chain biosensor for the GTPase Cdc42. The reduction of edge artifacts revealed persistent Asef activity in a narrow band (~640 nm wide) immediately adjacent to the cell edge. For Cdc42, the NCF method revealed an artifact that would have been obscured by traditional background subtraction approaches.

Keywords: ratiometric analysis, FRET biosensors, cell morphodynamics, image processing, Rho (Rho GTPase)

INTRODUCTION

Förster resonance energy transfer (FRET) biosensors are powerful, widely used tools for visualization and analysis of protein activities that include conformational changes, post-translational modification, and ligand interactions. Signaling proteins, like the Rho family GTPase and GEF studied here, function differently in their active and inactive conformations, so it is important to differentiate their overall distributions from the distribution of specific active conformations (Rossman et al., 2005; Hall, 2012). In FRET biosensors, the conformational changes of the target protein typically modulate the separation or orientation of two fluorophores, a FRET donor and a FRET acceptor (Hochreiter et al., 2015; Greenwald et al., 2018; Terai et al., 2019). This produces a conformation-dependence of the FRET intensity (acceptor emission upon donor excitation). In ratiometric imaging, the FRET intensity is divided by the fluorescence intensity of the directly excited donor or acceptor fluorophore at each point in the cell. This ratio reflects the conformation of the target protein. Use of a ratio rather than simply measuring FRET intensity reduces artifacts produced by variations in cell volume or biosensor distribution (Kurokawa et al., 2004; Pertz et al., 2006).

Processing FRET biosensor data to produce ratios involves a number of steps, each of which can affect the accuracy of the final result [e.g., shade correction, masking, subtraction of background fluorescence in each channel, correction for bleed-through between the channels, and correction for photobleaching (Machacek et al., 2009; Hodgson et al., 2010)]. Here we focus on artifacts produced when noise and background subtraction exert strong effects on the final ratio. Errors introduced by oft-used procedures can create artefactual, apparent gradients in the ratio near the cell edge, a region particularly important when studying cell morphodynamics. When relatively flat cells are used to study motility, important actin dynamics occur in a thin region within 2–3 microns of the edge (Pertz et al., 2006; Machacek et al., 2009; Marston et al., 2020). The small volume of this region decreases signal/noise and increases the magnitude of background subtraction errors relative to the real signal. Importantly these effects increase as we move toward the cell edge and volume decreases. We show here how and why this region is prone to artifacts, and propose a correction method, the noise correction factor (NCF), that eliminates the need for background subtraction. The method can be applied in many types of ratio imaging where background subtraction can be problematic.

The paper begins with a simplified model of the problem, based on considering a hypothetical cell with thickness gradually decreasing as we move closer to the edge. This model is used to illustrate issues with background subtraction and noise that generate artefactual gradients in ratios, and to explain the rationale behind the NCF method. We demonstrate the artefactual gradients in real cells and look more closely at the role that background subtraction plays in such artifacts. Using an "inert biosensor" that would be expected to produce a uniform ratio throughout the cell, we demonstrate why improving the accuracy of background subtraction actually amplifies the artefactual gradient associated with division by low signal-to-noise values. Finally, we provide mathematical derivations that justify the use of NCF to produce an artifact-free ratio. These theoretical considerations are tested by applying the NCF method to two additional biosensors: a single-chain biosensor for Asef, and a dual-chain biosensor for the GTPase Cdc42. For the Asef biosensor, by eliminating the noise-related artifact we eliminated spurious activity at the cell edge, revealing real GEF activation in a 2-pixel wide band along the periphery. For the GTPase biosensor, improved visualization of near edge regions revealed problematic areas that needed to be excluded from ratio analysis.

RESULTS

A Hypothetical Cell Model Illustrating Effects of Noise on Ratio Values

Here we consider a simple cell model to establish the new approach; it will be applied to real cells in the following sections. FRET is defined as the fluorescence intensity emitted from the acceptor upon donor excitation, excluding any contribution from background, spectral bleedthrough or other artifacts. Emission from the "FRET channel," on the other hand, is the intensity measured when the microscope is configured to monitor donor excitation and acceptor emission, including contributions from bleedthrough, background, etc. Analogously, monitoring the "Donor channel" refers to quantifying light actually collected when monitoring donor excitation and donor emission, including artefactual contributions. Let us consider a hypothetical cell in which the thickness gradually increased with the distance from the edge, starting with a value of zero thickness at the edge. Let's assume that the protein activity, as reflected by a FRET biosensor, is perfectly uniform throughout the volume of the cell. Ideally, the intensity of the signals in the FRET and donor channels will increase linearly with the distance from the edge, x, as $s_F x$ and $s_D x$, respectively, due to the increasing thickness of the cell. By taking the ratio of the signals, we get the constant value $\frac{s_F}{s_D}$, which tells us that the activity is uniform as expected. In reality, each signal is shifted by a background fluorescence: $s_F x +$ background and $s_D x +$ background. Thus, inaccurate subtraction of the background leads to the ratio $\frac{s_F x+b_F}{s_D x+b_D}$, which is a function of x instead of a constant ($\frac{s_F}{s_D}$). The more accurately we subtract the background, the more accurately we can determine the ratio. Let's assume that we found a way to subtract the background perfectly. Now we have another problem: each channel has some noise in the signal so that the ratio after background subtraction is $\frac{s_F x+n_F}{s_D x+n_D}$. Far enough from the edge, the signal dominates the noise ($s_F x \gg n_F$ and $s_D x \gg n_D$), so we get an accurate estimate of $\frac{s_F}{s_D}$. However, near the very edge, as $x \to 0$, the ratio is heavily affected by noise, producing large variance of the ratio values. The calculated ratios will tend to produce more large positive values when noise starts to dominate the signal (effects of noise that decrease the correct ratio value can only approach zero, whereas those that increase the ratio can become arbitrarily high). Importantly, this trend toward increasing values will have a spatial component, making the ratio appear to become higher as we approach the edge. The more high-intensity pixels are produced by this effect, the higher will be the apparent, artefactual increase in activity at the edge, which can be mistaken for a real protein activity gradient.

In this example, we can resolve these issues using the fact that $\frac{s_F x+b_F+n_F}{s_D x+b_D+n_D} = \frac{s_F\left(x+\frac{b_D}{s_D}\right)+\left(b_F-s_F\frac{b_D}{s_D}\right)+n_F}{s_D\left(x+\frac{b_D}{s_D}\right)+n_D}$ (**Supplementary Material**). Instead of subtracting background values from each channel, we can subtract one *correction factor*, $\left(b_F - s_F\frac{b_D}{s_D}\right)$, from the FRET channel only, producing the ratio $\frac{s_F\left(x+\frac{b_D}{s_D}\right)+n_F}{s_D\left(x+\frac{b_D}{s_D}\right)+n_D}$, which is a better estimate of $\frac{s_F}{s_D}$, because even as $x \rightarrow 0$, $s_D\left(x+\frac{b_D}{s_D}\right) \gg n_D$ and we never divide by noise.

In the following sections, we explore the applicability of this idea to actual biosensor data. The correction factor will be referred to as the NCF.

Effects of Noise Examined in Real Cells

To illustrate the effect of noise in wide field imaging of real cells, we examined Cos7 cells expressing two fluorescent proteins often used for FRET, mCerulean and CyPet. Although biosensor activity is frequently reported as the ratio of FRET intensity to the intensity of the directly excited donor fluorophore, other ratios are also used (e.g., FRET divided by a directly excited acceptor or a volume indicator). To keep our description more general, we refer to the numerator as image1 and the denominator as image2. When background subtraction is explicitly included, the ratio is:

$$Ratio\left(x,y\right) = \frac{image1\left(x,y\right) - BG_{image1}}{image2\left(x,y\right) - BG_{image2}},$$

where $\left(x,y\right)$ is the position of a pixel in the image.

Figure 1A shows the nonuniform intensity distribution in the FRET channel for two neighboring cells, containing linked fluorophores that should FRET but not reflect protein activity. **Figure 1B** shows the fluorescence ratio after background subtraction for the same cells, a much more uniform image. For the background of each image, we determined the average intensity of a region away from the cell, which we will refer to as a *distant background* (green box in **Figure 1A**). To more clearly show variations in ratio values, we set the pseudocolor scale by assigning the region outside the cells to equal the mean of the ratios inside (≈ 0.7). A line-scan across the cells (black line in **Figure 1B**) showed that some pixels at the cell edges had intensity values several-fold higher than those within the cell (arrows in **Figure 1C**), as predicted. **Figures 1D,E** show that such pixels create a statistical bias in the average intensity within the cell, which varies with the distance from the edge, d. Using the relative range of the mean intensity, $\left(\max_d \langle I\rangle - \min_d \langle I\rangle\right)/\min_d \langle I\rangle$, as the measure of the deviation from the expected constant mean, we find that the left and right cells are biased at their edges by 4.7 and 5.7%, respectively.

The Effects of Background Subtraction

Like noise, incorrect background subtraction can also generate artefactual gradients at thin parts of the cell. Importantly, the method we will propose here does not require direct background subtraction, so these artifacts will be eliminated. In this section we show why it is worth eliminating the need for background subtraction, and highlight potential artifacts for those who do use it.

Incorrect background subtraction artificially elevates or reduces ratios, depending on the relative extent of the error it introduces in the numerator and denominator. As the signal decreases toward the edge, such background errors contribute more to the ratio values calculated, producing an artefactual gradient of activity (see **Figure 2** for an extreme case of no background subtraction at all). The gradient can increase or decrease toward the cell edge, depending on the relative magnitude of errors in the denominator and numerator. To put it mathematically, as the signals $\left(image1\left(x,y\right) - BG_{image1}\right)$ and $\left(image2\left(x,y\right) - BG_{image2}\right)$ get smaller near the edge, the errors in the background subtraction make that ratio $\frac{image1\left(x,y\right) - BG_{image1} + BG_{error1}}{image2\left(x,y\right) - BG_{image2} + BG_{error2}}$ approach a number $\frac{BG_{error1}}{BG_{error2}}$, which has no biological meaning.

Determining the correct background to apply to each pixel in the cell can be challenging. In wide field imaging for example, parts of the cell outside the plane of focus generate out-of-focus light that is unevenly distributed across the in-focus pixels. Some of this light appears outside the cell, so averaging regions outside the cell to determine the background can be problematic. When averaging a region far from the cell edge, the background will be too low. To illustrate this effect, we compared the ratios obtained in **Figure 1** with those obtained by setting the backgrounds (BG_{image1} and BG_{image2}) halfway between the distant background value used for **Figure 1**, and the value used to define the cell mask, i.e., the value right at the cell edge. **Figures 3A,B** shows that the resulting bias becomes worse, giving a deviation of 4.2 and 10.6% from the flat level, on average, and the variance of the ratio values at the edge is significantly increased. This was because using an increased background value decreased the intensity after background subtraction, making it smaller relative to noise.

We tested whether this problem could be overcome by subtracting background values obtained near the edge of the cell, taking into account the fact that background near the edge varies along the periphery of the cell. We applied *nonuniform background subtraction* by subtracting $BG_{image1}\left(x,y\right)$ and $BG_{image2}\left(x,y\right)$ that depend on the position in the image. To capture the spatial variation of the background, the background intensity was measured along the cell edge right outside the cell, and the resulting values were applied to nearby regions within the cell, so that subtracted values more properly reflected the local background. **Figure 4** illustrates the approach.

First, we find the intensity at each pixel adjacent to the cell boundary $I\left(i\right)$ for each channel (blue curves in **Figures 4A,B**). This measurement reflects two contributions: (1) local pixel-to-pixel variation due to the intrinsic noise of the signal and (2) a larger-scale variation in the background at different regions around the cell. To estimate background fluorescence along the whole cell edge, we need to use this larger-scale trend in the intensity variation (red curves in **Figures 4A,B**). It is found by applying the Gaussian filter (Davies, 2005) to smooth out the noise, $\bar{I}\left(i\right) = \sum_j \frac{I(j)}{\sqrt{2\pi\sigma^2}}\exp\left(-\frac{(i-j)^2}{2\sigma^2}\right)$, where i and j are numerical indexes of the points along the edge and σ is a parameter representing the extent of the smoothing window. Next, we find the interpolated values inside the cell

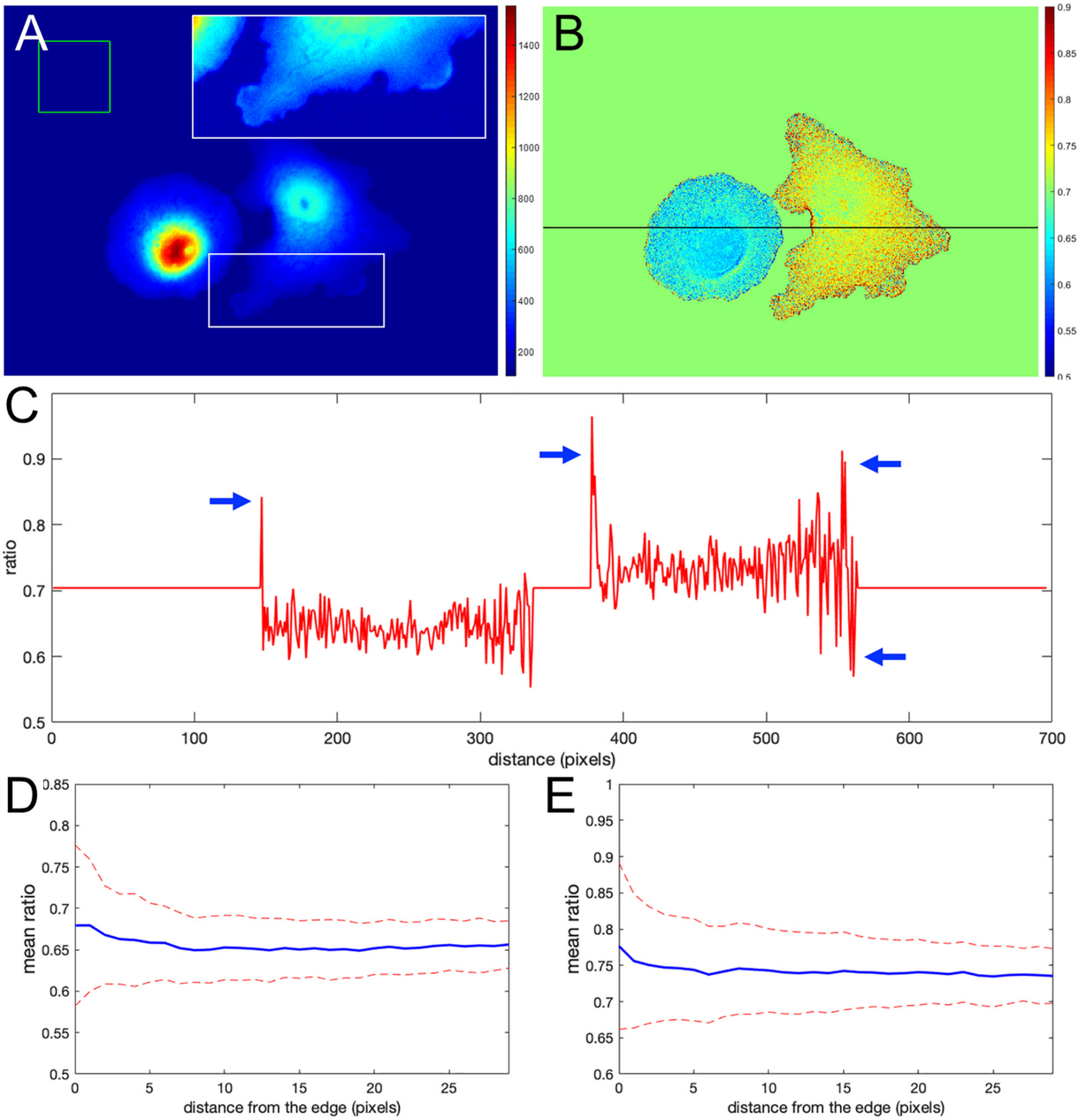

FIGURE 1 | Ratio calculation using the mean background subtraction method. **(A)** A colormap of the Förster resonance energy transfer (FRET) channel (mCerulean emission upon excitation of CyPet) after background subtraction, showing noneven distribution near the cell edge. The insert shows the signal from the white box in log scale for better contrast at the edge. The green box indicates the area of the image used to determine the mean and standard deviation of the background noise. **(B)** The resulting ratio signal with the background set to the mean ratio signal in the cells for a closer look at the nonuniform distribution. **(C)** The ratio profile from panel **(B)** along the black line. Blue arrows point to the artifact – at the edge very large deviations of the ratio from the expected constant mean level in the cells. **(D,E)** Mean ratio signal as a function of the distance toward the cell center from the edge for the left and right cells in panel **(B)**. Blue curves indicate the mean. Red dashed curves indicate the mean plus/minus one standard deviation.

as $BG(x, y) = \frac{\sum_i \bar{I}(i)/d_i^m(x,y)}{\sum_i 1/d_i^m(x,y)}$, where $d_i(x, y)$ is the distance from a pixel i to the point (x, y) and m is the parameter that controls how deep the local background values at the cell edge are extended inside the cell before the peripheral variation is smoothly connected across the cell. Such interpolation produces a meaningful estimation of the background intensity distribution near the curved edge. Interpolated distribution in the middle

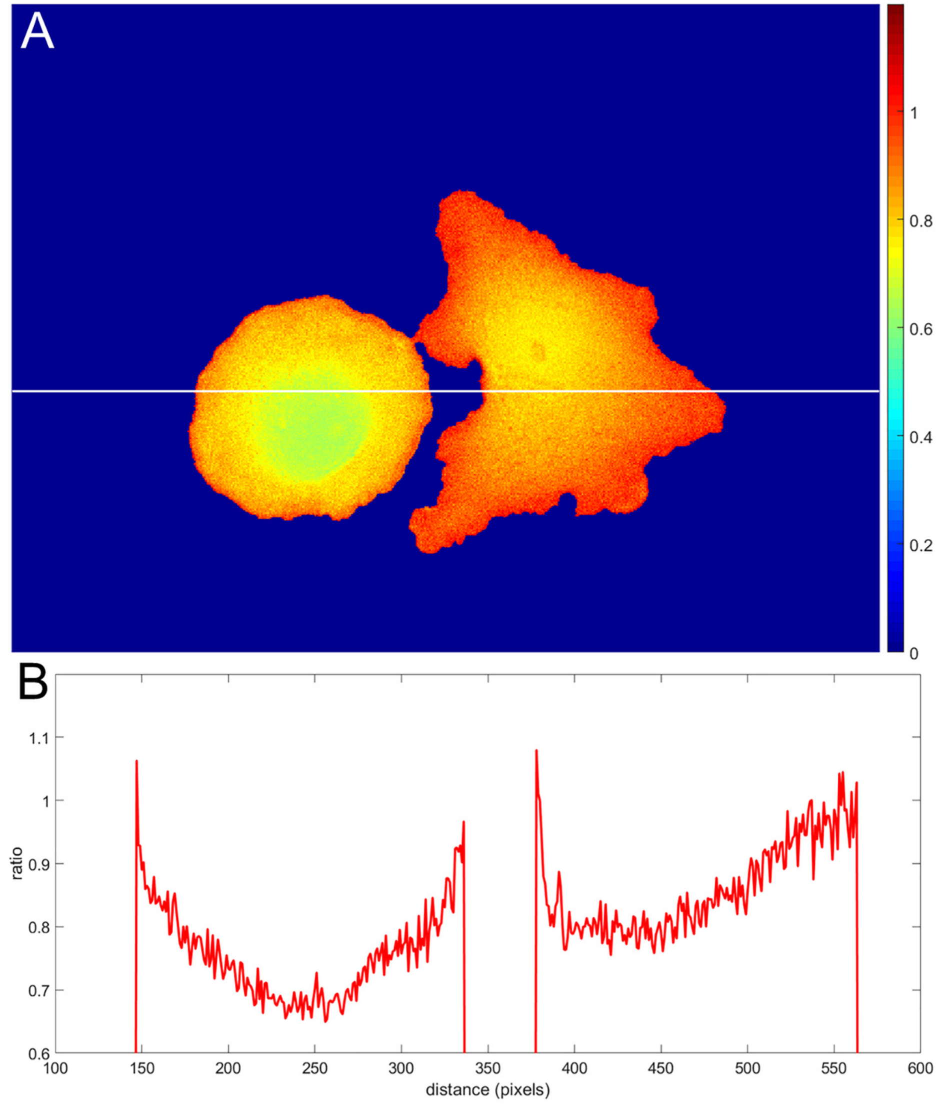

FIGURE 2 | Illustration of an extreme case of an error in background subtraction. **(A)** The ratio $\frac{\textbf{\textit{mCerulean}}}{\textbf{\textit{CyPet}}}$ without background subtraction at all. **(B)** The ratio profile from panel **(A)** along the white line.

of the cell may not be any more accurate than a global value of the background obtained from a distant region. The result of this operation is shown in **Figures 4C,D** for the FRET and donor channels, respectively (only the near edge regions are shown). Finally, we find the ratio after nonuniform background subtraction as:

$$Ratio\left(x,y\right) = \frac{FRET\left(x,y\right) - BG_{FRET}\left(x,y\right)}{CFP\left(x,y\right) - BG_{CFP}\left(x,y\right)},$$

Designed this way, our nonuniform background should provide a particularly accurate estimate of the actual background signal around the cell near its edge. However, the problem with the division by small numbers (weak donor signal at the very edge) is not resolved. The artifact is actually stronger because the subtracted values are closer to the fluorescent signal on the cell edge. Indeed, **Figure 4E** shows the mean intensity change in the cell with the distance from the edge. Our metric of the deviation from the expected flat distribution $\left(\max_d \langle I \rangle - \min_d \langle I \rangle\right)/\min_d \langle I \rangle$, gives 12.7%, which is about twofold more than the result of the distant background subtraction method (compare with **Figures 1D,E**).

Use of a Noise Correction Factor; Identification and Correction of Artifacts Without Using Direct Background Subtraction

The previous section shows that improving background subtraction may not be sufficient to avoid misleading ratiometric

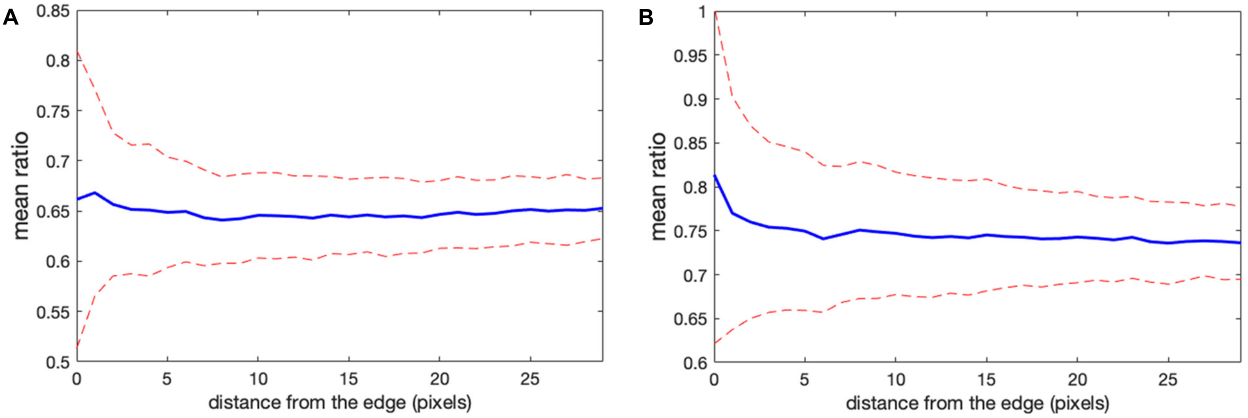

FIGURE 3 | Mean ratio signal as a function of the distance from the edge. Blue curves indicate the mean. Red dashed curves indicate the mean plus/minus one standard deviation. **(A,B)** The result for the left and right cells in **Figure 1** based on the subtraction of the values halfway between the distant background value and the value used to define the cell mask. Here the deviations from the expected constant mean are 4.2 and 10.6%, respectively.

artifacts at the edge of the cell. Let us therefore explore an alternative way to calculate the ratio of images 1, 2. We start with a theoretical estimation and then test the predictions with live-cell imaging.

Let's start with the situation considered above, where protein activity is constant throughout the cell, so that signal variation across the cell results from nonuniform cell thickness. We aim to determine the ratio between background- and noise-free florescent signals $S_1(x,y)$ and $S_2(x,y)$, which must be proportional to each other in this case. The ratio of the two images can be written as

$$Ratio\,(x,y) = \frac{image1\,(x,y)}{image2\,(x,y)} = \frac{a_0 S_2(x,y) + B_1 + N_1(x,y)}{S_2(x,y) + B_2 + N_2(x,y)}, \tag{1}$$

where a_0 is a coefficient of proportionality and $B_1, N_1(x,y), B_2, N_2(x,y)$ are the background levels and the noise in images 1, 2, respectively.

Background subtraction from each image (e.g., using mean background subtraction, MBS) reports:

$$Ratio_{MBS}\,(x,y) = \frac{image1\,(x,y) - B_1}{image2\,(x,y) - B_2} = \frac{a_0 S_2(x,y) + N_1(x,y)}{S_2(x,y) + N_2(x,y)}. \tag{2}$$

Using a simple algebraic rearrangement of terms in Equation 1, we find (see **Supplementary Material**)

$$Ratio\,(x,y) = \frac{image1\,(x,y)}{image2\,(x,y)} =$$

$$\frac{a_0\left(S_2(x,y) + B_2\right) + \left(B_1 - a_0 B_2\right) + N_1(x,y)}{\left(S_2(x,y) + B_2\right) + N_2(x,y)}. \tag{3}$$

Now we can show that subtracting a specific constant in the numerator – the NCF – eliminates the need for background subtraction in the denominator. Subtracting $NCF = B_1 - a_0 B_2$ produces:

$$Ratio_{NCF}\,(x,y) = \frac{image1\,(x,y) - NCF}{image2\,(x,y)} =$$

$$\frac{a_0\left(S_2(x,y) + B_2\right) + N_1(x,y)}{\left(S_2(x,y) + B_2\right) + N_2(x,y)}. \tag{4}$$

In any part of the cell away from the edge, where $S_2(x,y) \gg B_2 \gg N_2(x,y)$, both the MBS and NCF methods give the same correct (flat on average) result:

$$Ratio_{MBS}\,(x,y) \approx Ratio_{NCF}\,(x,y) \approx a_0 + \frac{N_1(x,y)}{S_2(x,y)}.$$

However, in thin regions near the edge, where $S_2(x,y) \to 0$, the MBS method generates the artifact

$$Ratio_{MBS}\,(x,y) \approx \frac{N_1(x,y)}{N_2(x,y)},$$

while the NCF method still gives the correct (flat on average) answer

$$Ratio_{NCF}\,(x,y) \approx a_0 + \frac{N_1(x,y)}{B_2},$$

When we use the correction factor, the artifact is not present because we did not subtract the background from the denominator and $B_2 \gg N_2(x,y)$. For the same reason, we can apply the correction factor approach to the whole image, including the region around the cells (with no biosensor signal). For these regions, we get:

$$\frac{B_1 + N_1(x,y) - CF}{B_2 + N_2(x,y)} = \frac{a_0 B_2 + N_1(x,y)}{B_2 + N_2(x,y)} \approx a_0 + \frac{N_1(x,y)}{B_2}.$$

So far, we considered an ideal (biologically uninteresting) situation where the FRET signal is strictly proportional to the

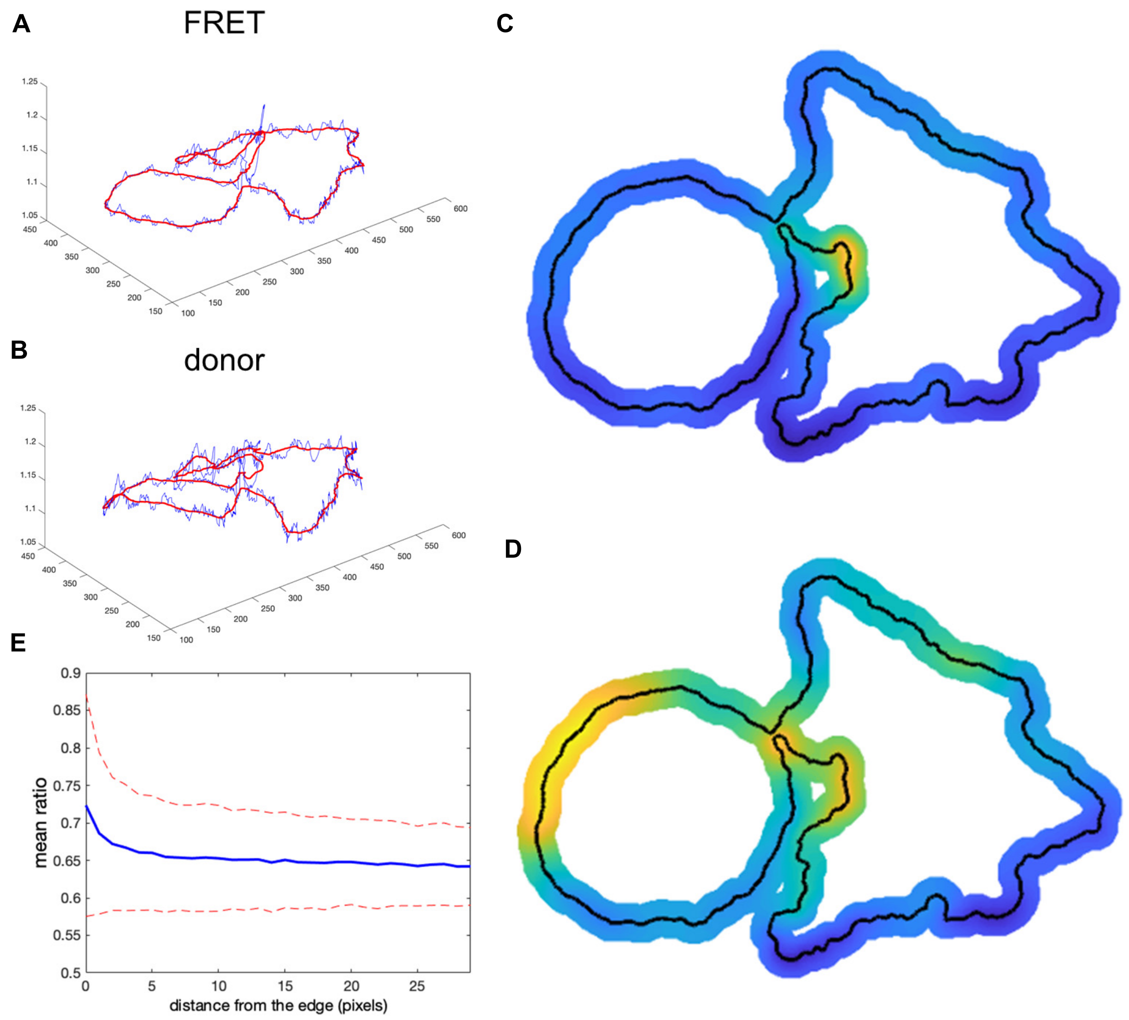

FIGURE 4 | Nonuniform background subtraction. **(A,B)** The fluorescence intensity in the FRET and donor channels outside the cell and near the edge (i.e., the local background along the cell periphery) is shown in blue. Smoothing these using a Gaussian filter generated the curve shown in red. **(C,D)** Spatial interpolation using the smoothed FRET and donor signals along the cell edge as the background for determining ratio values near the edge. **(E)** Mean ratio signal as a function of the distance toward the cell center from the edge, showing 12.7% deviation from the expected constant mean. This is due to the same edge artifacts shown in **Figure 1**, but further exaggerated by small values of the ratio denominator.

donor signal. Now, let's consider the next order of approximation, where biosensor activity deviates from the basal level so that the pure (background- and noise-free) part of the signal in image 1 is $S_1(x,y) = [a_0 + a_1(x,y)]\, S_2(x,y)$. As we will illustrate below, when we discuss imaging of a GEF biosensor, this is a good approximation for biosensors that are based on a single protein chain which contains both FRET fluorophores. Subtracting the correction factor $NCF = B_1 - a_0 B_2$ from image1 yields

$$Ratio_{NCF}(x,y) = \frac{image1(x,y) - NCF}{image2(x,y)} =$$

$$\frac{a_0\left(S_2(x,y) + B_2\right) + N_1(x,y)}{\left(S_2(x,y) + B_2\right) + N_2(x,y)} + \frac{a_1(x,y)\, S_2(x,y)}{\left(S_2(x,y) + B_2\right) + N_2(x,y)}.$$

In cell regions where the donor signal is strong $S_2(x,y) \gg B_2 \gg N_2(x,y)$, we again get the agreement between the MBS and NCF methods:

$$Ratio_{NCF}(x,y) \approx Ratio_{MBS}(x,y) \approx a_0 + a_1(x,y).$$

In the background of the image, we still get

$$\frac{B_1 + N_1(x,y) - NCF}{B_2 + N_2(x,y)} = \frac{a_0 B_2 + N_1(x,y)}{B_2 + N_2(x,y)} \approx a_0 + \frac{N_1(x,y)}{B_2},$$

while at the very edge of the cell, where $S_2(x,y) \to 0$, but $B_2 \gg N_2(x,y)$, the corrected ratio transitions between a_0 and $a_0 + a_1(x,y)$ as

$$Ratio_{NCF}(x,y) = a_0 + a_1(x,y)\frac{S_2(x,y)}{S_2(x,y) + B_2} + \frac{N_1(x,y)}{S_2(x,y) + B_2}.$$

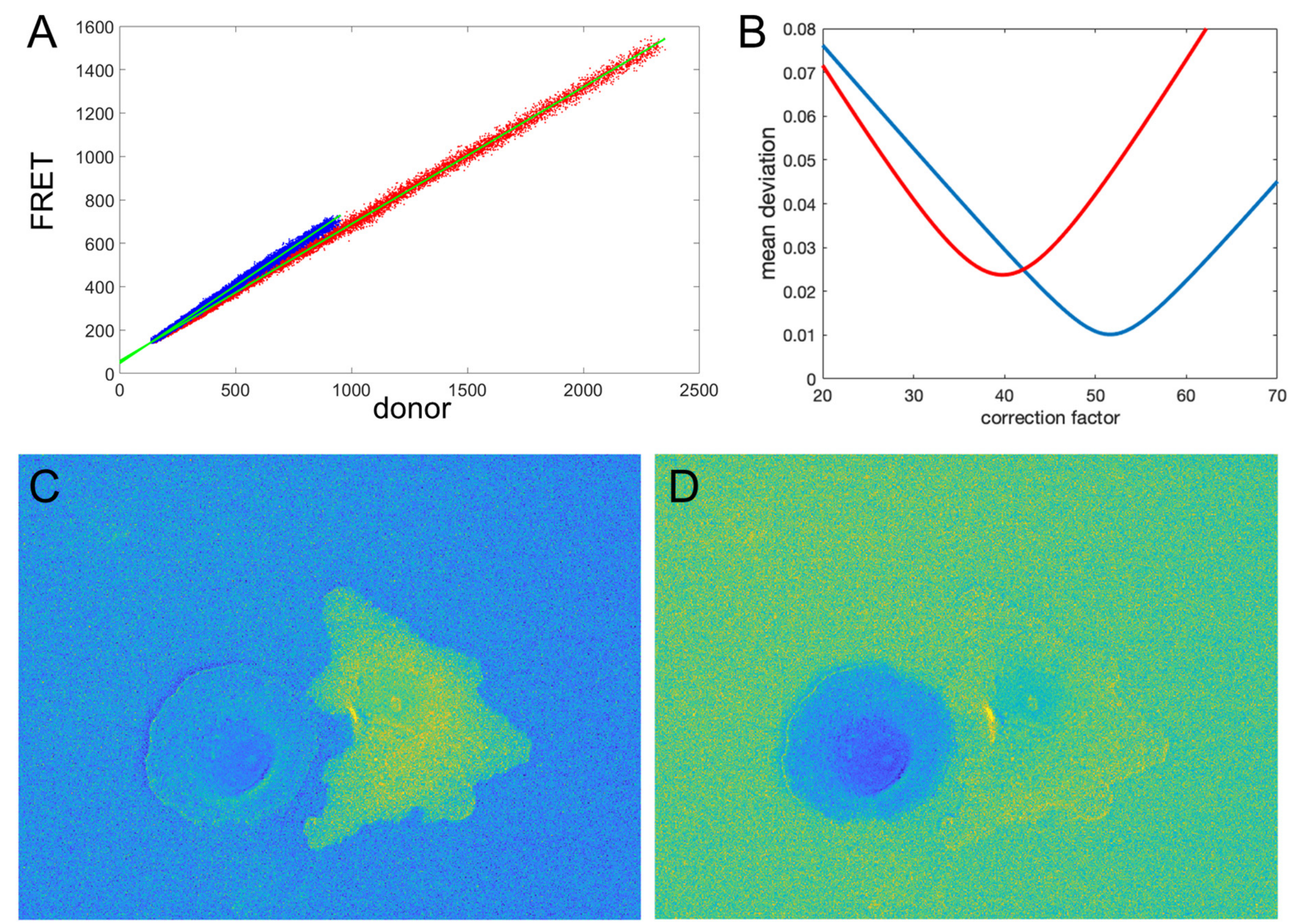

FIGURE 5 | Illustration of the correction factor method. **(A)** Intensity in the FRET vs. donor channels for each pixel. Red and blue colors indicate pixels in the left and right cells, respectively. The green lines indicate linear fits to the data points. **(B)** The deviation function (Equation 5) for a range of correction factor values. Red and blue curves are the functions calculated separately for the left and right cells in the image. The optimal correction factors are defined as the positions of the minima of these functions. **(C,D)** The ratio images resulted from the subtraction of the correction factors. In panel **(C)**, the signal in the left cell flattens with the background level as predicted by the mathematical analysis. Similarly, in panel **(D)**, the right cell flattens with the background. The flattening is so efficient that the noise fluctuations become visible.

These results suggest that in cell areas where the MBS method does not generate noise-related artifacts, the NCF gives the same ratio values. However, unlike the MBS method, the NCF method allows us to evaluate the ratio all the way to the cell edge. In addition, the NCF method allows us to visualize background noise outside the cell (**Figures 5**, **6**). This is useful because it enables comparison of background noise outside the cell with the FRET ratio inside the cell. With the MBS method, this is not possible because outside the cell we have one noise divided by another noise. Although the NCF method may underestimate the values at the very edge of the cell, these values would still be appreciably higher than the zero activity FRET ratio a_0. FRET signal measured when there is no protein activity reported by the biosensor could result from the FRET of the biosensor in its "off state" (e.g., for single chain biosensors where both fluorophores are always held in proximity within the biosensor) or from some systematic shift in the image acquisition (e.g., an uncorrected camera signal). The practical usefulness of this method is to visualize the ratio signal at the cell edge and other noisy portions of the cell, free from artifacts associated with division by a very weak donor signal.

Determining the Proper Noise Correction Factor in Practical Applications

The mathematical results in the previous section illustrated the benefits of using the NCF method. Here we show two alternative ways to find the right value of NCF for practical applications. In some cases, there will be appreciable "background FRET," measurable intensity in the FRET channel even when there is no protein activity. This could occur, for example, with single chain biosensors that contain two fluorophores held near each other in the biosensors "off" state (Pertz et al., 2006; Marston et al., 2020). In such cases, we can take advantage of the fact that the correct NCF value makes $Ratio_{NCF}\left(x, y\right) \approx Ratio_{MBS}\left(x, y\right)$ in the

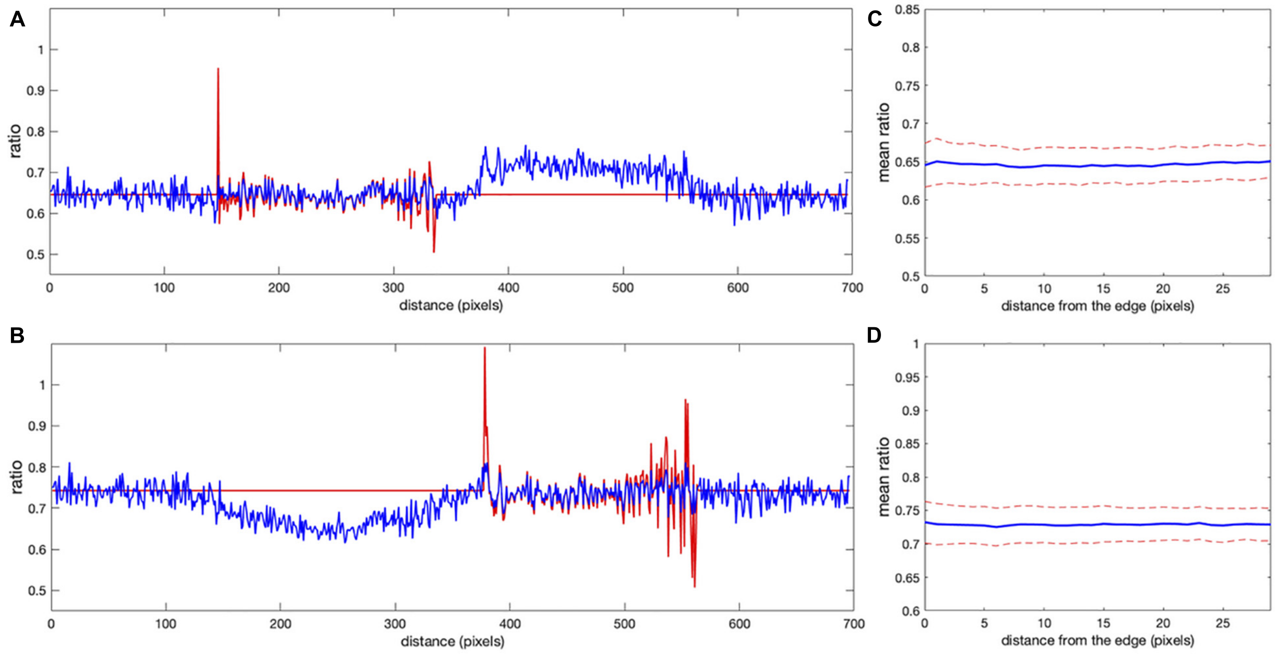

FIGURE 6 | Comparison of correction using the noise correction factor (NCF) versus mean background subtraction. **(A,B)** The ratio profiles from the images in **Figures 5C,D** along the line at the same location as in **Figure 1**. Red and blue colors indicate the ratios obtained with the mean background subtraction and NCF methods, respectively. Both results overlap inside the cells away from the edge [left cell in panel **(A)** and right cell in panel **(B)**]. Near the cell edges, the shape of the profile is still consistent between the methods, but the artifacts are not present in the result of the correction factor method. **(C,D)** Mean ratio signal as a function of the distance toward the cell center from the edge after applying the correction factor [panel **(C)** for the left cell and panel **(D)** for the right cell], showing the expected flat level with only 1.2 and 0.9% deviation from a perfectly constant line. The variance of the fluctuations is also flat all the way to the cell edge, in contrast to the background subtraction approaches (see **Figures 3**, **4E**).

cell regions away from the edge. It is easy to check for strong background FRET by plotting the intensity of image 1 vs. image 2 for each pixel. In such cases, the NCF can be found as the value that minimizes the deviation function

$$Dev_{in}\left(NCF\right) = \sqrt{\frac{1}{n}\sum\nolimits_{\text{off edge}}\left(Ratio_{NCF} - Ratio_{MBS}\right)^2} \quad (5)$$

where n is the number of pixels in the considered cell region away from the edge.

Another way to determine the NCF is to take advantage of the fact that the correct NCF value makes the background level near the edge outside the cell flat: $\frac{B_1+N_1(x,y)-NCF}{B_2+N_2(x,y)} \approx a_0 + \frac{N_1(x,y)}{B_2}$. Thus, the NCF can be found as the value that minimizes the deviation function

$$Dev_{out}\left(NCF\right) = \sqrt{\frac{1}{n}\sum\nolimits_{\text{bg near edge}}\left(Ratio_{NCF} - a_0\right)^2} \quad (6)$$

where n is the number of pixels in the considered background region. Since a_0 represents the zero protein activity "background ratio," we define it as the mean value of the ratio calculated with the MBS method inside the cell. This approach is preferable for biosensors where we cannot expect strong proportionality between background- and noise-free florescent signals $S_1\left(x,y\right)$ and $S_2\left(x,y\right)$, e.g., for biosensors consisting of two chains, with one fluorophore on each chain (Machacek et al., 2009; Marston et al., 2020).

Let us check how this optimization approach works for our example from the previous sections (two fluorophores with constant FRET throughout the cell). We first verify the proportionality between the signals in images 1, 2. **Figure 5A** shows FRET vs. donor signals for each pixel in the image with the expected strong proportionality. The linear fit gives the coefficients $a_0 = 0.63$ and $a_0 = 0.72$ for the left and right cells in the image, respectively. Knowing the background values, we can estimate the theoretical value $(B_F - a_0 B_D)$ of the noise correction factors as $NCF = 53.4$ and $NCF = 43.2$. Next, using morphological erosion (Soille, 2004) of the cell masks by 10 pixels, we determine the deviation values of the function (5), as shown in **Figure 5B** for each of the cells. The smallest deviation values are achieved when $NCF = 51.6$ and $NCF = 39.8$, which are close but not exactly equal to our estimation based on the fit of the FRET vs. donor plot. **Figures 5C,D** shows the resulting ratio images, and **Figures 6A,B** shows the corresponding line scans across the image.

Clearly, the MBS and NCF methods give the same intensity profile, except that the NCF method does not show noise-related artifacts, in agreement with the theoretical prediction. For $NCF = 51.8$ and $NCF = 43.3$ we found the smallest value of the flatness metric, $\left(\max\limits_{d}\left\langle I\right\rangle - \min\limits_{d}\left\langle I\right\rangle\right)/\min\limits_{d}\left\langle I\right\rangle$, when

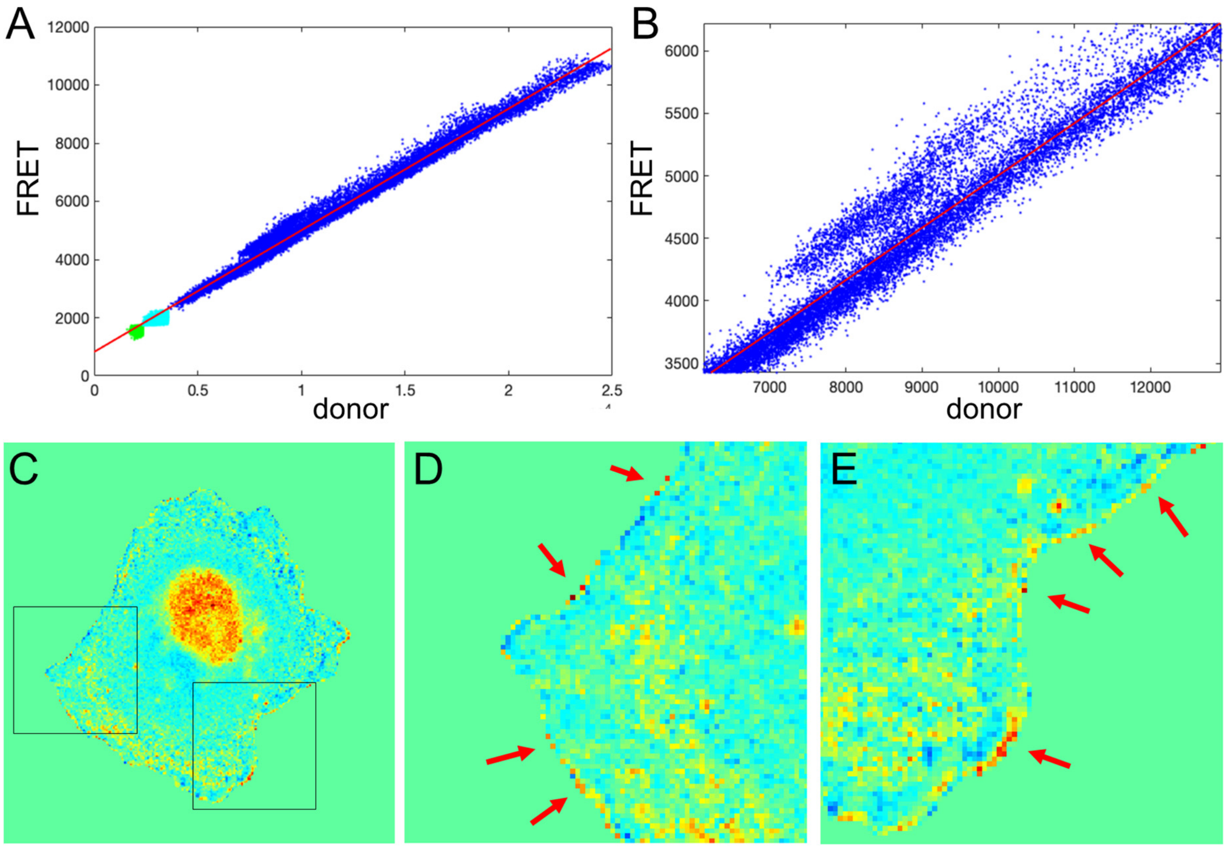

FIGURE 7 | Application of the mean background subtraction method to Asef biosensor data. **(A)** Uncorrected FRET vs. donor for each pixel. Blue indicates pixels with intensities above the mask threshold (i.e., inside the cell), green indicates pixels in the background with intensities below the mean plus three standard deviations of the noise in the box, and cyan indicates pixels in the background near the cell edge (with intensities between the threshold and mean + 3 std of the background noise). **(B)** A zoomed-in region of the image in panel **(A)**, confirming our theoretical assumption that there is strong basal activity of the GEF biosensor. **(C)** Ratio image resulting from the mean background subtraction method. Here we set the background level to the mean value of the ratio inside the cell (as in **Figure 2B**). **(D,E)** Two different zoomed-in regions from the image in panel **(C)** (black boxes). Red arrows point to high ratio pixels on the edge of the cell. With MBS method, these pixels appear similar to the noise artifact seen **Figure 1C**, so NCF is needed to analyze these pixels properly.

the mean intensity became close to a constant value over a range of distances from the edge (**Figures 6C,D**), as expected for this data. For these correction factors, the deviation from the constant became 1.2 and 0.9% for the left and right cells in the image, respectively. This is a fivefold improvement over the MBS method (see **Figures 3A,B**). All the values of NCF for each cell found through different means above are consistent with each other, which supports the mathematical rationale behind the NCF method.

Application of the Correction Factor Method to a Single-Chain Biosensor

We next tested the theoretical predictions of the previous sections using our single-chain biosensor for the guanine exchange factor (GEF) Asef (Marston et al., 2020). In this biosensor, a pair of fluorophores, mCerulean 3 and YPet, connected by a flexible linker, are inserted into a flexible hinge region between the active site and autoinhibitory domain (AID). Activation of the protein causes the AID to be displaced and the donor/FRET ratio to increase. The biosensor was imaged in moving fibroblasts constitutively expressing the biosensor. **Figure 7A** shows the plot of FRET vs. CFP values for each pixel of a biosensor image. Clearly, there is a strong linear trend due to the zero-activity background ratio of the connected fluorophores, a_0 with a number of pixels deviating from the line due to biological activation, $a_1(x,y)$, as can be seen in the zoomed region of the plot (**Figure 7B**). Therefore, our theoretical representation of this FRET vs. CFP relationship as $\frac{FRET}{CFP} = a_0 + a_1(x,y)$ is a good approximation. Now, **Figure 7C** shows the ratio of the two channels obtained with the MBS method. Close visual inspection of the pixels near the edge of the segmented cell (see **Figures 7D,E**) indicates that there are many very bright, somewhat irregularly distributed pixels along the edge. These pixels may well have been generated by the artifact that we investigated in the first sections.

How would we know if this is real biosensor activity or an artifact stemming from ratio calculation? The correction factor approach can help to answer this question. First, we use the deviation metric (Equation 5) to find the noise correction factor.

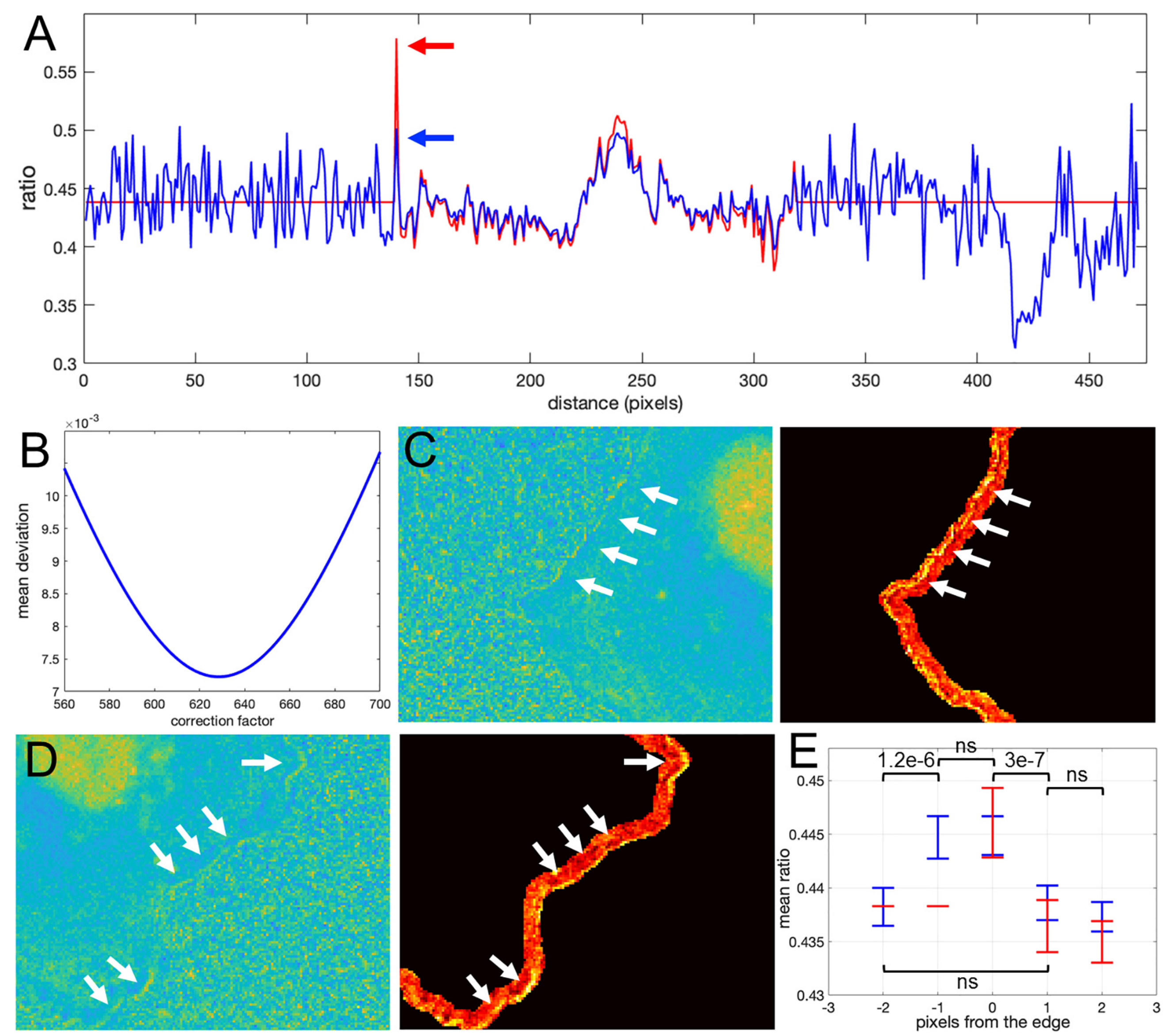

FIGURE 8 | Application of the correction factor method to Asef biosensor data. **(A)** The ratio values along a line in the ratio image resulting from the mean background subtraction method (red) and from the NCF method (blue). The red arrow indicates a pixel where the MBS method gives an artefactually high ratio value (noise-related artifact). The NCF method gives a value (blue arrow) that is within the distribution of ratio values seen throughout the cell (free of the noise related artifact). **(B)** The deviation function (Equation 5) for a range of NCF values. The correction factor giving the minimum deviation is used. **(C,D)** Two different zoomed-in regions of the ratio image calculated with the NCF method. Each zoomed-in region is presented in two colormaps. The regions are from the left and right sides of the cell shown in **Figure 7C**. For better contrast, the panels on the right also exclude all regions from the view except for the near edge region. White arrows point to a narrow band of bright pixels at the very edge of the cell. **(E)** Statistical measurement of the activity distribution (mean plus/minus two standard errors) for pixels along the contours at different distances from the cell edge. Blue and red color represents the result of the NCF and MBS methods, respectively. On average, a two-pixel band is elevated over the noise seen beside the band, either inside or outside the cell. The statistical significance of the differences in the mean values for the NCF results is indicated with *p*-values of the two-sample *t*-test ("ns" stands for $p \geq 0.05$).

As described in the previous section, by minimizing the deviation we find the correct NCF, for which the ratio values away from the edge (where signal to noise is high) match the values of the MBS method (see **Figures 8A,B**). Now, we can calculate the ratio values across the whole image (inside and outside of the cell). With the NCF method, the values of the pixels at the very edge are significantly lower than the values of the same pixels in the MBS method. We can consider these values to be free of noise-related artifacts. However, they are still clearly elevated relative to the background level. Thus, the NCF ratio image indicates that there is indeed a narrow band of high activity on the edge of the cell (see **Figures 8C,D**), which is not a processing artifact but a true biological activity. For a better quantitative measurement of this effect, we plot the confidence regions for

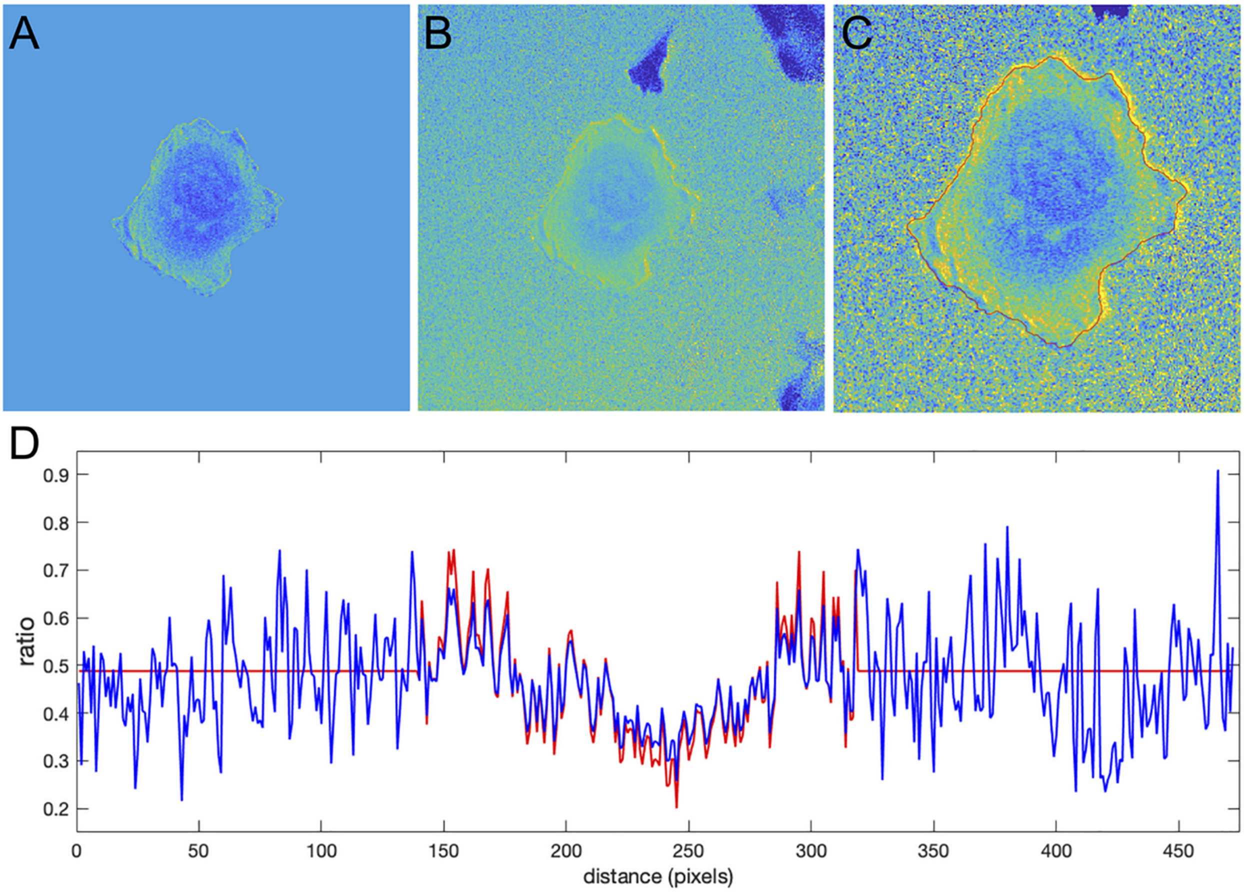

FIGURE 9 | Application of the correction factor method to the Cdc42 biosensor data. **(A)** The ratio image resulting from the mean background subtraction method. The background level is set to the mean value of the ratio inside the cell. **(B)** The ratio image resulting from the correction factor method. Now with the ratio signal in the background, a shade-like bias from the bottom-left to the top-right sides of the cell becomes clearly visible. **(C)** A zoomed-in image of the cell with the cell outline highlighted in red. The image shows that the artifact is mostly present outside the cell so that the ratio calculation inside the cell away from the edge should be accurate in both methods, but the bias is still present at the very edge. **(D)** The ratio values along a horizontal line running across the whole image. Red and blue colors represent the results of the mean background subtraction and correction factor methods, respectively.

mean intensity values of the contour pixels on the cell edge and up to 2 pixels away from the edge toward the cell center and toward the cell background (**Figure 8E**). This plot shows that the band of activity on the cell edge is just 2 pixels (0.64 um) wide, and it stands out over the mean intensities on each side of the band with *statistical significance* (p-values of the two-sample t-test are less than 0.0001).

Application of the Correction Factor Method to a Dual-Chain Biosensor

Our theoretical considerations relied on the assumption that there is a strong component in the FRET signal that is proportional to the donor signal. As we showed in the previous section, this assumption is accurate for the single chain Asef biosensor and should be accurate in general for single chain FRET biosensors due to their design. For dual-chain biosensors using intermolecular FRET, we cannot expect the same level of correlation because the donor and acceptor are not physically linked and may or may not be distributed similarly in the cell. However, we can still find the NCF based on the flattening of the background level near the cell edge outside the cell, using the deviation function defined by Equation 6. This background level can be used as a baseline with which to compare ratio values inside the cell. Notice that in all our previous examples, the mean level of the noise outside the cell becomes flat on average and levels up to the mean ratio inside the cell after subtracting the NCF (See **Figures 6A,B** and **8A**). This makes sense, because noise outside the cell should be flat on average regardless of the type of biosensor we use. Based on this minimization routine, we can expect that the proper NCF will suppress noise-related edge artifacts in ratiometric analysis of dual-chain biosensors. To investigate this, we applied it to the dual chain Cdc42 biosensor designed to be imaged simultaneously with the Asef biosensor. In this Cdc42 biosensor (Marston et al., 2020), LSSmOrange is attached to Cdc42, and mCherry is attached to the CRIB domain of WASP. When Cdc42 is activated the WASP fragment binds Cdc42, and mCherry

(FRET) emission can be detected upon LSSmOrange (donor) excitation. This biosensor could be used together with the Asef biosensor because the donor proteins in the two biosensors can be excited with the same wavelength, but they have substantially different emission maxima. Because this was a dual chain biosensor, we studied FRET and donor signals after correction for spectral bleedthrough. Ratios were then calculated using the MBS and NCF methods.

To define the region near the cell edge outside the cell, we used morphological dilation by 50 pixels. The minimum of the deviation function was achieved at $NCF = 550.6$. The resulting ratio images from the two methods are shown in **Figures 9A**,**C**. Perhaps surprisingly, the intensity profile inside the cell away from the edge was very consistent between the methods (**Figure 9D**), although here we did not use such criteria for finding NCF. Actually, if we do use the minimization based on the deviation function inside the cell, $Dev_{in}\,(NCF)$ (see Equation 5), we get the correction factor $NCF = 538$, which is close to the value we obtain with the minimization of $Dev_{out}(NCF)$. This result, confirming the agreement of the two types of optimization, further justifies our rationale for using flattening of the background level as a way to find the proper value of the NCF.

Despite the similarity of the intensity profiles between the methods, the correction method reveals that there is a ratio-imaging artifact. This artifact, the consistently higher ratio on one side of the cell is clearly visible near the cell edge. Now, after the fact, one may notice a hint of this bias in the ratio image from the MBS method, but only for a limited number of pixels at the very edge of the cell. Because the NCF method preserves the information near the edge outside the cell, the artifact is visible much more distinctly. This once again shows the practical benefits of using the NCF method. In summary, we found that the CDC42 biosensor signal at the very edge of the cell (i.e., within 1 pixel from edge) is artificially biased and does not represent a biological process, so that the affected pixels should be excluded from further analysis. In published analyses, noise and resultant difficulties with ratio imaging at the very edge have led to exclusion of the outermost 2 pixels from analysis.

DISCUSSION

For biosensors, ratiometric imaging is used to exclude the effects of uneven illumination, nonhomogeneous biosensor distribution, etc. In this article, we show that this procedure can create noise-related artifacts at the cell edge where the fluorescence is weak and contains a substantial noise component. In the past, these artifacts have been eliminated or reduced by excluding pixels at the very edge from consideration, or by averaging larger regions of the cell edge (Pertz et al., 2006; Machacek et al., 2009), but these fixes sacrificed spatial information or resolution. The regions near the edge of protruding membranes are important from a biological, mechanistic perspective. We therefore provide here a simple approach to investigate the ratio at the very edge of the cell, to identify potential issues and even mitigate their effects. Importantly, this NCF method enables calculation of the ratio in the portion of the image outside the cell, because this no longer requires division by very low values after background subtraction. The ratio outside the cell can be used to determine an NCF value and thereby eliminate artifacts within the cell.

In general, the NCF method is based on a minimization routine that flattens the noise level in the ratio near the edge outside the cells. Alternatively, for cases when the background ratio in cells is significant even in the absence of protein activity (e.g., for biosensors with FRET in the off state), the NCF value can be found by minimizing the difference between NCF and MBS ratios in the cell region away from the edge. Using a mathematical analysis, we showed that both calculation methods give NCF ratio measurements that are consistent with traditional MBS approaches but free from the noise-related artifacts (because we eliminate the need to divide the FRET signal by small numbers). We validated the accuracy of the theoretical predictions using data from two uniformly distributed fluorophores. Our method allowed us to achieve the expected flat ratio with ~1% accuracy, while the MBS method gave ~5% deviation at best. In parts of the cell where the FRET signal is weak, the ratio values from the NCF method are leveled with the background noise, unlike the MBS method that does not give a direct reference point for zero activity.

When we applied our method to analyze the activity of the Asef biosensor, we discovered that there was persistent Asef activity in a very narrow band (2 pixel = 640 nm) on the cell edge. In contrast, deeper within the cell, GEF activity varied significantly during protrusion and retraction (data not shown). These intriguing spatial differences in GEF activity will be pursued in further studies. Knowing that the signal at the very edge of the cell is not an artifact due to calculating ratios at the limit of image resolution is a critical first step.

Applying our NCF method to the dual-chain Cdc42 biosensor revealed a different artifact in the time-lapse cell images, a spatially biased background signal near the cell edge. Although such uneven distribution affected mostly the pixels right outside the cell mask, the pixels on the edge of the mask were still impacted by this bias. This was not obvious when background regions of the image were "zeroed out" using the traditional MBS method, but was clearly apparent when ratios inside and outside the edge could be compared.

Importantly, identifying a correct NCF value not only removes artifacts stemming from low signal/noise, but also produces a flat level of background noise in the ratio image. This can potentially be useful for stabilizing drift in time-lapse recordings, such as that produced by photobleaching.

MATERIALS AND METHODS

Live Cell Imaging

For the inactive biosensor experiments, Cerulean and YPet were transfected into Cos7 cells using Fugene6 (Roche) 24 h prior to imaging. On the day of imaging, cells were trypsinized using Trypsin/EDTA (Corning). They were then replated onto coverslips coated with Fibronectin (10 μg/ml 37C overnight) and allowed to attach in DMEM (Corning)/10% FBS (Hyclone). Cells were imaged in Hams/F12 (Caisson Labs)/5% FBS. Cells were imaged using a 40X, 1.3 NA objective on an Olympus IX–81 inverted microscope and using Metamorph screen acquisition software (Molecular Devices) and mercury arc lamp illumination. Filters used were Ex – ET436/20X, Em; donor- ET470/24M, FRET–ET535/30M and a 445/505/580 ET dichroic mirror. Images were obtained on a Flash4 sCMOS camera (Hamamatsu). Images were analyzed using MATLAB (Mathworks).

For the Asef and Cdc42 experiments, the Asef biosensor constructs were inserted into a tet-off inducible retroviral expression system and stable lines were produced in tet-off MDA-MB-231 cells (Johnson Lab, UNC-CH). Cells were maintained in DMEM (Cellgro) with 10% FBS (Hyclone) and 0.2 μg/ml doxycycline to repress biosensor expression. Biosensor expression was induced 48 h prior to imaging through trypsinization and culturing without doxycycline and the Cdc42 biosensors were transfected into the RhoGEF biosensor-expressing stable cell lines. On the day of imaging, cells were replated using Accumax (Innovative Cell Technologies) onto coverslips coated with collagen I (10 μg/ml 37C overnight) and allowed to attach in DMEM/10% FBS. After 2 h the media was replaced with Hams/F12 with 0.2% BSA, 10 ng/μl Epidermal growth factor (R and D systems) 10 mM HEPES, 100 μm Trolox, and 0.5 mM Ascorbate and cells were allowed to equilibrate. After a further 2–4 h, cells were imaged in a closed chamber with media treated with Oxyfluor (1/100). For single biosensor experiments, cells were imaged using the filters listed above. For dual biosensor experiments, the excitation filters used were FF-434/17 for Cerulean3/mTFP and LSSmOrange, and FF-546/6 for Cherry (Semrock) combined with a custom zt440/545 dichroic (Chroma). For emission, a TuCam (Andor) was fitted with a FF560-FDi01 imaging-flat dichroic and a Gemini dual view (Hamamatsu) was added to each emission port. For the short wavelength port of the Gemini, the filters used were donor-FF-482/35, FRET – FF-520/15 and a FF509-FDi01 imaging flat dichroic mirror. For the Red-shifted Gemini port, the filters used were Orange – FF01-575/15, FRET/mCherry – FF01-647/57 and a FF580-FDi01 imaging flat dichroic.

Image Pre-processing

Donor and FRET images were aligned using fluorescent beads as fiduciaries to produce a transformation matrix using the Matlab function "cp2tform" (Matlab, The Mathworks Inc.). This was then applied to the Donor image using the Matlab function "imtransform." The camera dark current was determined by obtaining images for each camera without excitation, and the dark current was subtracted from all images. Images were corrected for shading due to uneven illumination by taking images of a uniform dye solution under conditions used for each wavelength, normalizing this image to an average intensity of 1 to produce a reference image for each wavelength, and then dividing the images corrected for dark current by the shading correction reference image.

Noise Correction Factor Processing

MATLAB scripts for NCF application are available at https://github.com/tsygankov-lab/NoiseCorrectionFactor.

DATA AVAILABILITY STATEMENT

The raw data supporting the conclusions of this article will be made available by the authors, without undue reservation.

AUTHOR CONTRIBUTIONS

DT and KH designed the study and wrote the manuscript. DT developed the computational method, performed the data analysis, and prepared manuscript figures. DM and SS performed the experiments and collected imaging data. DM contributed to manuscript discussion and editing. All authors contributed to the article and approved the submitted version.

FUNDING

This work was supported by grants from the U.S. Army Research Office (ARO, W911NF-17-1-0395) and the National Science Foundation (CMMI 1942561) to DT, and by NIGMS grant GM-R35GM122596 to KH.

SUPPLEMENTARY MATERIAL

The Supplementary Material for this article can be found online at: https://www.frontiersin.org/articles/10.3389/fcell.2021.685825/full#supplementary-material

REFERENCES

Davies, E. R. (2005). *Machine Vision: Theory, Algorithms, Practicalities*. Amsterdam: Elsevier.

Greenwald, E. C., Mehta, S., and Zhang, J. (2018). Genetically encoded fluorescent biosensors illuminate the spatiotemporal regulation of signaling networks. *Chem. Rev.* 118, 11707–11794. doi: 10.1021/acs.chemrev.8b00333

Hall, A. (2012). Rho family GTPases. *Biochem. Soc. Trans.* 40, 1378–1382.

Hochreiter, B., Garcia, A. P., and Schmid, J. A. (2015). Fluorescent proteins as genetically encoded FRET biosensors in life sciences. *Sensors* 15, 26281–26314. doi: 10.3390/s151026281

Hodgson, L., Shen, F., and Hahn, K. (2010). Biosensors for characterizing the dynamics of rho family GTPases in living cells. *Curr. Protoc. Cell Biol.* Chapter 14, Unit 14.11.1–14.11.26.

Kurokawa, K., Itoh, R. E., Yoshizaki, H., Nakamura, Y. O., and Matsuda, M. (2004). Coactivation of Rac1 and Cdc42 at lamellipodia and membrane ruffles induced by epidermal growth factor. *Mol. Biol. Cell* 15, 1003–1010. doi: 10.1091/mbc.e03-08-0609

Machacek, M., Hodgson, L., Welch, C., Elliott, H., Pertz, O., Nalbant, P., et al. (2009). Coordination of Rho GTPase activities during cell protrusion. *Nature* 461, 99–103. doi: 10.1038/nature08242

Marston, D. J., Vilela, M., Huh, J., Ren, J., Azoitei, M. L., Glekas, G., et al. (2020). Multiplexed GTPase and GEF biosensor imaging enables network connectivity analysis. *Nat. Chem. Biol.* 16, 826–833. doi: 10.1038/s41589-020-0542-9

Pertz, O., Hodgson, L., Klemke, R. L., and Hahn, K. M. (2006). Spatiotemporal dynamics of RhoA activity in migrating cells. *Nature* 440, 1069–1072. doi: 10.1038/nature04665

Rossman, K. L., Der, C. J., and Sondek, J. (2005). GEF means go: turning on Rho GTPases with guanine nucleotide-exchange factors. *Nat. Rev. Mol. Cell Biol.* 6, 167–180. doi: 10.1038/nrm1587

Soille, P. (2004). *Morphological Image Analysis: Principles and Applications*. Berlin: Springer.

Terai, K., Imanishi, A., Li, C., and Matsuda, M. (2019). Two decades of genetically encoded biosensors based on forster resonance energy transfer. *Cell Struct. Funct.* 44, 153–169. doi: 10.1247/csf.18035

Conflict of Interest: The authors declare that the research was conducted in the absence of any commercial or financial relationships that could be construed as a potential conflict of interest.

frontiers
in Cell and Developmental Biology

REVIEW
published: 06 September 2021
doi: 10.3389/fcell.2021.706126

Visualizing the Invisible: Advanced Optical Microscopy as a Tool to Measure Biomechanical Forces

Chad M. Hobson[1], Jesse S. Aaron[1], John M. Heddleston[2] and Teng-Leong Chew[1]*

[1] Advanced Imaging Center, Janelia Research Campus, Howard Hughes Medical Institute, Ashburn, VA, United States,
[2] Cleveland Clinic Florida Research and Innovation Center, Port St. Lucie, FL, United States

The importance of mechanical force in biology is evident across diverse length scales, ranging from tissue morphogenesis during embryo development to mechanotransduction across single adhesion proteins at the cell surface. Consequently, many force measurement techniques rely on optical microscopy to measure forces being applied by cells on their environment, to visualize specimen deformations due to external forces, or even to directly apply a physical perturbation to the sample via photoablation or optogenetic tools. Recent developments in advanced microscopy offer improved approaches to enhance spatiotemporal resolution, imaging depth, and sample viability. These advances can be coupled with already existing force measurement methods to improve sensitivity, duration and speed, amongst other parameters. However, gaining access to advanced microscopy instrumentation and the expertise necessary to extract meaningful insights from these techniques is an unavoidable hurdle. In this Live Cell Imaging special issue Review, we survey common microscopy-based force measurement techniques and examine how they can be bolstered by emerging microscopy methods. We further explore challenges related to the accompanying data analysis in biomechanical studies and discuss the various resources available to tackle the global issue of technology dissemination, an important avenue for biologists to gain access to pre-commercial instruments that can be leveraged for biomechanical studies.

Keywords: biomechanical force, fluorescence microscopy, mechanobiology, light-sheet fluorescence microscopy, super-resolution microscopy

Edited by:
Abhishek Kumar,
Marine Biological Laboratory (MBL),
United States

Reviewed by:
Rajprasad Loganathan,
Johns Hopkins University,
United States
Makoto Sato,
Kanazawa University, Japan

****Correspondence:***
Teng-Leong Chew
chewt@janelia.hhmi.org

Specialty section:
This article was submitted to
Cell Growth and Division,
a section of the journal
Frontiers in Cell and Developmental
Biology

Received: *06 May 2021*
Accepted: *09 August 2021*
Published: *06 September 2021*

Citation:
Hobson CM, Aaron JS,
Heddleston JM and Chew T-L (2021)
Visualizing the Invisible: Advanced
Optical Microscopy as a Tool
to Measure Biomechanical Forces.
Front. Cell Dev. Biol. 9:706126.
doi: 10.3389/fcell.2021.706126

INTRODUCTION

Mechanical forces play important roles in many aspects of biology. They are known to modulate homeostasis (Guillot and Lecuit, 2013), intracellular signaling pathways (Liu et al., 1999; Han et al., 2004; Thompson et al., 2012), gene expression (Goldspink et al., 1992; Tajik et al., 2016), cell-cell interaction (Basu et al., 2016; Angulo-Urarte et al., 2020; Markovič et al., 2020), cancer progression (Kumar and Weaver, 2009; Jain et al., 2014), cardiovascular functions (Bishop and Lindahl, 1999; Pesce and Santoro, 2017; Beech and Kalli, 2019), and development (Mammoto and Ingber, 2010;

Agarwal and Zaidel-Bar, 2021). Yet, studies of biomechanical force can be rife with unique challenges (Roca-Cusachs et al., 2017). Specifically, (i) mechanical forces themselves cannot be directly labeled for visualization as with other biological components, (ii) the magnitude of many biological forces necessitates exquisite sensitivity for accurate quantification, (iii) integrating force measurement assays with live cell microscopy is often a complex engineering challenge, (iv) measuring forces can unwittingly perturb the biological systems or processes being studied, and (v) the complexity of subsequent data analysis can often hinder interpretation of results.

Assays that quantify biomechanical forces are often the result of interdisciplinary work that combines framing a biological hypothesis, synthesizing a force-sensing substrate or sensor, designing or adapting imaging instrumentation or other readout mechanisms, and careful analysis to extract meaningful information from the data. Many of the currently available force measurement tools have previously been expertly discussed (Bao and Suresh, 2003; Polacheck and Chen, 2016; Roca-Cusachs et al., 2017). Here, we will provide a brief synopsis of these force measurement methods as an overview. However, one of the most notable commonalities of many force measurement assays is their reliance on optical instrumentation to visualize and quantify cellular mechanical force. As a result, the choice of optical instrumentation matters immensely in determining the accuracy and sensitivity of the experimental readout. In light of this, our Review focuses on the constraints that microscopy places on many mechanobiological techniques, and how emerging advanced microscopy methods can be leveraged to overcome some of these limitations. Additionally, we will offer a guided tour of how readers can access this cadre of instruments, some of which have yet to be commercialized. Unfortunately, the hurdles facing biologists do not end with restricted access to emerging imaging technologies. The data size and complexity produced by modern microscopes can be daunting (Ouyang and Zimmer, 2017). We discuss some of the considerations that should be made when handling and analyzing this deluge of data. We will conclude by offering a perspective of remaining challenges, and how they may provide important opportunities for future development.

FORCE MEASUREMENT TECHNIQUES

The proper function of biological systems requires the intricate coordination between biochemical and mechanical signaling. Together, these signals allow living systems to respond to external and internal cues that span a wide range of biological length scales (Ingber, 2003; Discher et al., 2005; Guillot and Lecuit, 2013; Cho et al., 2017; Agarwal and Zaidel-Bar, 2021; Evers et al., 2021). Unlike many biochemical readouts, biomechanical forces must be measured *in situ*, in context, and transiently. Furthermore, the magnitude of these forces spans a large dynamic range (Du Roure et al., 2005; Sun et al., 2005; Rauzi et al., 2008; Xia et al., 2018). Yet, mechanical forces cannot be directly visualized, and are usually dependent on innovative methods to infer and quantify their location, direction, and magnitude. While some of these mechanobiology methods are capable of directly measuring small magnitude forces, most methods require light microscopy for visualization and quantification (Polacheck and Chen, 2016; Roca-Cusachs et al., 2017). Conversely, microscopy can also act as a limiting factor for the precision and sensitivity of force measurement methods. Here, we will survey commonly used force measurement techniques (**Figure 1**) with an emphasis on how their implementations are dependent upon fluorescence microscopy.

A plethora of tools have been developed to apply and measure forces at the cellular and sub-cellular level. One class of tools can be broadly described as perturbative – that is, the sample is actively deformed by some external means (**Figure 1A**). Physically perturbative techniques can be further categorized into whether the method can measure forces without light microscopy. Techniques such as atomic force microscopy (Krieg et al., 2019) and magnetic tweezers (Gosse and Croquette, 2002) directly measure the magnitude of the dynamically applied force without fluorescence microscopy. However, they can also be coupled with light microscopy to add additional dimensionality to an experiment (Beicker et al., 2018; Nelsen et al., 2020). Other physically perturbative techniques, such as micropipette aspiration (Hochmuth, 2000), substrate stretching (Caille et al., 1998; Moraes et al., 2010), and single-pipette micromanipulation (Neelam et al., 2015) necessitate fluorescence imaging to visualize the deformation of a sample. This supports the quantification of intracellular strains, stresses, and viscoelastic properties (Wu et al., 2018; Krieg et al., 2019). These dynamic methods are well-suited for replicating scenarios wherein samples experience perturbative forces from their environment. However, these capture only a subset of the conditions in which a cell may be subject to an external force.

To introduce additional molecular specificity, the illumination source in most modern microscopes can be leveraged to optically induce *in situ* perturbations through light-mediated potentiation of molecular motors (**Figure 1A**) with high spatiotemporal resolution. This is usually achieved with various optogenetic tools (Airan et al., 2009; Wu et al., 2009; Fenno et al., 2011; Oakes et al., 2017). These techniques also allow the experimenter to subsequently perform rapid live-cell observation. For example, photoactivatable Rac1 has been developed to induce and study cell motility, protrusions, and ruffling (Wu et al., 2009). It is also important to note that the maintenance of force (isometric tension) can play an equally important biomechanical role as transient force generation. Tension is a steady-state phenomenon, and even though it can be measured across larger platforms such as cell monolayers (Kolodney and Wysolmerski, 1992; Goeckeler and Wysolmerski, 1995), the *in situ* tension will be more effectively visualized upon its disruption. One means of targeting this disruption is through photoablation, which uses high-intensity focused light to break molecular bonds (Müller et al., 1991; Vogel and Venugopalan, 2003; Vogel et al., 2005). Subsequent observation of the relaxation area surrounding the ablation then allows one to infer the tension and forces prior to disruption.

Another interesting consideration is that under physiological conditions, perturbative forces can be exerted both dynamically

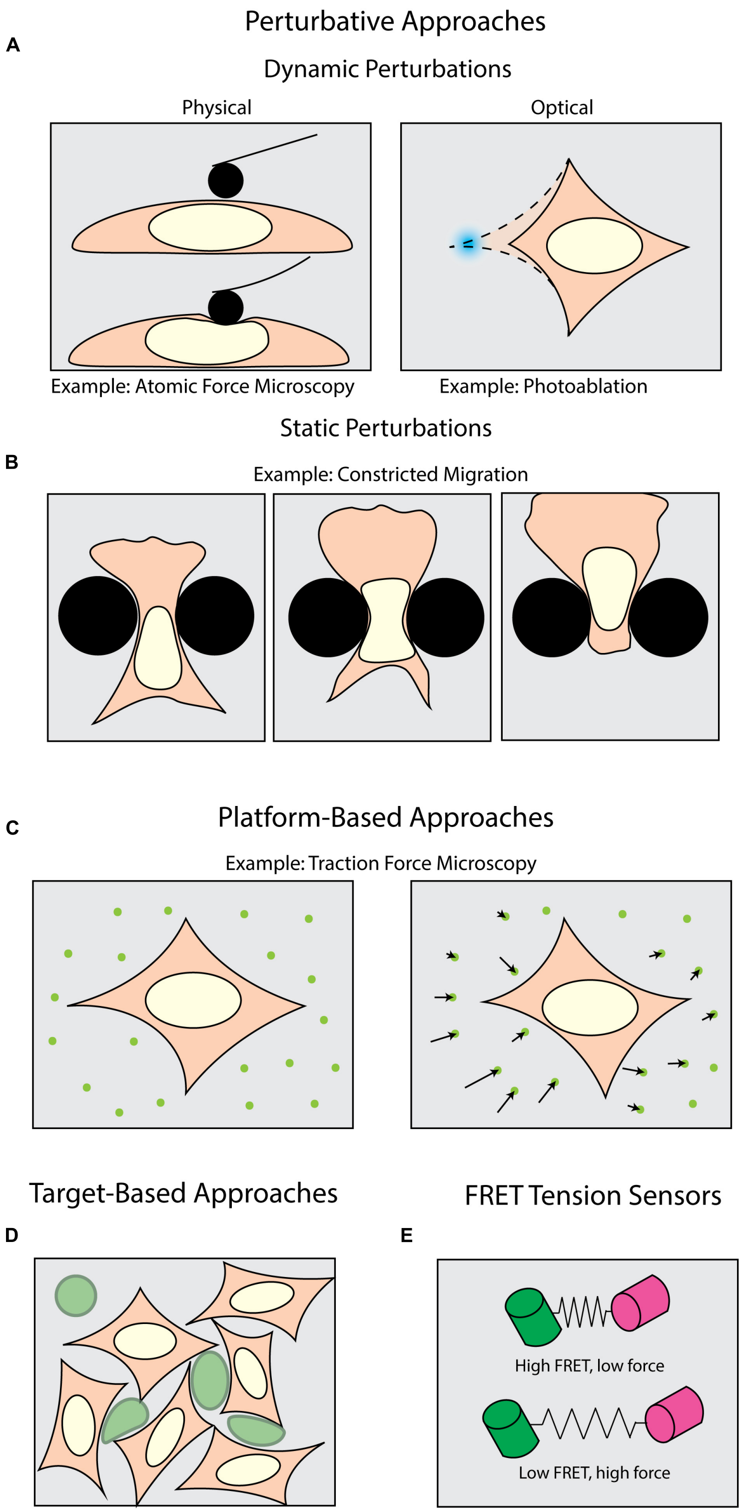

FIGURE 1 | Methods of measuring forces in biology. Perturbative techniques can be either **(A)** dynamic or **(B)** static. **(A)** Dynamic methods such as atomic force microscopy (AFM) use external physical probes to measure the force required to deform the sample. Dynamic optical perturbations use either photoablation to reveal underlying tension (as shown) or optogenetic tools to activate force generation. **(B)** Static perturbations (e.g., constricted migration assays) use rigid physical barriers to induce large-scale shape changes as cells navigate their environment. **(C)** Platform-based approaches, such as Traction Force Microscopy (TFM), monitor displacements of fiducial markers to measure mechanical forces cells apply to their surroundings. **(D)** Target-based approaches (e.g., liquid droplets) measure the deformation of micron-scale particles (green) to infer forces generated within tissues or during target engagement. **(E)** FRET tension sensors use molecular springs between donor and acceptor fluorophores to convert FRET signals to intracellular forces.

and statically. In the case of cells undergoing significant shape changes to navigate through tight interstitial spaces, the cells are subjected to self-generated forces against static barriers (**Figure 1B**; Paul et al., 2017). One means of mimicking such forces is the use of microfabricated substrates with micron-scale features and chemoattractant gradients (Heuzé et al., 2011; Davidson et al., 2015; Paul et al., 2016). Among many things, this class of force measurement techniques has historically been useful in measuring how cells dynamically respond to static perturbations (McGregor et al., 2016; Paul et al., 2017). Physically perturbative techniques, both static and dynamic, can leverage microscopy to visualize the deformations being induced upon a sample, but do not give insight into the magnitudes of and means by which cells apply forces to their surroundings. Accomplishing this necessitates a shift from visualizing the deformation of the sample to the deformation of the environment.

Measuring the force cells exert on their surroundings requires an experimental milieu that contains fluorescent fiducial markers and is deformable by cell-scale forces. These "platform-based" approaches primarily make use of optical tracking and computational modeling to monitor deformations induced by the biological samples and extract biomechanical forces (**Figure 1C**). Traction force microscopy (TFM) is one of the most well-established, platform-based methods, originating from the observation that migrating cells can deform thin, elastic substrates (Harris et al., 1980; Dembo and Wang, 1999). These methods rely on embedding fluorescent beads in a substrate upon which cells migrate (Munevar et al., 2001a,b). Forces exerted on the substrate lead to translation of the fiducial markers, which is then computationally converted into force vectors (Han et al., 2015). TFM can be used not only to map forces in two (2D) and three dimensions (3D) (Franck et al., 2011; del Álamo et al., 2013; Legant et al., 2013; Toyjanova et al., 2014), but also as a function of time (Peschetola et al., 2013). Another commonly used platform-based approach is micropillar arrays. Conceptually related to TFM, these assays use microscopy to track the bending of flexible micropatterned pillars (Tan et al., 2003; Xiao et al., 2018), which is then converted to force information through computational modeling (Schoen et al., 2010). This can be expanded for use with cell monolayers (Saez et al., 2010). Furthermore, magnetic actuation of post arrays can facilitate simultaneous force application and measurement in this type of assay (Sniadecki et al., 2007; Monticelli et al., 2018). Collectively these assays are tailored for investigating force generation (Shiu et al., 2004; Du Roure et al., 2005; Jannat et al., 2011; Umeshima et al., 2019). However, biomechanical forces occur under a multitude of other, more complex physiological conditions, thus necessitating additional methods beyond platform-based approaches.

In measuring intercellular forces within complex tissue or whole organisms, many investigators have turned toward "target-based" approaches (**Figure 1D**). The premise of target-based methods is to measure the shape change of an introduced object with a known stiffness. This has been achieved with liquid microdroplets or micron-scale polyacrylamide spheres, enabling investigators to study phenomena such as tissue morphogenesis (Campàs et al., 2014; Serwane et al., 2017; Mongera et al., 2018; Träber et al., 2019; Hofemeier et al., 2021), interstitial pressure in tumor growth (Dolega et al., 2017; Lee et al., 2019), and phagocytosis (Vorselen et al., 2020, 2021). However, none of the methods discussed so far directly identify the molecular source from which a force is potentiated. Accomplishing this requires introducing a genetically encoded mechanical sensor.

One of the most sensitive types of intracellular force sensors utilizes Förster Resonance Energy Transfer (FRET). FRET is a process by which energy from one fluorophore (the donor) is transferred to a neighboring fluorophore (the acceptor), typically when they are less than 10 nm apart (Jares-Erijman and Jovin, 2003). This allows for precise quantification of proximity, which can be leveraged to quantify mechanical forces (LaCroix et al., 2015; Gayrard and Borghi, 2016). Such "FRET tensions sensors" (Meng and Sachs, 2012; Cost et al., 2019) consist of a donor and acceptor fluorophore joined by a linker capable of sensing intramolecular tension within a molecule of interest (**Figure 1E**; LaCroix et al., 2015; Gayrard and Borghi, 2016). By calibrating the molecular spring stiffness, one can sensitively measure changes in force with single pN sensitivity (Freikamp et al., 2017; Ringer et al., 2017). For comparison, the detection range of TFM spans 100s of pN to 10s of nN (Style et al., 2014). FRET sensors have been of particular interest for studying tension across focal adhesions and their associated proteins (Grashoff et al., 2010; Ringer et al., 2017).

One important message from the technical survey above is that the accuracy and sensitivity of many of these assays is dependent on the capacity of the microscope to deliver the appropriate readout. In fact, the optical detection step is often the ultimate limitation of a force measurement assay. Further problems can often arise if microscopy instruments are not chosen carefully or the most appropriate instrument is not available. The optimal integration of light microscopy into a mechanobiological assay requires an equally detailed understanding of the microscope performance. In the following sections, we will discuss the major imaging parameters to consider when performing force measurements, and how advanced microscopy methods can be leveraged to improve them in complex biological systems.

INTEGRATING ADVANCED LIGHT MICROSCOPY WITH FORCE MEASUREMENTS

Fluorescence microscopy is fundamentally a game of trade-offs between several key imaging parameters, such as speed, dimensions, resolution, and phototoxic effects. The optimal balance is usually determined by both the quantitative experimental question as well as the characteristics of the sample. No single microscopy method is ideally suited to balance these imaging parameters for all specimens. Since the effects of biomechanical forces can manifest in countless biological processes, a broad diversity of samples – ranging from single cells to developing embryos – necessitates unique microscopy techniques. In this Review, we detail some of the imaging parameters critical for force measurements, and how the new generation of microscopes can tackle these previously unattainable parameters. In addition, we provide case studies wherein well-considered use of microscopy is beneficial to mechanobiological studies.

Resolution

Biology encapsulates a broad range of length scales, from individual molecules spanning mere nanometers to whole embryos measuring millimeters in length. Any method for visualizing biological processes, however, is subject to the physics of light – diffraction places a fundamental limitation on the minimum distance at which two objects can be distinguished, known as resolution. Resolution is a function of both the microscope numerical aperture (NA) and the wavelength of the emitted light (Amos et al., 2012; Goodwin, 2014), and is conventionally limited to a few hundred nanometers. As a consequence, the final, acquired image is not a true representation of the object being imaged. Due to light diffraction, the image is blurred by (i.e., convolved with) the point spread function (PSF) of the microscope (Pawley, 2006). Furthermore, most microscopes do not offer isotropic resolution, with the axial resolution being more severely compromised (Amos et al., 2012). When using microscopy to measure biological forces, any limitations in resolution will constrain the sensitivity and accuracy of force measurements. Therefore, in studying forces occurring on particularly small length scales, such as those across individual focal adhesions during cell migration (Beningo et al., 2001), the resolution of the microscope must be appropriately matched to the scale of the forces of interest.

A variety of techniques in recent years have been developed to surpass the diffraction limit. One class of these methods is collectively known as enhanced resolution techniques (**Figure 2**). Such techniques provide a maximum twofold improvement in spatial resolution in all directions, but are still ultimately bound by diffraction. Examples of such enhanced resolution methods include Structured Illumination Microscopy (SIM) (**Figures 2A,B**; Gustafsson, 2000; Gustafsson et al., 2008) and Image Scanning Microscopy (ISM) (**Figures 2C,D**; Sheppard, 1988; Müller and Enderlein, 2010; Sheppard et al., 2013) – of which the most popularized commercial system is the Zeiss Airyscan module (Huff, 2015). These methods are particularly well-suited for force measurements as they are relatively fast and are, in general, compatible with live samples.

As an example of the power of coupling enhanced resolution microscopy with force measurements, let us consider the recent work by Colin-York et al. (2019). Recognizing that many cellular processes occur on length scales below the diffraction limit, Colin-York et al. sought to improve the accuracy and resolution of TFM in all three directions with enhanced resolution microscopy (**Figure 3A**). The method of choice in this instance was 3D-SIM, as it allows for rapid, multicolor 3D imaging (11 ms per frame, 15 frames per SIM image plane). In TFM, the density of the beads in the substrate dictates the sensitivity of the force measurement (Colin-York and Fritzsche, 2018). In practice, the maximum bead density that can be incorporated into a traction force measurement is fundamentally dictated by the resolving power of the microscope, as higher resolution is needed to distinguish neighboring beads at a higher density. In studying the force generated during cell adhesion (**Figures 3C,D**), 3D-SIM-TFM enhanced the accuracy of measuring the normal and shear stresses over time (**Figures 3E,F**). The application of 3D-SIM was particularly necessary to more accurately determine the stresses perpendicular to the substrate, which are nominally much smaller than the shear stresses measured in 2D-TFM (Colin-York et al., 2019). Similar performance has recently been achieved through the incorporation of astigmatism in conjunction with TFM (Li et al., 2021). Astigmatism induces a shape change in the PSF that depends on axial position (Kao and Verkman, 1994; Holtzer et al., 2007). This optical distortion allows for high-precision determination of forces perpendicular to the substrate. Measuring these axial forces is important for revealing non-canonical mechanisms of cell motility (Legant et al., 2013). Though not quantified in the study shown in **Figure 3**, 3D-SIM-TFM is well-positioned to improve mechanistic insights with its unique capability of linking, with high resolution, biomechanical forces with morphological changes in the actomyosin network.

However, SIM and ISM can only improve the spatial resolution of a microscope by at most a factor of two. If additional resolving power is necessary, users may turn to a class of techniques collectively known as super-resolution microscopy. Super-resolution microscopy comes in a variety of adaptations, each designed to transcend the diffraction limit and achieve resolutions on the scale of tens of nanometers. One such adaptation is single molecule localization microscopy (SMLM) (Sauer and Heilemann, 2017). SMLM techniques, such as PALM (Betzig et al., 2006) and STORM (Rust et al., 2006), repeatedly image photo-switchable fluorophores to reconstruct biological features with near molecular-scale precision. The computational methods associated with localization-based microscopy have been leveraged to track particle deformations, for example in the context of phagocytosis (Vorselen et al., 2020), and recent strides have been made in coupling SMLM with DNA-based molecular force sensors (Brockman et al., 2020; Schlichthaerle et al., 2021). However, SMLM is still predominantly restricted to fixed samples, rendering them ineffective for studying dynamic force application.

On the other hand, stimulated emission depletion (STED) microscopy (Hell and Wichmann, 1994) is a super-resolution method that is compatible with dynamic force measurements. By leveraging the photophysics of fluorophores and altering the traditional illumination schemes, STED microscopy can reach resolutions beyond SIM and ISM. However, due to the relatively high light dose, STED microscopy provides only a brief window of opportunity to study dynamic forces before incurring photodamage. Despite this limitation, STED microscopy has been combined with TFM (Colin-York et al., 2016). This allowed for a fivefold increase in the density of the bead field relative to diffraction-limited methods, improving the sensitivity of the associated traction force measurements. This came at the cost of severely limited imaging duration, as compared to 3D-SIM-TFM. Such compromise is essential for mechanobiological studies because photodamage can lead to significant alterations in both morphology and function, ultimately leading to apoptosis in some cases (Icha et al., 2017). In measuring forces, such light-induced phenomena cannot be overlooked.

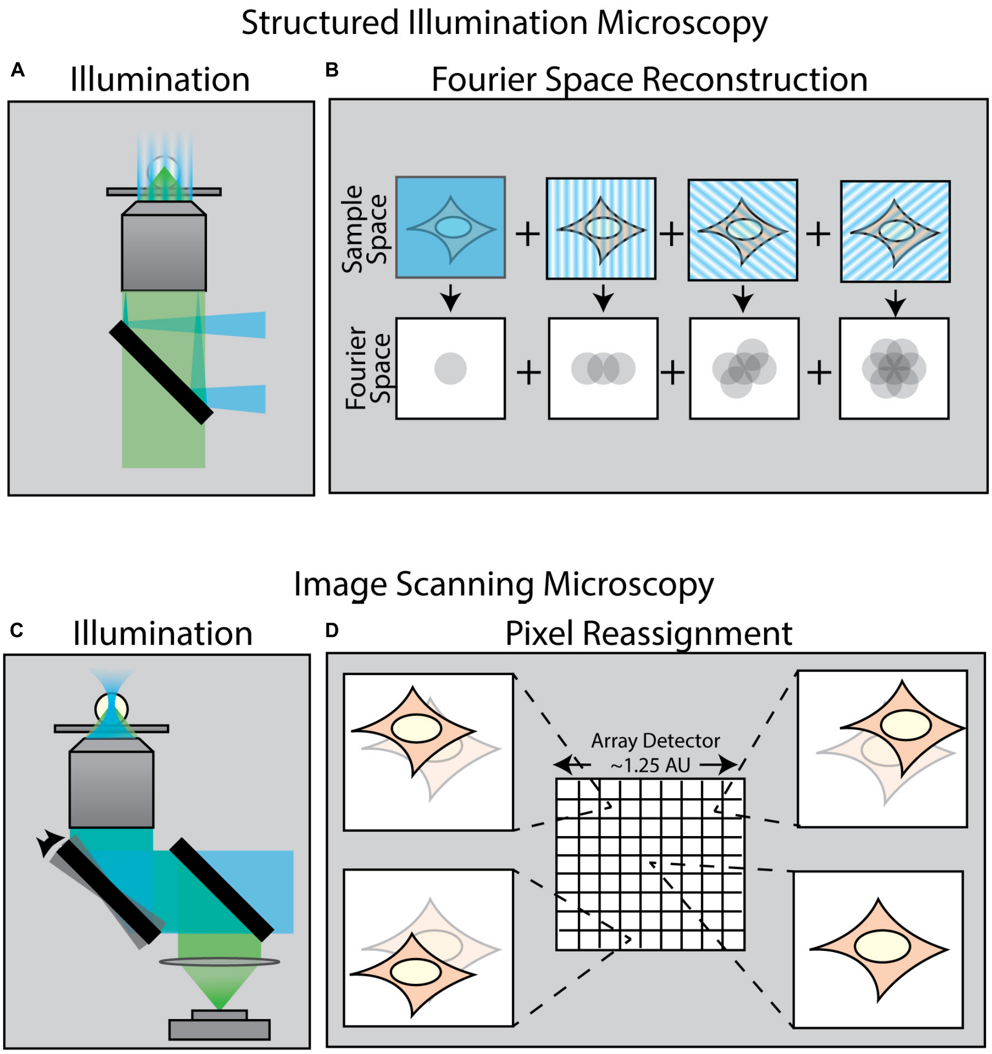

FIGURE 2 | Methods of enhancing resolution in optical microscopy. **(A)** Structured Illumination Microscopy (SIM) is a widefield technique capable of up to twofold resolution enhancement in all directions. It relies on projecting a sinusoidal illumination pattern onto the sample to generate Moiré interference. **(B)** The illumination pattern is rotated and shifted over a series of 9–15 images to introduce extended frequency information into the Fourier space of the image. **(C)** Image Scanning Microscopy (ISM) uses an illumination scheme identical to laser-scanning confocal microscopy; however, the scanned image is collected by an array detector in which each pixel in the array acts as an individual pinhole-restricted point detector. **(D)** In contrast to confocal microscopy wherein a single image is formed via a single point detector, each pixel in an ISM array detector captures its own unique image of the sample from a slightly different angle. This information is computationally combined to create an enhanced resolution image.

Photodamage

The act of illuminating the sample for imaging will inherently lead to photodamage to some extent. As a result, balancing the inevitable photodamage with the required imaging parameters will always be a necessary compromise. Photodamage manifests itself in two primary forms – photobleaching and phototoxicity – which can affect force measurements in distinct ways. Photobleaching (Diaspro et al., 2006b; Waters, 2009) causes a decrease in fluorescence signal-to-noise ratio (SNR), which subsequently reduces contrast and sets the photon budget of an experiment (Wait et al., 2020). This can in turn severely compromise either the timescale of forces that can be measured or the length of time one may observe and perform measurements. Equally important, the poor SNR caused by photobleaching can significantly increases the error in force measurements. On the other hand, phototoxicity results from light-induced damage to a live specimen. The unchecked damage to specimen health and viability calls into question the physiological relevance of the entire force measurement assay. Unfortunately, assessing phototoxicity is often not trivial. In practice, the specimen health is routinely assessed by empirical observation of morphology, which is not always a reliable phototoxicity metric (Icha et al., 2017). However, there are now several studies that explore more robust, quantitative, and sample-specific methods that focus on biological functions over time (such as cell division and proliferation) at various doses of

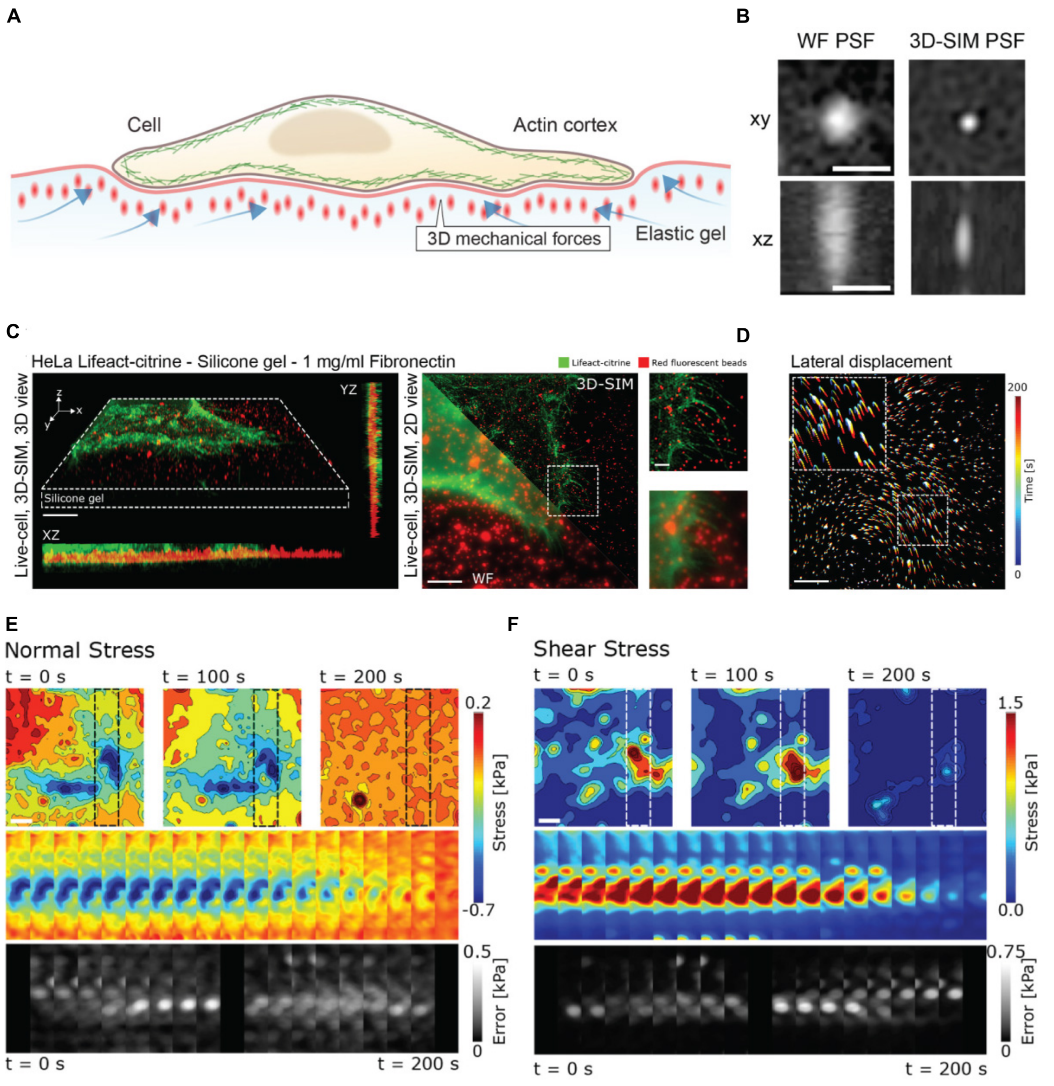

FIGURE 3 | 3D-SIM improves resolution and precision in measuring lateral and axial forces in TFM. **(A)** Schematic representation of 3D-TFM. **(B)** A comparison of PSFs demonstrates the enhanced resolution of 3D-SIM as compared to widefield (WF) microscopy. Scale bar: 0.5 μm. **(C)** (Left) Volumetric rendering and axial projections of 3D-SIM images of a HeLa cell expressing Lifeact-citrine (green) on a TFM substrate with fluorescent fiducial markers (red). (Right) A comparison of WF and 3D-SIM highlights the enhanced resolution. The dashed box inset for both WF and 3D-SIM is shown for direct comparison. Scale bar: 5 μm. **(D)** 2D translation of fiducial markers is shown color-coded for time, demonstrating dynamic cell-generated forces. Scale bar: 5 μm. **(E)** Normal and **(F)** shear stress fields from a 3D-SIM-TFM experiment. Top panels show the stress fields at different points in time. Middle panels show the full time series of stress maps for the region of interest shown in the upper panels indicated by dashed boxes. The lower panels show the estimated error for each time point. Scale bar: 5 μm. Images are reproduced with permission from Colin-York et al. (2019).

light (Tinevez et al., 2012; Douthwright and Sluder, 2017; Laissue et al., 2017; Tosheva et al., 2020).

In principle, photodamage can be alleviated by lessening the light dose on the sample (Icha et al., 2017). Unfortunately, many widely used imaging methods are not fundamentally designed to make lowering the light dose their primary operational principle (Tinevez et al., 2012); in fact, several of these common imaging techniques are particularly prone to incurring photodamage. Confocal microscopy, for example, often induces photodamage for two reasons. First, the light intensity at the focal plane in confocal microscopy is usually in the range of 10^2–10^6 W/cm^2 (Pawley, 2006; Ettinger and Wittmann, 2014), essentially exposing the biospecimen to 10^3–10^7 fold higher irradiance than lifeforms on earth have evolved to withstand (Seidlitz et al., 2001; Chen et al., 2014). Second, the excitation light illuminates the sample both above and below the observational plane. The confocal pinhole merely serves to block out-of-focus *emitted* light and does not prevent the excessive excitation light from damaging the sample outside of the focal plane. One means of mitigating such excessive and unnecessary illumination is to restrict the excitation light to the imaging plane. This can be achieved in several ways.

One method to confine the excitation light is total internal reflection fluorescence (TIRF) microscopy (Axelrod, 1989). TIRF operates by introducing light at or above the critical angle to prevent its propagation into the sample. When this occurs, only fluorophores at the cell-substrate interface are excited. The advantages of using TIRF microscopy are twofold. First, it reduces photodamage by limiting the excitation of the sample solely to within a few hundred nanometers of the coverslip. Second, this restricted excitation plane leads to a higher signal-to-background ratio because unnecessary excitation of fluorescent molecules beyond the focal plane is significantly minimized. This improved contrast allows users to lower the overall intensity of the excitation source. Together, these combined benefits make TIRF microscopy an ideal technique for minimizing photodamage. There are several canonical uses of TIRF microscopy with force measurements, primarily with TFM and FRET tension sensors. For example, coupling TIRF microscopy with FRET tension sensors has been used to study the distribution of forces generated by single integrins (Morimatsu et al., 2013). In addition, the reduced photobleaching associated with TIRF microscopy is particularly useful in FRET applications as unequal photobleaching rates between the donor and acceptor fluorophores can skew ratiometric calculations over time. In a similar way, TIRF microscopy facilitates correlating TFM with biological structures through reduced background (Gutierrez et al., 2011). Coupling of TIRF and TFM [and recently TIRF, SIM, and TFM (Barbieri et al., 2021)] has been used extensively to improve biological force measurements, demonstrating for example the colocalization of nascent focal adhesions with traction stresses (Han et al., 2015). Unfortunately, the specificity of TIRF illumination to the sample-coverslip interface precludes its use when the forces of interest have to be measured at a deeper plane away from the coverslip.

To overcome this limitation, a class of imaging techniques known either as light-sheet fluorescence microscopy (LSFM) or selective plane illumination microscopy (SPIM) can be used (**Figure 4**). These methods introduce a thin sheet of excitation light across the specimen that is coplanar with the image plane (**Figure 4A**). By sweeping the light sheet through the sample, LSFM can provide optical sectioning and contrast comparable to TIRF microscopy, but throughout the entire depth of the specimen. There exists a breadth of LSFM implementations, including multi-view LSFM (**Figure 4B**; Tomer et al., 2012; Kumar et al., 2014) and single-objective LSFM (**Figure 4C**; Bouchard et al., 2015; Liu et al., 2019; Yang et al., 2019; Sapoznik et al., 2020). Additionally, different light sheet profiles are available (**Figure 4D**; Durnin et al., 1987, 1988; Huisken et al., 2004; Planchon et al., 2011; Chen et al., 2014), each with their own specific benefits and limitations. Furthermore, commercialization of LSFM both through standalone systems as well as add-on LSFM modules that can be merged with conventional inverted microscopes (Fadero et al., 2018) has increased the accessibility of this method. A full survey of LSFM methodologies is beyond the scope of this Review; readers are encouraged to refer to several excellent reviews of this class of microscopes (Santi, 2011; Reynaud et al., 2014; Stelzer, 2014; Girkin and Carvalho, 2018).

With the increasingly widespread adoption of LSFM, the benefits of minimizing light exposure have likewise been leveraged in 3D biomechanical force studies. One such example is the recent work of Shah et al. (2021). During tumor invasion and metastasis, cells encounter interstitial spaces that force the cell – and more specifically, the nucleus – to undergo drastic deformations. This compression can often lead to nuclear rupture and DNA damage (Denais et al., 2016). To study this confined migration process and the associated DNA damage, LSFM was used to follow cells as they navigated through narrow pores within 3D collagen matrices (**Figure 5A**). The unique capabilities of LSFM enabled imaging of multiple color channels in 3D over the course of several hours. Laser-scanning confocal microscopy, however, impeded similar experiments by restricting the image to only a single plane (2D) due to photodamage. 3D LSFM imaging was essential for unambiguously detecting formation of new DNA damage foci for two reasons. First, confusion occurs when imaging this process in 2D, as the appearance of foci in this case can be attributed either to a new breakage in DNA or an existing damage site coming into focus. 3D imaging disentangles these two scenarios. Second, it is well documented that over-exposure of light itself can induce DNA damage (Sinha and Häder, 2002), which can conflate conclusion about the role of deformation. The reduced light exposure with LSFM helped isolate the mechanism by which damage sites were produced. Together, these benefits lent to the conclusion that nuclear deformation alone, independent of nuclear rupture, is sufficient to increase double-stranded DNA breaks (**Figures 5B,C**). While the present study did not quantify the magnitude of the forces that these cells underwent during confined migration, coupling of LSFM with labeled matrices would allow future investigators to quantify both the forces applied to the cell by the matrix, as well as the forces that the cell applies to generate motion. Such studies could then infer the magnitude of forces necessary to induce DNA damage or the mechanisms of force generation to facilitate movement through narrow constrictions. The significant reduction in photodamage offered by LSFM is an important technical advance, allowing biologists to probe the roles of biomechanical forces during morphogenesis (Bambardekar et al., 2015; Vedula et al., 2017; de Medeiros et al., 2020), phagocytosis (Nelsen et al., 2020; Vorselen et al., 2021) and T cell engagement (Tamzalit et al., 2019). In general, the ability to observe biological specimens under relatively low-stress conditions has opened new avenues for biologists to pursue their questions within a more physiologically relevant context while pushing the previous limitations on speed, dimensionality, and depth.

Speed and Dimensionality

Studying complex biological processes often dictates 3D observations in multiple color channels, while maintaining sufficient temporal resolution, so that the dynamic interplay among key molecular players can be visualized. Such demanding, multi-dimensional experiments are essential for exploring a range of biological length scales, from single cells to whole organisms. In practice, however, greater image size and dimensionality will come at the cost of reduced imaging speed.

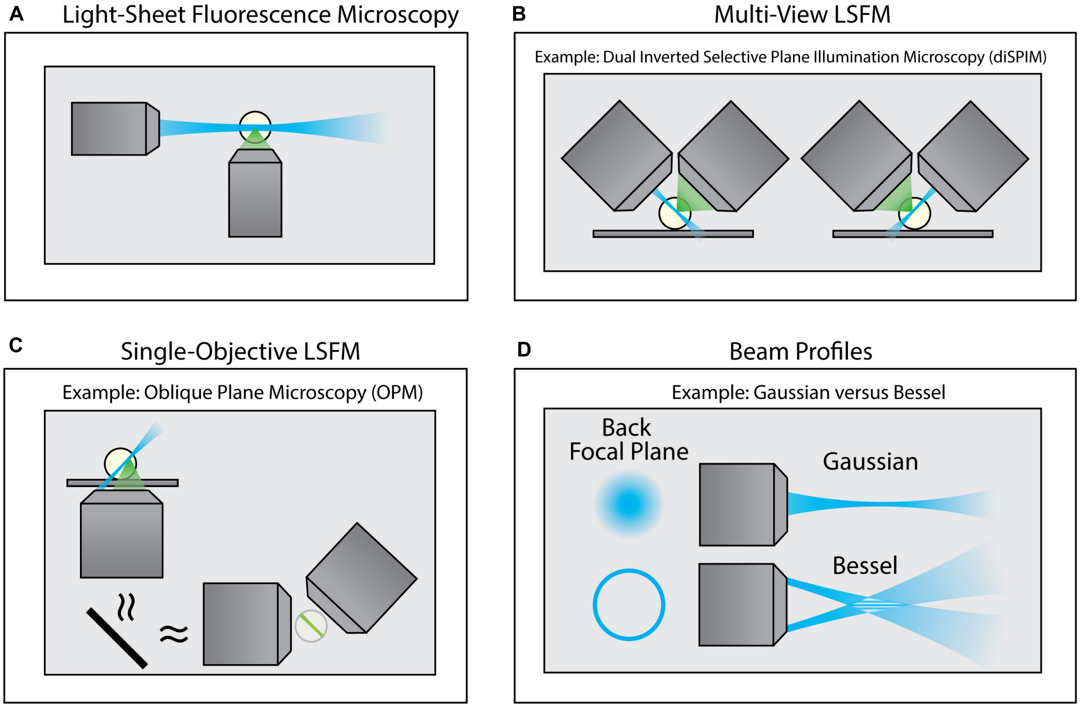

FIGURE 4 | Variants of Light-Sheet Fluorescence Microscopy (LSFM). **(A)** Using an illumination objective lens, conventional LSFM illuminates a thin section of the sample that is coplanar with a separate detection lens. This restricts excitation to only the portion of the sample being imaged, thus improving contrast and minimizing photodamage. **(B)** Multi-view LSFM (e.g., diSPIM) can achieve multiple viewing angles by alternating the function of both objective lenses (as shown) or by incorporating multiple detection objective lenses to image the sample. Computational fusion of these multiple viewing angles can enable isotropic resolution, as well as mitigate attenuation artifacts. **(C)** Single-Objective LSFM (e.g., OPM) uses the same objective lens for both excitation and detection, providing adaptability for a wide range of samples and external devices. **(D)** Light sheets can be formed with different beam profiles (e.g., Gaussian or Bessel beams) that offer unique advantages for specific biological applications.

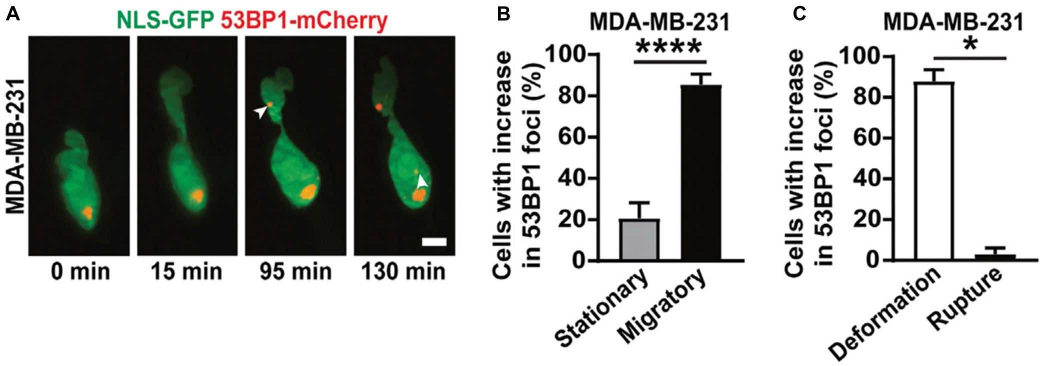

FIGURE 5 | 3D LSFM combined with confined migration minimizes photodamage during force-based experiments. **(A)** LSFM images of an MDA-MB-231 cell expressing GFP-tagged nuclear localization sequence (NLS-GFP), in green, and DNA damage marker (53BP1-mCherry), in red, navigating a 3D collagen matrix. The white arrows indicate new sites of DNA damage. Scale bar: 5 μm. **(B)** The percentage of MDA-MB-231 nuclei that show new sites of DNA damage when stationary or migratory. **** represents $p < 0.0001$ for a Fisher's test. **(C)** The percentage of MDA-MB-231 nuclei that show DNA damage due to deformation alone or due to nuclear rupture. * represents $p < 0.05$ for a chi-square test. Images are reproduced with permission from Shah et al. (2021).

Acquisition speed is a critical imaging parameter, as one needs to accurately follow in time the forces being studied. For certain physiological processes, the timescales are long enough such that the trade-off between speed and dimensionality is acceptable given conventional imaging methods. However, there are biological events that occur on single-second timescales – such as membrane tether rupture (Schmitz et al., 2008) and photoablation-induced tension relaxation (Kumar et al., 2006; Zhang et al., 2020) – that are best addressed by more advanced imaging methods.

By design, the versatility and gentle illumination of LSFM can be leveraged to tackle these demanding mechanobiological phenomena. As previously mentioned, LSFM minimizes out-of-plane fluorescence by restricting the excitation light to a thin sheet, thereby greatly improves image contrast. In comparison to widefield microscopy, this considerable contrast improvement enables shorter exposure times and faster imaging rates. While laser-scanning confocal microscopy can provide similar contrast to LSFM, it fails to offer the high imaging rates of LSFM. Together, the benefits of LSFM permit multi-channel volumetric acquisitions of single cells with rates approaching 1–5 s per volume. The work of Tamzalit et al. (2019) is an excellent case study on the benefits of improving speed and dimensionality in force measurements. The investigators sought to measure the forces associated with cytotoxic T lymphocyte (CTL) engagement with micropillar arrays (**Figure 6A**) and dynamically characterize the formation of synaptic protrusions. This experiment required multiple channels to visualize the micropillars themselves as well as track cellular structures associated with immune synapse formation. The investigators used lattice light-sheet microscopy (LLSM) (Chen et al., 2014), as it is particularly well-suited for fast 3D sub-cellular imaging. This coupling of LSFM with micropillar arrays gave sufficient temporal resolution to visualize actin protrusions permeating the array of micropillars and localize lytic granule fusion sites during synapse formation (**Figure 6B**). Furthermore, LSFM was used to monitor CTL-induced deformation of target cells, leading to quantification of synapse volume as a function of time (**Figure 6C**). Intriguingly, the investigators successfully used 2D confocal microscopy to track micropillar flexure, but were unable to achieve the necessary temporal resolution in 3D to monitor synapse formation (unpublished data). This lays the groundwork for using LSFM to quantify in 3D the full bending, twisting, and translation of micropillar arrays, rather than only the conventional 2D translations. This added dimensionality can be used to extract axial forces and to determine the precise location of force generation.

Recently, investigators have coupled AFM with LSFM (AFM-LS) to either directly image the plane of applied force with up to 10 ms temporal resolution (Beicker et al., 2018), or collect multi-channel volumetric images with simultaneous correlated force measurements (Nelsen et al., 2020). The additional speed and dimensionality that AFM-LS provides allowed investigators to separate the roles of individual nuclear substructures in response to an applied force (Hobson et al., 2020) as well as correlate actin dynamics with engulfment forces during phagocytosis (Nelsen et al., 2020). Similarly, LSFM was coupled with microparticle traction force microscopy to both quantify the forces associated with phagocytosis and identify novel actin structures responsible for their generation (**Figures 7A,B**; Vorselen et al., 2021). These examples display how microscopy can provide additional insight into the cellular structures responsible for generating or responding to mechanical stimuli. Furthermore, researchers have combined FRET with the benefits of LSFM, and developed publicly available software to analyze this challenging type of data (O'Shaughnessy et al., 2019). This opens the door for future studies to utilize FRET for quantifying molecular-scale tension forces in 3D at unprecedented speeds. These examples highlight how LSFM, in conjunction with force measurement, unlocks information that traditional microscopy cannot provide. We have thus far dwelled on mechanistic studies at the cellular level; yet, biomechanical force is an indispensable signal and regulator in morphogenesis and development as well (Guillot and Lecuit, 2013; Heisenberg and Bellaïche, 2013; Agarwal and Zaidel-Bar, 2021). When force measurements must be performed in the physiological context of a whole organism, the tissue heterogeneity, light scattering, and large-scale specimen movement can easily affect the precision and outcome. Overcoming these challenges will require further technical advances.

Imaging Depth

Imaging whole tissues and embryos presents a gamut of new challenges as compared to imaging single cells. While techniques such as LSFM have begun to enable biomechanical force measurements during tissue morphogenesis (Bambardekar et al., 2015; Vedula et al., 2017; de Medeiros et al., 2020), heterogeneity in large samples can cause significant aberrations due to refraction, scattering, and absorption (Schwertner et al., 2007). These complications will reduce spatial resolution and contrast, rendering force measurement experiments significantly less accurate or even impossible.

To gain better light penetration depth when imaging large samples, one may turn to using two-photon (2P) excitation (Denk et al., 1990; Diaspro et al., 2006a). In contrast to conventional fluorescence, 2P excitation uses two photons of double the required wavelength to excite a fluorophore. This permits deeper imaging for two reasons. First, longer wavelength excitation will generally experience fewer interactions with the sample. Second, 2P excitation events are far more rare than traditional fluorescence (Denk, 1996; Denk and Svoboda, 1997; Svoboda and Yasuda, 2006); therefore, emission occurs within a much smaller excitation volume. This minimizes background fluorescence, particularly in deep tissue. 2P excitation light is typically raster-scanned across the sample, similar to confocal microscopy. However, it has also been implemented in LSFM configurations to combine the benefits of both techniques (Truong et al., 2011; Mahou et al., 2014; Wolf et al., 2015). The predominant use of 2P microscopy in measuring biomechanical forces is through photoablation and measurement of subsequent tension relaxation (Shen et al., 2005; Rauzi et al., 2008, 2010; Ratheesh et al., 2012; Michael et al., 2016; Yamaguchi et al., 2020). While many studies leverage ultra-violet pulsed lasers to ablate specimen targets (Kiehart et al., 2000; Hutson et al., 2003; Fernandez-Gonzalez et al., 2009; Colombelli and Solon, 2013; Smutny et al., 2015; Hara et al., 2016; Zhang et al., 2020), the use of 2P microscopy improves both ablation depth and precision. This is of particular importance when measuring tension *in vivo*, as is exemplified by the work of Rauzi et al. (2008). In this case, 2P microscopy permitted ablation of individual *Drosophila* embryo cell-cell junctions during cell intercalation without disrupting the plasma membrane (**Figures 8A,B**). This led to the observation that tension is anisotropic within the tissue,

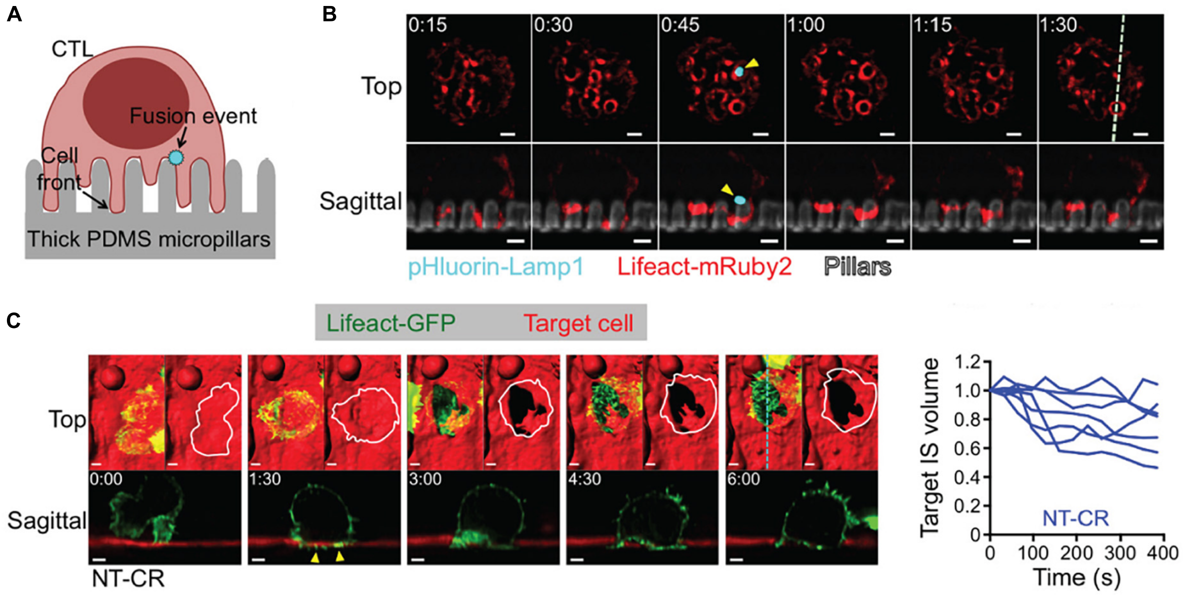

FIGURE 6 | 3D LSFM coupled with micropillar arrays improves temporal sampling during force measurements. **(A)** Schematic representation CTL engagement with micropillar arrays and the formation of synaptic protrusion and lytic granule fusion events. **(B)** LLSM of a CTL expressing Lifeact-mRuby2 (red) and pHluorin-Lamp1 (blue) engaged with a micropillar array (gray). The top row provides an x-y view from above. The bottom row shows an axial cross section of the region denoted by the dashed line in the upper right panel. Yellow arrows indicate the site of a fusion event. Time is given in minutes:seconds, scale bars: 2 μm. **(C)** (Left) LLSM of a CTL expressing Lifeact-GFP (green) engaging with a target cell (red). The top row provides an x-y view from above with a surface rendering visualization. The bottom row shows an axial cross section of the region denoted by the cyan dashed line in the upper right panel. Yellow arrows indicate protrusions into the target cell. Time is given in minutes:seconds, scale bars: 2 μm. (Right) Target cell volume plotted as a function of time. Each curve represents an individual CTL-target cell engagement. Images are reproduced with permission from Tamzalit et al. (2019).

which was posited as a mechanism to promote tissue elongation (Rauzi et al., 2008). However, 2P microscopy has rarely been used in conjunction with other force measurement techniques outside of photoablation. This is primarily due to the relative scarcity of force probes that are specifically designed for whole tissues. 2P microscopy furthermore has a limited repertoire for biomechanical studies in deep tissue: its acquisition speed limited by raster-scanning and its multicolor capability complicated by large excitation overlap between fluorophores.

To push the multidimensional capability deeper into the context of a whole organism, approaches based on adaptive optics (AO) have been developed. The overall goal of AO is to measure the image distortion induced by the sample and use that information to counter the aberration, rendering crisper and brighter images. One such method – the "guide star" technique (Primmerman et al., 1991) – images point sources at various locations in a sample to characterize the local wavefront distortion. An adaptive element, such as a deformable mirror, then applies the inverse of that distortion to recover the un-aberrated image. AO can be integrated into both standard microscopes (Azucena et al., 2011; Tao et al., 2011) as well as more advanced systems, such as the lattice light-sheet microscope (Liu et al., 2018). Likewise, AO can also be used to correct the excitation light wavefront, which is particularly important for methods that use some form of spatially structured excitation. The next frontier of exploration into the complex physiology of biomechanical force transduction will demand the strategic integration of (i) purpose-designed *in vivo* force sensors, (ii) advanced optical microscopes, and (iii) computational tools.

DATA ANALYSIS AND HANDLING

Any microscopy-based force measurement technique will require image processing and analysis to achieve meaningful results. Two of the most common techniques are particularly dependent in this regard: (i) traction force microscopy (TFM) and (ii) FRET tension biosensors. Both techniques require careful and often complex image-based calculations to arrive at an accurate force measurement. Here, we discuss the data handling and analysis challenges of these two methods, particularly in the context of their implementation with advanced imaging technologies.

Analysis of Traction Force Microscopy Data

Measuring the displacement of embedded fiducial markers provides a quantitative view into the minute forces cells exert on their environment. As described previously, TFM is considered one of the "classical" techniques of force measurement in mechanobiology (Harris et al., 1980; Dembo and Wang, 1999). The concept of TFM is deceptively simple: optical tracking of fiducial markers provides data that can be mathematically related to the physical forces that cells exert on a substrate. However, this straightforward premise requires several complex decisions

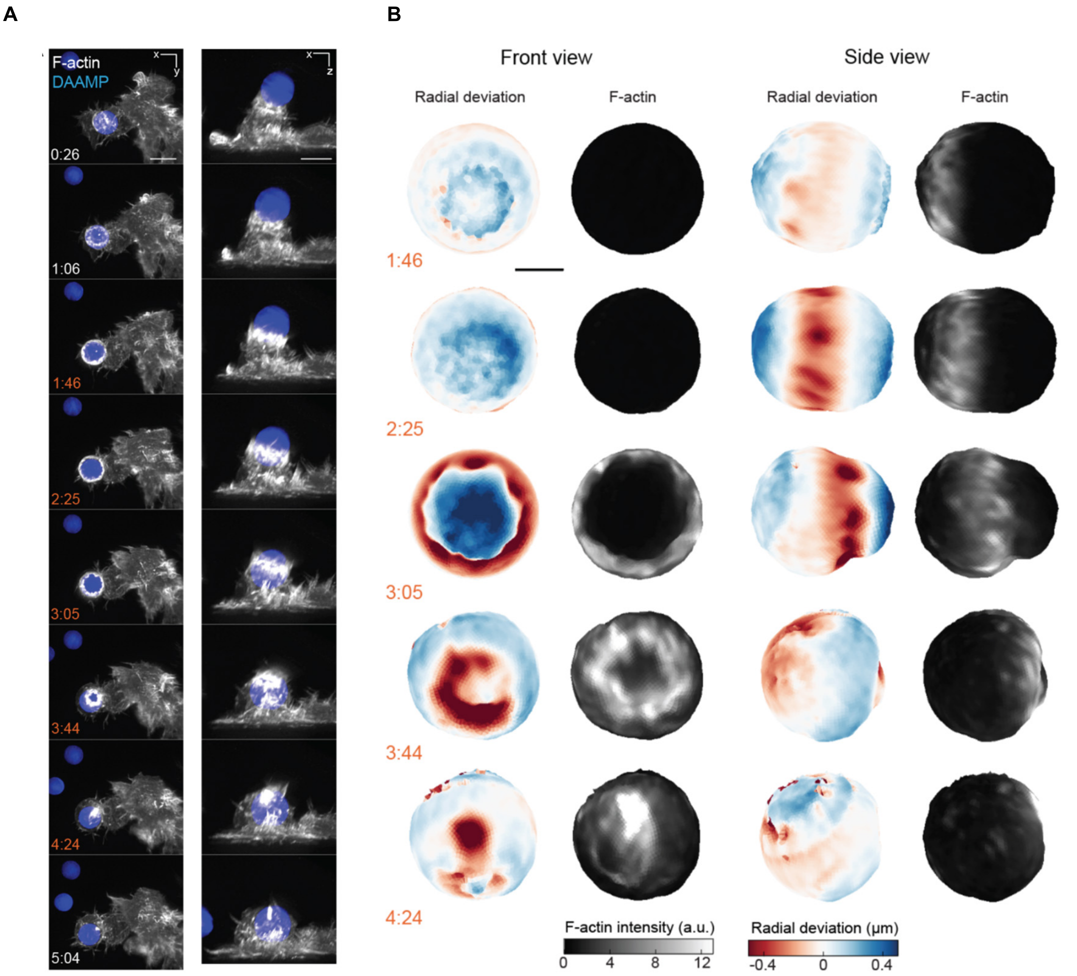

FIGURE 7 | 3D LSFM combined with microparticle traction force microscopy monitors target deformation during phagocytosis. **(A)** Maximum intensity projections of RAW macrophages expressing Lifeact-mEmerald (white) engulfing deformable particles labeled with AlexaFluor 647 (blue) imaged with LLSM. Time is given in minutes:seconds, scale bar: 5 μm. **(B)** Front and side view projections of target deformations and actin intensity around the target particle at various time points during the engulfment process. Time denoted in minutes:seconds, scale bar: 3 μm. Images are reproduced with permission from Vorselen et al. (2021).

in experimental design, analysis, and optical configuration to achieve the most biologically relevant data.

First, the choice for fiducial markers is critical to data quality. To maximize the force sampling density, it is recommended that fiducials be smaller than the spatial resolution of the optical system (e.g., 100 nm diameter). While larger particles (e.g., 500 nm diameter) can be more easily localized in lower resolution optical instruments, it restricts the maximum fiducial density in the substrate. This is important because higher density will provide better sampling of the minute changes in the displacement field, which translates to more refined force calculations. The maximum density of fiducials, and therefore the ability to sample biomechanical force, is ultimately limited by the optical resolution. However, two methods can circumvent this barrier. First, beads of multiple colors can be placed within the same substrate and imaged separately (Gardel et al., 2008; Sabass et al., 2008; Plotnikov et al., 2012). This technique, referred to as "high resolution TFM," improves the force measurement sampling by several fold (Plotnikov et al., 2014), but requires accurate multi-channel alignment. Recent advances in optical microscopy, such as SIM and ISM, enable similar gains in fiducial density by enhancing the spatial resolution up to twice the diffraction limit (Colin-York and Fritzsche, 2018; Colin-York et al., 2019; Barbieri et al., 2021). A combination of both enhanced-resolution microscopy and multi-color fiducial markers would allow even higher fiducial densities beyond either method alone. Fiducial density aside, it is also important to consider the assumptions inherent to TFM analysis.

There are two important assumptions that must be made for later force calculations. First, it is presumed that any motion of the fiducial markers is due only to cell-generated forces. This assumption does not always hold true; drift or degradation of the substrate itself can lead to non-biological fiducial displacement. Such effects can be identified either by imaging substrates without cells attached or imaging a large enough field of view to capture non-perturbed regions for comparison. The second potentially

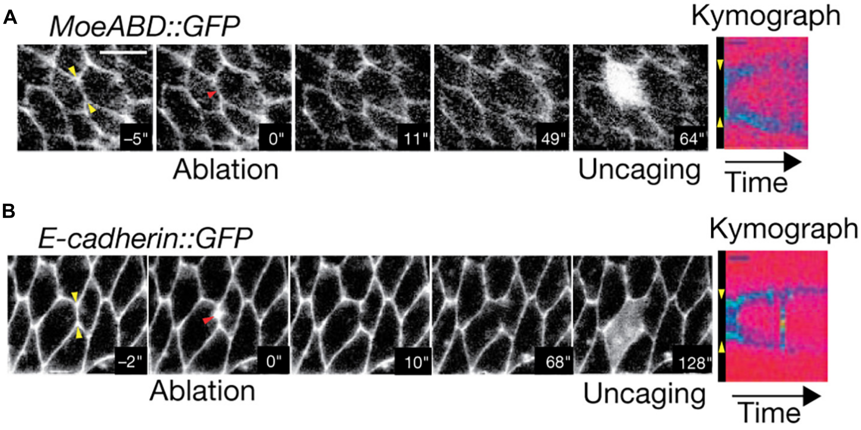

FIGURE 8 | Two-Photon photoablation reveals mechanical tension *in vivo*. Image sequences of *Drosophila* embryo expressing **(A)** MoeABD-GFP and **(B)** E-cadherin-GFP during 2P photoablation of cell-cell junctions. The red arrow in the second panel from the left represents the site of photoablation. Kymographs at the right (taken at the yellow arrows shown in first panel) show the release and retraction of the ablated region. Uncaging of fluorescein with three-photon microscopy (panel 5) demonstrates that the cell integrity is not disrupted by the photoablation. Scale bar: 5 μm. Images are reproduced with permission from Rauzi et al. (2008).

erroneous assumption is in the mechanical uniformity of the substrate. Numerous substrates have been used to interrogate specific behaviors, from simple polyacrylamide gels (PAAG) to more complex patterned microsurfaces (Balaban et al., 2001; Beningo et al., 2001; Tamzalit et al., 2019). To properly calculate force, the analysis must assume that the material rigidity is constant across the whole volume. In other words, TFM relies on the presumption that every bead in the substrate will experience an identical displacement from a given amount of force. Mechanical homogeneity of the substrate can be assessed by conventional stiffness measurement assays such as atomic force microscopy (Tse and Engler, 2010).

For conventional TFM, individual beads are optically tracked using localization or correlation-based particle image velocimetry (Butler et al., 2002; Toli-Nørrelykke et al., 2002). This analysis produces a set of bead displacements over time. From there, the mathematical and physical relationships that connect these displacements to underlying forces must be applied properly (Huang et al., 2019). These intensive calculations compound any error in the initial optical measurement of the displacement field. The use of optical-sectioning methods such as TIRF and LSFM minimizes inaccuracies by dramatically increasing the fiducial signal contrast and therefore localization precision (Gutierrez et al., 2011; Han et al., 2015; Barbieri et al., 2021). Finite element analysis, Bayesian models, or various regularization methods can provide more sophisticated information to better represent the true nature of complex biomechanical systems. It is beyond the scope of this review to compare mathematical models used in TFM which have been well-covered in the literature (Yang et al., 2006; Zielinski et al., 2013; Kulkarni et al., 2018; Huang et al., 2019). Better models and advanced instrumentation are necessary to investigate more complex multi-cellular systems (Franck et al., 2011; Tang et al., 2014), which require considering both cell-substrate and cell-cell interactions. While TFM represents a powerful technique to measure nanoscale forces exerted by various biological systems, it lacks a means to identify the source(s) of such forces with molecular specificity.

Analysis of FRET Tension Biosensor Data

Genetically encoded FRET-based biosensors can quantify biological tension with molecular specificity and picoNewton sensitivity (Cost et al., 2015, 2019; LaCroix et al., 2015; Gayrard and Borghi, 2016; Gates et al., 2019). This technique relies on microscopy to measure the sensor FRET efficiency, or the degree of energy transfer occurring between the donor and acceptor fluorophores to infer a tension force. However, analysis of such data must be performed judiciously, and advanced imaging methods can both complicate and ameliorate the generation of meaningful biological conclusion.

Arguably the most common way to measure FRET efficiency requires computing the ratio of acceptor-to-donor fluorescence intensity (Hoppe, 2007). However, numerous factors can render a naïvely calculated ratiometric image utterly non-informative. First, cross-excitation and spectral overlap will produce erroneous signal in both donor and acceptor channels. To account for this, it is imperative to prepare proper control samples labeled with tension sensors containing only donor or acceptor fluorophores alone (O'Shaughnessy et al., 2019).

However, other factors will also affect the accuracy of ratiometric FRET calculations. Microscope illumination intensity may vary by a surprising amount across the field of view. To account for this variability, homogeneous fluorescent samples should be imaged in both donor and acceptor channels (Model and Burkhardt, 2001) as a reference. Such "shade correction" can be of particular importance in more advanced microscopes such as LSFM or other patterned illumination systems that can be especially prone to uneven excitation light. In addition, the accuracy of ratiometric FRET measurements is dependent on the precision of color channel registration. Enhanced resolution techniques such as SIM and ISM can often reveal misalignments that are not apparent with lower resolution techniques (Baddeley et al., 2011). Multicolor fiducial markers provide a way to computationally register color channels with sub-diffraction accuracy (Manders, 1997). Finally, it is also important to normalize the measured donor signal by the overall donor photobleaching rate within the cell (Zal and Gascoigne, 2004), although LSFM can often reduce photobleaching to near negligible levels (Chen et al., 2014). While complex, such analysis can be successfully implemented to create high-quality FRET images. For example, O'Shaughnessy et al. (2019) have developed freely available FRET analysis software that is well suited for dealing with large volume LSFM data.

Other advanced imaging techniques can simplify ratiometric FRET measurements and analysis. For example, spectral imaging permits detection and computational extraction of both donor and acceptor signals from a single acquisition (Ecker et al., 2004), making image registration and crosstalk correction unnecessary. However, spectrally resolved detection is most common in laser-scanning confocal microscopes (Zimmermann et al., 2003), with fewer implementations in other more advanced modalities. Additionally, the presence of endogenous fluorescent molecules in the sample can complicate accurate analysis (Rossetti et al., 2020). Once an accurate ratio of donor-to-acceptor fluorophore intensity has been established, an image of FRET efficiency can be calculated (Chen et al., 2006).

Conversely, fluorescence lifetime imaging microscopy (FLIM) is an alternative to intensity-based methods for measuring FRET efficiency (Becker, 2012; Ebrecht et al., 2014). In this case, the donor fluorescence lifetime, rather than the ratio of donor and acceptor intensities, can be used to determine FRET efficiency directly. FLIM is a powerful technique to characterize FRET-based tension sensors and is subject to far fewer confounding issues than ratiometric approaches. However, the necessary instrumentation is more specialized and less commonly available than other imaging technologies. It can also suffer from slower acquisition speed compared to widefield or raster-scanning techniques, although recent advancements have begun to address this issue. For example, Mizuno et al. (2021) devised a system whereby a sample was illuminated sinusoidally in time, with a unique modulation frequency at each pixel location. Through this, they were able to perform frequency domain FLIM without serially scanning a focal spot across the sample, thereby greatly improving FLIM speed over previous methods.

Regardless of the method chosen, an appropriate calibration curve is required to translate a measured FRET efficiency into force (Grashoff et al., 2010; Gayrard and Borghi, 2016). Such a relationship is essential to establish because FRET efficiency will not, in general, be linearly proportional to force. The most common procedure to experimentally calibrate FRET tension biosensors has been via the use of optical tweezers (Hohng et al., 2007; Grashoff et al., 2010). While this procedure can be technically challenging, a number of FRET-based tension sensors have been previously characterized in the literature (Grashoff et al., 2010; Ringer et al., 2017; Salmon and Bloom, 2017; Li et al., 2018), allowing subsequent users to more easily translate their own measured image data into high quality force maps.

DISCUSSION

Biomechanical forces underpin a wide array of life processes, ranging from mediating cellular behavior, regulating signaling pathways, sculpting morphogenesis, governing embryonic development, facilitating immune response, to influencing the pathogenesis of many diseases that include cancer, cardiovascular failure, and musculoskeletal disorders. It is therefore no surprise that mechanobiology continues to gain prominence and the attention of biologists across many fields. Unlike many biochemical signals, biomechanical forces cannot be directly tagged for visualization and therefore must be inferred. The methods discussed here provide innovative solutions for measuring force with exquisite sensitivity. However, in practice, their accuracy and precision are ultimately limited by the capabilities of the accompanying microscope. In that regard, many emerging microscopy techniques hold the promise of considerable technological improvements which, when appropriately integrated into a force measurement assay, can reveal further biomechanical insights that have hitherto remained out of reach.

One considerable barrier not commonly discussed in the surveys of emerging microscopy technologies is the lack of accessibility for most biologists to this cadre of instruments, many of which are not commercially available. These instruments are usually developed in engineering or biophysics laboratories that historically have limited interaction with biologists. The inherent academic compartmentalization between research disciplines as disparate as life sciences and optical engineering can often impede the adoption of the nascent imaging technologies by mechano-biologists. This is especially the case when the creation of new microscopy technology far outpaces the speed of commercialization. However, with the idea of open science continuing to gain prevalence, many initiatives have been created to tear down these barriers. There are now numerous international and regional initiatives dedicated to bridging the chasm between technology development and adoption, thus making advanced microscopes and the associated expertise accessible to the broader life sciences community. Some of these centers – e.g., the Advanced Imaging Center at HHMI Janelia Research Campus (Chew et al., 2017) and the Advanced Bioimaging Center at the University of California-Berkeley – are specifically designed to provide peer-reviewed, proposal-driven, free-of-charge accessibility to these emerging microscopy technologies well before they become commercially available. For initiatives such as these to make an effective impact, a myriad of institutional support and imaging science expertise is essential, requiring significant investment.

An alternative open-access model is the concept of a "traveling microscope." One effort by Huisken and colleagues, dubbed the "Flamingo," seeks to address instrument access by designing a modular, portable light sheet system (Power and Huisken, 2019). The instrument is customizable and shipped with full installation instructions to institutes across the world. While this concept is limited to optical techniques that will survive shipping, it can be a useful option for mechanobiologists who are impeded by instrument access through any other means. Another laudable approach is the recent paradigm shift toward sharing design blueprints of newly developed, pre-published microscopy tools, through open access mechanisms (Pitrone et al., 2013; Chew et al., 2017; Millett-Sikking et al., 2019; Voigt et al., 2019; Kumar et al., 2021). For groups with the necessary expertise and resources, replicating these instruments is a viable and sustainable choice.

Taken together, the remarkable confluence of advanced optics and the unprecedented access to microscopy resources makes this the opportune time to sharpen the toolkit for biomechanical force measurement. Advanced microscopy now enables imaging with unprecedented versatility; developing force probes that fully take advantage of such tools for *in vivo* mechanobiological studies is a necessary next step. Overall, synergistic development of force measurement techniques, new optical tools, and novel computational strategies will be critical for elevating biomechanical studies to the next frontier.

AUTHOR CONTRIBUTIONS

All authors contributed to the conceptualization, writing and editing of this manuscript, and approved the submitted version.

FUNDING

This Advanced Imaging Center at Janelia Research Campus was generously supported by the Howard Hughes Medical Institute and the Gordon and Betty Moore Foundation.

REFERENCES

Agarwal, P., and Zaidel-Bar, R. (2021). Mechanosensing in embryogenesis. *Curr. Opin. Cell Biol.* 68, 1–9. doi: 10.1016/j.ceb.2020.08.007

Airan, R. D., Thompson, K. R., Fenno, L. E., Bernstein, H., and Deisseroth, K. (2009). Temporally precise in vivo control of intracellular signalling. *Nature* 458, 1025–1029. doi: 10.1038/nature07926

Amos, B., McConnell, G., and Wilson, T. (2012). "Confocal microscopy," in *Comprehensive Biophysics* ed, E. Egelman, (Amsterdam: Elsevier), 3–23. doi: 10.1016/B978-0-12-374920-8.00203-4

Angulo-Urarte, A., van der Wal, T., and Huveneers, S. (2020). Cell-cell junctions as sensors and transducers of mechanical forces. *Biochim. Biophys. Acta Biomembr.* 1862:183316. doi: 10.1016/j.bbamem.2020.183316

Axelrod, D. (1989). Total Internal Reflection Fluorescence (TIRF) Microscopy. *Methods Cell Biol.* 30, 245–270. doi: 10.1016/S0091-679X(08)60982-6

Azucena, O., Crest, J., Kotadia, S., Sullivan, W., Tao, X., Reinig, M., et al. (2011). Adaptive optics wide-field microscopy using direct wavefront sensing. *Opt. Lett.* 36, 825–827. doi: 10.1364/ol.36.000825

Baddeley, D., Crossman, D., Rossberger, S., Cheyne, J. E., Montgomery, J. M., Jayasinghe, I. D., et al. (2011). 4D super-resolution microscopy with conventional fluorophores and single wavelength excitation in optically thick cells and tissues. *PLoS One* 6:e20645. doi: 10.1371/journal.pone.0020645

Balaban, N. Q., Schwarz, U. S., Riveline, D., Goichberg, P., Tzur, G., Sabanay, I., et al. (2001). Force and focal adhesion assembly: A close relationship studied using elastic micropatterned substrates. *Nat. Cell Biol.* 3, 466–472. doi: 10.1038/35074532

Bambardekar, K., Clément, R., Blanc, O., Chardès, C., and Lenne, P. F. (2015). Direct laser manipulation reveals the mechanics of cell contacts in vivo. *Proc. Natl. Acad. Sci. U.S.A.* 112, 1416–1421. doi: 10.1073/pnas.1418732112

Bao, G., and Suresh, S. (2003). Cell and molecular mechanics of biological materials. *Nat. Mater.* 2, 715–725. doi: 10.1038/nmat1001

Barbieri, L., Colin-York, H., Korobchevskaya, K., Li, D., Wolfson, D. L., Karedla, N., et al. (2021). Two-dimensional TIRF-SIM–traction force microscopy (2D TIRF-SIM-TFM). *Nat. Commun.* 12:2169. doi: 10.1038/s41467-021-22377-9

Basu, R., Whitlock, B. M., Husson, J., Le Floc'h, A., Jin, W., Oyler-Yaniv, A., et al. (2016). Cytotoxic T Cells Use Mechanical Force to Potentiate Target Cell Killing. *Cell* 165, 100–110. doi: 10.1016/j.cell.2016.01.021

Becker, W. (2012). Fluorescence lifetime imaging - techniques and applications. *J. Microsc.* 247, 119–136. doi: 10.1111/j.1365-2818.2012.03618.x

Beech, D. J., and Kalli, A. C. (2019). Force Sensing by Piezo Channels in Cardiovascular Health and Disease. *Arterioscler. Thromb. Vasc. Biol.* 39, 2228–2239. doi: 10.1161/ATVBAHA.119.313348

Beicker, K., O'Brien, E. T., Falvo, M. R., and Superfine, R. (2018). Vertical Light Sheet Enhanced Side-View Imaging for AFM Cell Mechanics Studies. *Sci. Rep.* 8:1504. doi: 10.1038/s41598-018-19791-3

Beningo, K. A., Dembo, M., Kaverina, I., Small, J. V., and Wang, Y. L. (2001). Nascent focal adhesions are responsible for the generation of strong propulsive forces in migrating fibroblasts. *J. Cell Biol.* 153, 881–887. doi: 10.1083/jcb.153.4.881

Betzig, E., Patterson, G. H., Sougrat, R., Lindwasser, O. W., Olenych, S., Bonifacino, J. S., et al. (2006). Imaging intracellular fluorescent proteins at nanometer resolution. *Science* 313, 1642–1645. doi: 10.1126/science.1127344

Bishop, J. E., and Lindahl, G. (1999). Regulation of cardiovascular collagen synthesis by mechanical load. *Cardiovasc. Res.* 42, 27–44. doi: 10.1016/S0008-6363(99)00021-8

Bouchard, M. B., Voleti, V., Mendes, C. S., Lacefield, C., Grueber, W. B., Mann, R. S., et al. (2015). Swept confocally-aligned planar excitation (SCAPE) microscopy for high-speed volumetric imaging of behaving organisms. *Nat. Photonics* 9, 113–119. doi: 10.1038/nphoton.2014.323

Brockman, J. M., Su, H., Blanchard, A. T., Duan, Y., Meyer, T., Quach, M. E., et al. (2020). Live-cell super-resolved PAINT imaging of piconewton cellular traction forces. *Nat. Methods* 17, 1018–1024. doi: 10.1038/s41592-020-0929-2

Butler, J. P., Toli-Nørrelykke, I. M., Fabry, B., and Fredberg, J. J. (2002). Traction fields, moments, and strain energy that cells exert on their surroundings. *Am. J. Physiol. Cell Physiol.* 282, 595–605. doi: 10.1152/ajpcell.00270.2001

Caille, N., Tardy, Y., and Meister, J. J. (1998). Assessment of strain field in endothelial cells subjected to uniaxial deformation of their substrate. *Ann. Biomed. Eng.* 26, 409–416. doi: 10.1114/1.132

Campàs, O., Mammoto, T., Hasso, S., Sperling, R. A., O'connell, D., Bischof, A. G., et al. (2014). Quantifying cell-generated mechanical forces within living embryonic tissues. *Nat. Methods* 11, 183–189. doi: 10.1038/nmeth.2761

Chen, B. C., Legant, W. R., Wang, K., Shao, L., Milkie, D. E., Davidson, M. W., et al. (2014). Lattice light-sheet microscopy: Imaging molecules to embryos at high spatiotemporal resolution. *Science* 346:1257998. doi: 10.1126/science.1257998

Chen, H., Puhl, H. L., Koushik, S. V., Vogel, S. S., and Ikeda, S. R. (2006). Measurement of FRET Efficiency and Ratio of Donor to Acceptor Concentration in Living Cells. *Biophys. J.* 91, L39–L41. doi: 10.1529/biophysj.106.088773

Chew, T.-L., George, R., Soell, A., and Betzig, E. (2017). Opening a Path to Commercialization. *Opt. Photonics News* 28, 42–49. doi: 10.1364/opn.28.7.000042

Cho, S., Irianto, J., and Discher, D. E. (2017). Mechanosensing by the nucleus: From pathways to scaling relationships. *J. Cell Biol.* 216, 305–315. doi: 10.1083/jcb.201610042

Colin-York, H., and Fritzsche, M. (2018). The future of traction force microscopy. *Curr. Opin. Biomed. Eng.* 5, 1–5. doi: 10.1016/j.cobme.2017.10.002

Colin-York, H., Javanmardi, Y., Barbieri, L., Li, D., Korobchevskaya, K., Guo, Y., et al. (2019). Spatiotemporally Super-Resolved Volumetric Traction Force Microscopy. *Nano Lett.* 19, 4427–4434. doi: 10.1021/acs.nanolett.9b01196

Colin-York, H., Shrestha, D., Felce, J. H., Waithe, D., Moeendarbary, E., Davis, S. J., et al. (2016). Super-Resolved Traction Force Microscopy (STFM). *Nano Lett.* 16, 2633–2638. doi: 10.1021/acs.nanolett.6b00273

Colombelli, J., and Solon, J. (2013). Force communication in multicellular tissues addressed by laser nanosurgery. *Cell Tissue Res.* 352, 133–147. doi: 10.1007/s00441-012-1445-1

Cost, A. L., Khalaji, S., and Grashoff, C. (2019). Genetically Encoded FRET-Based Tension Sensors. *Curr. Protoc. Cell Biol.* 83:e85. doi: 10.1002/cpcb.85

Cost, A. L., Ringer, P., Chrostek-Grashoff, A., and Grashoff, C. (2015). How to Measure Molecular Forces in Cells: A Guide to Evaluating Genetically-Encoded FRET-Based Tension Sensors. *Cell. Mol. Bioeng.* 8, 96–105. doi: 10.1007/s12195-014-0368-1

Davidson, P. M., Sliz, J., Isermann, P., Denais, C., and Lammerding, J. (2015). Design of a microfluidic device to quantify dynamic intra-nuclear deformation during cell migration through confining environments. *Integr. Biol.* 7, 1534–1546. doi: 10.1039/c5ib00200a

de Medeiros, G., Kromm, D., Balazs, B., Norlin, N., Günther, S., Izquierdo, E., et al. (2020). Cell and tissue manipulation with ultrashort infrared laser pulses in light-sheet microscopy. *Sci. Rep.* 10:1942. doi: 10.1038/s41598-019-54349-x

del Álamo, J. C., Meili, R., Álvarez-González, B., Alonso-Latorre, B., Bastounis, E., et al. (2013). Three-Dimensional Quantification of Cellular Traction Forces and Mechanosensing of Thin Substrata by Fourier Traction Force Microscopy. *PLoS One* 8:e69850. doi: 10.1371/journal.pone.0069850

Dembo, M., and Wang, Y. L. (1999). Stresses at the cell-to-substrate interface during locomotion of fibroblasts. *Biophys. J.* 76, 2307–2316. doi: 10.1016/S0006-3495(99)77386-8

Denais, C. M., Gilbert, R. M., Isermann, P., McGregor, A. L., Te Lindert, M., Weigelin, B., et al. (2016). Nuclear envelope rupture and repair during cancer cell migration. *Science* 352, 353–358. doi: 10.1126/science.aad7297

Denk, W. (1996). Two-photon excitation in functional biological imaging. *J. Biomed. Opt.* 1, 296–304. doi: 10.1117/12.242945

Denk, W., Strickler, J. H., and Webb, W. W. (1990). Two-photon laser scanning fluorescence microscopy. *Science* 248, 73–76. doi: 10.1126/science.2321027

Denk, W., and Svoboda, K. (1997). Photon upmanship: Why multiphoton imaging is more than a gimmick. *Neuron* 18, 351–357. doi: 10.1016/S0896-6273(00)81237-4

Diaspro, A., Bianchini, P., Vicidomini, G., Faretta, M., Ramoino, P., and Usai, C. (2006a). Multi-photon excitation microscopy. *Biomed. Eng. Online* 5:36. doi: 10.1186/1475-925X-5-36

Diaspro, A., Chirico, G., Usai, C., Ramoino, P., and Dobrucki, J. (2006b). "Photobleaching," in *Handbook of Biological Confocal Microscopy: Third Edition*, ed. J. B. Pawley (New York, NY: Springer), 690–702. doi: 10.1007/978-0-387-45524-2-39

Discher, D. E., Janmey, P., and Wang, Y. L. (2005). Tissue cells feel and respond to the stiffness of their substrate. *Science* 310, 1139–1143. doi: 10.1126/science.1116995

Dolega, M. E., Delarue, M., Ingremeau, F., Prost, J., Delon, A., and Cappello, G. (2017). Cell-like pressure sensors reveal increase of mechanical stress towards the core of multicellular spheroids under compression. *Nat. Commun.* 8:14056. doi: 10.1038/ncomms14056

Douthwright, S., and Sluder, G. (2017). Live Cell Imaging: Assessing the Phototoxicity of 488 and 546 nm Light and Methods to Alleviate it. *J. Cell. Physiol.* 232, 2461–2468. doi: 10.1002/jcp.25588

Du Roure, O., Saez, A., Buguin, A., Austin, R. H., Chavrier, P., Siberzan, P., et al. (2005). Force mapping in epithelial cell migration. *Proc. Natl. Acad. Sci. U.S.A.* 102, 2390–2395. doi: 10.1073/pnas.0408482102

Durnin, J., Eberly, J. H., and Miceli, J. J. (1988). Comparison of Bessel and Gaussian beams. *Opt. Lett.* 13, 79–80. doi: 10.1364/ol.13.000079

Durnin, J., Miceli, J., and Eberly, J. H. (1987). Diffraction-free beams. *Phys. Rev. Lett.* 58, 1499–1501. doi: 10.1103/PhysRevLett.58.1499

Ebrecht, R., Don Paul, C., and Wouters, F. S. (2014). Fluorescence lifetime imaging microscopy in the medical sciences. *Protoplasma* 251, 293–305. doi: 10.1007/s00709-013-0598-4

Ecker, R. C., De Martin, R., Steiner, G. E., and Schmid, J. A. (2004). Application of spectral imaging microscopy in cytomics and fluorescence resonance energy transfer (FRET) analysis. *Cytom. Part A* 59, 172–181. doi: 10.1002/cyto.a.20053

Ettinger, A., and Wittmann, T. (2014). Fluorescence live cell imaging. *Methods Cell Biol.* 123, 77–94. doi: 10.1016/B978-0-12-420138-5.00005-7

Evers, T. M. J., Holt, L. J., Alberti, S., and Mashaghi, A. (2021). Reciprocal regulation of cellular mechanics and metabolism. *Nat. Metab.* 3, 456–468. doi: 10.1038/s42255-021-00384-w

Fadero, T. C., Gerbich, T. M., Rana, K., Suzuki, A., DiSalvo, M., Schaefer, K. N., et al. (2018). LITE microscopy: Tilted light-sheet excitation of model organisms offers high resolution and low photobleaching. *J. Cell Biol.* 217, 1869–1882. doi: 10.1083/jcb.201710087

Fenno, L., Yizhar, O., and Deisseroth, K. (2011). The development and application of optogenetics. *Annu. Rev. Neurosci.* 34, 389–412. doi: 10.1146/annurev-neuro-061010-113817

Fernandez-Gonzalez, R., Simoes, S., de, M., Röper, J. C., Eaton, S., and Zallen, J. A. (2009). Myosin II Dynamics Are Regulated by Tension in Intercalating Cells. *Dev. Cell* 17, 736–743. doi: 10.1016/j.devcel.2009.09.003

Franck, C., Maskarinec, S. A., Tirrell, D. A., and Ravichandran, G. (2011). Three-dimensional traction force microscopy: A new tool for quantifying cell-matrix interactions. *PLoS One* 6:e17833. doi: 10.1371/journal.pone.0017833

Freikamp, A., Mehlich, A., Klingner, C., and Grashoff, C. (2017). Investigating piconewton forces in cells by FRET-based molecular force microscopy. *J. Struct. Biol.* 197, 37–42. doi: 10.1016/j.jsb.2016.03.011

Gardel, M. L., Sabass, B., Ji, L., Danuser, G., Schwarz, U. S., and Waterman, C. M. (2008). Traction stress in focal adhesions correlates biphasically with actin retrograde fl ow speed. *J. Cell Biol.* 183, 999–1005. doi: 10.1083/jcb.200810060

Gates, E. M., LaCroix, A. S., Rothenberg, K. E., and Hoffman, B. D. (2019). Improving Quality, Reproducibility, and Usability of FRET-Based Tension Sensors. *Cytom. Part A* 95, 201–213. doi: 10.1002/cyto.a.23688

Gayrard, C., and Borghi, N. (2016). FRET-based Molecular Tension Microscopy. *Methods* 94, 33–42. doi: 10.1016/j.ymeth.2015.07.010

Girkin, J. M., and Carvalho, M. T. (2018). The light-sheet microscopy revolution. *J. Opt.* 20:053002. doi: 10.1088/2040-8986/aab58a

Goeckeler, Z. M., and Wysolmerski, R. B. (1995). Myosin light chain kinase-regulated endothelial cell contraction: The relationship between isometric tension, actin polymerization, and myosin phosphorylation. *J. Cell Biol.* 130, 613–627. doi: 10.1083/jcb.130.3.613

Goldspink, G., Scutt, A., Loughna, P. T., Wells, D. J., Jaenicke, T., and Gerlach, G. F. (1992). Gene expression in skeletal muscle in response to stretch and force generation. *Am. J. Physiol.* 262, R356–63. doi: 10.1152/ajpregu.1992.262.3.r356

Goodwin, P. C. (2014). Quantitative deconvolution microscopy. *Methods Cell Biol.* 123, 177–192. doi: 10.1016/B978-0-12-420138-5.00010-0

Gosse, C., and Croquette, V. (2002). Magnetic tweezers: Micromanipulation and force measurement at the molecular level. *Biophys. J.* 82, 3314–3329. doi: 10.1016/S0006-3495(02)75672-5

Grashoff, C., Hoffman, B. D., Brenner, M. D., Zhou, R., Parsons, M., Yang, M. T., et al. (2010). Measuring mechanical tension across vinculin reveals regulation of focal adhesion dynamics. *Nature* 466, 263–266. doi: 10.1038/nature09198

Guillot, C., and Lecuit, T. (2013). Mechanics of epithelial tissue homeostasis and morphogenesis. *Science* 340, 1185–1189. doi: 10.1126/science.1235249

Gustafsson, M. G. L. (2000). Surpassing the lateral resolution limit by a factor of two using structured illumination microscopy. *J. Microsc.* 198, 82–87. doi: 10.1046/j.1365-2818.2000.00710.x

Gustafsson, M. G. L., Shao, L., Carlton, P. M., Wang, C. J. R., Golubovskaya, I. N., Cande, W. Z., et al. (2008). Three-dimensional resolution doubling in wide-field fluorescence microscopy by structured illumination. *Biophys. J.* 94, 4957–4970. doi: 10.1529/biophysj.107.120345

Gutierrez, E., Tkachenko, E., Besser, A., Sundd, P., Ley, K., Danuser, G., et al. (2011). High refractive index silicone gels for simultaneous total internal reflection fluorescence and traction force microscopy of adherent cells. *PLoS One* 6:e23807. doi: 10.1371/journal.pone.0023807

Han, B., Bai, X. H., Lodyga, M., Xu, J., Yang, B. B., Keshavjee, S., et al. (2004). Conversion of mechanical force into biochemical signaling. *J. Biol. Chem.* 279, 54793–54801. doi: 10.1074/jbc.M406880200

Han, S. J., Oak, Y., Groisman, A., and Danuser, G. (2015). Traction microscopy to identify force modulation in subresolution adhesions. *Nat. Methods* 12, 653–656. doi: 10.1038/nmeth.3430

Hara, Y., Shagirov, M., and Toyama, Y. (2016). Cell Boundary Elongation by Non-autonomous Contractility in Cell Oscillation. *Curr. Biol.* 26, 2388–2396. doi: 10.1016/j.cub.2016.07.003

Harris, A. K., Wild, P., and Stopak, D. (1980). Silicone rubber substrata: A new wrinkle in the study of cell locomotion. *Science* 208, 177–179. doi: 10.1126/science.6987736

Heisenberg, C. P., and Bellaïche, Y. (2013). Forces in tissue morphogenesis and patterning. *Cell* 153, 948–962. doi: 10.1016/j.cell.2013.05.008

Hell, S. W., and Wichmann, J. (1994). Breaking the diffraction resolution limit by stimulated emission: stimulated-emission-depletion fluorescence microscopy. *Opt. Lett.* 19, 780–782. doi: 10.1364/ol.19.000780

Heuzé, M. L., Collin, O., Terriac, E., Lennon-Duménil, A. M., and Piel, M. (2011). Cell migration in confinement: A micro-channel-based assay. *Methods Mol. Biol.* 769, 415–434. doi: 10.1007/978-1-61779-207-6_28

Hobson, C. M., Kern, M., O'Brien, E. T., Stephens, A. D., Falvo, M. R., and Superfine, R. (2020). Correlating nuclear morphology and external force with combined atomic force microscopy and light sheet imaging separates roles of chromatin and lamin A/C in nuclear mechanics. *Mol. Biol. Cell* 31, 1788–1801. doi: 10.1091/mbc.E20-01-0073

Hochmuth, R. M. (2000). Micropipette aspiration of living cells. *J. Biomech.* 33, 15–22. doi: 10.1016/S0021-9290(99)00175-X

Hofemeier, A. D., Limon, T., Muenker, T. M., Wallmeyer, B., Jurado, A., Afshar, M. E., et al. (2021). Global and local tension measurements in biomimetic skeletal muscle tissues reveals early mechanical homeostasis. *Elife* 10, 1–27. doi: 10.7554/eLife.60145

Hohng, S., Zhou, R., Nahas, M. K., Yu, J., Schulten, K., Lilley, D. M. J., et al. (2007). Fluorescence-force spectroscopy maps two-dimensional reaction landscape of the holliday junction. *Science* 318, 279–283. doi: 10.1126/science.1146113

Holtzer, L., Meckel, T., and Schmidt, T. (2007). Nanometric three-dimensional tracking of individual quantum dots in cells. *Appl. Phys. Lett.* 90:053902. doi: 10.1063/1.2437066

Hoppe, A. D. (2007). ""Quantitative FRET Microscopy of Live Cells,"," in *Imaging Cellular and Molecular Biological Functions*, eds S. L. Shorte and F. Frischknecht (Berlin: Springer), 157–181. doi: 10.1007/978-3-540-71331-9_6

Huang, Y., Schell, C., Huber, T. B., Şimşek, A. N., Hersch, N., Merkel, R., et al. (2019). Traction force microscopy with optimized regularization and automated Bayesian parameter selection for comparing cells. *Sci. Rep.* 9:539. doi: 10.1038/s41598-018-36896-x

Huff, J. (2015). The Airyscan detector from ZEISS: confocal imaging with improved signal-to-noise ratio and super-resolution. *Nat. Methods* 12, i–ii. doi: 10.1038/nmeth.f.388

Huisken, J., Swoger, J., Del Bene, F., Wittbrodt, J., and Stelzer, E. H. K. (2004). Optical sectioning deep inside live embryos by selective plane illumination microscopy. *Science* 305, 1007–1009. doi: 10.1126/science.1100035

Hutson, M. S., Tokutake, Y., Chang, M. S., Bloor, J. W., Venakides, S., Kiehart, D. P., et al. (2003). Forces for morphogenesis investigated with laser microsurgery and quantitative modeling. *Science* 300, 145–149. doi: 10.1126/science.1079552

Icha, J., Weber, M., Waters, J. C., and Norden, C. (2017). Phototoxicity in live fluorescence microscopy, and how to avoid it. *BioEssays* 39:1700003. doi: 10.1002/bies.201700003

Ingber, D. E. (2003). Mechanosensation through integrins: Cells act locally but think globally. *Proc. Natl. Acad. Sci. U.S.A.* 100, 1472–1474. doi: 10.1073/pnas.0530201100

Jain, R. K., Martin, J. D., and Stylianopoulos, T. (2014). The role of mechanical forces in tumor growth and therapy. *Annu. Rev. Biomed. Eng.* 16, 321–346. doi: 10.1146/annurev-bioeng-071813-105259

Jannat, R. A., Dembo, M., and Hammer, D. A. (2011). Traction forces of neutrophils migrating on compliant substrates. *Biophys. J.* 101, 575–584. doi: 10.1016/j.bpj.2011.05.040

Jares-Erijman, E. A., and Jovin, T. M. (2003). FRET imaging. *Nat. Biotechnol.* 21, 1387–1395. doi: 10.1038/nbt896

Kao, H. P., and Verkman, A. S. (1994). Tracking of single fluorescent particles in three dimensions: use of cylindrical optics to encode particle position. *Biophys. J.* 67, 1291–1300. doi: 10.1016/S0006-3495(94)80601-0

Kiehart, D. P., Galbraith, C. G., Edwards, K. A., Rickoll, W. L., and Montague, R. A. (2000). Multiple forces contribute to cell sheet morphogenesis for dorsal closure in Drosophila. *J. Cell Biol.* 149, 471–490. doi: 10.1083/jcb.149.2.471

Kolodney, M. S., and Wysolmerski, R. B. (1992). Isometric contraction by fibroblasts and endothelial cells in tissue culture: A quantitative study. *J. Cell Biol.* 117, 73–82. doi: 10.1083/jcb.117.1.73

Krieg, M., Fläschner, G., Alsteens, D., Gaub, B. M., Roos, W. H., Wuite, G. J. L., et al. (2019). Atomic force microscopy-based mechanobiology. *Nat. Rev. Phys.* 1, 41–57. doi: 10.1038/s42254-018-0001-7

Kulkarni, A. H., Ghosh, P., Seetharaman, A., Kondaiah, P., and Gundiah, N. (2018). Traction cytometry: Regularization in the Fourier approach and comparisons with finite element method. *Soft. Matter* 14, 4687–4695. doi: 10.1039/c7sm02214j

Kumar, A., Wu, Y., Christensen, R., Chandris, P., Gandler, W., McCreedy, E., et al. (2014). Dual-view plane illumination microscopy for rapid and spatially isotropic imaging. *Nat. Protoc.* 9, 2555–2573. doi: 10.1038/nprot.2014.172

Kumar, M., Kishore, S., McLean, D., and Kozorovitskiy, Y. (2021). Crossbill: an open access single objective light-sheet microscopy platform. *bioRxiv*, 2021.04.30.442190 [preprint]. doi: 10.1101/2021.04.30.442190

Kumar, S., Maxwell, I. Z., Heisterkamp, A., Polte, T. R., Lele, T. P., Salanga, M., et al. (2006). Viscoelastic retraction of single living stress fibers and its impact on cell shape, cytoskeletal organization, and extracellular matrix mechanics. *Biophys. J.* 90, 3762–3773. doi: 10.1529/biophysj.105.071506

Kumar, S., and Weaver, V. M. (2009). Mechanics, malignancy, and metastasis: The force journey of a tumor cell. *Cancer Metastasis Rev.* 28, 113–127. doi: 10.1007/s10555-008-9173-4

LaCroix, A. S., Rothenberg, K. E., Berginski, M. E., Urs, A. N., and Hoffman, B. D. (2015). Construction, imaging, and analysis of FRET-based tension sensors in living cells. *Methods Cell Biol.* 125, 161–186. doi: 10.1016/bs.mcb.2014.10.033

Laissue, P. P., Alghamdi, R. A., Tomancak, P., Reynaud, E. G., and Shroff, H. (2017). Assessing phototoxicity in live fluorescence imaging. *Nat. Methods* 14, 657–661. doi: 10.1038/nmeth.4344

Lee, W., Kalashnikov, N., Mok, S., Halaoui, R., Kuzmin, E., Putnam, A. J., et al. (2019). Dispersible hydrogel force sensors reveal patterns of solid mechanical stress in multicellular spheroid cultures. *Nat. Commun.* 10:144. doi: 10.1038/s41467-018-07967-4

Legant, W. R., Choi, C. K., Miller, J. S., Shao, L., Gao, L., Betzig, E., et al. (2013). Multidimensional traction force microscopy reveals out-of-plane rotational moments about focal adhesions. *Proc. Natl. Acad. Sci. U.SA.* 110, 881–886. doi: 10.1073/pnas.1207997110

Li, D., Colin-York, H., Barbieri, L., Javanmardi, Y., Guo, Y., Korobchevskaya, K., et al. (2021). Astigmatic traction force microscopy (aTFM). *Nat. Commun.* 12:2168. doi: 10.1038/s41467-021-22376-w

Li, W., Yu, X., Xie, F., Zhang, B., Shao, S., Geng, C., et al. (2018). A Membrane-Bound Biosensor Visualizes Shear Stress-Induced Inhomogeneous Alteration of Cell Membrane Tension. *iScience* 7, 180–190. doi: 10.1016/j.isci.2018.09.002

Liu, B., Hobson, C. M., Pimenta, F. M., Nelsen, E., Hsiao, J., O'Brien, T., et al. (2019). VIEW-MOD: a versatile illumination engine with a modular optical design for fluorescence microscopy. *Opt. Express* 27, 19950–19972. doi: 10.1364/oe.27.019950

Liu, M., Tanswell, A. K., and Post, M. (1999). Mechanical force-induced signal transduction in lung cells. *Am. J. Physiol.* 277, 667–683. doi: 10.1152/ajplung.1999.277.4.l667

Liu, T. L., Upadhyayula, S., Milkie, D. E., Singh, V., Wang, K., Swinburne, I. A., et al. (2018). Observing the cell in its native state: Imaging subcellular dynamics in multicellular organisms. *Science* 360:eaaq1392. doi: 10.1126/science.aaq1392

Mahou, P., Vermot, J., Beaurepaire, E., and Supatto, W. (2014). Multicolor two-photon light-sheet microscopy. *Nat. Methods* 11, 600–601. doi: 10.1038/nmeth.2963

Mammoto, T., and Ingber, D. E. (2010). Mechanical control of tissue and organ development. *Development* 137, 1407–1420. doi: 10.1242/dev.024166

Manders, E. M. M. (1997). Chromatic shift in multicolour confocal microscopy. *J. Microsc.* 185, 321–328. doi: 10.1046/j.1365-2818.1997.d01-625.x

Markovič, R., Marhl, M., and Gosak, M. (2020). Mechanical Cell-to-Cell Interactions as a Regulator of Topological Defects in Planar Cell Polarity Patterns in Epithelial Tissues. *Front. Mater.* 7:264. doi: 10.3389/fmats.2020.00264

McGregor, A. L., Hsia, C. R., and Lammerding, J. (2016). Squish and squeeze - the nucleus as a physical barrier during migration in confined environments. *Curr. Opin. Cell Biol.* 40, 32–40. doi: 10.1016/j.ceb.2016.01.011

Meng, F., and Sachs, F. (2012). Orientation-based FRET sensor for real-time imaging of cellular forces. *J. Cell Sci.* 125, 743–750. doi: 10.1242/jcs.093104

Michael, M., Meiring, J. C. M., Acharya, B. R., Matthews, D. R., Verma, S., Han, S. P., et al. (2016). Coronin 1B Reorganizes the Architecture of F-Actin Networks for Contractility at Steady-State and Apoptotic Adherens Junctions. *Dev. Cell* 37, 58–71. doi: 10.1016/j.devcel.2016.03.008

Millett-Sikking, A., Dean, K. M., Fiolka, R., Fardad, A., Whitehead, L., and York, A. G. (2019). High NA single-objective light-sheet. Available online at: https://andrewgyork.github.io/high_na_single_objective_lightsheet/

Mizuno, T., Hase, E., Minamikawa, T., Tokizane, Y., Oe, R., Koresawa, H., et al. (2021). Full-field fluorescence lifetime dual-comb microscopy using spectral mapping and frequency multiplexing of dual-comb optical beats. *Sci. Adv.* 7:eabd2102. doi: 10.1126/sciadv.abd2102

Model, M. A., and Burkhardt, J. K. (2001). A standard for calibration and shading correction of a fluorescence microscope. *Commun. Clin. Cytom.* 46, 309–316. doi: 10.1002/1097-0320(20010801)44:4

Mongera, A., Rowghanian, P., Gustafson, H. J., Shelton, E., Kealhofer, D. A., Carn, E. K., et al. (2018). A fluid-to-solid jamming transition underlies vertebrate body axis elongation. *Nature* 561, 401–405. doi: 10.1038/s41586-018-0479-2

Monticelli, M., Jokhun, D. S., Petti, D., Shivashankar, G. V., and Bertacco, R. (2018). Localized mechanical stimulation of single cells with engineered spatio-temporal profile. *Lab Chip* 18, 2955–2965. doi: 10.1039/c8lc00393a

Moraes, C., Chen, J. H., Sun, Y., and Simmons, C. A. (2010). Microfabricated arrays for high-throughput screening of cellular response to cyclic substrate deformation. *Lab Chip* 10, 227–234. doi: 10.1039/b914460a

Morimatsu, M., Mekhdjian, A. H., Adhikari, A. S., and Dunn, A. R. (2013). Molecular tension sensors report forces generated by single integrin molecules in living cells. *Nano Lett.* 13, 3985–3989. doi: 10.1021/nl4005145

Müller, C. B., and Enderlein, J. (2010). Image scanning microscopy. *Phys. Rev. Lett.* 104:198101. doi: 10.1103/PhysRevLett.104.198101

Müller, G., Dörschel, K., and Kar, H. (1991). Biophysics of the photoablation process. *Lasers Med. Sci.* 6, 241–254. doi: 10.1007/BF02030877

Munevar, S., Wang, Y. L., and Dembo, M. (2001a). Distinct roles of frontal and rear cell-substrate adhesions in fibroblast migration. *Mol. Biol. Cell* 12, 3947–3954. doi: 10.1091/mbc.12.12.3947

Munevar, S., Wang, Y. L., and Dembo, M. (2001b). Traction force microscopy of migrating normal and H-ras transformed 3T3 fibroblasts. *Biophys. J.* 80, 1744–1757. doi: 10.1016/S0006-3495(01)76145-0

Neelam, S., Chancellor, T. J., Li, Y., Nickerson, J. A., Roux, K. J., Dickinson, R. B., et al. (2015). Direct force probe reveals the mechanics of nuclear homeostasis in the mammalian cell. *Proc. Natl. Acad. Sci. U.S.A.* 112, 5720–5725. doi: 10.1073/pnas.1502111112

Nelsen, E., Hobson, C. M., Kern, M. E., Hsiao, J. P., O'Brien, E. T., Watanabe, T., et al. (2020). Combined Atomic Force Microscope and Volumetric Light Sheet System for Correlative Force and Fluorescence Mechanobiology Studies. *Sci. Rep.* 10:8133. doi: 10.1038/s41598-020-65205-8

Oakes, P. W., Wagner, E., Brand, C. A., Probst, D., Linke, M., Schwarz, U. S., et al. (2017). Optogenetic control of RhoA reveals zyxin-mediated elasticity of stress fibres. *Nat. Commun.* 8:15817. doi: 10.1038/ncomms15817

O'Shaughnessy, E. C., Stone, O. J., LaFosse, P. K., Azoitei, M. L., Tsygankov, D., Heddleston, J. M., et al. (2019). Software for lattice light-sheet imaging of FRET biosensors, illustrated with a new Rap1 biosensor. *J. Cell Biol.* 218, 3153–3160. doi: 10.1083/JCB.201903019

Ouyang, W., and Zimmer, C. (2017). The imaging tsunami: Computational opportunities and challenges. *Curr. Opin. Syst. Biol.* 4, 105–113. doi: 10.1016/j.coisb.2017.07.011

Paul, C. D., Hung, W. C., Wirtz, D., and Konstantopoulos, K. (2016). Engineered Models of Confined Cell Migration. *Annu. Rev. Biomed. Eng.* 18, 159–180. doi: 10.1146/annurev-bioeng-071114-040654

Paul, C. D., Mistriotis, P., and Konstantopoulos, K. (2017). Cancer cell motility: Lessons from migration in confined spaces. *Nat. Rev. Cancer* 17, 131–140. doi: 10.1038/nrc.2016.123

Pawley, J. B. (2006). *Handbook of Biological Confocal Microscopy: Third edition*. New York, NY: Springer. doi: 10.1007/978-0-387-45524-2

Pesce, M., and Santoro, R. (2017). Feeling the right force: How to contextualize the cell mechanical behavior in physiologic turnover and pathologic evolution of the cardiovascular system. *Pharmacol. Ther.* 171, 75–82. doi: 10.1016/j.pharmthera.2016.08.002

Peschetola, V., Laurent, V. M., Duperray, A., Michel, R., Ambrosi, D., Preziosi, L., et al. (2013). Time-dependent traction force microscopy for cancer cells as a measure of invasiveness. *Cytoskeleton* 70, 201–214. doi: 10.1002/cm.21100

Pitrone, P. G., Schindelin, J., Stuyvenberg, L., Preibisch, S., Weber, M., Eliceiri, K. W., et al. (2013). OpenSPIM: An open-access light-sheet microscopy platform. *Nat. Methods* 10, 598–599. doi: 10.1038/nmeth.2507

Planchon, T. A., Gao, L., Milkie, D. E., Davidson, M. W., Galbraith, J. A., Galbraith, C. G., et al. (2011). Rapid three-dimensional isotropic imaging of living cells using Bessel beam plane illumination. *Nat. Methods* 8, 417–423. doi: 10.1038/nmeth.1586

Plotnikov, S. V., Pasapera, A. M., Sabass, B., and Waterman, C. M. (2012). Force fluctuations within focal adhesions mediate ECM-rigidity sensing to guide directed cell migration. *Cell* 151, 1513–1527. doi: 10.1016/j.cell.2012.11.034

Plotnikov, S. V., Sabass, B., Schwarz, U. S., and Waterman, C. M. (2014). "High-Resolution Traction Force Microscopy," in *Methods in Cell Biology*, eds J. C. Waters and C. B. Wittman (Cambridge: Academic Press), 367–394. doi: 10.1016/B978-0-12-420138-5.00020-3

Polacheck, W. J., and Chen, C. S. (2016). Measuring cell-generated forces: A guide to the available tools. *Nat. Methods* 13, 415–423. doi: 10.1038/nmeth.3834

Power, R. M., and Huisken, J. (2019). Putting advanced microscopy in the hands of biologists. *Nat. Methods* 16, 1069–1073. doi: 10.1038/s41592-019-0618-1

Primmerman, C. A., Murphy, D. V., Page, D. A., Zollars, B. G., and Barclay, H. T. (1991). Compensation of atmospheric optical distortion using a synthetic beacon. *Nature* 353, 141–143. doi: 10.1038/353141a0

Ratheesh, A., Gomez, G. A., Priya, R., Verma, S., Kovacs, E. M., Jiang, K., et al. (2012). Centralspindlin and α-catenin regulate Rho signalling at the epithelial zonula adherens. *Nat. Cell Biol.* 14, 818–828. doi: 10.1038/ncb2532

Rauzi, M., Lenne, P. F., and Lecuit, T. (2010). Planar polarized actomyosin contractile flows control epithelial junction remodelling. *Nature* 468, 1110–1115. doi: 10.1038/nature09566

Rauzi, M., Verant, P., Lecuit, T., and Lenne, P. F. (2008). Nature and anisotropy of cortical forces orienting Drosophila tissue morphogenesis. *Nat. Cell Biol.* 10, 1401–1410. doi: 10.1038/ncb1798

Reynaud, E. G., Peychl, J., Huisken, J., and Tomancak, P. (2014). Guide to light-sheet microscopy for adventurous biologists. *Nat. Methods* 12, 30–34. doi: 10.1038/nmeth.3222

Ringer, P., Weißl, A., Cost, A. L., Freikamp, A., Sabass, B., Mehlich, A., et al. (2017). Multiplexing molecular tension sensors reveals piconewton force gradient across talin-1. *Nat. Methods* 14, 1090–1096. doi: 10.1038/nmeth.4431

Roca-Cusachs, P., Conte, V., and Trepat, X. (2017). Quantifying forces in cell biology. *Nat. Cell Biol.* 19, 742–751. doi: 10.1038/ncb3564

Rossetti, B. J., Wilbert, S. A., Mark Welch, J. L., Borisy, G. G., and Nagy, J. G. (2020). Semi-blind sparse affine spectral unmixing of autofluorescence-contaminated micrographs. *Bioinformatics* 36, 910–917. doi: 10.1093/bioinformatics/btz674

Rust, M. J., Bates, M., and Zhuang, X. (2006). Sub-diffraction-limit imaging by stochastic optical reconstruction microscopy (STORM). *Nat. Methods* 3, 793–795. doi: 10.1038/nmeth929

Sabass, B., Gardel, M. L., Waterman, C. M., and Schwarz, U. S. (2008). High resolution traction force microscopy based on experimental and computational advances. *Biophys. J.* 94, 207–220. doi: 10.1529/biophysj.107.113670

Saez, A., Anon, E., Ghibaudo, M., Du Roure, O., Di Meglio, J. M., Hersen, P., et al. (2010). Traction forces exerted by epithelial cell sheets. *J. Phys. Condens. Matter* 22:194119. doi: 10.1088/0953-8984/22/19/194119

Salmon, E. D., and Bloom, K. (2017). Tension sensors reveal how the kinetochore shares its load. *BioEssays* 39:1600216. doi: 10.1002/bies.201600216

Santi, P. A. (2011). Light sheet fluorescence microscopy: A review. *J. Histochem. Cytochem.* 59, 129–138. doi: 10.1369/0022155410394857

Sapoznik, E., Chang, B. J., Huh, J., Ju, R. J., Azarova, E. V., Pohlkamp, T., et al. (2020). A versatile oblique plane microscope for large-scale and high-resolution imaging of subcellular dynamics. *Elife* 9:e57681. doi: 10.7554/eLife.57681

Sauer, M., and Heilemann, M. (2017). Single-Molecule Localization Microscopy in Eukaryotes. *Chem. Rev.* 117, 7478–7509. doi: 10.1021/acs.chemrev.6b00667

Schlichthaerle, T., Lindner, C., and Jungmann, R. (2021). Super-resolved visualization of single DNA-based tension sensors in cell adhesion. *Nat. Commun.* 12:2510. doi: 10.1038/s41467-021-22606-1

Schmitz, J., Benoit, M., and Gottschalk, K. E. (2008). The viscoelasticity of membrane tethers and its importance for cell adhesion. *Biophys. J.* 95, 1448–1459. doi: 10.1529/biophysj.107.124289

Schoen, I., Hu, W., Klotzsch, E., and Vogel, V. (2010). Probing cellular traction forces by micropillar arrays: Contribution of substrate warping to pillar deflection. *Nano Lett.* 10, 1823–1830. doi: 10.1021/nl100533c

Schwertner, M., Booth, M. J., and Wilson, T. (2007). Specimen-induced distortions in light microscopy. *J. Microsc.* 228, 97–102. doi: 10.1111/j.1365-2818.2007.01827.x

Seidlitz, H. K., Thiel, S., Krins, A., and Mayer, H. (2001). "Chapter 36 Solar radiation at the Earth's surface," in *Comprehensive Series in Photosciences*, ed.

P. Giacomoni (Netherland: Elsevier), 705–738. doi: 10.1016/S1568-461X(01)80071-5

Serwane, F., Mongera, A., Rowghanian, P., Kealhofer, D. A., Lucio, A. A., Hockenbery, Z. M., et al. (2017). In vivo quantification of spatially varying mechanical properties in developing tissues. *Nat. Methods* 14, 181–186. doi: 10.1038/nmeth.4101

Shah, P., Hobson, C. M., Cheng, S., Colville, M. J., Paszek, M. J., Superfine, R., et al. (2021). Nuclear Deformation Causes DNA Damage by Increasing Replication Stress. *Curr. Biol.* 31, 753–765.e6. doi: 10.1016/j.cub.2020.11.037

Shen, N., Datta, D., Schaffer, C. B., LeDuc, P., Ingber, D. E., and Mazur, E. (2005). Ablation of cytoskeletal filaments and mitochondria in live cells using a femtosecond laser nanoscissor. *MCB Mech. Chem. Biosyst.* 2, 17–25. doi: 10.3970/mcb.2005.002.017

Sheppard, C. J. R. (1988). Super-resolution in confocal imaging. *Optik* 80, 53–54. doi: 10.1117/12.967201

Sheppard, C. J. R., Mehta, S. B., and Heintzmann, R. (2013). Superresolution by image scanning microscopy using pixel reassignment. *Opt. Lett.* 38, 2889–2892. doi: 10.1364/ol.38.002889

Shiu, Y. T., Li, S., Marganski, W. A., Usami, S., Schwartz, M. A., Wang, Y. L., et al. (2004). Rho Mediates the Shear-Enhancement of Endothelial Cell Migration and Traction Force Generation. *Biophys. J.* 86, 2558–2565. doi: 10.1016/S0006-3495(04)74311-8

Sinha, R. P., and Häder, D. P. (2002). UV-induced DNA damage and repair: A review. *Photochem. Photobiol. Sci.* 1, 225–236. doi: 10.1039/b201230h

Smutny, M., Behrndt, M., Campinho, P., Ruprecht, V., and Heisenberg, C. P. (2015). UV laser ablation to measure cell and tissue-generated forces in the zebrafish embryo in vivo and ex vivo. *Methods Mol. Biol.* 1189, 219–235. doi: 10.1007/978-1-4939-1164-6_15

Sniadecki, N. J., Anguelouch, A., Yang, M. T., Lamb, C. M., Liu, Z., Kirschner, S. B., et al. (2007). Magnetic microposts as an approach to apply forces to living cells. *Proc. Natl. Acad. Sci. U.S.A.* 104, 14553–14558. doi: 10.1073/pnas.0611613104

Stelzer, E. H. K. (2014). Light-sheet fluorescence microscopy for quantitative biology. *Nat. Methods* 12, 23–26. doi: 10.1038/nmeth.3219

Style, R. W., Boltyanskiy, R., German, G. K., Hyland, C., Macminn, C. W., Mertz, A. F., et al. (2014). Traction force microscopy in physics and biology. *Soft. Matter* 10, 4047–4055. doi: 10.1039/c4sm00264d

Sun, M., Graham, J. S., Hegedüs, B., Marga, F., Zhang, Y., Forgacs, G., et al. (2005). Multiple membrane tethers probed by atomic force microscopy. *Biophys. J.* 89, 4320–4329. doi: 10.1529/biophysj.104.058180

Svoboda, K., and Yasuda, R. (2006). Principles of Two-Photon Excitation Microscopy and Its Applications to Neuroscience. *Neuron* 50, 823–839. doi: 10.1016/j.neuron.2006.05.019

Tajik, A., Zhang, Y., Wei, F., Sun, J., Jia, Q., Zhou, W., et al. (2016). Transcription upregulation via force-induced direct stretching of chromatin. *Nat. Mater.* 15, 1287–1296. doi: 10.1038/nmat4729

Tamzalit, F., Wang, M. S., Jin, W., Tello-Lafoz, M., Boyko, V., Heddleston, J. M., et al. (2019). Interfacial actin protrusions mechanically enhance killing by cytotoxic T cells. *Sci. Immunol.* 4:eaav5445. doi: 10.1126/sciimmunol.aav5445

Tan, J. L., Tien, J., Pirone, D. M., Gray, D. S., Bhadriraju, K., and Chen, C. S. (2003). Cells lying on a bed of microneedles: An approach to isolate mechanical force. *Proc. Natl. Acad. Sci. U.S.A.* 100, 1484–1489. doi: 10.1073/pnas.0235407100

Tang, X., Tofangchi, A., Anand, S. V., and Saif, T. A. (2014). A Novel Cell Traction Force Microscopy to Study Multi-Cellular System. *PLoS Comput. Biol.* 10:e1003631. doi: 10.1371/journal.pcbi.1003631

Tao, X., Fernandez, B., Azucena, O., Fu, M., Garcia, D., Zuo, Y., et al. (2011). Adaptive optics confocal microscopy using direct wavefront sensing. *Opt. Lett.* 36, 1062–1064. doi: 10.1364/ol.36.001062

Thompson, W. R., Rubin, C. T., and Rubin, J. (2012). Mechanical regulation of signaling pathways in bone. *Gene* 503, 179–193. doi: 10.1016/j.gene.2012.04.076

Tinevez, J. Y., Dragavon, J., Baba-Aissa, L., Roux, P., Perret, E., Canivet, A., et al. (2012). A quantitative method for measuring phototoxicity of a live cell imaging microscope. *Methods Enzymology* 506, 291–309. doi: 10.1016/B978-0-12-391856-7.00039-1

Toli-Nørrelykke, I. M., Butler, J. P., Chen, J., and Wang, N. (2002). Spatial and temporal traction response in human airway smooth muscle cells. *Am. J. Physiol.* 283, 1254–1266. doi: 10.1152/ajpcell.00169.2002

Tomer, R., Khairy, K., Amat, F., and Keller, P. J. (2012). Quantitative high-speed imaging of entire developing embryos with simultaneous multiview light-sheet microscopy. *Nat. Methods* 9, 755–763. doi: 10.1038/nmeth.2062

Tosheva, K. L., Yuan, Y., Matos Pereira, P., Culley, S. N., and Henriques, R. (2020). Between life and death: Strategies to reduce phototoxicity in super-resolution microscopy. *J. Phys. D. Appl. Phys.* 53:163001. doi: 10.1088/1361-6463/ab6b95

Toyjanova, J., Hannen, E., Bar-Kochba, E., Darling, E. M., Henann, D. L., and Franck, C. (2014). 3D Viscoelastic traction force microscopy. *Soft. Matter* 10, 8095–8106. doi: 10.1039/c4sm01271b

Träber, N., Uhlmann, K., Girardo, S., Kesavan, G., Wagner, K., Friedrichs, J., et al. (2019). Polyacrylamide Bead Sensors for in vivo Quantification of Cell-Scale Stress in Zebrafish Development. *Sci. Rep.* 9:17031. doi: 10.1038/s41598-019-53425-6

Truong, T. V., Supatto, W., Koos, D. S., Choi, J. M., and Fraser, S. E. (2011). Deep and fast live imaging with two-photon scanned light-sheet microscopy. *Nat. Methods* 8, 757–762. doi: 10.1038/nmeth.1652

Tse, J. R., and Engler, A. J. (2010). Preparation of hydrogel substrates with tunable mechanical properties. *Curr. Protoc. Cell Biol.* 10:10. doi: 10.1002/0471143030.cb1016s47

Umeshima, H., Nomura, K.-I., Yoshikawa, S., Hörning, M., Tanaka, M., Sakuma, S., et al. (2019). Local traction force in the proximal leading process triggers nuclear translocation during neuronal migration. *Neurosci. Res.* 142, 38–48. doi: 10.1016/j.neures.2018.04.001

Vedula, V., Lee, J., Xu, H., Kuo, C. C. J., Hsiai, T. K., and Marsden, A. L. (2017). A method to quantify mechanobiologic forces during zebrafish cardiac development using 4-D light sheet imaging and computational modeling. *PLoS Comput. Biol.* 13:e1005828. doi: 10.1371/journal.pcbi.1005828

Vogel, A., Noack, J., Hüttman, G., and Paltauf, G. (2005). Mechanisms of femtosecond laser nanosurgery of cells and tissues. *Appl. Phys. B Lasers Opt.* 81, 1015–1047. doi: 10.1007/s00340-005-2036-6

Vogel, A., and Venugopalan, V. (2003). Mechanisms of pulsed laser ablation of biological tissues. *Chem. Rev.* 103, 577–644. doi: 10.1021/cr010379n

Voigt, F. F., Kirschenbaum, D., Platonova, E., Pagès, S., Campbell, R. A. A., Kastli, R., et al. (2019). The mesoSPIM initiative: open-source light-sheet microscopes for imaging cleared tissue. *Nat. Methods* 16, 1105–1108. doi: 10.1038/s41592-019-0554-0

Vorselen, D., Barger, S. R., Wang, Y., Cai, W., Theriot, J. A., Gauthier, N. C., et al. (2021). Phagocytic "teeth" and myosin-II "jaw" power target constriction during phagocytosis 1 2 3. *bioRxiv*, 2021.03.14.435346 [preprint]. doi: 10.1101/2021.03.14.435346

Vorselen, D., Wang, Y., de Jesus, M. M., Shah, P. K., Footer, M. J., Huse, M., et al. (2020). Microparticle traction force microscopy reveals subcellular force exertion patterns in immune cell–target interactions. *Nat. Commun.* 11:20. doi: 10.1038/s41467-019-13804-z

Wait, E. C., Reiche, M. A., and Chew, T. L. (2020). Hypothesis-driven quantitative fluorescence microscopy - The importance of reverse-thinking in experimental design. *J. Cell Sci.* 133:jcs250027. doi: 10.1242/jcs.250027

Waters, J. C. (2009). Accuracy and precision in quantitative fluorescence microscopy. *J. Cell Biol.* 185, 1135–1148. doi: 10.1083/jcb.200903097

Wolf, S., Supatto, W., Debrégeas, G., Mahou, P., Kruglik, S. G., Sintes, J. M., et al. (2015). Whole-brain functional imaging with two-photon light-sheet microscopy. *Nat. Methods* 12, 379–380. doi: 10.1038/nmeth.3371

Wu, P. H., Aroush, D. R., Ben, Asnacios, A., Chen, W. C., Dokukin, M. E., et al. (2018). A comparison of methods to assess cell mechanical properties. *Nat. Methods* 15, 491–498. doi: 10.1038/s41592-018-0015-1

Wu, Y. I., Frey, D., Lungu, O. I., Jaehrig, A., Schlichting, I., Kuhlman, B., et al. (2009). A genetically encoded photoactivatable Rac controls the motility of living cells. *Nature* 461, 104–108. doi: 10.1038/nature08241

Xia, Y., Ivanovska, I. L., Zhu, K., Smith, L., Irianto, J., Pfeifer, C. R., et al. (2018). Nuclear rupture at sites of high curvature compromises retention of DNA repair factors. *J. Cell Biol.* 217, 3796–3808. doi: 10.1083/jcb.201711161

Xiao, F., Wen, X., Tan, X. H. M., and Chiou, P. Y. (2018). Plasmonic micropillars for precision cell force measurement across a large field-of-view. *Appl. Phys. Lett.* 112:10.1063/1.5005525. doi: 10.1063/1.5005525

Yamaguchi, K., Kitamura, R., Kawakami, R., Otomo, K., and Nemoto, T. (2020). In vivo two-photon microscopic observation and ablation in deeper brain regions realized by modifications of excitation beam diameter and immersion liquid. *PLoS One* 15:e0237230. doi: 10.1371/journal.pone.0237230

Yang, B., Chen, X., Wang, Y., Feng, S., Pessino, V., Stuurman, N., et al. (2019). Epi-illumination SPIM for volumetric imaging with high spatial-temporal resolution. *Nat. Methods* 16, 501–504. doi: 10.1038/s41592-019-0401-3

Yang, Z., Lin, J. S., Chen, J., and Wang, J. H. C. (2006). Determining substrate displacement and cell traction fields-a new approach. *J. Theor. Biol.* 242, 607–616. doi: 10.1016/j.jtbi.2006.05.005

Zal, T., and Gascoigne, N. R. J. (2004). Photobleaching-corrected FRET efficiency imaging of live cells. *Biophys. J.* 86, 3923–3939. doi: 10.1529/biophysj.103.022087

Zhang, S., Teng, X., Toyama, Y., and Saunders, T. E. (2020). Periodic Oscillations of Myosin-II Mechanically Proofread Cell-Cell Connections to Ensure Robust Formation of the Cardiac Vessel. *Curr. Biol.* 30, 3364–3377.e4. doi: 10.1016/j.cub.2020.06.041

Zielinski, R., Mihai, C., Kniss, D., and Ghadiali, S. N. (2013). Finite element analysis of traction force microscopy: Influence of cell mechanics, adhesion, and morphology. *J. Biomech. Eng.* 135, 0710091–0710099. doi: 10.1115/1.4024467

Zimmermann, T., Rietdorf, J., and Pepperkok, R. (2003). Spectral imaging and its applications in live cell microscopy. *FEBS Lett.* 546, 87–92. doi: 10.1016/S0014-5793(03)00521-0

Conflict of Interest: The authors declare that the research was conducted in the absence of any commercial or financial relationships that could be construed as a potential conflict of interest.

frontiers
in Cell and Developmental Biology

METHODS
published: 24 September 2021
doi: 10.3389/fcell.2021.697584

An Open-Source Framework for Automated High-Throughput Cell Biology Experiments

Pavel Katunin[1,2]*, Jianbo Zhou[3], Ola M. Shehata[3], Andrew A. Peden[3], Ashley Cadby[4] and Anton Nikolaev[3]*

[1] Fresco Labs, London, United Kingdom, [2] Information Technologies and Programming Faculty, ITMO University, St. Petersburg, Russia, [3] Department of Biomedical Sciences, University of Sheffield, Sheffield, United Kingdom, [4] Department of Physics and Astronomy, University of Sheffield, Sheffield, United Kingdom

Modern data analysis methods, such as optimization algorithms or deep learning have been successfully applied to a number of biotechnological and medical questions. For these methods to be efficient, a large number of high-quality and reproducible experiments needs to be conducted, requiring a high degree of automation. Here, we present an open-source hardware and low-cost framework that allows for automatic high-throughput generation of large amounts of cell biology data. Our design consists of an epifluorescent microscope with automated XY stage for moving a multiwell plate containing cells and a perfusion manifold allowing programmed application of up to eight different solutions. Our system is very flexible and can be adapted easily for individual experimental needs. To demonstrate the utility of the system, we have used it to perform high-throughput Ca^{2+} imaging and large-scale fluorescent labeling experiments.

Keywords: imaging, automation, calcium imaging, immunolabeling, open-source hardware, high-throughput

Edited by:
Abhishek Kumar,
Marine Biological Laboratory (MBL),
United States

Reviewed by:
Sarah Sabatinos,
Ryerson University, Canada
Tom Baden,
University of Sussex, United Kingdom
Mark Pickering,
University College Dublin, Ireland

****Correspondence:***
Pavel Katunin
pavel@frescolabs.co.uk
Anton Nikolaev
a.nikolaev@sheffield.ac.uk

Specialty section:
This article was submitted to
Cell Growth and Division,
a section of the journal
Frontiers in Cell and Developmental
Biology

Received: *19 April 2021*
Accepted: *19 August 2021*
Published: *24 September 2021*

Citation:
Katunin P, Zhou J, Shehata OM,
Peden AA, Cadby A and Nikolaev A
(2021) An Open-Source Framework
for Automated High-Throughput Cell
Biology Experiments.
Front. Cell Dev. Biol. 9:697584.
doi: 10.3389/fcell.2021.697584

INTRODUCTION

Deep learning and artificial neural networks (ANNs) developed in the past decade have been proven useful for image analysis, optimization tasks, and robotics (LeCun et al., 2015; Hinton, 2018; Hinton et al., 2019). They are also becoming increasingly popular in solving biological problems. For example, ANN-based algorithms of cell segmentation are more accurate and much faster than conventional methods (Hilsenbeck et al., 2017). Deep learning also helps to detect transformed cells in human tissues (Van Valen et al., 2016; Coudray et al., 2018), optimize treatment conditions (Kusumoto and Yuasa, 2019), and explain animal behavior (Heras et al., 2019). Recently, an online platform has been developed to allow researchers without any prior knowledge of deep learning to use it in their own applications (von Chamier et al., 2020), further increasing the usefulness of deep learning as an analytical tool.

One important consideration when applying deep learning and other machine learning methods is the size of the training datasets. Typically, deep learning requires thousands to tens of thousands of data points (O'Mahony et al., 2019). This is often not feasible in biological experiments as they often take a long time to conduct. As a consequence, there is demand for automated systems that can perform hundreds or thousands of experiments with minimal human supervision. Such automation systems should allow for (a) single-cell microscopy (bright-field and/or fluorescent) in multiple wells (i.e., possess an XY stage); (b) automatic application of a number of different solutions; and (c) automated online analysis (e.g., cell segmentation and calculation of average brightness).

Commercially available fluorescent microscopes (e.g., Olympus BX61, Nikon Ti Widefield or Nikon A1 confocal systems, and live-cell imaging systems, such as Echo Revolve or Sartorius Incucyte) are often equipped with an XY stage that allows for multi-well fluorescent imaging. However, these systems are expensive (£15,000–£150,000) and offer any only limited automated solution application capabilities. This is allowed by many commercially available systems, such as Hamilton or Andrew, but these are difficult to incorporate with live imaging due to their size and cost.

Development of 3D printing as well as cheap electronic devices, such as Arduino and Raspberry Pie has led to a revolution in custom-building of affordable scientific equipment that earlier could only be available in big laboratories or university facilities. This equipment is not only cost-effective but also customizable for individual laboratory needs. One example of such technology is labware.net developed by Baden et al. (2015) and Maia Chagas et al. (2017), allowing 3D printing of extremely cheap lab equipment ranging from standard usable micropipettes and micromanipulators to fluorescent microscopes and optogenetic solutions.

Several open-source high-quality microscopes have been recently developed. For example, Diederich et al. (2020) have developed a customizable 3D printed open-source framework that allows for building a wide range of microscopes: from simple bright-field microscopes with autofocusing to more sophisticated systems with optical sectioning of the sample. However, these resources lack open-source systems for scanning a large number of samples. This was addressed by Sharkey et al. (2016) for small movements and by Merces et al. (2021) for robust imaging of multiwell plates. These solutions, however, do not offer any cell manipulation, although open-source liquid handling solutions have been recently developed (e.g., Wijnen et al., 2014; Almada et al., 2019; Amarante et al., 2019; Booeshaghi et al., 2019; Samokhin, 2020; Baas and Saggiomo, 2021).

Here, we present an open-source system that combines high-throughput microscopy in multiwell plates, automated solution application, simultaneous fluorescent imaging, and image analysis. It is low cost (£400–600 without and £2,500 with the fluorescent microscope), is fully customizable, and allows for up to 96 or 384 experiments to be performed, sequentially or, if experiments do not require a high sampling rate (e.g., 1 frame per minute or more), simultaneously. The platform is equipped with a 1-channel epifluorescent microscope head, which can be used to image dynamic fluorescent reporters (e.g., GCaMP and synthetic calcium dyes; Razlivanov et al., 2018) and/or samples labeled with fluorescent antibodies or dyes. We demonstrate how our system allows generating cell-biological data rapidly, under tightly controlled and reproducible experimental conditions, and at large scale.

RESULTS

A typical cell biology experimental paradigm often involves treatment of cells with bioactive compounds (e.g., growth factors, calcium mobilizing agonists, and cytotoxic agents) and monitoring cell behavior using fluorescent reporters or fixing cells for subsequent immunofluorescent labeling or gene expression profiling. To automate such experiments, we have developed an experimental platform that allows automatic imaging of a 96-well plate and application of eight solutions using syringe pumps. We first introduce the platform and showcase its applicability and then describe hardware, software, and systems performance in more detail.

The Automation Platform and Its Applicability

The fully assembled system is shown in **Figure 1A**. The hardware consists of several principal modules: the X-Y stage moving a multiwell plate horizontally; a small epifluorescent microscope with autofocusing system (**Supplementary Video 1**); and a perfusion manifold performing application of eight solutions into individual wells (**Supplementary Video 2**). Building instructions and all files for 3D printing are available at https://github.com/frescolabs/FrescoM (see also **Supplementary Text**). The hardware can be operated using a Python written User Interface (**Figure 1B**, see section "Software" for more details) that controls the platform, objective, and manifold as well as autofocusing, exposure, illumination, and overall management of the experimental protocols.

To showcase this platform, we first demonstrate how it can be used in large-scale fluorescent imaging experiments (Nasu et al., 2021). A typical experimental protocol involving fluorescent reporters requires imaging cells for some time before and after application of agonists, growth factors, or other active compounds. To demonstrate the usability of the developed experimental platform for such an experimental paradigm, we performed calcium imaging using synthetic fluorescent indicators of calcium concentration. Cells were automatically labeled with fluorescent calcium dye Fluo4-AM (**Figure 1C**) and subjected to calcium imaging in response to 100 μm ATP. The cells were then automatically segmented (**Figure 1C**, right) using Cellpose algorithm (Stringer et al., 2021) and the fluorescence dynamics of individual cells were extracted (**Figure 1D**). The same experimental procedure and analysis was then automatically repeated in 30 other wells (**Figures 1E,F** and **Supplementary Video 3**). These experiments demonstrate that the developed platform allows for robust and automatic high-throughput imaging of fluorescent reporters.

Another important advantage of the developed system is that it allows for a large-scale generation of images in a large number of wells. To demonstrate this usability, we have generated a Python protocol class (**Supplementary Protocol 1**, see section "Software" for more details) that makes the platform move over all 96 wells, perform focusing on each cell, and capture bright-field or fluorescent images. Example of such an experiment is shown in **Figures 2A,B**. Importantly, the system allows for scanning single well and make multiple images of the same well (**Figure 2C**), which will be useful for finding rare cells (e.g., cells undergoing mitosis/apoptosis or positive cells when transfection efficiency is low).

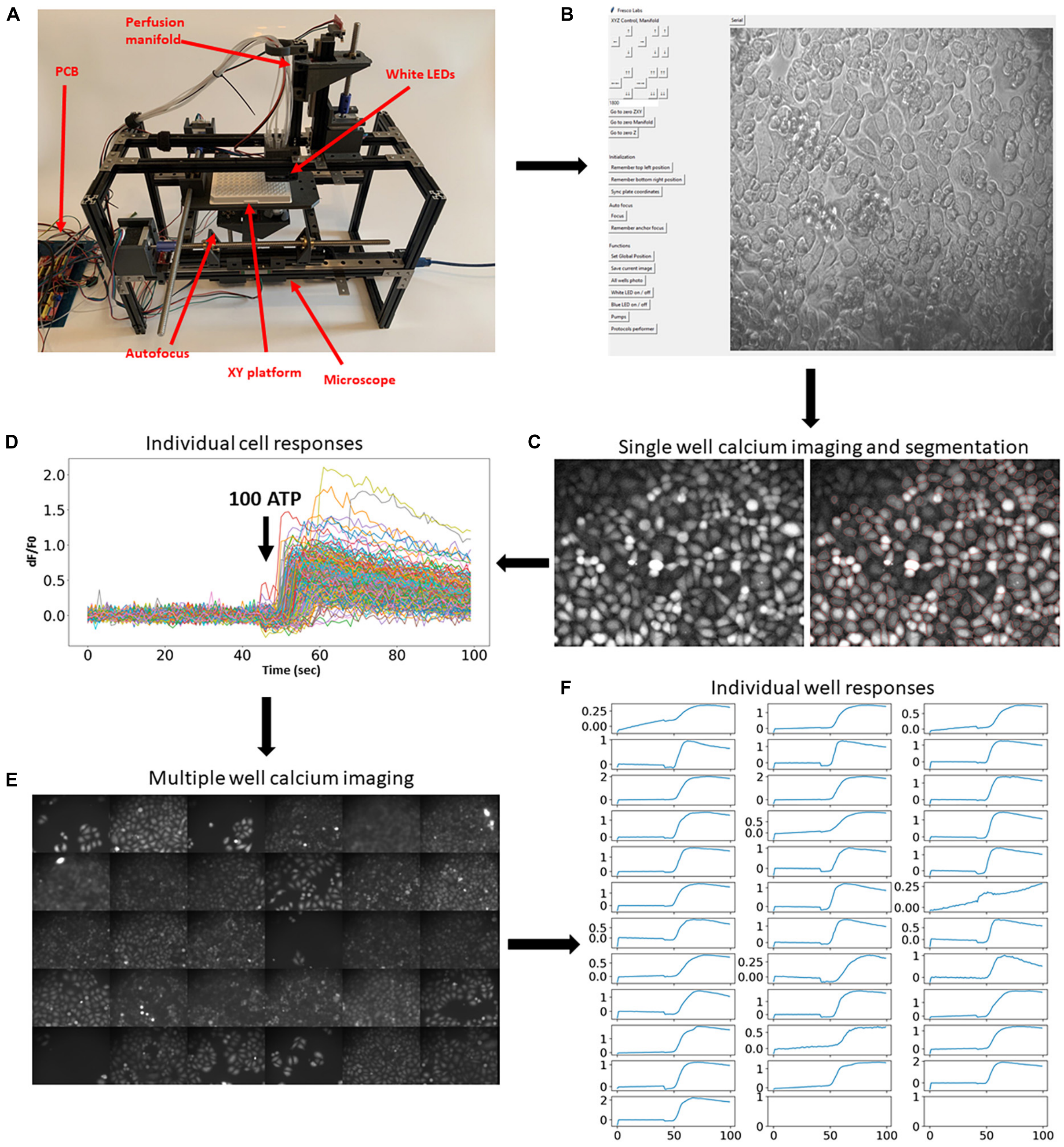

FIGURE 1 | Implementation of the developed platform and its applicability in imaging fluorescent reporters. **(A)** The developed hardware and the circuit board. The key modules are assigned in red. **(B)** Hardware operating software. Top buttons operate movement of the multiwell plate, perfusion manifold, and the focusing system. Middle set of buttons drive movement of all motors to zero position. Bottom buttons operate the camera, white and blue LEDs, and pumps, and run selected protocols. **(C,D)** Example of a single calcium imaging experiment. Cells were automatically labeled with Fluo4-AM calcium dye and imaged before and after application of 100 µm ATP. Right graph shows cell segmentation using Cellpose algorithm (cell borders are highlighted in red). **(E,F)** The same calcium imaging experiment was repeated 30 times and average responses in multiple cells in each individual well were calculated and shown in panel **(E)**. Application of 100 µm ATP robustly evoked elevation of calcium concentrations in all wells. Scale bars in panels **(C,E)** are 100 µm.

To demonstrate the usability of the developed experimental platform in labeling experiments, we used fluorescent Wheat Germ Agglutinin (WGA) that highlights cell membranes. Five rows of wells (48 wells altogether) were automatically washed with PBS and then loaded with a solution containing 5 mg/ml of fluorescent WGA. After 10 min at room temperature, the WGA was washed out with PBS and subjected to fluorescent microscopy. The resulting fluorescent images are shown in **Figure 2D**. The automatic labeling produces clear images of cells with well-defined plasma membranes, thus showing

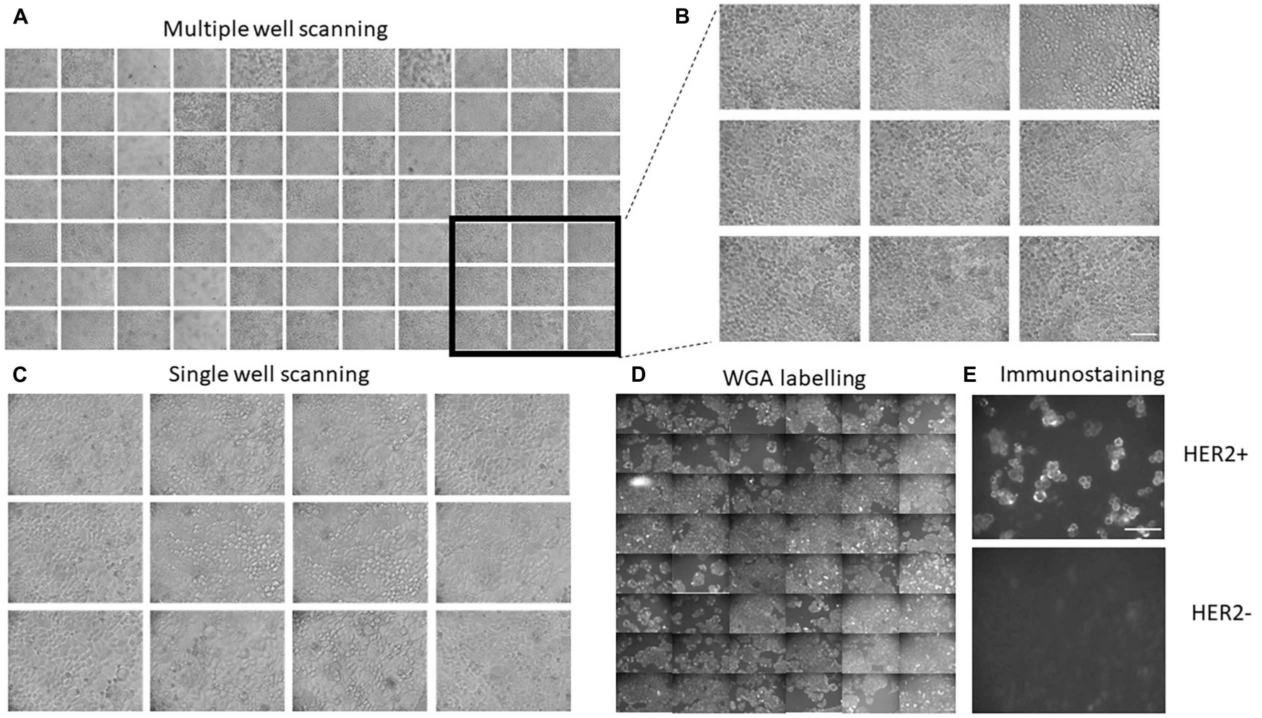

FIGURE 2 | Further examples demonstrating the applicability of the developed platform. **(A,B)** Generation of a large number of images from multiple wells. **(C)** Single-well scanning. The XY platform is positioned in the center of a single well and multiple images of images of HeLa cells were taken from the same well. **(D)** Examples of automatic labeling of HeLa cells with Wheat Germ Agglutinin and subsequent automatic imaging. Panel shows examples of imaging from 48 different wells. Autofocusing was performed in white light. **(E)** Example of immunostaining experiment using Herceptin as primary antibody and Alexa 488-conjugated antihuman antibody. Strong immunolabeling was observed in SKBR3 cells but not in the HeLa cells that have relatively low levels of the receptor. Scale bars are 100 μm.

that routine labeling procedures can be automated using the developed platform.

Finally, we also tested whether the developed platform can be used for immunofluorescent staining using the anti-HER2 antibody (Herceptin) as primary antibody and Alexa 488-conjugated secondary antibody. Wells containing either SKBR3 cells (high HER2 expression) or HeLa (low HER2 expression) were automatically perfused with PBS and Herceptin. After 40 min of incubation at room temperature, cells were perfused with PBS and then secondary antibodies. After another 30 min of incubation at room temperature, the wells were perfused with imaging solution and subjected to fluorescent imaging (**Figure 2E** and **Supplementary Figure 1**). The resulting images show clear labeling of cell membranes in SKBR3 cells, which have high levels of HER2, but not HeLa cells, which have low levels of the receptor, thus demonstrating the robustness of the automatic labeling procedure.

These examples demonstrate the broad usability of the developed experimental platform in automation of the different types of cell biology experiments. Below, we describe the platform in detail and demonstrate its performance in a series of tests.

Hardware Design

The overall structure is built with MakerbeamXL 15 mm × 15 mm extrusions connected either by L- and T-shaped aluminum brackets or by 3D printed parts. We found that using aluminum extrusion frame instead of fully 3D printed parts (both models available on https://github.com/frescolabs/FrescoM) makes the whole system more stable and reduces the vibration (data not shown). The frame consists of eight side extrusions (four vertical 300 mm and three horizontal 200 mm, two at the top and one at the bottom, **Figure 3A**). The sides are connected with two 400-mm extrusions holding MGH12 rails driving the *x*-axis. The *y*-axis (**Figure 3B**) resides on a square frame constructed of four 200-mm extrusions and connected to the *x*-axis by two 3D printed holders. Two MGH12 rails are positioned on the frame and hold one Nema 17 motor and a 96-well plate holder (**Figure 3B**, y_plate_holder.stl file).

The perfusion manifold (**Figure 3F**) consists of a holder for eight gel loading tips attached to flexible tubing *via* luer connectors. One of the tips is connected to a peristaltic pump. It is located higher than the application tips, thus providing constant solution height in each well. Alternatively, the peristaltic pump tip can be placed lower than others, thus providing more efficient washout of solution with a smaller volume. Solution change in individual wells is achieved by perfusing the wells with three to five well volumes or removal of the old solution and subsequent addition of a new solution.

The perfusion manifold is connected to a vertical 150-mm extrusion, which is connected to a vertically oriented linear

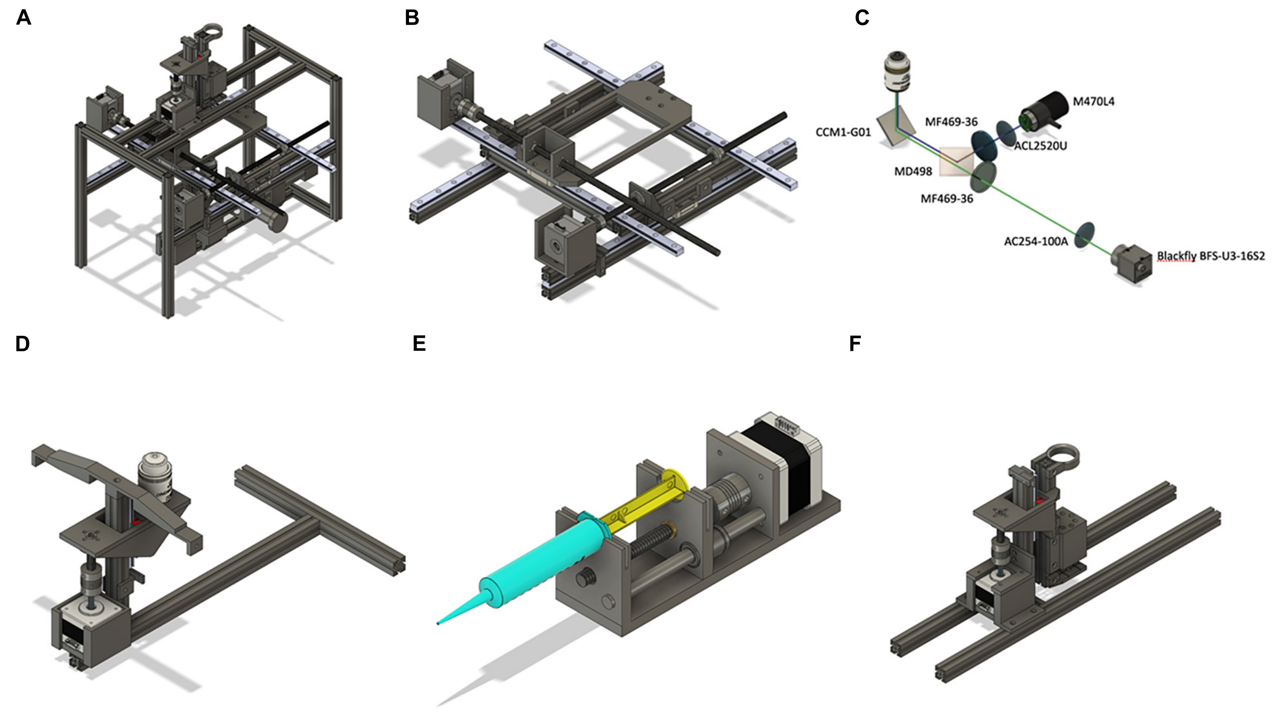

FIGURE 3 | Overview of the hardware design. **(A)** Assembled hardware consists of three modules: XY platform moving in horizontal directions; perfusion manifold moving up and down, epifluorescent microscope with a Z-stage. **(B)** The XY-stage consists of two side frames made of aluminum extrusions. Two long horizontal extrusions hold MGH12 rails forming the *x*-axis. A Nema 17 motor is attached to the side frame and moves the plate along the *x*-axis. Rotation of the stepper motor moves the leading screw that is attached to either the top platform or to a plate holder. The Y stage is based on an aluminum frame holding the plate holder. The *y*-axis motor is attached directly to one of the rails. **(C,D)** Optical design of the microscope and the autofocusing system. Numbers represent Thorlabs (all optics) and FLIR (camera) item numbers. The system implements a standard inverted fluorescent microscope with the objective attached separately to a vertically oriented linear actuator driven by a Nema 17 motor **(D)**. **(E)** Design of a syringe pump. The main platform holds one Nema 17 motor, lead screw, and an 8-mm rod. The moving part represents a holder for a nut and linear bearing. **(F)** Perfusion manifold for eight syringe pumps. Manifold holds eight pipette tips with one connected to the peristaltic pump. The latter is located slightly higher than others, which helps to keep the volume in each well constant. The manifold is fixed on a linear actuator and is driven by a Nema 17 motor. The whole system is fixed on two long horizontal extrusions attached to the top of the main frame. Four white LEDs connected in series are attached to the bottom of the manifold to provide bright-field microscope functionality.

actuator consisting of MGN12 rail, T8 lead screw, and a Nema 17 motor. The actuator is attached to two horizontal extrusions. Standard syringe pumps (**Figure 3E**) are used for solution application. The manifold is designed to have a modular structure—other modules can be attached below, above, or instead of the perfusion module. For example, we have designed a set of four white LEDs to be attached at the bottom of the manifold for bright-field microscopy as well as a holding ring for additional tubing attached at the top (**Supplementary Figure 2**). The LEDs are located vertically and, for high-quality image, require the manifold to be in the highest position. However, when manifold is at low position (zero distance from the LEDs and the top of the 96-well plate), cells can still be visible with higher exposure of the camera. Other modules, such as an electrode holder for simple electrophysiological experiments, holder for a miniature light guide for spatially controlled optogenetics experiments, or minipumps for individual cell manipulation, can be designed and integrated for additional experimental customization.

The schematics of the fluorescent microscope are shown in **Figures 3C,D**, 4A. It is a standard inverted fluorescent microscopy system with the following key features. We use a non-infinity-corrected objective (Nikon Plan 20/0.4 or, alternatively, small aspheric lens, $f = 2.75$, $NA = 0.64$) and a 100-mm camera lens ($D = 25.4$ mm). The GFP cube consists of blue and green Thorlabs filters (MF469-35 and MF525-39) and a dichroic mirror (MD498, Thorlabs). The objective is not attached to the rest of the microscope but is moving separately in a Z-stage (**Figure 3D**), connected to the main frame *via* an aluminum extrusion. If the size of the sample is an issue, a more expensive infinity-corrected objective can be used instead. In this case, there will be no fluctuations in the estimated size when focusing varies from well to well.

Automatic Control and Electric Circuits

All motors are operated *via* three CNC shields connected to Arduino Mega *via* a PCB board (**Supplementary Figure 3**). Shield 1 operates the XY stage, perfusion module, and autofocusing (Arduino pins 5–12 and enabling pin 13). Shields 2 and 3 operate eight perfusion pumps (Arduino pins 23–53, odd numbers). In order for the software to have accurate estimates of the position of each axis and pump, endstops are attached to the rail of each axis (Arduino pins 22–44, even numbers). The Gerber file for PCB generation can be downloaded from https://github.com/frescolabs/FrescoM/tree/master/hardware/pcb.

The microscope is operated by two sets of LEDs—transmitting white light for bright-field microscopy and excitation blue (488 nm) light for fluorescent microscopy. Four white LEDs connected in series (**Supplementary Figure 2**) are then connected to Mosfet IRF520, which, in turn, is connected to a 12-V power supply, ground, and pin 46 of the Arduino. The blue LED is operated using a TTL pulse applied to a Thorlabs LED driver connected to pin 48 of the Arduino.

Additional pins are reserved for the microSD card (Arduino pins 46–52, even numbers), rotary encoder (Arduino pins 2–4), and small LCD display connected to Arduino *via* i2c protocol (Arduino pins A4 and A5). The circuit can be modified to accommodate more CNC shields to increase the overall number of pumps to 22.

Software

The hardware is operated *via* an Arduino board that receives instructions from a computer *via* serial port. Functionality where commands are sent *via* wifi module or stored in a file in a microSD card are reserved for future versions (all commands are shown in **Supplementary Table 1**).

The main operating software (**Figure 1B**) is written in Python 3 and can be downloaded from https://github.com/frescolabs/FrescoM/blob/master/software. The software is very basic, easy to use, and modifiable to fit individual needs. The key functions are as follows:

1. Choose COM port to connect to Arduino (button “Serial”).
2. Move platform forward, backward, left, and right. Two sets of buttons allow for large steps or single-step movements to be made. The step size can be set.
3. Move application manifold and objective up and down.
4. Return to zero position—returns XY platform, the application manifold, and Z-focus into the start position.
5. Set top-right and set bottom-right positions of the multiwell plate.
6. Switch ON and OFF white and blue LEDs.
7. Increase or decrease camera exposure.
8. Move pumps forward and backward. To be used to fill pumps with solutions and cleaning the system after the experiment.
9. Run experiment. Each protocol is implemented as a Python class inherited from a BaseProtocol class (see **Supplementary Text** for more information) and overriding the self.perform() function. The following classes should be used for running the key functions:
    a. FrescoXYZ moves multiwell plate in X and Y, manifold, objective, and syringe pumps.
    b. ZCamera operates the key camera functions.
    c. ImageStorage saves files generated by the camera.

A few examples of protocol classes are shown in **Supplementary Protocols 1–3**.

SYSTEM PERFORMANCE

Optical Resolution

To define the microscope’s (**Figure 4A**) resolution, we used the USAF 1951 test chart (**Figure 4B**). For 20× objective and under white illumination, we can observe the sixth set of elements in group 7 giving us a resolution of at least 228 line pairs per millimeter. The size of one pixel was 0.365 μm for a 20× objective. These numbers give only approximate values as the platform employs non-infinity-corrected objectives, and during focusing, the distance between the objective and the camera lens may vary. We have also calculated the slant edge modulation transfer function (MTF) of the designed microscope using USAF 1951 (**Figure 4C**) and found that the resolution of our system was lower than that in similar open-source microscopes (Merces et al., 2021). This was probably due to the camera resolution as higher-quality objectives only slightly improved the MTF (**Figure 4C**, red). We therefore advise the users to consider more expensive, infinity-corrected objectives with higher NA, and higher-resolution cameras if high-resolution imaging is required for their experiments.

The fluorescent illumination showed mild vignetting. This was tested by using a fluorescent slide with auto-fluorescence evenly distributed across the slide (Chroma, #92001). The result of such test is shown in **Figure 4D**—the illumination is well-centered but there is less illumination on the sides of the micrograph, a sign of vignetting. This result has to be taken into account when measuring fluorescent reporters and comparing brightness in individual cells across the same micrograph.

Because we aimed at creating a cheap system, we used non-infinity-corrected objectives that do not allow for correct size estimation and are lower quality. However, in some applications, it is critical to have high-quality objectives with infinity correction. We therefore tested the system’s performance using a range of different objectives (**Supplementary Table 2**). Three different infinity-corrected objectives (EC Plan Neofluar, Zeiss; LC Plan Fl, Olympus; and C Plan L, Leika) produced similar resolution to our objective but were considerably better in terms of vignetting and the quality of fluorescent images.

System Vibration and Robustness

To test whether there is any significant vibration in the system, we took 50 images, 1 image every 1 s without making the system perform any other tasks (**Supplementary Protocol 1**). We then found the key points in each image using the SIFT algorithm (**Supplementary Figure 6**) and calculated transformation between the key points using the RANSAC algorithm for each pair of photos (2,500 data points altogether). Based on this information, we calculated the translation vector and found that the average difference between individual frames was 1.8 pixels (0.475 μm) and the maximum difference was 6 pixels (2.19 μm). When the application manifold is moving, a small vibration in the system was detected during the first second of movement (**Supplementary Video 4**). In this case, the average distance between individual frames was 4.3 pixels (1.56 μm) and the maximal error was 13.8 pixels (5 μm).

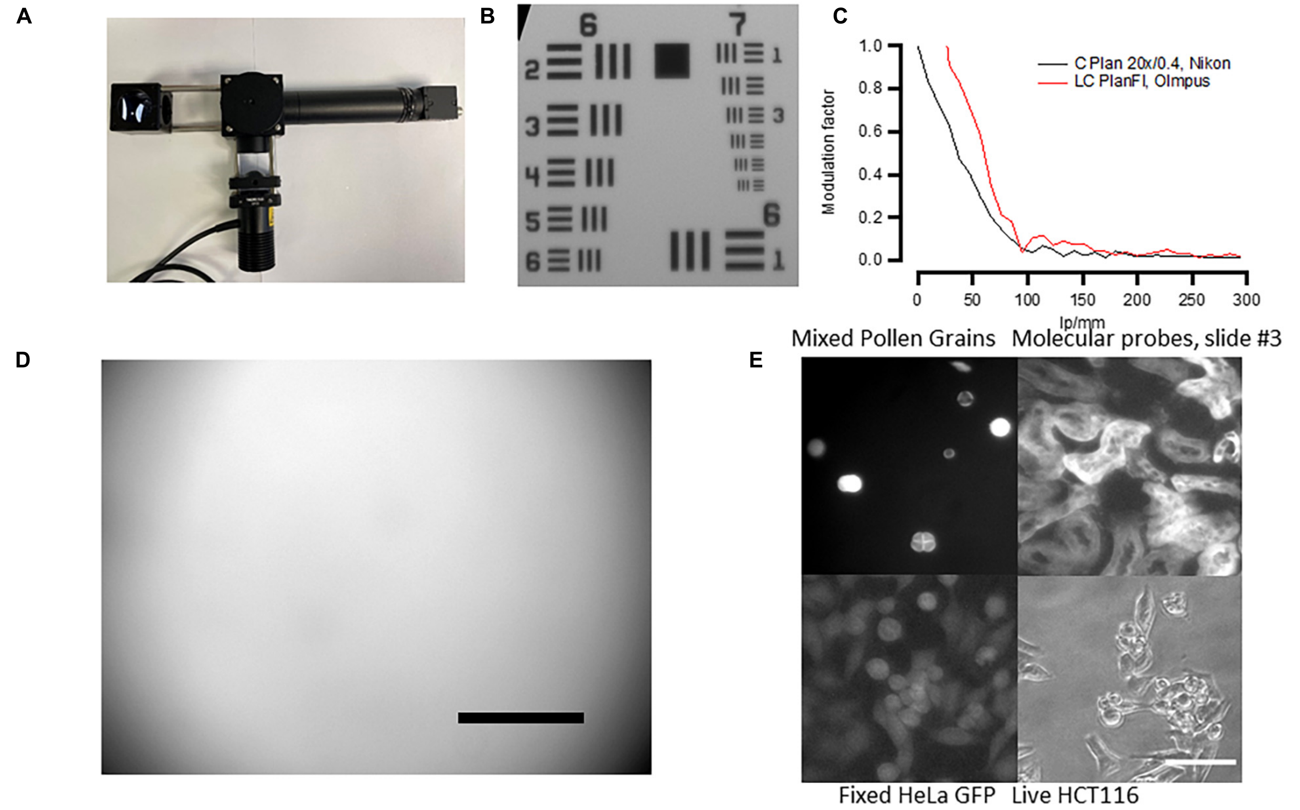

FIGURE 4 | Fluorescent microscope's performance. **(A)** Assembled microscope and the autofocusing system. See **Supplementary Material** for the building instructions. **(B)** Micrograph of the USAF 1951 standard. The microscope can resolve Group 7/Element 6 features (2.19 μm size). **(C)** Modulation transfer function calculated from USAF 1951 standard using Fiji SE_MTF plugin (Mitija et al., 2011) Black trace—cheap Nikon Plan 20× non-infinity-corrected objective. Red trace—more expensive Olympus infinity-corrected microscope (see **Supplementary Table 2** for more information). **(D)** Micrograph of green Chroma slides showing mild vignetting. Scale bar, 100 μm. Note that the scale bar only provides an approximate value because non-infinity-corrected objective was used. **(E)** Example of the autofocusing system performance in both white transillumination and fluorescence. Scale bar, 30 μm.

Autofocusing also produced a small displacement (13 ± 8 pixels, 4.745 μm on average).

To test how well the system moves from well to well, we repeated the same analysis, but in this case, we moved the multiwell plate from A1 position to H8 and back (**Supplementary Protocol 2**). The plate always went to the same well and approximately the same field of view; however, the position slightly varied from trial to trial. On average, the offset was 295 pixels (107 μm), which corresponds to 20% of the field of view and 0.1% of the total distance moved. Thus, parallel imaging of multiple well plates requires bringing the plate position to exactly the same position using additional image analysis and programming and/or image registration after the experiment is completed. When calculated separately, the displacement on *x*- and *y*-axes was 159 and 153 pixels (58 and 55 μm), respectively.

Autofocusing

The designed autofocusing system allows for automatic focusing when moving from well to well (**Supplementary Video 1**). The autofocusing algorithm is based on measuring the image sharpness and consists of the following steps.

Step 1. Move the objective to zero position.

Step 2. Move the objective to a position defined by the user (stored in the ZCamera: auto_focus_anchor variable in ZCamera.py file).

Step 3. Move the objective up from the position defined in the step 2 moving by five motor steps 20 times (these values are stored in the ZCamera:auto_focus_delta_number_of_jumps and ZCamera:one_jump, respectively). At each focal plane, the algorithm calculates the focus measure, a value that defines how sharp the image is at this focal plane.

Step 4. Position the objective 10 steps lower than the position where maximum sharpness is achieved.

Step 5. Repeat step 3 with smaller steps (two motor steps).

We have implemented and tested four different measures of sharpness described in Bueno-Ibarra et al. (2005): (1) Tenengrad (TENG)—a sum of the square of X and Y magnitudes of a Sobel operator of an image; (2) MLOG—a maximum value of the Laplacian operator of an image; (3) LAPM—average of the Laplacian operator of an image; and (4) variance of a Laplacian operator of an image. We found that TENG is the most robust for both wide field and fluorescent images (**Supplementary Figure 4**). The result of the autofocusing performed on different samples using TENG is shown in **Figure 4E**.

Perfusion System

To test how well the perfusion system (**Figures 3E**, **5A**) exchanges solutions in individual wells, we have conducted two series of tests. First, we have estimated the linearity and errors of the volume released by the syringe pumps as a function of the number of steps moved by the pump's stepper motor (**Figures 5B,C**). We then used fluorescent solution to estimate how well individual wells are perfused by the developed system.

To test the robustness of the syringe pumps, we applied different steps of the stepper motor driving the syringe pump and weighed the amount of water that is ejected in each individual session. This was repeated 10 times for the same number of steps and for a 10-ml syringe. The results of this experiment are shown in **Figures 5B,C**. The amount of the ejected water linearly depends on the number of steps (**Figure 5B**), and the error, calculated as a coefficient of variance of 10 measurements, is between 1 and 3%. This is approximately 3–10 times as large as required by ISO 86552.

How well the perfusion system exchanges liquids in a well was tested using two different solutions. One solution contained deionized water, while the other contained 12.5 μg/ml Lucifer Yellow dissolved in deionized water. These two solutions were sequentially applied while taking images by the fluorescent microscope under blue light illumination. To give a rough estimation of how well the solution is washed out, we first applied 0.1 μg/ml of Lucifer Yellow and then washed it out observing a small decrease in fluorescence. This suggests that the sensitivity of the camera is sufficient enough to detect a change from 0.1 μg/ml of Lucifer Yellow to 0 (**Figure 5D**). If fluorescence after washout drops to the level of 0.1 μg/ml, then it means that at least 99% of the fluorescent solution is washed out. To test this, we used two perfusion protocols. In one protocol (Perfusion Protocol 1), we applied the fluorescent solution while sucking the excess using a peristaltic pump connected to a tip located a few millimeters above the other tips. The result of this experiment is shown in **Figure 5D**, top. In the second test, we used Perfusion Protocol 2, in which we positioned one of the applying tips lower than the others, sucked the solution *via* this tip using a syringe pump, and then applied another solution (**Figure 3B**, bottom). Both methods yielded a similar degree of washout (>99%) after two back-to-back washouts with Perfusion Protocol 2 using smaller volumes but providing less control over the liquid level. Both ways of perfusion have their advantages and can be used in different experimental paradigms. For instance, when one needs quick application of agonist using functional imaging, Perfusion Protocol 1 may be preferable as it offers better control over liquid level. On the other hand, methods, such as immunolabeling, particularly using expensive antibodies or other chemicals, may benefit from Perfusion Protocol 2.

DISCUSSION

There is a high demand for designing affordable and flexible tools for high-scale generation of biological data. Here, we report a combination of hardware and software that allows for up to several hundred cell biology experiments performed simultaneously and automatically. The framework here and the recently developed OpenTrons-based framework (Ouyang et al., 2021) allow for simultaneous solution handling and microscopy experiments. Below, we discuss applicability of the developed experimental platform and possible ways for its future improvement.

Importance of Automation of Biological Experiments

Automation of biological experiments is important for two main reasons. First, a large number of data points are required when using modern methods of analysis, such as machine learning and deep learning. A good convolutional neural network algorithm typically requires in the region of 10,000–100,000 data points (O'Mahony et al., 2019). Considering that there are only a few thousands of cells in a field of view, the same experiments need to be reproduced 10–100 times. This number increases significantly if the experimental goal is to optimize conditions for biological experiments.

Second, there is a growing discussion on reproducibility of biological data (Ioannidis, 2005; Pusztai et al., 2013; Freedman et al., 2015; Miura and Norrelykke, 2021). This is particularly crucial when the results have direct translational applications and can affect future expensive clinical trials. The reproducibility can be improved when the experiments are standardized and when experimentation and data analysis are performed automatically to avoid human errors. The reproducibility of experiments can be further improved when performed on different sources (different cell types, cells with different genetic backgrounds, etc.), further highlighting the necessity of automation of biological experiments.

Applicability of the Developed Experimental Platform

High-Throughput Screening Experiments

Expansion of the compound libraries (Root et al., 2003; Cases et al., 2005; Rickardson et al., 2006) provided a valuable tool to search for new chemicals affecting biological functions. For example, drugs affecting physiological signaling pathways (e.g., GPCRs) can be assessed by calcium imaging (Berridge, 2001; Bootman et al., 2002; Berridge et al., 2003) or any other forms of functional imaging with a single-cell resolution. However, this requires a large number of experiments, which is laborious. The framework developed here easily allows for automatic labeling of cells with fluorescent labels and reporters (**Figures 3D–F**), application of different agonists (**Figures 3B,G**), and measurements of calcium signaling (**Figure 3G**) in a large number of wells.

Optimization Experiments

Many biological experiments require optimization of treatment conditions. For example, differentiation of stem cells requires treatment with a large number of growth factors and morphogens at different times and with different dynamics (Kim et al., 2002; Panchision and McKay, 2002). The framework developed here

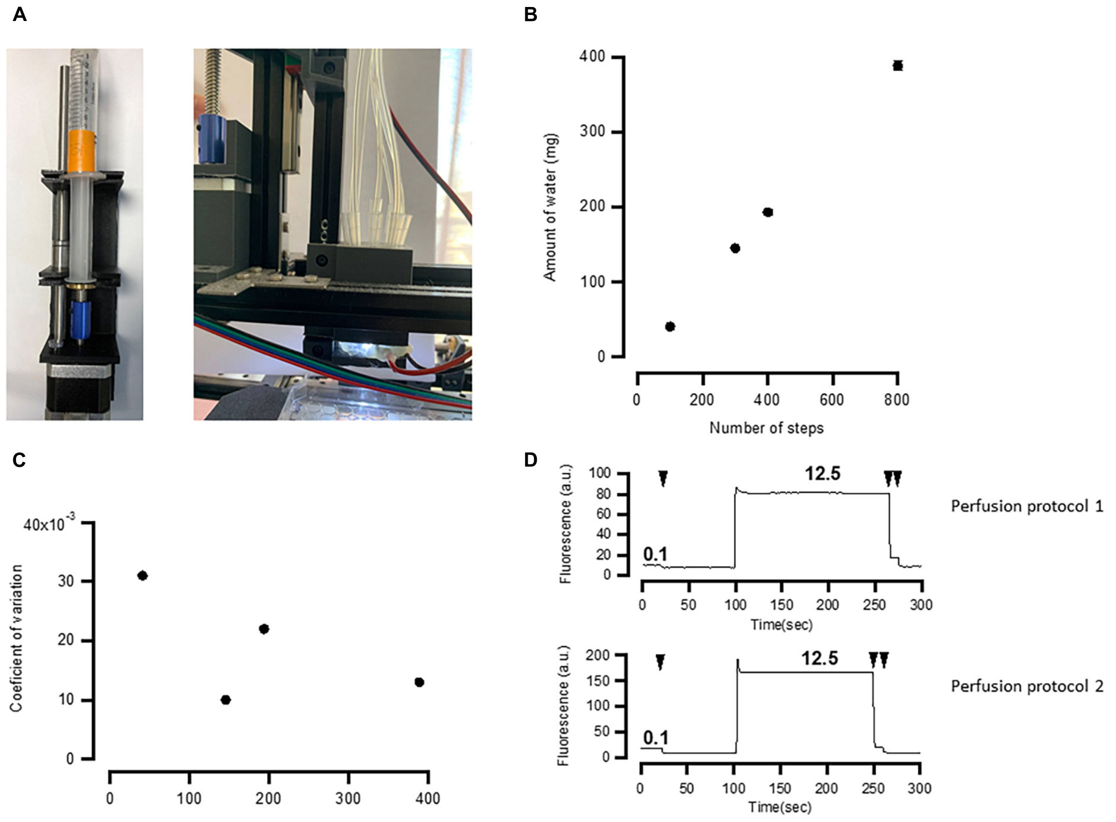

FIGURE 5 | Application manifold performance. **(A)** Assembled pump and solution application manifold. **(B)** Relationship between number of steps and the amount of water ejected by the 10-ml syringe. The relationship is linear. **(C)** Random error of the pumps calculated expressed as coefficient of variation of 10 measurements. **(D)** Application and washout of fluorescent solution (Lucifer Yellow) recorded by the fluorescent microscope. See details in the main text. Washouts are shown by arrows. Both perfusion protocols exhibit ~99% washout. Numbers indicate the concentration of fluorescent compound in µg/ml. Two back-to-back washouts were more effective in both protocols, as revealed by the further decrease in fluorescence after the second washout.

allows for experiments, such as this to be performed in an automatic manner. The outcome of an experiment can then be automatically tested using one of two methods: labeling of cells with synthetic dyes (**Figure 3E**) and antibodies against appropriate surface markers or a functional experiment (e.g., neurons can be detected by calcium imaging and application of potassium chloride or neurotransmitters).

Large-Scale Characterization of Cells Derived From Individual Patients

Substitution of standard cell lines with cells recently derived from individual patients is now becoming increasingly important (Rominiyi et al., 2019; Stringer et al., 2019). The experimental framework developed here would allow a large number of cell lines derived from individual experiments to be tested in a standardized way.

Routine Cell Biology Procedures

The developed experimental platform will also be useful in routine lab procedures, such as concentration dependence curves, cell dilutions, and cytotoxicity studies.

Data Collection for Deep Learning Model Training

Tasks, such as cell segmentation and classification may be solved by deep learning but they require a large number of cells to be automatically recorded and labeled. The developed platform can be used to image thousands of cells and combine fluorescent and bright-field imaging to perform automatic labeling of cell borders, nuclei, and specific cell types (e.g., differentiated vs. non-differentiated stem cells).

Education

The developed platform will also be extremely useful for teaching in higher education institutions. It has a potential to assist in teaching the basics of optics, bright light and fluorescence microscopy, microfluidics, building scientific equipment, and python coding for experimental automation and data analysis.

System's Limitations and How to Address Them

Increasing Optical Resolution

When developing the fluorescent microscope, we aimed at making it as cheap as possible but using high-quality filters and dichroic mirrors to improve the fluorescent signal. Therefore, we decided to use a cheap camera with a relatively small sensor size and non-infinity-corrected objectives that can readily be found on any microscope. As a result, the optical system is not idealistic in two major respects.

First, a mild vignetting is observed, which results in unequal excitation of the fluorescent sample (**Figure 4C**). This can be improved by extending the beam through substituting the 100-mm tube lens with one that has a longer focal distance. This could also allow the use of a camera with a larger sensor and larger number of pixels, which in turn will improve the spatial resolution of the system.

The second disadvantage is that we have used a non-infinity-corrected objective that results in variable distances between the objective and the tube lens. This should lead to a small error in size estimation and lower resolution as defined by the MTF (**Figure 4**). This can be addressed by using infinity-corrected objective. In this case, the camera should be positioned precisely in the focus of the tube lens, which is not required in the current configuration (**Supplementary Figure 5**).

Increasing the Robustness of the Mechanical System

The precision of the developed system can be further improved by using better mechanical parts. For example, substitution of the standard T8 lead screws with a T8-2 for the *x*- and *y*-axes will decrease the step size. Using 8-mm nuts with a spring will also likely improve the precision as it will reduce the vibration in the system. Step size can also be decreased through using and configuring a DRV8825 motor driver instead of the A4988 used here. These measures will increase the precision of the system but will decrease its speed.

Any rotational movements arising from the fact that both X and Y lead screws are located aside of the plate can be reduced by adding a second stepper motor for each axis located on the other side of the plate. However, this will reduce the number of stepper motors that can otherwise be used for syringe pumps.

Improving Perfusion

Single chamber perfusion achieves ∼99% of the solution washout (**Figure 5D**), which is sufficient for most possible applications. However, if the experimental design requires washout of the active compound, this may pose a problem as concentration curves often span for two to three orders of magnitudes (Communi et al., 1996, 1999; Hur et al., 2004), and therefore, even after the washout, cells can be stimulated with the active compound. Therefore, it is recommended to do several washouts sequentially to achieve better solution exchange (**Figure 5B**). High-precision glass syringes (e.g., Hamilton) may also improve the robustness of solution application.

Decreasing Price

The price of the system can be decreased by several hundred pounds in the following ways.

1. Substitute Thorlabs LED (£222) with cheaper 460-nm 1-W alternatives (e.g., Bright Blue LED from Future Eden—£1.09).
2. Substitution of the Thorlabs LED driver (£242) with RCD24 driver (£21).
3. Substitution of the GFP filter cube (£577) with a filter cube from an old fluorescent microscope (free).
4. Substitution of FLIR camera (£370) with Raspberry Pi camera (v24, £47).

The substitutions described above will decrease the price of the microscope but will also likely lead to a worsening of the imaging quality and stability. Therefore, they should be applied with caution.

Further Development

The modular structure of the platform developed here allows for fairly easy future adjustments to fit individual experimental needs. For example:

1. Substitution of the microscope (**Figure 3**) with a heat block will allow to incorporate PCR capability into the analysis. Other means of detection of the experimental outcome (e.g., mini spectrophotometer) will increase the amount of experiments that can be performed.
2. Currently, the microscope only provides simple wide-field one-color fluorescence. It can be improved by adding some optical sectioning functionality, such as HiLo or light sheet microscopy (OpenSPIM).
3. The number of applied solutions can be increased by redesigning the solution application manifold and the PCB.
4. Cleaning the multi-syringe system can be automated by adding storages for distilled water, alcohol, and waste.
5. Experiments can take a long time to perform and cells may need occasional passaging. An algorithm of detecting confluence and then splitting cells into new wells would allow the outcome of experiments to not be affected by overconfluence. In addition to that, selection of individual cells and transferring them into a new well will allow for generation selection of new clones for generation of new lines using transfection or CRISPR.

MATERIALS AND METHODS

Cell Cultures

SKBR3 and HeLa cells were grown in standard Dulbecco modified Eagle's media (DMEM) supplemented with 10% fetal bovine serum. Cells were passaged once a week when they reached 90% confluence.

Fluorescent Labeling

Fluo4-AM and Oregon Green BAPTA-1 AM (Thermo Fisher Scientific) were dissolved in DMSO (50 μg per 50 μl). Ten microliters of stock solution and 3 μl of pluronic acid were dissolved in 10 ml, added to the cells. Cells were then incubated at 37°C for 45 min. Imaging procedure is described in the main text.

Production of Recombinant Herceptin Antibody

The recombinant Herceptin antibody was generated by transfecting a 10-cm^2 dish of HEK cells with 5 μg of heavy chain (pFUSEss-CHIg-hG1) and 5 μg of light chain (pFUSE2ss-cLIg-hK) plasmids in complex with 50 μg of PEI. Three days post-transfection, the media was collected from the cells and frozen.

DATA AVAILABILITY STATEMENT

The hardware and software published in work are freely available under Apache 2.0 license. All hardware, firmware, software, and Python protocols are available at https://github.com/frescolabs/FrescoM. Spinnaker license agreement can be downloaded at https://www.flir.co.uk/globalassets/support/iis/knowledge-base/flirspinnaker-sdk-eula-2018.pdf.

AUTHOR CONTRIBUTIONS

AN and PK: conceptualization, mechanics and electronics design, mechanics and electronics implementation, and software design. AN and AC: fluorescent microscope design. PK: software implementation. PK, AC, AN, and AP: writing—original draft. AN and JZ: biological experiments. OS and AP: generation of herceptin antibodies. All authors contributed to the article and approved the submitted version.

FUNDING

Microscope was sponsored by the University of Sheffield Alumni Fund and used for teaching level 2 students at the University of Sheffield. Mechanical parts and circuit board were sponsored by AN and PK private funds. AP was supported by a BBSRC Grant (BB/S009566/1).

ACKNOWLEDGMENTS

We thank Elliot Birkett for reading and comments on the manuscript.

SUPPLEMENTARY MATERIAL

The Supplementary Material for this article can be found online at: https://www.frontiersin.org/articles/10.3389/fcell.2021.697584/full#supplementary-material

REFERENCES

Almada, P., Pereira, P. M., Culley, S., Caillol, G., Boroni-Rueda, F., Dix, C. L., et al. (2019). Automating multimodal microscopy with NanoJ-Fluidics. *Nat. Commun.* 10:1223. doi: 10.1038/s41467-019-09231-9

Amarante, L. M., Newport, J., Mitchell, M., Wilson, J., and Laubach, M. (2019). An open source syringe pump controller for fluid delivery of multiple volumes. *eNeuro* 6:ENEURO.0240-19.2019. doi: 10.1523/ENEURO.0240-19.2019

Baas, S., and Saggiomo, V. (2021). Ender3 3D printer kit transformed into open, programmable syringe pump set. *chemRxiv* [Preprint]. doi: 10.26434/chemrxiv.14718183.v2

Baden, T., Chagas, A. M., Gage, G. J., Marzullo, T. C., Prieto-Godino, L. L., and Euler, T. (2015). Open Labware: 3-D printing your own lab equipment. *PLoS Biol.* 13:e1002086. doi: 10.1371/journal.pbio.1002086

Berridge, M. J. (2001). The versatility and complexity of calcium signalling. *Novart. Found Symp.* 239, 52–64. doi: 10.1002/0470846674.ch6

Berridge, M. J., Bootman, M. D., and Roderick, H. L. (2003). Calcium signalling: dynamics, homeostasis and remodelling. *Nat. Rev. Mol. Cell Biol.* 4, 517–529. doi: 10.1038/nrm1155

Booeshaghi, A. S., Beltrame, E. D. V., Bannon, D., Gehring, J., and Pachter, L. (2019). Principles of open source bioinstrumentation applied to the poseidon syringe pump system. *Sci. Rep.* 9:12385. doi: 10.1038/s41598-019-48815-9

Bootman, M. D., Berridge, M. J., and Roderick, H. L. (2002). Calcium signalling: more messengers, more channels, more complexity. *Curr. Biol.* 12, R563–R565. doi: 10.1016/S0960-9822(02)01055-2

Bueno-Ibarra, M. A., Álvarez-Borrego, J., Acho, L., and Chávez-Sánchez, M. C. (2005). Fast autofocus algorithms for automated microscopes. *Optic. Eng.* 44:063601. doi: 10.1117/1.1925119

Cases, M., Garcia-Serna, R., Hettne, K., Weeber, M., van der Lei, J., Boyer, S., et al. (2005). Chemical and biological profiling of an annotated compound library directed to the nuclear receptor family. *Curr. Top. Med. Chem.* 5, 763–772. doi: 10.2174/1568026054637665

Communi, D., Motte, S., Boeynaems, J. M., and Pirotton, S. (1996). Pharmacological characterization of the human P2Y4 receptor. *Eur. J. Pharmacol.* 317, 383–389. doi: 10.1016/s0014-2999(96)00740-6

Communi, D., Robaye, B., and Boeynaems, J. M. (1999). Pharmacological characterization of the human P2Y11 receptor. *Br. J. Pharmacol.* 128, 1199–1206. doi: 10.1038/sj.bjp.0702909

Coudray, N., Ocampo, P. S., Sakellaropoulos, T., Narula, N., Snuderl, M., Fenyo, D., et al. (2018). Classification and mutation prediction from non-small cell lung cancer histopathology images using deep learning. *Nat. Med.* 24, 1559–1567. doi: 10.1038/s41591-018-0177-5

Diederich, B., Lachmann, R., Carlstedt, S., Marsikova, B., Wang, H., Uwurukundo, X., et al. (2020). A versatile and customizable low-cost 3D-printed open standard for microscopic imaging. *Nat. Commun.* 11:5979. doi: 10.1101/2020.03.02.973073

Freedman, L. P., Cockburn, I. M., and Simcoe, T. S. (2015). The economics of reproducibility in preclinical research. *PLoS Biol.* 13:e1002165. doi: 10.1371/journal.pbio.1002165

Heras, F. J. H., Romero-Ferrero, F., Hinz, R. C., and de Polavieja, G. G. (2019). Deep attention networks reveal the rules of collective motion in zebrafish. *PLoS Comput. Biol.* 15:e1007354. doi: 10.1371/journal.pcbi.1007354

Hilsenbeck, O., Schwarzfischer, M., Loeffler, D., Dimopoulos, S., Hastreiter, S., Marr, C., et al. (2017). fastER: a user-friendly tool for ultrafast and robust cell segmentation in large-scale microscopy. *Bioinformatics* 33, 2020–2028. doi: 10.1093/bioinformatics/btx107

Hinton, B., Ma, L., Mahmoudzadeh, A. P., Malkov, S., Fan, B., Greenwood, H., et al. (2019). Deep learning networks find unique mammographic differences in previous negative mammograms between interval and screen-detected cancers: a case-case study. *Cancer Imag.* 19:41. doi: 10.1186/s40644-019-0227-3

Hinton, G. (2018). Deep Learning-A technology with the potential to transform health care. *JAMA* 320, 1101–1102. doi: 10.1001/jama.2018.11100

Hur, E. M., Park, Y. S., Lee, B. D., Jang, I. H., Kim, H. S., Kim, T. D., et al. (2004). Sensitization of epidermal growth factor-induced signaling by bradykinin is mediated by c-Src. Implications for a role of lipid microdomains. *J. Biol. Chem.* 279, 5852–5860. doi: 10.1074/jbc.m311687200

Ioannidis, J. P. (2005). Why most published research findings are false. *PLoS Med.* 2:e124. doi: 10.1371/journal.pmed.0020124

Kim, J. H., Auerbach, J. M., Rodriguez-Gomez, J. A., Velasco, I., Gavin, D., Lumelsky, N., et al. (2002). Dopamine neurons derived from embryonic stem cells function in an animal model of Parkinson's disease. *Nature* 418, 50–56. doi: 10.1038/nature00900

Kusumoto, D., and Yuasa, S. (2019). The application of convolutional neural network to stem cell biology. *Inflamm. Regen.* 39:14. doi: 10.1186/s41232-019-0103-3

LeCun, Y., Bengio, Y., and Hinton, G. (2015). Deep learning. *Nature* 521, 436–444. doi: 10.1038/nature14539

Maia Chagas, A., Prieto-Godino, L. L., Arrenberg, A. B., and Baden, T. (2017). The euro100 lab: a 3D-printable open-source platform for fluorescence microscopy, optogenetics, and accurate temperature control during behaviour of Zebrafish, *Drosophila*, and *Caenorhabditis elegans*. *PLoS Biol.* 15:e2002702. doi: 10.1371/journal.pbio.2002702

Merces, G. O. T., Kennedy, C., Lenoci, B., Reynaud, E. G., Burke, N., and Pickering, M. (2021). The incubot: A 3D printer-based microscope for long-term live cell imaging within a tissue culture incubator. *Hardwarex* 9:e00189. doi: 10.1016/j.ohx.2021.e00189

Mitija, C. E. J., Tacho, A., and Revuelta, R. (2011). *Slanted Edge MTF*. Available online at: https://imagej.nih.gov/ij/plugins/se-mtf/index.html (accessed August 3, 2021).

Miura, K., and Norrelykke, S. F. (2021). Reproducible image handling and analysis. *EMBO J.* 40:e105889. doi: 10.15252/embj.2020105889

Nasu, Y., Shen, Y., Kramer, L., and Campbell, R. E. (2021). Structure- and mechanism-guided design of single fluorescent protein-based biosensors. *Nat. Chem. Biol.* 17, 509–518. doi: 10.1038/s41589-020-00718-x

Welcome to OpenSPIM. () Available online at: https://openspim.org/ (accessed August 3, 2021).

O'Mahony, N., Campbell, S., Carvalho, A., Harapanahalli, S., Velasco-Hernandez, G., Krpalkova, L., et al. (2019). Deep learning vs. traditional computer vision. *arXiv* [Preprint]. Available online at: https://arxiv.org/abs/1910.13796 (accessed August 3, 2021).

Ouyang, W., Bowman, R., Wang, H., Bumke, K. E., Collins, J. T., Spjuth, O., et al. (2021). An open-source modular framework for automated pipetting and imaging applications. *bioRxiv* [Preprint]. doi: 10.1101/2021.06.24.449732

Panchision, D. M., and McKay, R. D. (2002). The control of neural stem cells by morphogenic signals. *Curr. Opin. Genet. Dev.* 12, 478–487. doi: 10.1016/s0959-437x(02)00329-5

Pusztai, L., Hatzis, C., and Andre, F. (2013). Reproducibility of research and preclinical validation: problems and solutions. *Nat. Rev. Clin. Oncol.* 10, 720–724. doi: 10.1038/nrclinonc.2013.171

Razlivanov, I., Liew, T., Moore, E. W., Al-Kathiri, A., Bartram, T., Kuvshinov, D., et al. (2018). Long-term imaging of calcium dynamics using genetically encoded calcium indicators and automatic tracking of cultured cells. *Biotechniques* 65, 37–39. doi: 10.2144/btn-2018-0024

Rickardson, L., Fryknas, M., Haglund, C., Lovborg, H., Nygren, P., Gustafsson, M. G., et al. (2006). Screening of an annotated compound library for drug activity in a resistant myeloma cell line. *Cancer Chemother. Pharmacol.* 58, 749–758. doi: 10.1007/s00280-006-0216-7

Rominiyi, O., Al-Tamimi, Y., and Collis, S. J. (2019). The 'Ins and Outs' of early preclinical models for brain tumor research: are they valuable and have we been doing it wrong? *Cancers* 11:426. doi: 10.3390/cancers11030426

Root, D. E., Flaherty, S. P., Kelley, B. P., and Stockwell, B. R. (2003). Biological mechanism profiling using an annotated compound library. *Chem. Biol.* 10, 881–892. doi: 10.1016/j.chembiol.2003.08.009

Samokhin, A. S. (2020). Syringe pump created using 3D printing technology and arduino platform. *J. Analyt. Chem.* 75, 416–421. doi: 10.1134/s1061934820030156

Sharkey, J. P., Foo, D. C., Kabla, A., Baumberg, J. J., and Bowman, R. W. (2016). A one-piece 3D printed flexure translation stage for open-source microscopy. *Rev. Sci. Instrum.* 87:025104. doi: 10.1063/1.4941068

Stringer, B. W., Day, B. W., D'Souza, R. C. J., Jamieson, P. R., Ensbey, K. S., Bruce, Z. C., et al. (2019). A reference collection of patient-derived cell line and xenograft models of proneural, classical and mesenchymal glioblastoma. *Sci. Rep.* 9:4902. doi: 10.1038/s41598-019-41277-z

Stringer, C., Wang, T., Michaelos, M., and Pachitariu, M. (2021). Cellpose: a generalist algorithm for cellular segmentation. *Nat. Methods* 18, 100–106. doi: 10.1038/s41592-020-01018-x

Van Valen, D. A., Kudo, T., Lane, K. M., Macklin, D. N., Quach, N. T., DeFelice, M. M., et al. (2016). Deep learning automates the quantitative analysis of individual cells in live-cell imaging experiments. *PLoS Comput. Biol.* 12:e1005177. doi: 10.1371/journal.pcbi.1005177

von Chamier, L., Laine, R. F., Jukkala, J., Spahn, C., Krentzel, D., Nehme, E., et al. (2020). ZeroCostDL4Mic: an open platform to use Deep-learning in microscopy. *bioRxiv* [Preprint]. doi: 10.1101/2020.03.20.0001

Wijnen, B., Hunt, E. J., Anzalone, G. C., and Pearce, J. M. (2014). Open-source syringe pump library. *PLoS One* 9:e107216. doi: 10.1371/journal.pone.0107216

Conflict of Interest: The authors declare that the research was conducted in the absence of any commercial or financial relationships that could be construed as a potential conflict of interest.

frontiers
in Cell and Developmental Biology

PERSPECTIVE
published: 21 October 2021
doi: 10.3389/fcell.2021.739015

Multidisciplinarity Is Critical to Unlock the Full Potential of Modern Light Microscopy

Michael Weber and Jan Huisken*

Morgridge Institute for Research, Madison, WI, United States

Keywords: light microscopy, open science, multidisciplinary, biology, imaging, technology, access

Edited by:
Abhishek Kumar,
Marine Biological Laboratory (MBL),
United States

Reviewed by:
Dorothy Lerit,
Emory University, United States
Claudio Areias Franco,
Universidade de Lisboa, Portugal
Partha Pratim Mondal,
Indian Institute of Science (IISc), India

****Correspondence:***
Michael Weber
mweber@morgridge.org

Specialty section:
This article was submitted to Cell Growth and Division, a section of the journal Frontiers in Cell and Developmental Biology

Received: *09 July 2021*
Accepted: *24 September 2021*
Published: *21 October 2021*

Citation:
Weber M and Huisken J (2021) Multidisciplinarity Is Critical to Unlock the Full Potential of Modern Light Microscopy.
Front. Cell Dev. Biol. 9:739015.
doi: 10.3389/fcell.2021.739015

LIGHT MICROSCOPY HAS BECOME INCREASINGLY CAPABLE

Optical microscopy is a cornerstone of the biological sciences. It has become the most important imaging technique in biomedical research by providing high spatial resolution, high specificity, and suitability for living specimens. From the first microscopic observations of embryos and living cells in the 17th century over the first mass-produced optical microscopes and the formal definition of optical resolution in the 19th century to a sheer endless list of technological inventions that helped discover and unravel many biological mysteries throughout the 20th century, many scientifically minded people have contributed their part to develop and establish light microscopy as the powerful technique it is today (Rayleigh, 1896; Clara, 1966; van Zuylen, 1981; Paddock and Eliceiri, 2014; Zanacchi et al., 2014; Wollman et al., 2015; Maienschein, 2016). Despite its long history, light microscopy is experiencing rapid development in the 21st century. For example, recent developments like light sheet microscopy (Huisken et al., 2004) and super-resolution microscopy (Gustafsson, 2000; Klar et al., 2000; Rust et al., 2006; York et al., 2013) provide biologists with tools to image fragile organisms in close-to-native conditions over long periods of time (**Figure 1B**) and capture images of samples with spatial resolution exceeding the diffraction limit (**Figure 1C**), respectively.

MODERN LIGHT MICROSCOPY PRESENTS BIOLOGISTS WITH NEW POSSIBILITIES AND CHALLENGES

Technological advancements in light microscopy are driven by – and drive – biologists' needs to study and explore their samples in more detail. Recently, there has been the desire to move from imaging single layers of cells to recording images in a more physiological context, e.g., three-dimensional cell cultures or whole organisms, to move more to live samples to avoid side effects of fixation, or to increase throughput and automation to gain statistically relevant results. As a result, modern light microscopes do not resemble the compact optical devices they once were and are now rather complex setups that blend well-proven lens arrangements with newly designed optics, powerful electronics and intelligent software (**Figure 1A**). Early light microscopy was driven by polymaths and involved only very few people: one person developing and building the microscope and a second person preparing samples and documenting microscopic discoveries (Clara, 1966; van Zuylen, 1981). Prior to the debut of film and later digital cameras in this field, microscopy images were drawn by hand (Morrison and Gardner, 2015). While good microscope performance was crucial to make new observations, the quality and usefulness of the images were largely determined by the biologist's artistic skills and *a priori* knowledge applied in the process of drawing. Today's digital imaging is crucial to record microscopic observations in a reproducible and quantifiable way, but an entirely new set of skills is required to be successful in this endeavor. Modern light microscopy has become a collaborative effort where many experts and a multitude of disciplines are needed to develop and use the technology to its full extent.

The desire to extract quantitative data from microscopy images and the increasingly multidisciplinary aspect of optical microscopy results in both opportunities and challenges. With many features of modern light microscopes, such as optical sectioning, reduced photo-damage, increased spatial and temporal resolution, multi-sample imaging, automation, or optical manipulation, biologists have the potential to gain exciting new insights into their sample of interest. Unfortunately, for many researchers these new features might not be accessible: the increasing technical complexity of light microscopy, the plethora of image data, and the multitude of skills needed challenge traditional biologists. For example, a lack of compatibility of existing microscope hard- and software asks for programming and engineering skills that are not taught in conventional biology courses. Moreover, rapid technological advancements and frequent scientific publications suggesting technological breakthroughs make it difficult to keep track of promising developments and judge their feasibility for specific imaging experiments. Many light microscopy techniques, such as stochastic optical reconstruction microscopy, structured illumination microscopy, deconvolution and multi-view microscopy, ask for post-processing steps like restoration, registration or reconstruction of hundreds or thousands of images before the final result is seen (Agard and Sedat, 1983; Gustafsson, 2000; Rust et al., 2006; Preibisch et al., 2010); the required computer skills and information technology infrastructure are rarely present in a biology lab.

COMMERCIAL AND CUSTOM-BUILT LIGHT MICROSCOPES

From a biologist's perspective, commercial microscope setups seem to provide all-in-one solutions to most of the aforementioned challenges. Indeed, more and more advanced imaging technology is a great opportunity for vendors to develop and promote well integrated light microscopes that balance consistent performance and ease of use. Such commercial setups can provide a list of benefits for many researchers and present them with the one accessible route to high-end optical microscopy. With a common user interface, good integration of established technologies, intelligent soft- and hardware solutions, more and more automation features and on-site support from the vendor, commercial microscopes can form the core of a biology lab's imaging needs. However, commercial optical microscopes are often designed as "black boxes" with at least partly concealed hard- and software solutions to simplify the user experience and avoid user error, but also to protect the companies' intellectual property. Together with a tighter system integration and images pre-processed with proprietary algorithms, such "turn-key" instruments might prevent researchers from custom-fitting their microscopes and integrating them in their individual imaging workflows. Last but not least, the adaptation of new optical microscope technologies in a lab environment is delayed by the time it takes the company to turn an invention into a stable, easy-to-use and serviceable product and make it commercially available, a process that typically takes many years. As a result, many new light microscopy techniques only become accessible to a wider user base in a streamlined fashion upon commercialization many years after the initial scientific publication.

For many light microscopy applications in the life sciences, the advantages of commercial setups easily outweigh their downsides. However, the biologists' ingenuity and curiosity can quickly call for more tailor-made light microscopes, be it to pioneer a new sample or to test a new hypothesis with unconventional techniques. Those skilled in the art can build custom light microscopes around the sample with just the right combination of components, specifically tailored for novel biological imaging projects. Such custom-built microscopes tend to provide unique features and performance not available in commercial microscopes, such as physiological conditions for day-long imaging of Arabidopsis thaliana (Maizel et al., 2011) or high-speed microscopy and post-acquisition synchronization to reconstruct the beating zebrafish heart in three dimensions (Mickoleit et al., 2014). Because patents and company associations, as well as aspects like mass market compatibility, scalability and interface optimizations are of lower priority for scientists, custom microscopes can be finalized in a timely manner and provide quicker access to new technology. In many cases, though, the biologist's desire for custom-built light microscopes is limited by a historical disconnect between scientific disciplines: optical microscopes are mostly developed in physics-oriented environments, often far away from biological samples and real-world applications. Therefore, biologists might not be aware of new developments and might not be able to access such microscopes. Even when published in full detail, custom microscopes can remain exclusive builds only accessible to the developer and close collaborators. Their often unique and complex designs require substantial engineering, optics, and computer science skills and make it next to impossible for interested biologists to build a similar setup, reproduce published results and facilitate custom microscope technology for their own imaging ideas.

OPEN SCIENCE IS GAINING IMPORTANCE

How well a technology is shared and used within a community is a good indicator of how collaborative its development has been. The inherent openness of multidisciplinary work directly contributes to more accessible, reliable, and reproducible science. In recent years, open science projects, such as the development of open-source soft- and hardware, gained more and more traction among developers and users of light microscopy. Today, biologists have access to open-source software for image analysis and even microscope control (Carpenter et al., 2006; Edelstein et al., 2010; Schindelin et al., 2012). Open hardware projects

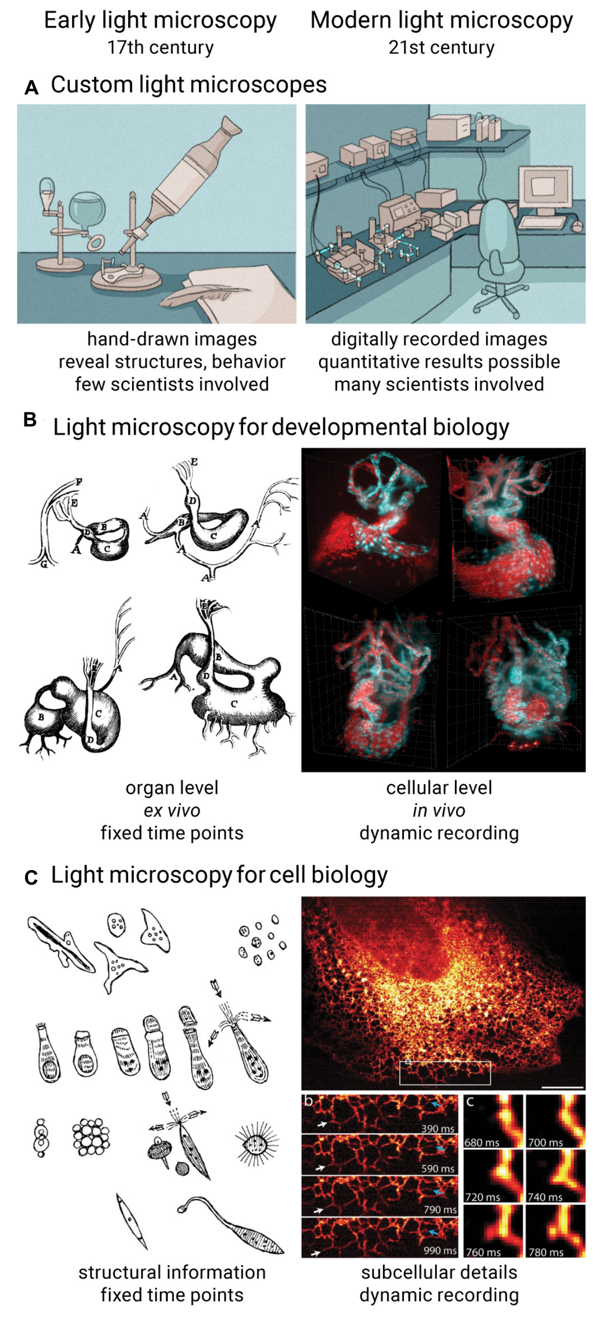

Early light microscopy
17th century

Modern light microscopy
21st century

A Custom light microscopes

hand-drawn images
reveal structures, behavior
few scientists involved

digitally recorded images
quantitative results possible
many scientists involved

B Light microscopy for developmental biology

organ level
ex vivo
fixed time points

cellular level
in vivo
dynamic recording

C Light microscopy for cell biology

structural information
fixed time points

subcellular details
dynamic recording

FIGURE 1 | Comparison of early and modern light microscopy. Over the course of 400 years, light microscopes transformed from pure lens arrangements into complex and automated devices **(A)**. Light microscopy techniques in developmental biology can now capture dynamic processes in tissues, organs and organisms under nearly physiological conditions **(B)** (West, 2013; Mickoleit et al., 2014). In cell biology, light microscopes are now capable of recording fine subcellular details **(C)** (York et al., 2013; Rob et al., 2016). Previously published images reused under license 5144871109849.

provide building plans for custom components to upgrade existing microscopes or build entire light microscope setups (Pitrone et al., 2013; Nicovich et al., 2017; Voigt et al., 2019; Diederich et al., 2020; Kumar et al., 2021). In addition, different models have been proposed to enable new biological experiments and give researchers better access to light microscopy technology by either streamlining the submission of fixed specimens or bringing mobile microscopes right to where the biological sample is located (Power and Huisken, 2019; Schweigreiter et al., 2019). While open solutions tend to require significantly lower initial costs, they might pose risks like unforeseeable additional investments and a lack of support. Here, institutions and funding agencies are asked to step in and provide reliable and long-term backing.

MASTERING MODERN LIGHT MICROSCOPY REQUIRES A UNIQUE COMBINATION OF SKILLS

In addition to the hurdles when accessing modern microscopy technology, making full use of it is not without challenges, either. Performing reproducible and scientifically sound imaging experiments is a complex task often only covered in passing during biology training (Boehm et al., 2021). Advertisements for commercial light microscopes can give the impression that such setups are straightforward to use, like a camera or a smartphone set to "Auto." Along the same lines, scientific publications tend to oversell new microscopes and glance over shortcomings and difficulties when building, aligning, and using the technique on a regular basis. In reality, modern light microscopy, much like any other scientific technique, requires a diverse set of skills, good planning, time, and precise execution in order to yield reliable results. A lack of knowledge and not following established best practices can inadvertently lead to misleading conclusions (Lambert and Waters, 2017; Montero Llopis et al., 2021). Consequently, previously unrelated disciplines need to be included in bioimaging workflows to extend the skill set and make full use of new optical microscopy technologies emerging for biological research. Experts who can make meaningful contributions to common modern imaging experiments with biologists include physicists, engineers, biochemists, computer scientists, imaging scientists, image analysts, and animal caretakers, among others (**Figure 2**).

A large variety of disciplines covering everything that is needed to perform the ideal imaging experiment is rarely found in traditional biology labs – often not even within individual research institutions. Meanwhile, modern science has become a multidisciplinary effort, requiring diverse groups of researchers from different fields to work together to tackle scientific challenges. In fact, technology development in light microscopy does repeatedly benefit from multidisciplinary collaborations and from knowledge transfer across disciplines. Examples include the use of deconvolution to computationally reverse optical distortion, a signal processing technology that was first established in seismology and later applied in astronomy before a biochemist and biophysicist introduced it to optical microscopy (Wiener, 1949; Agard, 1984; Wallace et al., 2001). Another precedent is the development of photoactivated localization microscopy (PALM), a super-resolution technique that required scientists with different backgrounds to join forces and leverage

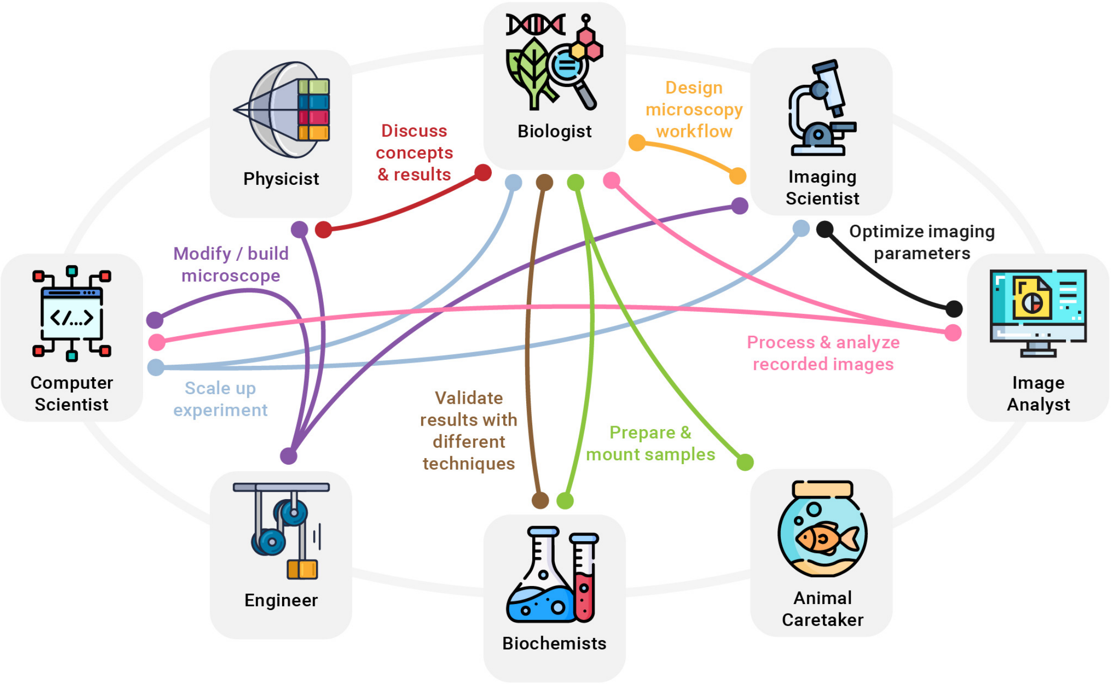

FIGURE 2 | A few examples of how a multitude of disciplines need to work hand in hand to turn new imaging ideas into reality. For example, an imaging scientist can provide valuable help to the biologist in designing a clear and reproducible microscopy workflow, while a biochemist might be needed to develop specialized fluorophores. At the same time, computer scientists, physicists, and engineers collaborate to modify or build an optical microscope needed for the experiment.

knowledge of biology, biochemistry, optics, and image processing (Betzig et al., 2006; Hess and Betzig, 2010).

Importantly, multidisciplinary research helps form a more complete and objective description by combining different perspectives of the same scientific topic (Amato et al., 2019). For example, in an imaging experiment, a biologist might interpret varying intensities across one or more recorded images as different expression levels, whereas an imaging scientist might find it being caused by uneven illumination or an unstable light source (**Figure 2**). In addition, multidisciplinary work is invaluable for both well-designed presentations that communicate results to a broad audience and for better reporting on imaging methods for reproducible science (Marques et al., 2020). Future challenges in light microscopy will increasingly ask for close collaborations of different professions and the integration of insights from other scientific fields. For example, the growing need to integrate image processing and analysis into imaging workflows, as well as the increasing data sizes will further raise the importance of computer science. Furthermore, streamlining the design of microscope hardware and increasing its accessibility will require efforts from engineering. Last but not least, designing reproducible imaging experiments, encouraging open microscopy efforts, and establishing comprehensive light microscopy education will ask for more input from imaging scientists.

BOX 1 | Core values research institutions should embrace to support collaborative and multidisciplinary work.

1 Acknowledge multidisciplinarity as a strength and not dismiss it as being superficial and not specialized.
2 Appreciation of interdisciplinary work of individuals for career and publications.
3 Foster communication among experts of different disciplines.
4 Willingness to delve into new and unknown science.
5 Demand a proof of concept and a demonstration of meaningful applications beyond fundamental science.
6 Be critical of new ideas being sold as revolutionary when they are in fact only evolutionary.
7 Acknowledge the meaning of true innovation, which has to enable others to progress.
8 Expectation to share results and make them accessible for non-experts.
9 Work toward more open and reproducible science across all levels and disciplines.

PATHS TO MORE MULTIDISCIPLINARITY

An individual research lab can become more multidisciplinary in two ways: establishing collaborations with labs of other disciplines or including researchers of different backgrounds in their own lab. A common example of the former is a collaboration between biology labs, microscope developers, and computer science labs, such as the one resulting in the first lattice light sheet microscope (Chen et al., 2014). In many ways, this is a fast way of extending and combining skill sets to successfully work on larger projects, but obtaining conclusive and reproducible results can take a lot of time and effort with every new collaboration. Whereas established structures of individual labs work well for internal projects, workflows and routines will need to be adjusted for effective external collaborations. In addition, good communication needs to be established between the labs, experts need to adjust their language and explain concepts specific to their discipline in more detail, and everyone involved must provide useful and understandable feedback to facilitate progress. Additional technical challenges include how biological samples, tools, and large amounts of data can be shared across labs and institutions. The second strategy, including most of the required disciplines in a single lab, is a long-term effort, but each imaging project will benefit and show results much faster. Multidisciplinary research labs with expertise from multiple fields interacting on a daily basis are at the forefront of developing viable light microscopy technology. Our own lab has embraced the idea of multidisciplinarity early on and has a long history of developing custom light sheet microscopy around specific biological samples and questions (Schmid et al., 2013; Weber et al., 2017; Daetwyler et al., 2019). These projects were team efforts from scientists of diverse disciplines collaborating in the lab every day and resulted in powerful microscopes that record the best possible images from the respective living and developing organisms. We are convinced that an optics development lab greatly benefits from including biologists, as it helps to connect with the biological community and steer microscope development in a meaningful direction. In the same way, we believe it is highly beneficial for a biology lab to hire scientists with different and often considered unrelated professions, such as engineering and computer science. Having all experts right in the lab is the most direct and effective way of establishing a multidisciplinary lab. All experts learn to speak the same language, share their experience and technology and expand their perspective every day, right from the start.

SCIENTIFIC ENVIRONMENTS NEED TO ACTIVELY SUPPORT MULTIDISCIPLINARY WORK

Establishing a multidisciplinary lab requires not only a critical mass of people, but also a supportive institution. Especially in the early phase of building a research lab, its skill set can be extended by the right environment: animal and cell facilities can assist with handling and preparing samples, a machine shop can help out with tools and engineering skills, a computer department can build a reliable data backbone, and a light microscopy core facility can be a crucial contributor of imaging expertise (Ferrando-May et al., 2016; Lippens et al., 2019). Importantly, the support of the institution should go well beyond maintaining existing facilities and helping with technical challenges for collaborative efforts and multidisciplinary labs to succeed. Universities and research institutes need to accept and respect new lab structures and the inclusion of previously foreign disciplines and must see themselves as a unit of experts working together to do the best possible science, not as individual labs competing for independence. More appreciation from universities for unconventional projects and community efforts can lower the risks for individual labs and make additional investments for technology development worthwhile (Fantner and Oates, 2021). Research institutions also need to bolster core facilities with well-trained staff and allow for time and resources to engage into scientific collaborations and technology development (Adami et al., 2020; Ravindran, 2020; Waters, 2020). Ideally, the scientific environment not only accepts, but encourages scientists to engage in multidisciplinary work. Research institutions might find our list of core values (**Box 1**) helpful to make the productive, multi-disciplinary workplace a reality. As light microscopy keeps evolving over the coming years, multidisciplinarity on all levels will remain critical to unlock its full potential.

DATA AVAILABILITY STATEMENT

The raw data supporting the conclusions of this article will be made available by the authors, without undue reservation.

AUTHOR CONTRIBUTIONS

MW wrote the first version of the manuscript. JH wrote sections of the manuscript. Both authors contributed to manuscript revision and read and approved the submitted version.

FUNDING

We acknowledge funding by the Morgridge Institute for Research and the Chan Zuckerberg Initiative.

ACKNOWLEDGMENTS

We thank K. Weiss and L. Herzel for their comments and discussion on the manuscript. Illustrations for **Figure 1** were done by M. Neufeld (madyrose.com).

REFERENCES

Adami, V., Homer, N., Utz, N., Lippens, S., Rappoport, J. Z., Fernandez-Rodriguez, J., et al. (2020). An international survey of Training Needs and Career Paths of Core Facility Staff. *J. Biomol. Tech.* 20, jbt.2021–3201–002. doi: 10.7171/jbt.2021-3201-002

Agard, D. A. (1984). Optical sectioning microscopy: cellular architecture in three dimensions. *Annu. Rev. Biophys. Bioeng.* 13, 191–219. doi: 10.1146/annurev.bb.13.060184.001203

Agard, D. A., and Sedat, J. W. (1983). Three-dimensional architecture of a polytene nucleus. *Nature* 302, 676–681. doi: 10.1038/302676a0

Amato, K. R., Maurice, C. F., Guillemin, K., and Giles-Vernick, T. (2019). Multidisciplinarity in Microbiome Research: a Challenge and Opportunity to Rethink Causation, Variability, and Scale. *Bioessays* 41:e1900007.

Betzig, E., Patterson, G. H., Sougrat, R., Lindwasser, O. W., Olenych, S., Bonifacino, J. S., et al. (2006). Imaging intracellular fluorescent proteins at nanometer resolution. *Science* 313, 1642–1645. doi: 10.1126/science.1127344

Boehm, U., Nelson, G., Brown, C. M., Bagley, S., Bajcsy, P., Bischof, J., et al. (2021). QUAREP-LiMi: a community endeavor to advance quality assessment and reproducibility in light microscopy. *Nat. Methods* 2:54. doi: 10.1038/s41592-021-01162-y

Carpenter, A. E., Jones, T. R., Lamprecht, M. R., Clarke, C., Kang, I. H., Friman, O., et al. (2006). CellProfiler: image analysis software for identifying and quantifying cell phenotypes. *Genome Biol.* 7:R100.

Chen, B. C., Legant, W. R., Wang, K., Shao, L., Milkie, D. E., Davidson, M. W., et al. (2014). Lattice light-sheet microscopy: imaging molecules to embryos at high spatiotemporal resolution. *Science* 346:1257998.

Clara, S. B. (1966). The Early History of the Compound Microscope. *Bios* 37, 51–60.

Daetwyler, S., Günther, U., Modes, C. D., Harrington, K., and Huisken, J. (2019). Multi-sample SPIM image acquisition, processing and analysis of vascular growth in zebrafish. *Development* 146:dev173757.

Diederich, B., Lachmann, R., Carlstedt, S., Marsikova, B., Wang, H., Uwurukundo, X., et al. (2020). A versatile and customizable low-cost 3D-printed open standard for microscopic imaging. *Nat. Commun.* 11:5979.

Edelstein, A., Amodaj, N., Hoover, K., Vale, R., and Stuurman, N. (2010). Computer control of microscopes using μManager. *Curr. Protoc. Mol. Biol.* 14:Unit14.20.

Fantner, G. E., and Oates, A. C. (2021). Instruments of change for academic tool development. *Nat. Phys.* 17, 421–424. doi: 10.1038/s41567-021-01221-3

Ferrando-May, E., Hartmann, H., Reymann, J., Ansari, N., Utz, N., Fried, H. U., et al. (2016). Advanced light microscopy core facilities: balancing service, science and career. *Microsc. Res. Tech.* 79, 463–479. doi: 10.1002/jemt.22648

Gustafsson, M. G. (2000). Surpassing the lateral resolution limit by a factor of two using structured illumination microscopy. *J. Microsc.* 198, 82–87.

Hess, H., and Betzig, E. (2010). *Developing PALM Microscopy. iBioMagazine Research Talk*. Available online at: https://www.ibiology.org/techniques/palm-microscopy/

Huisken, J., Swoger, J., Del Bene, F., Wittbrodt, J., and Stelzer, E. H. K. (2004). Optical sectioning deep inside live embryos by selective plane illumination microscopy. *Science* 305, 1007–1009. doi: 10.1126/science.1100035

Klar, T. A., Jakobs, S., Dyba, M., Egner, A., and Hell, S. W. (2000). Fluorescence microscopy with diffraction resolution barrier broken by stimulated emission. *Proc. Natl. Acad. Sci. U. S. A.* 97, 8206–8210. doi: 10.1073/pnas.97.15.8206

Kumar, M., Kishore, S., McLean, D., and Kozorovitskiy, Y. (2021). Crossbill: an open access single objective light-sheet microscopy platform. *Biorxiv* doi: 10.1101/2021.04.30.442190

Lambert, T. J., and Waters, J. C. (2017). Navigating challenges in the application of superresolution microscopy. *J. Cell Biol.* 216, 53–63. doi: 10.1083/jcb.201610011

Lippens, S., D'Enfert, C., Farkas, L., Kehres, A., Korn, B., Morales, M., et al. (2019). One step ahead: innovation in core facilities. *EMBO Rep.* 20:e48017.

Maienschein, J. (2016). Embryos, microscopes, and society. *Stud. Hist. Philos. Biol. Biomed. Sci.* 57, 129–136.

Maizel, A., von Wangenheim, D., Federici, F., Haseloff, J., and Stelzer, E. H. K. (2011). High-resolution live imaging of plant growth in near physiological bright conditions using light sheet fluorescence microscopy. *Plant J.* 68, 377–385.

Marques, G., Pengo, T., and Sanders, M. A. (2020). Science Forum: imaging methods are vastly underreported in biomedical research. *Elife* 9:e55133.

Mickoleit, M., Schmid, B., Weber, M., Fahrbach, F. O., Hombach, S., Reischauer, S., et al. (2014). High-resolution reconstruction of the beating zebrafish heart. *Nat. Methods* 11, 919–922. doi: 10.1038/nmeth.3037

Montero Llopis, P., Senft, R. A., Ross-Elliott, T. J., Stephansky, R., Keeley, D. P., Koshar, P., et al. (2021). Best practices and tools for reporting reproducible fluorescence microscopy methods. *Nat. Methods* doi: 10.1038/s41592-021-01156-w Epub online ahead of print.

Morrison, A. O., and Gardner, J. M. (2015). Microscopic Image Photography Techniques of the Past. Present, and Future. *Arch. Pathol. Lab. Med.* 139, 1558–1564. doi: 10.5858/arpa.2014-0315-ra

Nicovich, P. R., Walsh, J., Böcking, T., and Gaus, K. (2017). NicoLase-An open-source diode laser combiner, fiber launch, and sequencing controller for fluorescence microscopy. *PLoS One* 12:e0173879. doi: 10.1371/journal.pone.0173879

Paddock, S. W., and Eliceiri, K. W. (2014). Laser scanning confocal microscopy: history, applications, and related optical sectioning techniques. *Methods Mol. Biol.* 1075, 9–47. doi: 10.1007/978-1-60761-847-8_2

Pitrone, P. G., Schindelin, J., Stuyvenberg, L., Preibisch, S., Weber, M., Eliceiri, K. W., et al. (2013). OpenSPIM: an open-access light-sheet microscopy platform. *Nat. Methods* 10, 598–599. doi: 10.1038/nmeth.2507

Power, R. M., and Huisken, J. (2019). Putting advanced microscopy in the hands of biologists. *Nat. Methods* 16, 1069–1073.

Preibisch, S., Saalfeld, S., Schindelin, J., and Tomancak, P. (2010). Software for bead-based registration of selective plane illumination microscopy data. *Nat. Methods* 7, 418–419. doi: 10.1038/nmeth0610-418

Ravindran, S. (2020). Core curriculum: learning to manage a shared microscopy facility. *Nature* 588, 358–360. doi: 10.1038/d41586-020-03466-z

Rayleigh, X. V. (1896). On the theory of optical images, with special reference to the microscope. *Lond. Edinbur. Dub. Philos. Magaz. J. Sci.* 42, 167–195. doi: 10.1080/14786449608620902

Rob, D., Perkins, S. L., and Wynne, P. J. (2016). *Welcome to the Microbiome*. United States: Yale Press.

Rust, M. J., Bates, M., and Zhuang, X. (2006). Sub-diffraction-limit imaging by stochastic optical reconstruction microscopy (STORM). *Nat. Methods* 3, 793–795. doi: 10.1038/nmeth929

Schindelin, J., Arganda-Carreras, I., Frise, E., Kaynig, V., Longair, M., Pietzsch, T., et al. (2012). Fiji: an open-source platform for biological-image analysis. *Nat. Methods* 9, 676–682. doi: 10.1038/nmeth.2019

Schmid, B., Shah, G., Scherf, N., Weber, M., Thierbach, K., Campos, C. P., et al. (2013). High-speed panoramic light-sheet microscopy reveals global endodermal cell dynamics. *Nat. Commun.* 4:2207.

Schweigreiter, R., Cawthorne, C., Lippens, S., Van Minnebruggen, G., and Munck, S. (2019). Collaborating by courier, imaging by mail. *EMBO Rep.* 21:e49755.

van Zuylen, J. (1981). The microscopes of Antoni van Leeuwenhoek. *J. Microsc.* 121, 309–328. doi: 10.1111/j.1365-2818.1981.tb01227.x

Voigt, F. F., Kirschenbaum, D., Platonova, E., Pagès, S., Campbell, R. A. A., Kastli, R., et al. (2019). The mesoSPIM initiative: open-source light-sheet microscopes for imaging cleared tissue. *Nat. Methods* 16, 1105–1108. doi: 10.1038/s41592-019-0554-0

Wallace, W., Schaefer, L. H., and Swedlow, J. R. (2001). A workingperson's guide to deconvolution in light microscopy. *Biotechniques* 31:1082.

Waters, J. C. A. (2020). Novel Paradigm for Expert Core Facility Staff Training. *Trends Cell Biol.* 30, 669–672. doi: 10.1016/j.tcb.2020.06.001

Weber, M., Scherf, N., Meyer, A. M., Panáková, D., Kohl, P., Huisken, J., et al. (2017). Cell-accurate optical mapping across the entire developing heart. *Elife* 6:e28307.

West, J. B. (2013). Marcello Malpighi and the discovery of the pulmonary capillaries and alveoli. *Am. J. Physiol. Lung Cell. Mol. Physiol.* 304, L383–L390.

Wiener, N. (1949). *Extrapolation, Interpolation, and Smoothing of Stationary Time Series: with Engineering Applications*. United States: MIT Press.

Wollman, A. J. M., Nudd, R., Hedlund, E. G., and Leake, M. C. (2015). From Animaculum to single molecules: 300 years of the light microscope. *Open Biol.* 5:150019. doi: 10.1098/rsob.150019

York, A. G., Chandris, P., Nogare, D. D., Head, J., Wawrzusin, P., and Fischer, R. S. (2013). Instant super-resolution imaging in live cells and embryos via analog image processing. *Nat. Methods* 10, 1122–1126. doi: 10.1038/nmeth.2687

Zanacchi, F. C., Bianchini, P., and Vicidomini, G. (2014). Fluorescence microscopy in the spotlight. *Microsc. Res. Tech.* 77, 479–482. doi: 10.1002/jemt.22393

Conflict of Interest: The authors declare that the research was conducted in the absence of any commercial or financial relationships that could be construed as a potential conflict of interest.

frontiers
in Cell and Developmental Biology

REVIEW
published: 01 November 2021
doi: 10.3389/fcell.2021.739079

Navigating the Light-Sheet Image Analysis Software Landscape: Concepts for Driving Cohesion From Data Acquisition to Analysis

Holly C. Gibbs[1,2]*, Sakina M. Mota[1], Nathan A. Hart[1], Sun Won Min[3], Alex O. Vernino[3], Anna L. Pritchard[1], Anindito Sen[2], Stan Vitha[2], Sreeja Sarasamma[4], Avery L. McIntosh[2], Alvin T. Yeh[1], Arne C. Lekven[5], Dylan A. McCreedy[1,3], Kristen C. Maitland[1,2] and Lisa M. Perez[6]

[1] Department of Biomedical Engineering, Texas A&M University, College Station, TX, United States, [2] Microscopy and Imaging Center, Texas A&M University, College Station, TX, United States, [3] Department of Biology, Texas A&M University, College Station, TX, United States, [4] Department of Neurology, Baylor College of Medicine, Houston, TX, United States, [5] Department of Biology and Biochemistry, University of Houston, Houston, TX, United States, [6] High Performance Research Computing, Texas A&M University, College Station, TX, United States

OPEN ACCESS

Edited by:
Michelle S. Itano,
University of North Carolina at Chapel Hill, United States

Reviewed by:
Adam Glaser,
University of Washington, United States
Shaoli Song,
Fudan University, China

***Correspondence:**
Holly C. Gibbs
hgibbs@tamu.edu

Specialty section:
This article was submitted to Cell Growth and Division, a section of the journal Frontiers in Cell and Developmental Biology

Received: 10 July 2021
Accepted: 16 September 2021
Published: 01 November 2021

Citation:
Gibbs HC, Mota SM, Hart NA, Min SW, Vernino AO, Pritchard AL, Sen A, Vitha S, Sarasamma S, McIntosh AL, Yeh AT, Lekven AC, McCreedy DA, Maitland KC and Perez LM (2021) Navigating the Light-Sheet Image Analysis Software Landscape: Concepts for Driving Cohesion From Data Acquisition to Analysis. Front. Cell Dev. Biol. 9:739079. doi: 10.3389/fcell.2021.739079

From the combined perspective of biologists, microscope instrumentation developers, imaging core facility scientists, and high performance computing experts, we discuss the challenges faced when selecting imaging and analysis tools in the field of light-sheet microscopy. Our goal is to provide a contextual framework of basic computing concepts that cell and developmental biologists can refer to when mapping the peculiarities of different light-sheet data to specific existing computing environments and image analysis pipelines. We provide our perspective on efficient processes for tool selection and review current hardware and software commonly used in light-sheet image analysis, as well as discuss what ideal tools for the future may look like.

Keywords: light-sheet, image analysis, parallel processing, multiview deconvolution, tool selection

INTRODUCTION

Since light-sheet microscopy was introduced to the life and biomedical science communities in 1993 (Voie et al., 1993) and more broadly in 2004 (Huisken et al., 2004), there has been a virtual Cambrian explosion of light-sheet instrumentation and image analysis tools [see here for recent reviews (Reynaud et al., 2015; Albert-Smet et al., 2019; Wan et al., 2019)]. Science and technology has always been a moving target, but the pace of light-sheet instrumentation and software development has been staggering. Researchers have adapted the basic light-sheet body plan to different applications with different lens geometries (Huisken and Stainier, 2007; Dunsby, 2009; Wu et al., 2011, 2013; Tomer et al., 2012; Kumar et al., 2014, 2018; Voleti et al., 2016, 2019; Sapoznik et al., 2020), beam shaping strategies (Keller et al., 2008; Planchon et al., 2011; Chen et al., 2014; Vettenburg et al., 2014; Liu et al., 2018; Chang et al., 2019), sample mounting and scanning techniques (Bouchard et al., 2015; Royer et al., 2016; Wu et al., 2017; Fadero et al., 2018; Glaser et al., 2019), and contrast mechanisms (Truong et al., 2011; Di Battista et al., 2019). The ability to image intact tissues, now made possible with advances in clearing protocols (Richardson and Lichtman, 2015; Matryba et al., 2019; Ueda et al., 2020; McCreedy et al., 2021), and also the desire to image naturally dynamic 3D biological systems with live-cell imaging are the two main forces driving this unusual technological variety. This variety stands in comparison to the more purely performance driven development of, for example, confocal microscopy where samples are typically uniformly thin layers, sections, or cell cultures on a slide.

All of these species of light-sheet microscopes result in large data acquisitions with unique, context-specific image processing considerations requiring savvy compression or computation strategies and often high-performance computing (HPC) hardware. Potential solutions in both the commercial and open-source software space employ a variety of strategies for managing the flow of data through a given image analysis pipeline. Light-sheet imaging hardware developments are overviewed in **Figure 1** alongside the development of relevant software. Initially, microscope developers cobbled their own image analysis solutions together, typically made available upon request but not commonly actively maintained as they were iteratively improved. However, as broader interest in light-sheet microscopy increased, research groups employing or led by software developers have worked to make light-sheet image visualization and analysis tools more stable and accessible to biologists through web browser tools (Saalfeld et al., 2009), the java-based ImageJ/FIJI community (Preibisch et al., 2010, 2014; Pietzsch et al., 2012, 2015; Wolff et al., 2018; Hörl et al., 2019; Haase et al., 2020; Tischer et al., 2021), packaged C++ applications (Amat et al., 2014; Peng et al., 2014; Stegmaier et al., 2016), MATLAB code, and python libraries (Campagnola et al., 2015; Crist, 2016; Dask Development Team, 2016; Napari Contributors, 2019; Swaney et al., 2019; Harris et al., 2020; AICSImageIO Contributors, 2021). Likewise, instrumentation research groups have made light-sheet hardware more accessible through open-source DIY projects such as OpenSPIM (Pitrone et al., 2013) and UC2 (Diederich et al., 2020) as well as sharing initiatives such as the Flamingo (Power and Huisken, 2019). Given these investments, there is high motivation to enable the cell and developmental biology community to utilize these tools.

With this brief overview, it is easy to appreciate that biologists seeking to newly utilize light-sheet microscopy in their scientific investigations are faced with an overwhelming number of hardware (both optical and computing) and software choices. Without a background in computer science, many biologists find existing image analysis options difficult to distinguish, let alone choose between, in part for technical reasons and in part due to hype in the fields of "accelerated computing," "big data," and "deep learning." Often scientists excited about a "visualization" tool only later are disappointed to appreciate the fact that "visualization" is just being able to visually examine the raw data and may not encompass any processing/computational functionality. In institutions, departmental IT staff may or may not be aware of the unique computational needs demanded by light-sheet datasets for visualization or analysis and thus not understand the justification for the cost of high-end analysis workstations, fast network transfer, or access to on-premises and cloud computing resources. Bringing to bear biological insight from light-sheet microscopy data is such a multidisciplinary endeavor that typically no single person has a clear and comprehensive understanding of the requisite steps, creating potential pitfalls and further exacerbating this challenge. To help biologists communicate with software developers, sales representatives, IT professionals, and HPC experts about their image processing needs, we attempt to provide structure and context to relevant basic computing concepts and a process for selecting analysis tools.

CONSTANTLY FLUCTUATING LANDSCAPE OF TOOLS

By the time one has surveyed the landscape of light-sheet analysis tools it has already changed. Once the hardware is purchased, arrived, and tested, it is out of date. Software dependencies are difficult to keep compatible. While these common issues can feel overwhelming, they are not insurmountable once one is familiar with the nature of this development process. Since the light-sheet imaging and analysis landscape is a multifaceted, rapidly moving target, we believe familiarity with a few basic computing concepts will help biologists keep up with this moving target and be able to confidently provide invaluable feedback to software developers.

Creating a robust image analysis pipeline was already a difficult task as one had to sort through the different processing steps and order them in a way to produce the most reliable outcomes compared to ground truth annotations. However, with light-sheet data we are now confronted with the possibility that the data do not easily fit in the pipes we choose. At which point of handling light-sheet data do we need to think more carefully compared to typical confocal microscopy data sets? For most light-sheet microscopy applications, we should adapt our thinking with respect to the items listed in **Figure 2**. If a good strategy is laid out from end to end of this data-handling continuum, from acquisition to analysis, bottlenecks in processing and excessive data wrangling/resaving may be avoided.

COMMON DATA SETS AND COMPUTATIONAL TASKS FOR LIGHT-SHEET MICROSCOPY

Light-sheet data must first be acquired before any analysis can be performed, and beforehand it is useful to understand the expected size of the data, the computational environments available in a given lab or institution to process the data, and the typical components of a light-sheet data processing pipeline.

Raw data size can be estimated with a combined understanding of the biological system in question and the type of light-sheet imaging planned. **Figure 3A** shows a set of example data across a wide spectrum of sizes along with computing environments that are generally useful at a given scale. The examples we provide are 16-bit encoded, meaning each voxel takes 2 bytes of memory to store in the absence of some compression scheme, and the samples are imaged with either 5× 0.16 NA objective or 20× 1.0 NA objective on a Zeiss Z.1 light-sheet microscope. On the smaller end of

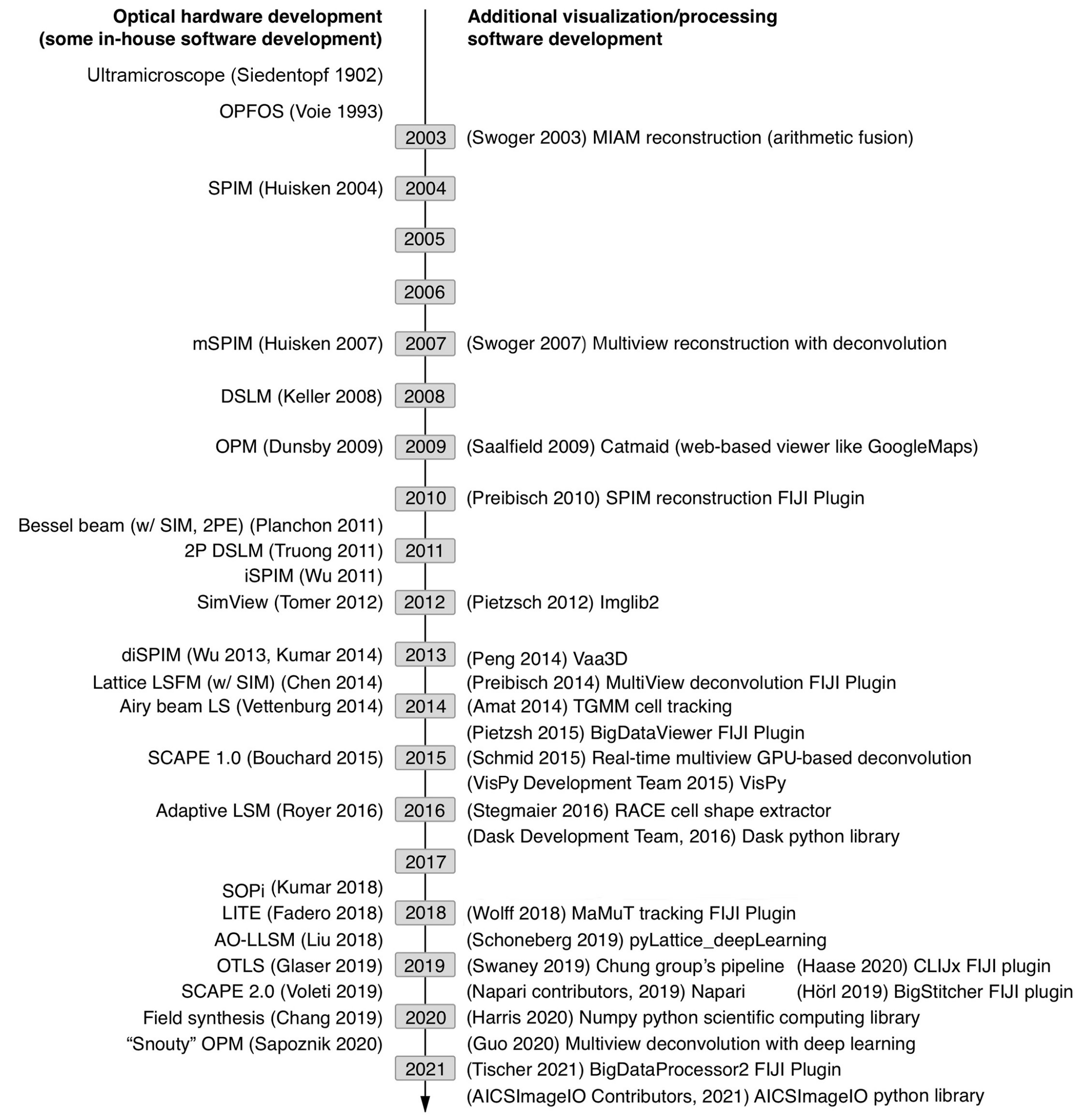

FIGURE 1 | Timeline of sampled light-sheet microscopy optical hardware development and processing software across a variety of applications. As unique species of light-sheet microscopes have been developed, unique analysis solutions have been created.

the scale, we show a multi-channel data set of a cleared adult zebrafish brain imaged at relatively low resolution resulting in a dataset typically tens of gigabytes (GBs). The purpose of this experiment was to simply map the anatomical distribution of a developmentally important reporter gene in the central nervous system, and since this investigation does not require single-cell resolution, a higher-resolution data set would make visualization and analysis more difficult than necessary. The quality of the clearing is also such that only a single view is required, further reducing the data size. In general, it is desirable to try to use the minimum sampling in any dimension that can address a particular biological question, meaning higher resolution is not always better. However, if illumination is decreased across the specimen due to light scattering, or if more isotropic resolution is desirable, it is possible to utilize several image volumes acquired from different illumination angles to create a more faithful representation of the original specimen. These additional acquisitions increase the initial amount of data needing to be visualized and processed by a factor of the number of views and can begin to approach 100's of GBs. Here we show an example of a passive clarity technique (PACT) cleared mouse spinal cord imaged from five different angles so that the views can be deconvolved and fused into a single isotropic dataset for improved tracing of spinal neural tracts. This approach increases the data size needing to be handled in pre-processing steps but for downstream processing yields comparable size data to a single

Considerations for handling light-sheet data

Acquisition: Write data quickly enough to fault-tolerant systems, potentially use on-the-fly processing.

File formats/Image compression: Write data in an informed, lossless structure for quick access, and to minimize storage space.

Storage: Where will data live, how accessible will it be, and for how long?

Data transfer: How to send data to/from the requisite computing environment in a reasonable amount of time?

Visualization: How to easily visually inspect n-dimensional image data at multiple scales from end-to-end of the analysis pipeline?

Measurement: How large are the storage and memory requirements for measured objects or other annotations?

Analysis: What types of numbers will be compared and how?

FIGURE 2 | Data handling steps that require special attention with light-sheet image data. If possible, it is advantageous to select a compressed file format that can be utilized by the requisite analysis software. Unfortunately, not all analysis software can read all image formats and often data must be resaved or restructured as it travels through an analysis pipeline.

volume (depending on how anisotropic the original data volumes were, and if the deblurred data is saved at higher bit-depth). For measurement of features at cellular and potentially sub-cellular scale, however, higher resolution volumes tiled across a region of interest may be acquired, increasing the data size by a factor of the number of tiles. This approach typically yields larger data sizes in both the pre-processing and the processing steps of image analysis as the datasets are both high-resolution and over a large spatial scale and can easily fall in the terabyte (TB) range. For dynamic processes, live specimens add the temporal dimension, with data size scaling according to the number of time points as shown in our example of the time-lapse of zebrafish embryonic brain development. Such datasets can approach the petabyte (PB) scale. These examples illustrate the usual fundamental dimensions of what is often referred to as "n-dimensional" imaging in light-sheet microscopy including spatial dimensions *x*, *y*, *z*, spectral channels, illumination angles (can also have different detection angles), tile numbers, and timepoints. To keep data sets of manageable size, balancing the data size in each of these dimensions is wise but also requires detailed knowledge of the biological system in question.

A computing environment is the combination of hardware and software used for a particular computing task. **Figure 3A** shows how these computing environments can scale to accommodate increasingly larger sizes of light-sheet image data from nominal laptops or desktops, to analysis workstations of various sizes, to local servers, to high performance computing clusters (whether on-premises or through cloud computing services). We provide a range of usual specifications of the hardware along this spectrum, though machines with specifications outside of these ranges can of course be constructed. One of the most important things to consider early on is what computational resources are available for a given project, which will guide the software approach implemented. It is usually the case that non-computer scientists find single shared memory systems easier to interface with, so there has been a strong drive to create workstations with larger shared memory that can accommodate the dataset and intermediate calculations during a processing algorithm. Such high-end workstations with TBs of shared memory can be quite expensive. Also, understanding how much memory will be required for a given analysis task, even when the data size is known, can be difficult because such algorithmic and software details are often not specified in a way that is accessible to the end user. This situation is a relic of the days when biologists could take for granted that the computational resources they were familiar with and had easy access to would be more than sufficient to process their image data. Since it is now frequently not the case that the entire data set can be loaded into computer memory, efforts have been made to create visualization and analysis tools that handle data-intensive computation by feeding smaller parts of the data to the memory at a time so as not to exceed the system memory ("lazy" load/process) or on heterogeneous distributed memory systems (that typically require more computer science expertise to interact with). In both approaches, graphics processing unit (GPU) acceleration may be employed, requiring transfer of data between system and GPU memory for external GPU boards.

In enumerating common tasks in a light-sheet image analysis pipeline in **Figure 3B**, the "visualization" step is drawn across all other individual "pre-processing" and "processing" tasks. It is difficult to understate how important visualization at every step of any image processing pipeline is, especially for quality control, tuning processing parameters (such as various threshold values, kernel sizes, etc.) efficiently, and to detect processing artifacts. The ability to quickly preview the data and computational results, especially when an analysis pipeline is being drafted or an existing one is applied to a new kind of image data, should be non-negotiable. The reality that most bioimage analysis pipelines,

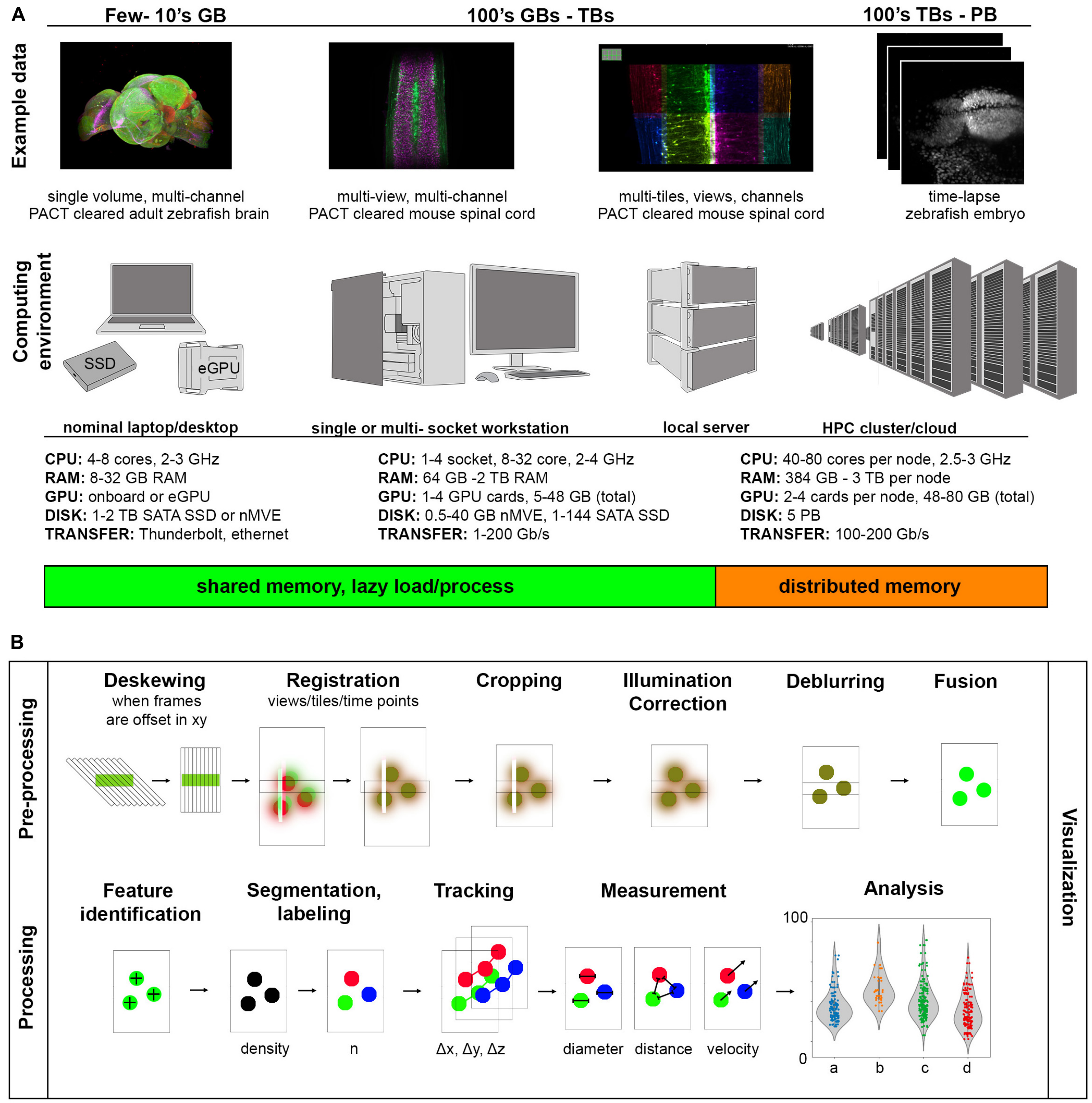

FIGURE 3 | Range of light-sheet data sizes, computing environments, and processing tasks. **(A)** As data size increases, increasingly parallel computation helps to prevent bottlenecking during image analysis. **(B)** Components of a light-sheet image analysis pipeline have highly variable pre-processing steps dependent on the particular type of light-sheet microscope used and more uniform processing steps depending on the biological measurement of interest.

including those applied to light-sheet data sets, often need to be adapted or modified from project to project and are more frequently semi-automated than fully-automated, underscores the importance of previewing results step-by-step.

The term "pre-processing" typically refers to computational effort put toward accounting for measurement artifacts and reconstructing an even more fiducial representation of the object being imaged (that could potentially be compressed with out loss of important information). The geometric peculiarities of the type of light-sheet microscope being used, the particular imaging parameters, and the optical quality of the sample will affect the kinds of pre-processing steps one must consider. For those light-sheet acquisitions where the sample or light-sheet move relative to each other at a tilted angle to the detection objective (for some modes of lattice light-sheet microscopy, open-top light-sheet microscopes, and single objective light-sheet microscopes), the first step will typically be to deskew the data so that visualization and analysis software can interpret the voxels from each volumetric acquisition on a common global three-dimensional coordinate space. Next, if there are multiple volumetric acquisitions (different channels, angle views, tiles, or time-points), interpolation and registration algorithms will be used to put these onto a common global coordinate system. This step is necessary because of imprecision in stage coordinates, sample motion relative to the microscope stage system, and spherical and chromatic aberrations. Inclusion of fiducial markers such as fluorescent beads are often utilized to register views to each other. At this point in the pipeline, the data at a given spatial location are all still separate unique values. To reconcile these differences into a coherent single spatial representation of the data at a given time, some type of fusion algorithm is applied, often in concert with a deblurring/deconvolution step to improve image contrast and resolution if possible. Another aspect to consider, which may be done prior to, after, or in the absence of deconvolution/fusion is illumination correction. It is sometimes possible to correct for uneven illumination (such as vignetting in the case of some larger FOV acquisitions) or striping artifacts (occurring when angular spread of the illumination light is low and/or parts of the sample or other objects scatter or absorb the light, casting a shadow through the image). In the case of time-lapse data sets, photobleaching correction can be applied.

Once a reasonable representation of the object is created, the object may be registered anatomically to an existing atlas, such as the Allen Brain Atlas for the adult mouse (Lein et al., 2007), or the "processing" component of the analysis pipeline begins. Processing typically refers to computations applied to the image data to extract specific features of interest. The "extraction" can refer to providing a spatial coordinate where the feature is located (as in spot detection algorithms) or enumerating a volume in the image where a particular feature is located (as in segmentation algorithms). The type of information extracted could also be a property of the object at a certain location in space, such as identifying anisotropy of features and orientation of objects or structures in the space. In the temporal regime, it will be useful to track objects and their properties over time. If we think of our example data sets, it would be useful to segment anatomical brain regions, follow axonal tracts, segment cells and examine their morphology, or identify cell nuclei and track their movements and divisions, to name a few biologically relevant aims. It is useful at this point of the analysis pipeline to perform an assessment of the quality of the results of the computationally derived objects compared to those produced by expert annotation (Taha and Hanbury, 2015). With these types of objects we can then compute further measurements, such as the relative reporter expression in different brain regions, connectivity in different regions of the spinal cord, variability of cellular morphologies within a particular tissue, or cellular velocities. Typically these measurements are acquired for replicate groups, a control and experimental group in the simplest case, and the experiment is performed multiple times to ensure repeatability. But what sort of indication is there that the experiment is repeatable? Statistical analysis of the measured outputs is used to look at the distribution of the data sets and test for significant differences. It is certainly also desirable that when an image analysis pipeline is developed using one experimental data set and the experiment is repeated, that the same analysis pipeline can be employed without tinkering with parameters, and produce the same results. When there is confidence in the results, they may be used as parameters in computational models of biological processes or they could serve as an experimental result to compare with a theoretical result.

THE JOURNEY OF A VOXEL

Having provided an overview of different scales of computing infrastructure and common image analysis pipeline components, we turn to enumerate computer hardware in finer detail. An integrated overview of basic computing hardware is shown in **Figure 4**. In the same way that understanding the compartments of a cell and their functions is important for thinking about different types of signal transduction pathways in cells and tissues, understanding the basic compartments of computing infrastructure is important for thinking about different pathways for scaling an image processing pipeline on an individual workstation or high performance cluster, which is still generally a unique composition for each research project involving light-sheet microscopy data.

Camera to Peripheral Component Interconnect Express Bus

A voxel is the three-dimensional unit of a digital image that arises from the design of modern digital cameras and the physical spacing between acquired image frames. The most popular cameras for light-sheet microscopy are sCMOS cameras with low read noise (<2.0 electrons), high quantum efficiency ($>80\%$), with sensor architectures trending toward larger, faster chip sizes for capturing larger, dynamic, diffraction-limited fields of view or for multiplexing smaller fields of view (from different channels or image planes) projected to different areas of a single chip. Back-thinned illumination for better sensitivity is increasingly desirable when read noise can remain comparably low. Other camera options include CCDs, EM-CCDs, and intensified cameras. The key overarching concept to understand is that photons hitting the discrete pixel elements of the camera sensor are transduced into electrical energy that flows under the control of electronic circuits built into the camera itself to an analog-to-digital converter (ADC). The purpose of the ADC, which in most systems is now on the camera itself, is to assign a binary-encoded value to each individual voxel proportional to the number of photons that were captured at each location. These values can be transferred to an electronics board called a frame grabber through a specific protocol, typically camera link for high-speed imaging in many light-sheet microscopes. The frame grabber has its own hardware and software that connects the device to the motherboard of a computing system with a peripheral component interconnect express (PCIe) interface and relays acquisition instructions to the camera from the acquisition software run within the operating system. An important component on the frame grabber is the direct memory address (DMA) controller that can relay image frames to GPUs to be rendered to the computer screen or for computational pre-processing, to computer memory to buffer for storage, or directly to disk without having to use central processing unit (CPU) resources for each voxel. The extent of these different DMA functionalities will depend on the design of

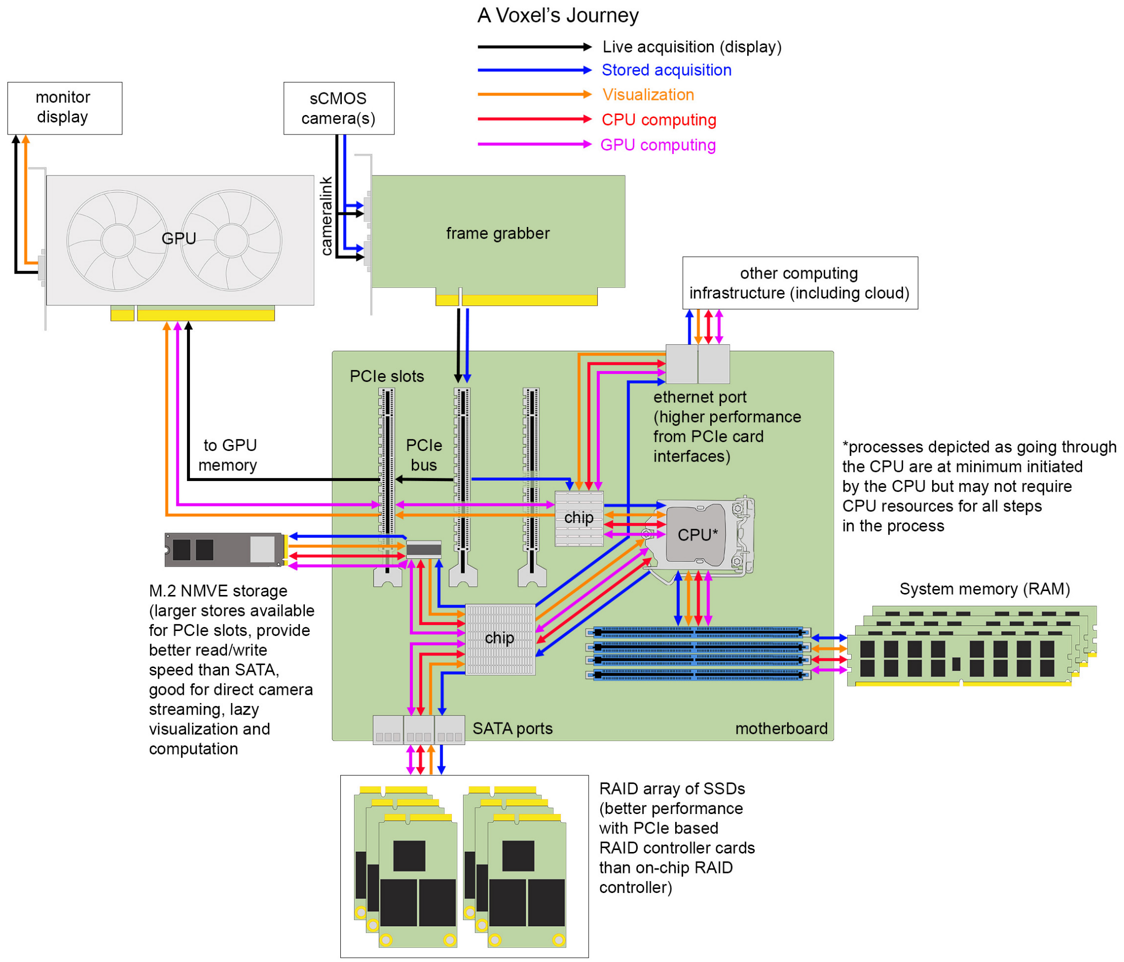

FIGURE 4 | The journey of a voxel. Hardware components and interfaces for transferring data between them on one example of a typical image analysis workstation.

the peripheral device and the architecture of the motherboard. Real estate of PCIe lanes is in short supply when multiple devices need to communicate on the PCIe bus, which is the electronics of the motherboard that voxels must flow through. In addition to frame grabbers, GPUs, RAID controllers, fast read/write storage, and network cards may occupy this space. Complicating matters, the total number of pins present on the PCIe slots may exceed the number of lanes available for simultaneous use, so care must be taken that components are selected to allow for near optimum performance. Devices plugged into a PCIe ×16 slot, if not provided enough lanes on the bus, will not be able to perform to specification.

Peripheral Component Interconnect Express Bus to Central Processing Unit, Memory, Graphics Processing Unit

PCIe bus traffic is directed by the computer's operating system with the help of the CPU and several smaller processors built into the motherboard. For light-sheet acquisitions including multiple cameras operating at high frame rates, the rate of data generation can exceed the typical write speed of many storage devices and so the data is often buffered in system memory. System memory refers to the random access memory (RAM) storage that operates only when a computer is powered on (as opposed to persistent storage that can retain values when power is off) that holds instructions and data that will be accessed directly by the CPU. Acquisition software for light-sheet microscopes can be incorporated with on-the-fly image pre-processing and processing steps that utilize GPU or CPU computational resources prior to data storage. This approach can reduce overall analysis time significantly but also runs the risk of loss of information from the raw data. The limitations of pre-processing steps that involve interpolation (e.g., deskewing) and assumption of point spread function shape (e.g., deconvolution) are still debated. Additionally, registration results are not always optimal and fusion of the data under these circumstances significantly degrades image quality. Finally, some funding and state agencies have requirements for preservation of raw data for a certain period of time, in which case one must be careful to consider what is a reasonable definition of "raw" data.

The core of a computer is the CPU which must be running a program to trigger the acquisition of frames from the microscope camera(s). Not long ago, processors contained a single computational core, often referred to as an arithmetic logic unit (ALU) that takes two binary inputs (data) and an instruction (also translated from higher-level programming languages into a binary-encoded input) and performs a rudimentary operation resulting in a binary-encoded output. These inputs are progressively moved from system memory through a series of on-processor memory stores called caches (e.g., L3, L2, and L1) until they can be loaded into the registers operated on by the ALU. More complex operations are combinations of rudimentary calculations. Modern CPUs have increased the number of cores up to tens of cores per processor, with most of these cores having multi-threading capabilities (discussed later). In this modern configuration, several software can operate in parallel as their processes can be assigned to different cores. Additionally, motherboards that support more than one CPU are now commonly used. Most of the major computer programming languages people are familiar with (e.g., C++, java, and python) are abstractions to interface a human-language computer user or programmer with the binary language of a CPU to accomplish image processing and data analysis tasks (and of course emails, gaming, etc.).

Most motherboards have an on-board GPU that prepares data to be rendered to a computer screen, but the capabilities of these GPUs can be minimal compared to the PCIe-based GPU boards that have space for more dedicated memory and GPU cores. GPU architecture is different from CPU architecture in that there are orders of magnitude more computing cores (ALUs) on a GPU. The field of computer graphics encompasses some standard operations, especially those involving manipulation of matrices (which are a common way to represent n-dimensional light-sheet data). However, giving software developers access to these functions is not accomplished through the standard computing languages but rather graphics-specific application programming interfaces (APIs) (e.g., CUDA developed by NVIDIA, OpenGL, and OpenCL). When needing to interactively display large data acquisitions or rapidly render 2D representations of a three-dimensional object, one will benefit greatly from a GPU. The larger the on-board memory of the GPU, the better it can be utilized for other computational image pre- and processing tasks as well. The data must be first loaded into the GPU's dedicated memory, computed on, then returned to system memory. Since these memory allocation processes take time, computation is best accelerated when several computing operations are chained together before a final result is delivered back to system memory. One of the most popular types of image processing performed primarily on GPUs are the training of deep-learning networks and their use for prediction of objects and other types of image properties.

To Data Storage

Voxels waiting in system memory will be short-lived unless they are written to one of a wide variety of long-term, non-volatile data storage devices. This writing process involves software instructions concerning where the data will be stored, how the data should be efficiently organized on disk, whether, or more likely, which compression scheme should be applied, how long the data will need to be stored, and how accessible it should be.

Generally, the farther voxels must travel, the slower the write speed will be. However, multiple factors along the way have significant impact on write performance. It is important to consider the speed of data reading (and writing) by the storage drive controller (a small computer chip that lives on the drive itself), the speed of the connectivity between the drive and the computer, the size of the drive, and the ways in which such a drive can be combined with others into a larger unit. Solid State Drives (SSDs) are typically built on a floating transistor technology called NAND flash memory and, having no mechanical moving parts like their older disk-spinning counterparts Hard Disk Drives (HDDs), are orders of magnitude faster at reading and writing data (microseconds compare to milliseconds). SSDs can connect to the motherboard using SAS or serial ATA ports (SATA), as the HDDs these ports were designed for typically do; however, the SATA interface controller is not fast enough to keep up with the data read and write speeds achievable by SSDs. To take full advantage of the speed of SSDs, faster interfaces such as non-volatile memory express (NVMe) were created that use PCIe protocols to interface with permanent storage devices. Size of the drive is often referred to as the form factor, which is relevant when configuring workstations or servers to ensure efficient use of space and heat dissipation. For workstations, motherboards will usually have one or two M.2 slots, which accommodate small SSDs that have PCIe ×2 or ×4 connectors, as well as PCIe slots for E3 form factor SSDs that have larger bandwidth and storage (PCIe ×8 or ×16). Additionally, there will be connections on the motherboard for SAS or SATA cables to transfer U.2 drives (2.5″ SSDs), though these can also be NVMe capable.

Going up from the level of the individual disk, it is important to understand how multiple disks can be utilized together to improve data read and write speed, as well as data stability, using Redundant Array of Independent Disks (RAID) controllers. Moderate performance raid controllers can be found already built-in to motherboards or such functionality provided by RAID software applications, however, it is likely the data streaming demands of light-sheet microscope acquisition will require an external RAID controller card installed into a PCIe slot. Common RAID configurations are RAID 0, RAID 1, and RAID 10. In a RAID 0 configuration, the RAID controller spreads the data across separate disks simultaneously (called striping), which parallelizes and thus speeds up data writing. While this sounds immediately useful, this approach puts the data at risk since if one drive fails, the entire data set is unrecoverable. Alternatively, in a RAID 1 configuration, the RAID controller sends the same data to all the disks (called mirroring), writing the same data on multiple drives as backups. RAID 1 protects against drive failure but provides no speed-up and decreases effective storage size by half. Both speed and redundancy, however, are design components of a RAID 10 configuration, where data is both striped and mirrored to a minimum of four drives. The effective storage of RAID 10 configurations is still cut in half, however, which is expensive. RAID 5 is a popular alternative that reduces the excess amount of space required for data redundancy by using a strategy called parity, which is a logic calculation between two bits of data striped to different disks. Rather than both bits being also mirrored, instead the and/or logic between the bits is encoded as a single bit that stored on a third disk. This strategy requires an extra calculation and care to keep the bit pairs together, but if one disk fails the missing data can be reconstructed from the parity bit that has been striped to either of the other two disks.

On-board drives are common for acquisition and short-term storage, but ultimately data is often sent to be stored on an external device such as a local storage server, HPC cluster, or the cloud for sharing, computing, and/or long-term storage. Recommendations for networked device solutions depend on available resources and data size (Andreev and Koo, 2020). Consulting with department IT or institutional HPC colleagues will help to identify the best solution given available resources, but for those labs without such support, DIY direct-attached storage [such as Just a Bunch Of Disks (JBOD)] that connect with a SAS connection may be a good option, or if the acquisition computer has a high-speed network port (10–100 Gb/s), a network-attached server can also be assembled or purchased. These longer-term, larger storage solutions are still often composed of HDDs due to cost. These external devices can then be accessed remotely, networked to other HPC resources on premises or to the cloud. One counter-intuitive point is that cloud resources are most reliable for mid-range data sizes (∼10 GB) as larger data transfers can trigger slow-downs by service providers, require specialized file transfer software, and even under the best of conditions may still result in impractical file transfer times. In the future, development of edge computing workflows that aim to minimize network travel by providing computational and storage resources to an edge device (in this case a light-sheet microscope) at the most physically proximal node of a provider network (edge node), could address some cloud service constraints. Intelligent pre-processing, compression, and/or data abstraction at such edge nodes could also limit the data size subsequently sent to cloud storage.

While many scientists that routinely use microscopy tools are familiar with the TIFF file as a reliable data storage format, this file specification is not well-suited for large image data. Given the size of most light-sheet data, the type and structure of the file the voxels will be stored in is important to consider in advance to reduce the need to perform "data wrangling," that is, to re-save or modify the structure of the data so it can be computed on by a given analysis software and to improve data access speeds. Such considerations can also be very important for speedy data visualization. Recall in the discussion of RAID configurations that data sent to multiple disks was called "striping." This is the case because, even though we think of image data as 2D, 3D, or ND arrays, on disk they are by default stored as a single stripe of bits ordered into a line that must be accessed sequentially. Now consider these bits are lined up on disk row-by-row so that the last voxel of one row is next to the first voxel of the next row. If one was interested to access the voxel physically below the last voxel of a row, it would be necessary to search an entire extra row. However, if the image is split into smaller 2D "chunks" and each chunk is stored row-by-row, the time to access the related voxels is reduced. Useful file formats also frequently support image "pyramids" that store the chunked multi-dimensional data at full resolution and increasingly lower resolution versions. In combination, multi-resolution chunks enable the most rapid access to spatially relevant subsets of image data. When browsing the data with visualization software that supports these file types, lower resolution data rapidly give the impression of the sample structure while the high-resolution data are quickly read and displayed, providing a real-time experience. Multi-resolution chunks can also be useful for speeding certain computations that may not require full resolution. When using commercial microscopes and software, it is often not possible to write data to a more generally open chunked pyramid file type (e.g., HDF5, zarr, OME-TIFF, and N5), but companies are increasingly utilizing these techniques along with lossless compression techniques. In addition to the values of the voxels in which we are primarily interested, it is usually the case that important metadata about the microscope and camera settings are stored with the image data and keeping these pieces of information together is an important aspect of scientific reproducibility. Unfortunately, there is not a single consensus on the overall best file structure and therefore some conversion and data wrangling is likely (Moore et al., 2021).

Out of Storage for Processing

Having seen the path that a voxel must traverse to be stored, one has already seen the relevant paths that would be traversed for additional processing. Data must be available in system memory to be operated on, so the data will be loaded from storage to RAM. Then, if the computation is to be carried out on the CPU, the data will be sent to the processor as requested, or if the computation is to be carried out on the GPU, the data will travel on the bus from system memory to the GPU's dedicated memory and operated on by the GPU. Computational results are temporarily stored as variables in either system memory or GPU memory and at some point, written back to permanent storage. One important thing to consider when putting together an image processing pipeline is to try to minimize the effort put toward transferring data and only do so (for example load the data into GPU memory) if the speed-up in computation outweighs the data transfer time. Another key consideration is whether the data fits in the relevant memory storage space and if not, what can be done to split the data into usable chunks for a given processing task.

Computing hardware and software changes have been slow and steady but could change drastically in the near future, creating an ever-bigger challenge requiring more computing literacy and even better communication across disciplines. We hope this brief overview of computing hardware is empowering to biologists and microscopists so they can consider the steps of designing and implementing demanding image processing workflows in a more concrete and less abstract way.

WHAT CAN PARALLEL COMPUTING MEAN?

We have observed that scientists who are unfamiliar with larger data intensive computing workloads often assume that computational hardware resources available will be automatically utilized by a given software. However, as discussed in the previous section, data that is to be processed must be in an accessible location to the given computing hardware, whether CPU or

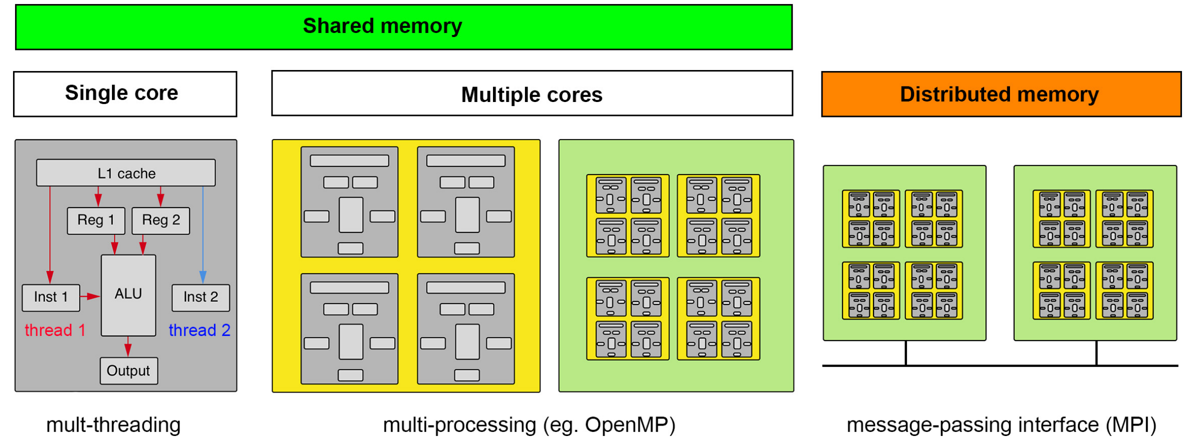

FIGURE 5 | Computing concepts for scaling up and scaling out. Computation requires data and instructions to be loaded into registers directly accessible by an arithmetic logic unit (ALU). Multi-threading makes computations parallel by taking advantage of dead time when data are being fetched. Multi-processing is when the computation can be spread to multiple cores (ALUs), whether on a CPU or GPU, that have access to the same memory (GPU's typically having their own smaller on-board memory). If the data and/or computations do not fit in shared memory, a message-passing interface must help coordinate the broadcasting of data and computations across a distributed memory system. (gray, core; yellow, CPU; green, motherboard).

GPU cores, and these directions must be explicit. If multiple nodes of a computational cluster are to be utilized, the software also has to make this explicit. Thus, it is regrettably possible to select software that fails to take advantage of all available computing resources, especially when hoping to scale across a distributed memory system.

Parallel computing is often a good solution for light-sheet image analysis, but to best utilize the power of parallel computing one must appreciate the different types of hardware approaches to parallel computing and the algorithmic nature of a particular task-specific parallel computing problem. The former is shown in **Figure 5**. One approach to parallel computing, called multi-threading, takes advantage of the extra time required to retrieve data and deliver it to a cache to await a particular computing instruction. On a given computing core, instructions are threaded through the ALU as data become available. It is worth noting that this is not truly parallel computing. Multi-threading is programmed at the level of the standard libraries of a given software language that will most likely relate to a C++ compiled code. The next level of parallelism is to compute on multiple cores on a given processor chip, which is typically referred to as multi-processing and relies on particular software libraries that direct data and instructions to different cores of one or more processor chips on a single mother board. For certain types of computations, using the cores of a GPU is highly advantageous but requires the data be sent to the GPU's on-board memory which may be significantly limited compared to the overall system memory. Light-sheet data thus typically requires some cropping, compression, or thoughtful chunking to be processed on a GPU. Finally, if even more computational power is required, a "master" computer will pass instructions and data to different computing nodes, each operating as independent computers with their own isolated memory, which will execute computations that will be sent back to be compiled by the master node. The "nodes" can be comprised of CPUs and GPUs depending on the nature of the computational task.

It is easiest to implement parallel computing when the nature of the computational step is "embarrassingly parallel," meaning the data can be cleanly and arbitrarily split into convenient sizes to spread across available computational cores and/or nodes. An example of this type of parallel problem would be having many timepoints in a dataset that are each small enough to be handled by a single node. Instances of the image analysis software can be created on as many nodes as available, in the case there are as many nodes as timepoints one could process each time point simultaneously. However, the spatial dimensions of many light-sheet data volumes make it possible that a single time point may not fit on a single workstation or computational node. In this case, one must divide the data into chunks that can fit on a given node (this will also sometimes be the case for fitting data into GPU memory). While the chunk size that is specified by the file structure of the data may be a natural choice, this is not always the case. We again must assess the nature of the parallel problem. For example, convolutional filters that are commonly used in image analysis calculate a new voxel value using voxels surrounding the voxel in question, meaning that the chunks distributed across available nodes or to GPU memory must be overlapping and in some cases how to best recombine the spatial volume is unclear. The overlap has the effect of increasing the overall data size, but if these already exist from tiled acquisition they could be useful.

EVOLUTION OF COMPUTING ENVIRONMENTS FOR LIGHT-SHEET IMAGE VISUALIZATION AND ANALYSIS

Computing hardware components have the potential to be utilized in a light-sheet image processing workflow provided the communication between the parts is supported by the requisite software. **Table 1** provides an overview of the hardware/software solutions employed by several research groups referred to in **Figure 1**, where such details are available in the literature. From these specifications, one can see that light-sheet image

TABLE 1 | Sampling of light-sheet computing environments.

Paper	Data size	Data storage	CPU resources	RAM	GPU resources	Software	File Type	Performance (volume <5 GB)
Huisken et al., 2004	<100 GB	–	1.8 GHz, single-core	–	–	Matlab 6.1		fusing one volume took 24 h
Swoger et al., 2007	–	–	2.8 GHz, dual-core			Matlab 7.0.4, C#		Weiner MVD on one volume overnight
	–	–	10 CPU cluster	20 GB		Python		MAPPG MVD on one volume in 1 h
Keller et al., 2008	3.5 TB	2 RAID 0 (6 TB total storage)	5000 CPU cluster	–	–	Matlab		48 h to track single time-lapse
Preibisch et al., 2010	–	–	2.8 GHz, quad-core	64 GB	–	Java/FIJI		constellation bead-based registration in 2.5 min
Planchon et al., 2011	–	–	–	–	–	Amira 5.3		iterative max liklihood deconv. in 12–15 iterations
Truong et al., 2011	–	–	–	–	–	Matlab, Imaris		–
Tomer et al., 2012	<100 TB	100 TB SATA drives (separate server)	2x 3.3 GHz, 6-core, 12-thread	96 GB	Quadro FX 5800, 4GB	Matlab R2011b, C++		single timepoint fused on a multi-threading core in 180 s
								up to 12 time points in parallel across 12 cores
Wu et al., 2011	˜260 GB	–	–	–	–	Matlab, StarryNite, AceTree		semi-automated C.Elegans lineage tracing
						DeconvolutionLab (ImageJ)		
Wu et al., 2013		–	2.4 GHz, 6-core, 12-thread	6 GB	–	MIPAV, python, matlab		registration, joint deconvolution of 1000 volumes in 7 h
Kumar et al., 2014	–	2 TB SATA drives	2x 2.3 GHz, 6-core, 12-thread	64 GB	Quadro K5000, 4 GB	ImageJ, MIPAV		joint deconvolution 6 volumes/minute
Chen et al., 2014		–	2x 3.33 GHz, 6-core, 12-thread	96 GB	GeForce GTX TITAN, 6 GB	Matlab, CUDA, ImageJ, Amira		deskew, deconvolution, photobleach correction
Preibisch et al., 2014	GB-TB	–	4 node cluster	128 GB	2x Quadro 4000, 2 GB	Java/FIJI, CUDA	.xml/HDF5	Bayesian joint multiview deconvolution
			2x 2.7 GHz, 8-core, 16-thread		4x Tesla			depending on implementation, 1 volume in ≤15 min
Bouchard et al., 2015	–	–	–	–	–	Matlab, Amira		–
Pietzsch et al., 2015	up to 60 GB	750 GB SSD	2.8 GHz, 8-core, 16-thread	16 GB	–	Java 1.6/FIJI	.xml/HDF5	convert 60 GB to .xml/.HDF5 in less than an hour
Royer et al., 2016	–	1 TB SSD, 12 TB HDD	2x 3.1 GHz, 8-core, 16-thread	256 GB				autopilot control, image quality estimations
Liu et al., 2018	3 TB/h	–	cluster, 16-32 cores	120-240 GB	presumed	Matlab, CUDA, FIJI, ITK		deskew, deconvolution, illumination correction,
			per node	per node		ITK-SNAP, Amira, Imaris, Aivia		segmentation of cell, nucleus, and trans-Gogli apparatus
						u-track		cell tracking
Hörl et al., 2019	GB->2TB	RAID 0 SSD	2x 3.2 GHz, 8 core, 16-thread	512 GB	variable	Java/FIJI, CUDA	.xml/HDF5	stitching, fusion of 300 Gb in <9 h

(Continued)

TABLE 1 | (Continued)

Paper	Data size	Data storage	CPU resources	RAM	GPU resources	Software	File Type	Performance (volume <5 GB)
Glaser et al., 2019	˜1 TB	512 GB M.2, 16 TB SSD, 96 TB HDD	2x 3.2 GHz, 8-core, 16-thread	384 GB	Titan XP, 12 GB	python, BigStitcher,	.xml/HDF5 w/ B3D compression, .tiff	1 TB of tiles fused and re-saved 12–24 h
					Quadro P6000, 24 GB	Aivia, Imaris		
Voleti et al., 2019	GB-TB	–	–	–	–	Matlab, BigStitcher, TrackPy	16-bit .tiff	registration, deskew, stitching
Haase et al., 2020	200 MB x 300	–	1.9 GHz, 4-core, 8-thread	–	Intel UHD 6230	FIJI/CLIJ, OpenCL		speed-up of common analysis tasks 2-188X
			2x 2.1 GHz, 8-core, 16-thread	–	Quadro P6000, 24 GB			
Chang et al., 2019	–	2 TB SSD	3.1 GHz, 10-core, 20-thread	128 GB	–	FIJI, Matlab 2017a	OME-TIFF	deconvolution, shearing
Sapoznik et al., 2020	–	16 TB SSD RAID 0	2x 2.2 GHz, 8-core, 16-thread	128 GB	Titan RTX, 24 GB	python (Numpy, Numba) BigStitcher		deskewing, deconvolution on a volume in 125 s

processing has evolved over time from computations executed on a single thread of a single CPU core to computations that can be scheduled in parallel to multiple multi-threaded CPU cores and GPU cores on a single or across several computer nodes. Storage solutions have shifted from uncompressed TIFF files on standard HDDs to multi-resolution chunked pyramid file types with lossless compression on SSDs. These examples are from academic research, but commercial light-sheet acquisition software (e.g., Zeiss Zen) and other image analysis softwares (Imaris, Vision4D, and Amira) have similarly been adapting their computing environments to accommodate larger image data files.

One area that highlights the special difficulties with light-sheet microscopy data is that of multiview image reconstruction. As we have emphasized, there are frequently multiple views of the sample in question that could theoretically be combined in any number of ways. What is especially interesting to biologists is the possibility of increasing the spatial resolution of the resulting image by utilizing information coming from views with complementary spatial frequency information. Computational work toward this goal preceded the first SPIM microscope in a successful attempt to improve widefield fluorescence microscopy resolution by acquisition and fusion of multiple views (Swoger et al., 2003). This work was extended to include deconvolution (Swoger et al., 2007). Deconvolution is a signal processing concept recognizing that any measurement of an object by an instrument is the convolution of the object with the instrument's impulse response. Thus, if one has a measurement of a given instrument's impulse response, one can attempt to computationally recover a higher-resolution version of the object in question by deconvolving the measurement with the impulse response. In the case of a fluorescence microscope, the impulse response is the microscope's point spread function (PSF) which can be theoretically computed and experimentally measured (often from the fluorescent beads embedded with the sample in agarose for fiducial markers) and has its Fourier transform produced counterpart in the frequency domain as the optical transfer function (OTF). This fact is of interest as a convolution in the spatial domain becomes multiplication in the frequency domain, so operations are often less computationally expensive in the frequency domain despite the requisite Fourier transform. A variety of different deconvolution algorithms take different approaches to estimate the underlying image in the spatial domain or frequency domain, often as an iterative process with or without the PSF (as in blind deconvolution algorithms) (Sibarita, 2005).

There have been many efforts to apply these different deconvolution algorithms to light-sheet microscopy data, the simplest of these being ones that deconvolve the individual views prior to fusing the images together. However, due to the computational cost of this approach, even with GPU acceleration, more effort has been made to adapt the iterative steps in these different approaches to incorporate the information from different views in a single joint deconvolution. The Richardson-Lucy (R-L) algorithm has been adapted to switch between one of two orthogonal views as it iterates progressively toward a maximum likelihood estimation of the underlying image, which is implemented in a combination of MATLAB and python

(Wu et al., 2013). Using an unmatched back projector (the function that maps from the measurement to the underlying object) was shown to produce similar results in tenfold fewer iterations (Guo et al., 2020). R-L has also been adapted to a Bayesian/Probabilistic algorithm implemented as a FIJI plugin that can reduce computation time on a CPU by two orders of magnitude when 5 or more views are considered in the estimation (Preibisch et al., 2014). A clever plane-wise deconvolution algorithm allows more efficient GPU acceleration (Schmid and Huisken, 2015). In all implementations, using the views jointly for deconvolution appears to provide superior reconstruction. Whether a more accurate space-variant PSF algorithm would be useful is unclear. Several reports implement spatially varying PSFs that typically are theoretically modeled based on the species of the light-sheet microscope (as the PSF calculation depends on the optics of both the illumination and the detection paths) (Temerinac-Ott et al., 2011; Chen et al., 2018), but these improvements appear to be modest (Becker et al., 2019).

Deep-learning neural networks (DNNs) trained on traditionally deconvolved images have also been used to infer the underlying object in an image (Weigert et al., 2018; Bai et al., 2019; Guo et al., 2020). Once trained, such networks can use basic linear algebra operations to quickly predict a desired outcome. Care must be taken to validate such approaches, however, since training data sets for such models are never comprehensive. Another appealing aspect of this approach, in addition to incomparable computational speed, is that it may no longer be necessary to embed fluorescent beads with specimens (provided a performant non-bead-based registration algorithm is available), which is desirable as it can be difficult to find compatible fluorescent beads for certain clearing solutions and the beads often must be computationally extracted for other visualization and image processing steps.

Deep learning techniques are increasingly popular for light-sheet image analysis and frequently implemented as python scripts utilizing libraries that build on GPU APIs (e.g., PyTorch and TensorFlow). Some examples include detecting bacteria in larval zebrafish intestine with 3D convolutional neural network (CNN) (Hay and Parthasarathy, 2018), puncta segmentation in sub-cellular lattice light-sheet microscopy volumes with 3D-UNET architecture (Schoneberg et al., 2019), high-content screening of mitotic phenotypes in spheroid cultures using diSPIM and deep learning (Eismann et al., 2020), and Deep-SLAM, an add-on device for inverted microscopes for light-sheet imaging and DNN deblurring (Zhao et al., 2020).

TOOL SELECTION PROCESS AND LEARNING TO DRAFT AND TEST IMAGE ANALYSIS PIPELINES

Having discussed the relevant concepts, we now present an outline to follow when drafting and testing light-sheet image analysis pipelines shown in **Figure 6**. The first step in the tool selection process is to understand the size of data that will be generated and to what extent the data can be cropped or compressed without loss of detail relevant to the biological question at hand. The next step is to survey the computational resources that are available and connect with the personnel responsible for maintenance of those resources (IT staff and HPC staff). With information about the limits of computational resources and data size, it is possible to predict if software capable of lazy loading/processing will be required. It is good, if one has familiarity with typical image analysis pipelines, to draft an initial image analysis pipeline with theoretical steps and without committing to any particular software or algorithm. Once the general steps are enumerated from end-to-end, one can search for candidate softwares that can handle the entire pipeline from end-to-end, or more likely, to identify a handful of software packages that best address different components of the pipeline and minimize the amount of data resaving or data wrangling required. In this endeavor, it is useful to pay attention to the quality of customer service if one is searching the commercial software space and assess the developmental trajectory of a given software (is it actively maintained, used by a variety of similar researchers) if searching the open software space. If time allows, it can be beneficial to construct several candidate pipelines to test side-by-side. During this drafting, it will benefit one greatly to keep notes in a lab book or some other documentation on the details of different software, where they are available, how to overcome any installation issues experienced, available details of algorithmic processes and computational performance, specific parameters and step-by-step execution of processing. Ideally during this testing, a manually annotated ground truth is available to quantify the accuracy of a pipeline under slightly different configurations (order of operations) or with different parameters. Without rigorous note-taking, as one would maintain in the wet lab to go back and refer to for troubleshooting, informing future experiments, and communicating results, it is easy to lose track of what has already been tried for a given computational task. Worse, one may strike on a satisfactory pipeline and combination of parameters but fail to record what was the exact implementation that gave such accurate results. Once a reasonable result is produced, write a protocol. Depending on the makeup of a given research group that seeks to utilize light-sheet microscopy data, it is also useful to consider whether collaboration is a more viable option in the case no one in the group is interested in developing the expertise required for light-sheet image analysis. Increasingly more computer scientists are drawn to the specific computational challenges associated with big image data and collaborations with them could lead to interesting new advances. Increasingly more core facilities are harboring light-sheet microscopes and the researchers there may be able to assist on-boarding students, post-docs, and investigators to the field or serve as collaborators themselves.

DISCUSSION

We have presented a high-level overview of computing concepts we find relevant to navigating the existing software available for analysis of light-sheet microscopy data. More detailed information is easily available online and in the cited literature. In

Tool selection process

1. Understand the size of the data needing to be handled.
2. Asses the computational resources at your institution and whether you will need to scale up, scale out, or use a lazy approach.
3. Draft an initial pipeline.
4. Identify candidate software (from industry reps, image.sc, literature).
   a. Read software documentation looking for references to parallel and distributed computing or lazy loading/processing (eg. website, github readme file).
   b. Try software and monitor system resources.
   c. Directly ask the software developers (image.sc, github).
   d. Look at the source code if it's available.
5. Iteratively build and test the image processing pipeline, documenting the work as in a wet lab.
6. If a solution doesn't come together, seek collaborators.

FIGURE 6 | Outline of software tool selection process.

reviewing these concepts, we have also discussed the progression of light-sheet microscopy development from optical hardware to computing hardware and analysis software.

We also want to point out some features to strive for when designing future software solutions, from the end-user's perspective. Many biologists would say it is desirable to have analysis tools that work quickly and easily. This statement is often related to difficulties encountered when installing open source software and difficulties with learning the scope of functionality of a given software that may or may not include some basic scripting/programming. In the recent past, efforts toward providing better support for open source software through receptive developers patiently helping scientists wanting to use their software have been increasing (see image.sc forum), as well as efforts made to create better software documentation and tutorial videos. Communities like the NEUBIAS group, with their seminars broadcast online now, as well as conferences like the Images 2 Knowledge Janelia conference that went virtual during the pandemic, have made quality tutorials more accessible. We hope such efforts will continue and will make it easier for scientists to use and provide feedback to active software development teams. While on one hand end-users can be overwhelmed with too many customizable options and functionality, it is also very powerful to be able to tune parameters interactively with tightly coupled computation and visualization [e.g., FIJI's CLIJ assistant (Haase et al., 2021)]. Having the ability to access/write data stores from a variety of software packages without resaving data would be tremendously useful. Currently, depending on the format and size of the existing data, a search for software solutions is usually confined to those that can handle the data in its existing form. Software that can enumerate memory needs clearly in advance (such as BigStitcher does for some functions) and potentially detect available computing hardware and automatically scale computation up as needed would be very powerful. Alternatively, acquisition systems that can incorporate more processing steps on-the-fly, provided they are clearly described and accepted by the scientific community, could reduce the image and data analysis bottleneck. Rather than collecting a dataset that takes years to analyze, analysis could be finished the same day. Having more application context from instrument and software developers and less hype, with software benchmarked against existing techniques with a variety of standard data sets is also desirable.

From the perspective of developers, it is helpful to enumerate these computational concepts to drive better appreciation among biologists for the need to value software maintenance and to invest in proper analysis pipeline development. Biologists can value these endeavors by citing open-source software, hiring bioimage analysts and including them as authors on papers, and advocating to funding agencies and institutions for support for software maintenance. While we have focused mostly on the world of open-source software solutions for light-sheet image analysis, it will be important to better engage the commercial sector so that more light-sheet specific analysis functions can be incorporated in powerful analysis environments like Imaris and Arivis. It would also be helpful for commercial software to be more compatible with HPC systems.

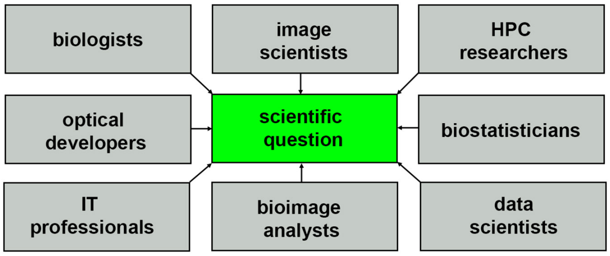

FIGURE 7 | Community of researchers that help to turn light-sheet image data into scientific insight.

The nature of HPC systems will continue to evolve to support composable virtual machines and software containers, driving the need for more diverse communities of researchers with the right expertise to extract biological insights from light-sheet data sets, as shown in **Figure 7**. Incentives for collaborative multidisciplinary research will require more holistic storytelling, and a scientific culture that is more conscientious about sharing credit so that all parties can be equally invested in a multidisciplinary question. Consider how the story of light-sheet microscopy (Siedentopf and Zsigmondy, 1902; Néculcéa, 1903) is told, often focusing on just one name, Zsigmondy, or Siedentopf, chemist and optical physicists, respectively, depending on which field the report is from Masters (2020). Multi-disciplinary science will be benefited by increased tolerance for more nuance and complexity where recognition of scientific contributions is concerned, hopefully resulting in better communication and quicker time to biological insight.

AUTHOR CONTRIBUTIONS

HG and KM devised the figures. HG wrote the initial manuscript and performed all imaging. HG, SMM, NH, AP, SV, SS, AM, AY, AL, DM, KM, and LP provided revisions based on their different expertise. HG, SWM, and AV prepared samples. All authors contributed to the article and approved the submitted version.

FUNDING

This work was supported by the Chan Zuckerberg Initiative through the Silicon Valley Community Foundation (CZI Imaging Scientist Program, 2019-198168), National Institutes of Health (R01 NS088564 and R21 NS109504), and TIRR Foundation.

ACKNOWLEDGMENTS

We would like to acknowledge the Microscopy and Imaging Center and High Performance Research Center at Texas A&M University for providing access to the Zeiss Z.1 light-sheet microscope and computing clusters, respectively. We would also like to thank Bruce Riley and Jennifer Dong for zebrafish care and maintenance.

REFERENCES

AICSImageIO Contributors (2021). *AICSImageIO: Image Reading, Metadata Conversion, and Image Writing for Microscopy Images in Pure Python [Computer software]*. GitHub. Available online at: https://github.com/AllenCellModeling/aicsimageio (accessed October 7, 2021).

Albert-Smet, I., Marcos-Vidal, A., Vaquero, J. J., Desco, M., Muñoz-Barrutia, A., and Ripoll, J. (2019). Applications of Light-Sheet Microscopy in Microdevices. *Front. Neuroanat.* 13:1.

Amat, F., Lemon, W., Mossing, D. P., McDole, K., Wan, Y., Branson, K., et al. (2014). Fast, accurate reconstruction of cell lineages from large-scale fluorescence microscopy data. *Nat. Methods* 11, 951–958. doi: 10.1038/nmeth.3036

Andreev, A., and Koo, D. E. S. (2020). Practical guide to storing large amounts of microscopy data. *Microsc. Today* 28, 42–45. doi: 10.1017/s1551929520001091

Bai, C., Liu, C., Yu, X., Peng, T., Min, J., Yan, S., et al. (2019). Imaging Enhancement of Light-Sheet Fluorescence Microscopy via Deep Learning. *IEEE Photon. Technol. Lett.* 31, 1803–1806. doi: 10.1109/lpt.2019.2948030

Becker, K., Saghafi, S., Pende, M., Sabdyusheva-Litschauer, I., Hahn, C. M., Foroughipour, M., et al. (2019). Deconvolution of light sheet microscopy recordings. *Sci. Rep.* 9:17625.

Bouchard, M. B., Voleti, V., Mendes, C. S., Lacefield, C., Grueber, W. B., Mann, R. S., et al. (2015). Swept confocally-aligned planar excitation (SCAPE) microscopy for high speed volumetric imaging of behaving organisms. *Nat. Phot.* 9, 113–119.

Campagnola, L., Klein, A., Larson, E., Rossant, C., and Rougier, N. (2015). VisPy: Harnessing The GPU For Fast, High-Level Visualization. *Proc. Python Sci. Conf.* 2015:25080. doi: 10.25080/majora-7b98e3ed-00e

Chang, B.-J., Kittisopikul, M., Dean, K. M., Roudot, P., Welf, E. S., and Fiolka, R. (2019). Universal light-sheet generation with field synthesis. *Nat. Methods* 16, 235–238. doi: 10.1038/s41592-019-0327-9

Chen, B.-C., Legant, W. R., Wang, K., Shao, L., Milkie, D. E., Davidson, M. W., et al. (2014). Lattice light-sheet microscopy: imaging molecules to embryos at high spatiotemporal resolution. *Science* 346:1257998.

Chen, Y., Chen, M., Zhu, L., Wu, J. Y., Du, S., and Li, Y. (2018). Measure and model a 3-D space-variant PSF for fluorescence microscopy image deblurring. *Opt. Exp.* 26:14375. doi: 10.1364/oe.26.014375

Crist, J. (2016). Dask & Numba: Simple libraries for optimizing scientific python code. *IEEE Internat. Conf. Big Data* 2016:7840867. doi: 10.1109/bigdata.2016.7840867

Dask Development Team (2016). *Dask: Library for Diynamic Task Scheduling.* Available online at: https://dask.org (accessed October 7, 2021).

Di Battista, D., Merino, D., Zacharakis, G., Loza-Alvarez, P., and Olarte, O. E. (2019). Enhanced Light Sheet Elastic Scattering Microscopy by Using a Supercontinuum Laser. *Methods Protoc.* 2:2030057. doi: 10.3390/mps2030057

Diederich, B., Lachmann, R., Carlstedt, S., Marsikova, B., Wang, H., Uwurukundo, X., et al. (2020). A versatile and customizable low-cost 3D-printed open standard for microscopic imaging. *Nat. Comm.* 11:5979.

Dunsby, C. (2009). Optically Sectioned Imaging by Oblique Plane Microscopy. *Adv. Microsc. Tech.* 2009:7367. doi: 10.1364/ecbo.2009.7367_0h

Eismann, B., Krieger, T. G., Beneke, J., Bulkescher, R., Adam, L., Erfle, H., et al. (2020). Automated 3D light-sheet screening with high spatiotemporal resolution reveals mitotic phenotypes. *J. Cell Sci.* 133:245043. doi: 10.1242/jcs.245043

Fadero, T. C., Gerbich, T. M., Rana, K., Suzuki, A., DiSalvo, M., Schaefer, K. N., et al. (2018). LITE microscopy: Tilted light-sheet excitation of model organisms offers high resolution and low photobleaching. *J. Cell Biol.* 217, 1869–1882. doi: 10.1083/jcb.201710087

Glaser, A. K., Reder, N. P., Chen, Y., Yin, C., Wei, L., Kang, S., et al. (2019). Multi-immersion open-top light-sheet microscope for high-throughput imaging of cleared tissues. *Nat. Commun.* 10:2781.

Guo, M., Li, Y., Su, Y., Lambert, T., Nogare, D. D., Moyle, M. W., et al. (2020). Rapid image deconvolution and multiview fusion for optical microscopy. *Nat. Biotechnol.* 38, 1337–1346. doi: 10.1038/s41587-020-0560-x

Haase, R., Jain, A., Rigaud, S., Vorkel, D., Rajasekhar, P., Suckert, T., et al. (2021). Interactive deisng of GPU-accelerated Image data flow graphs and cross-platform deployment using multi-lingual code generation. *bioRxiv* [Preprint]. doi: 10.1101/2020.11.19.386565v1

Haase, R., Royer, L. A., Steinbach, P., Schmidt, D., Dibrov, A., Schmidt, U., et al. (2020). CLIJ: GPU-accelerated image processing for everyone. *Nat. Methods* 17, 5–6. doi: 10.1038/s41592-019-0650-1

Harris, C. R., Millman, K. J., van der Walt, S. J., Gommers, R., Virtanen, P., Cournapeau, D., et al. (2020). Array programming with NumPy. *Nature* 585, 357–362.

Hay, E. A., and Parthasarathy, R. (2018). Performance of convolutional neural networks for identification of bacteria in 3D microscopy datasets. *PLoS Comput. Biol.* 14:e1006628. doi: 10.1371/journal.pcbi.1006628

Hörl, D., Rojas Rusak, F., Preusser, F., Tillberg, P., Randel, N., Chhetri, R. K., et al. (2019). BigStitcher: reconstructing high-resolution image datasets of cleared and expanded samples. *Nat. Methods* 16, 870–874. doi: 10.1038/s41592-019-0501-0

Huisken, J., and Stainier, D. Y. R. (2007). Even fluorescence excitation by multidirectional selective plane illumination microscopy (mSPIM). *Opt. Lett.* 32, 2608–2610. doi: 10.1364/ol.32.002608

Huisken, J., Swoger, J., Del Bene, F., Wittbrodt, J., and Stelzer, E. H. K. (2004). Optical sectioning deep inside live embryos by selective plane illumination microscopy. *Science* 305, 1007–1009. doi: 10.1126/science.1100035

Keller, P. J., Schmidt, A. D., Wittbrodt, J., and Stelzer, E. H. K. (2008). Reconstruction of Zebrafish Early Embryonic Development by Scanned Light Sheet Microscopy. *Science* 322, 1065–1069. doi: 10.1126/science.1162493

Kumar, A., Wu, Y., Christensen, R., Chandris, P., Gandler, W., McCreedy, E., et al. (2014). Dual-view plane illumination microscopy for rapid and spatially isotropic imaging. *Nat. Protoc.* 9, 2555–2573. doi: 10.1038/nprot.2014.172

Kumar, M., Kishore, S., Nasenbeny, J., McLean, D. L., and Kozorovitskiy, Y. (2018). Integrated one- and two-photon scanned oblique plane illumination (SOPi) microscopy for rapid volumetric imaging. *Opt. Express* 26, 13027–13041. doi: 10.1364/oe.26.013027

Lein, E. S., Hawrylycz, M. J., Ao, N., Ayres, M., Bensinger, A., Bernard, A., et al. (2007). Genome-wide atlas of gene expression in the adult mouse brain. *Nature* 445, 168–176.

Liu, T.-L., Upadhyayula, S., Milkie, D. E., Singh, V., Wang, K., Swinburne, I. A., et al. (2018). Observing the cell in its native state: Imaging subcellular dynamics in multicellular organisms. *Science* 360:1392. doi: 10.1126/science.aaq1392

Masters, B. R. (2020). Richard Zsigmondy and Henry Siedentopf's Ultramicroscope. *Spr. Ser. Opt. Sci.* 2020, 165–172. doi: 10.1007/978-3-030-21691-7_10

Matryba, P., Kaczmarek, L., and Golab, J. (2019). Advances in ex situ tissue optical clearing. *Laser Phot. Rev.* 13:1800292. doi: 10.1002/lpor.201800292

McCreedy, D. A., Jalufka, F. L., Platt, M. E., Min, S. W., Kirchoff, M. A., Pritchard, A. L., et al. (2021). Passive clearing and 3D lightsheet imaging of intact and injured spinal cord in mice. *Front. Cell Neurosci.* 15:684792.

Moore, J., Allan, C., Besson, S., Burel, J.-M., Diel, E., Gault, D., et al. (2021). OME-NGFF: scalable format strategies for interoperable bioimaging data. *BioRxiv* 2021:437929. doi: 10.1101/2021.03.31.437929

Napari Contributors (2019). *Napari: A Multi-Dimensional Image Viewer for Python.* Available online at: https://doi.org/10.5281/zenodo.3555620 (accessed October 7, 2021).

Néculcéa, E. (1903). II. SIEDENTOPF et R. ZSIGMONDY. — Ueber Sichtbarmachung ultramikroskopischer Teilchen, mit besonderer Anwendung auf Goldrubingläser (Méthode permettant de voir les particules ultramicroscopiques et d'en évaluer les dimensions; application spéciale aux verres rubis à l′or). — Drude's Annalen der Physik, t. X, p. 1-39. *J. de Physique Théorique et Appliquée* 2, 692–702. doi: 10.1051/jphystap:019030020069201

Peng, H., Bria, A., Zhou, Z., Iannello, G., and Long, F. (2014). Extensible visualization and analysis for multidimensional images using Vaa3D. *Nat. Protoc.* 9, 193–208. doi: 10.1038/nprot.2014.011

Pietzsch, T., Preibisch, S., Tomančák, P., and Saalfeld, S. (2012). ImgLib2—generic image processing in Java. *Bioinformatics* 28, 3009–3011. doi: 10.1093/bioinformatics/bts543

Pietzsch, T., Saalfeld, S., Preibisch, S., and Tomancak, P. (2015). BigDataViewer: visualization and processing for large image data sets. *Nat. Methods* 12, 481–483. doi: 10.1038/nmeth.3392

Pitrone, P. G., Schindelin, J., Stuyvenberg, L., Preibisch, S., Weber, M., Eliceiri, K. W., et al. (2013). OpenSPIM: an open-access light-sheet microscopy platform. *Nat. Methods* 10, 598–599. doi: 10.1038/nmeth.2507

Planchon, T. A., Gao, L., Milkie, D. E., Davidson, M. W., Galbraith, J. A., Galbraith, C. G., et al. (2011). Rapid three-dimensional isotropic imaging of living cells using Bessel beam plane illumination. *Nat. Methods* 8, 417–423. doi: 10.1038/nmeth.1586

Power, R. M., and Huisken, J. (2019). Putting advanced microscopy in the hands of biologists. *Nat. Methods* 16, 1069–1073. doi: 10.1038/s41592-019-0618-1

Preibisch, S., Amat, F., Stamataki, E., Sarov, M., Singer, R. H., Myers, E., et al. (2014). Efficient Bayesian-based multiview deconvolution. *Nat. Methods* 11, 645–648. doi: 10.1038/nmeth.2929

Preibisch, S., Saalfeld, S., Schindelin, J., and Tomancak, P. (2010). Software for bead-based registration of selective plane illumination microscopy data. *Nat. Methods* 7, 418–419. doi: 10.1038/nmeth0610-418

Reynaud, E. G., Peychl, J., Huisken, J., and Tomancak, P. (2015). Guide to light-sheet microscopy for adventurous biologists. *Nat. Methods* 12, 30–34. doi: 10.1038/nmeth.3222

Richardson, D. S., and Lichtman, J. W. (2015). Clarifying Tissue Clearing. *Cell* 162, 246–257. doi: 10.1016/j.cell.2015.06.067

Royer, L. A., Lemon, W. C., Chhetri, R. K., Wan, Y., Coleman, M., Myers, E. W., et al. (2016). Adaptive light-sheet microscopy for long-term, high-resolution imaging in living organisms. *Nat. Biotechnol.* 34, 1267–1278. doi: 10.1038/nbt.3708

Saalfeld, S., Cardona, A., Hartenstein, V., and Tomancak, P. (2009). CATMAID: collaborative annotation toolkit for massive amounts of image data. *Bioinformatics* 25, 1984–1986. doi: 10.1093/bioinformatics/btp266

Sapoznik, E., Chang, B.-J., Huh, J., Ju, R. J., Azarova, E. V., Pohlkamp, T., et al. (2020). A versatile oblique plane microscope for large-scale and high-resolution imaging of subcellular dynamics. *Elife* 9:57681. doi: 10.7554/eLife.57681

Schmid, B., and Huisken, J. (2015). Real-time multi-view deconvolution. *Bioinformatics* 31, 3398–3400. doi: 10.1093/bioinformatics/btv387

Schoneberg, J., Raghupathi, G., Betzig, E., and Drubin, D. (2019). 3D Deep Convolutional Neural Networks in Lattice Light-Sheet Data Puncta Segmentation. *IEEE Internat. Conf. Bioinform. Biomed.* 2019:8983012. doi: 10.1109/bibm47256.2019.8983012

Sibarita, J.-B. (2005). Deconvolution microscopy. *Adv. Biochem. Eng. Biotechnol.* 95, 201–243.

Siedentopf, H., and Zsigmondy, R. (1902). Uber sichtbarmachung und Größenbestimmung ultramikoskopischer† teilchen, mit besonderer anwendung auf Goldrubingläser. *Ann. Phys.* 315, 1–39.

Stegmaier, J., Amat, F., Lemon, W. C., McDole, K., Wan, Y., Teodoro, G., et al. (2016). Real-Time Three-Dimensional Cell Segmentation in Large-Scale Microscopy Data of Developing Embryos. *Dev. Cell* 36, 225–240. doi: 10.1016/j.devcel.2015.12.028

Swaney, J., Kamentsky, L., Evans, N. B., Xie, K., Park, Y.-G., Drummond, G., et al. (2019). Scalable image processing techniques for quantitative analysis of volumetric biological images from light-sheet microscopy. *bioRxiv* doi: 10.1101/576595

Swoger, J., Huisken, J., and Stelzer, E. H. K. (2003). Multiple imaging axis microscopy improves resolution for thick-sample applications. *Opt. Lett.* 28, 1654–1656. doi: 10.1364/ol.28.001654

Swoger, J., Verveer, P., Greger, K., Huisken, J., and Stelzer, E. H. K. (2007). Multi-view image fusion improves resolution in three-dimensional microscopy. *Opt. Express* 15, 8029–8042. doi: 10.1364/oe.15.008029

Taha, A. A., and Hanbury, A. (2015). Metrics for evaluating 3D medical image segmentation: analysis, selection, and tool. *BMC Med. Imag.* 15:68. doi: 10.1186/s12880-015-0068-x

Temerinac-Ott, M., Ronneberger, O., Nitschke, R., Driever, W., and Burkhardt, H. (2011). Spatially-variant Lucy-Richardson deconvolution for multiview fusion of microscopical 3D images. *IEEE Internat. Symp. Biomed. Imag.* 2011:5872549. doi: 10.1109/isbi.2011.5872549

Tischer, C., Ravindran, A., Reither, S., Chiaruttini, N., Pepperkok, R., and Norlin, N. (2021). BigDataProcessor2: A free and open-source Fiji plugin for inspection and processing of TB sized image data. *Bioinformatics* 2021:106. doi: 10.1093/bioinformatics/btab106

Tomer, R., Khairy, K., Amat, F., and Keller, P. J. (2012). Quantitative high-speed imaging of entire developing embryos with simultaneous multiview light-sheet microscopy. *Nat. Methods* 9, 755–763. doi: 10.1038/nmeth.2062

Truong, T. V., Supatto, W., Koos, D. S., Choi, J. M., and Fraser, S. E. (2011). Deep and fast live imaging with two-photon scanned light-sheet microscopy. *Nat. Methods* 8, 757–760. doi: 10.1038/nmeth.1652

Ueda, H. R., Erturk, A., Chung, K., Gradinaru, V., Chedotal, A., Tomancak, P., et al. (2020). Tissue clearing and its applications in neuroscience. *Nat. Rev. Neurosci.* 21, 61–79. doi: 10.1038/s41583-019-0250-1

Vettenburg, T., Dalgarno, H. I. C., Nylk, J., Coll-Lladó, C., Ferrier, D. E. K., Čižmár, T., et al. (2014). Light-sheet microscopy using an Airy beam. *Nat. Methods* 11, 541–544. doi: 10.1038/nmeth.2922

Voie, A. H., Burns, D. H., and Spelman, F. A. (1993). Orthogonal-plane fluorescence optical sectioning: three-dimensional imaging of macroscopic biological specimens. *J. Microsc.* 170, 229–236. doi: 10.1111/j.1365-2818.1993.tb03346.x

Voleti, V., Li, W., Greaney, M., Lacefield, C., Schoppik, D., Bruno, R., et al. (2016). SCAPE microscopy for high-speed volumetric functional imaging of the awake, behaving brain. *Biomed. Optics* 2016:3. doi: 10.1364/brain.2016.btu2d.3

Voleti, V., Patel, K. B., Li, W., Campos, C. P., Bharadwaj, S., Yu, H., et al. (2019). Real-time volumetric microscopy of in vivo dynamics and large-scale samples with SCAPE 2.0. *Nat. Methods* 16, 1054–1062. doi: 10.1038/s41592-019-0579-4

Wan, Y., McDole, K., and Keller, P. J. (2019). Light-Sheet Microscopy and Its Potential for Understanding Developmental Processes. *Annu. Rev. Cell Dev. Biol.* 35, 655–681.

Weigert, M., Schmidt, U., Boothe, T., Müller, A., Dibrov, A., Jain, A., et al. (2018). Content-aware image restoration: pushing the limits of fluorescence microscopy. *Nat. Methods* 15, 1090–1097. doi: 10.1038/s41592-018-0216-7

Wolff, C., Tinevez, J.-Y., Pietzsch, T., Stamataki, E., Harich, B., Guignard, L., et al. (2018). Multi-view light-sheet imaging and tracking with the MaMuT software reveals the cell lineage of a direct developing arthropod limb. *Elife* 7:34410. doi: 10.7554/eLife.34410

Wu, Y., Ghitani, A., Christensen, R., Santella, A., Du, Z., Rondeau, G., et al. (2011). Inverted selective plane illumination microscopy (iSPIM) enables coupled cell identity lineaging and neurodevelopmental imaging in Caenorhabditis elegans. *Proc. Natl. Acad. Sci. U. S. A.* 108, 17708–17713. doi: 10.1073/pnas.1108494108

Wu, Y., Kumar, A., Smith, C., Ardiel, E., Chandris, P., Christensen, R., et al. (2017). Reflective imaging improves spatiotemporal resolution and collection efficiency in light sheet microscopy. *Nat. Commun.* 8:1452.

Wu, Y., Wawrzusin, P., Senseney, J., Fischer, R. S., Christensen, R., Santella, A., et al. (2013). Spatially isotropic four-dimensional imaging with dual-view plane illumination microscopy. *Nat. Biotechnol.* 31, 1032–1038. doi: 10.1038/nbt.2713

Zhao, F., Zhu, L., Fang, C., Yu, T., Zhu, D., and Fei, P. (2020). Deep-learning super-resolution light-sheet add-on microscopy (Deep-SLAM) for easy isotropic volumetric imaging of large biological specimens. *Biomed. Opt. Express* 11, 7273–7285. doi: 10.1364/boe.409732

Conflict of Interest: The authors declare that the research was conducted in the absence of any commercial or financial relationships that could be construed as a potential conflict of interest.

frontiers
in Cell and Developmental Biology

ORIGINAL RESEARCH
published: 17 December 2021
doi: 10.3389/fcell.2021.738786

Assessing Phototoxicity in a Mammalian Cell Line: How Low Levels of Blue Light Affect Motility in PC3 Cells

Rana A. Alghamdi[1,2], *Marino Exposito-Rodriguez*[2,3], *Philip M. Mullineaux*[2], *Greg N. Brooke*[2] *and Philippe P. Laissue*[2]*

[1]*Department of Chemistry, Science and Arts College, Rabigh Campus, King Abdulaziz University, Jeddah, Saudi Arabia,* [2]*School of Life Sciences, University of Essex, Colchester, United Kingdom,* [3]*Sainsbury Laboratory, University of Cambridge, Cambridge, United Kingdom*

Phototoxicity is a significant constraint for live cell fluorescence microscopy. Excessive excitation light intensities change the homeostasis of the observed cells. Erroneous and misleading conclusions may be the problematic consequence of observing such light-induced pathophysiology. In this study, we assess the effect of blue light, as commonly used for GFP and YFP excitation, on a motile mammalian cell line. Tracking PC3 cells at different light doses and intensities, we show how motility can be used to reliably assess subtle positive and negative effects of illumination. We further show that the effects are a factor of intensity rather than light dose. Mitotic delay was not a sensitive indicator of phototoxicity. For early detection of the effect of blue light, we analysed the expression of genes involved in oxidative stress. This study addresses the need for relatively simple and sensitive methods to establish a dose-response curve for phototoxicity in mammalian cell line models. We conclude with a working model for phototoxicity and recommendations for its assessment.

Keywords: fluorescence, microscopy—light, live imaging, reactive oxygen species (ROS), light intensity (irradiance)

Edited by:
Michelle S. Itano,
University of North Carolina at Chapel Hill, United States

Reviewed by:
Yonggeun Hong,
Inje University, South Korea
Ejaz Ahmad,
Michigan Medicine, University of Michigan, United States

***Correspondence:**
Philippe P. Laissue
plaissue@essex.ac.uk

Specialty section:
This article was submitted to Cell Growth and Division, a section of the journal Frontiers in Cell and Developmental Biology

Received: *09 July 2021*
Accepted: *16 November 2021*
Published: *17 December 2021*

Citation:
Alghamdi RA, Exposito-Rodriguez M, Mullineaux PM, Brooke GN and Laissue PP (2021) Assessing Phototoxicity in a Mammalian Cell Line: How Low Levels of Blue Light Affect Motility in PC3 Cells. Front. Cell Dev. Biol. 9:738786. doi: 10.3389/fcell.2021.738786

INTRODUCTION

Phototoxicity in Live Fluorescence Microscopy

In the context of live fluorescence microscopy, phototoxicity describes the phenomenon by which the light used for fluorescence excitation leads to physiological changes in the observed living sample, be that single cells in culture or a multicellular organism such as a zebrafish. With the excitation light intensities widely used in fluorescence microscopy, these physiological changes are often severe and detrimental and may lead to significant alterations in the biochemistry, physiology and dynamic behaviour of the observed sample. It is also possible that, when observing physiological processes for the first time, more subtle phototoxic effects may go unnoticed as the unperturbed activity is unknown. In either case, the conclusions drawn from these observations could be erroneous and, more dangerously, misleading—since we are not observing a living sample in homeostasis, but documenting the light-induced pathophysiological changes caused by the microscopy method.

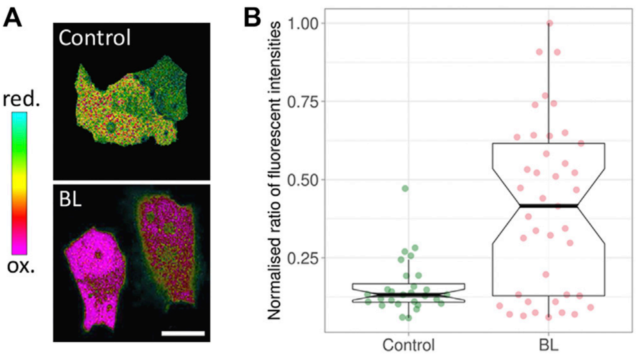

FIGURE 1 | Response of HyPer, a ratiometric hydrogen peroxide biosensor. **(A)** Green Monkey Kidney cells containing HyPer. The control cells (top) were not exposed to blue light prior to taking the ratiometric image, while the cells at the bottom were imaged immediately after being exposed to 77 mW/cm^2 for 5 minutes of blue light (BL). The noted oxidation state indicates the presence of H_2O_2. **(B)** The corresponding box plots. BL: blue light. The middle line in the box represents the median value. Modified from (Alghamdi, 2017).

Reactive Oxygen Species in Phototoxicity

A key factor of phototoxicity is the generation of free radicals—reactive chemical species with a single unpaired electron in an outer orbit (Riley, 1994; Greenbaum et al., 2000; Dröge, 2002; Redmond and Kochevar, 2006). This unstable configuration promotes reactions with adjacent molecules such as lipids, carbohydrates, and nucleic acids. The majority of free radicals relevant to photodamage are reactive oxygen species (ROS) (Diaspro et al., 2006; Laloi and Havaux, 2015; Kiepas et al., 2020). Several ROS species exist, such as superoxide, hydroxyl and hydrogen peroxide. To demonstrate the generation of hydrogen peroxide upon blue light illumination (**Figure 1**), a mammalian cell line was transfected with HyPer, a ratiometric biosensor for hydrogen peroxide (Belousov et al., 2006; Markvicheva et al., 2011). The ratio changed immediately after illuminating at a low intensity of 77 mW/cm^2 for 5 minutes, with the HyPer signal increasing towards the oxidative state (**Figure 1**; Alghamdi, 2017). The generation of ROS using blue light has been shown in other cell types (Seko et al., 2001; Dixit and Cyr, 2003; Becker et al., 2016; Icha et al., 2017; Yuan et al., 2017).

ROS are important signalling molecules and play key roles in many physiological and pathological processes: stress response, apoptosis, activation of signal cascades, gene expression changes, normal development and regulation of lifespan (Cadenas and Davies, 2000; Hancock et al., 2001; Poli et al., 2004). Intensity and duration of the exposure to ROS determines their effect on a given cell. ROS are a product of normal cellular functioning, but excessive amounts can cause deleterious effects. While low concentrations of ROS can be buffered by the cell without damaging it, they may trigger a stress response. A cell may delay or exit the cell cycle and enter into G0 upon expression of cyclin-dependent kinase inhibitors. At higher levels, ROS directly react with such inhibitors, leading to DNA and mitochondrial damage, oxidation of amino acids in nearby proteins, lipid peroxidation, and inactivation of specific enzymes, often resulting in apoptosis (Laloi and Havaux, 2015; Mullineaux et al., 2018).

Parameters for Assessing Phototoxicity

Phototoxicity depends on many different factors, ranging from sample type, developmental stage, localization of the fluorescent protein(s) or dye(s) and media to excitation wavelength(s), microscopy method and the precise image acquisition parameters (Laissue et al., 2017). For this study, the key parameters we consider (as shown in **Table 1**) are 1) the physico-optical parameters on the side of the fluorescence excitation, and 2) the biological readouts used to assess phototoxic effects. Physical parameters comprise the power of the excitation light (in mW), the intensity of the excitation light (i.e., the power per area, also known as irradiance or surface power density and in this study measured in mW/cm^2), the time the sample is exposed to the excitation light (i.e., the exposure time) measured in seconds (or minutes or hours) and the total light dose (defined as the product of power and exposure time) measured in mJ.

Biological Readouts of Phototoxicity: Morphology, Dynamics and Gene Expression

A crucial consideration for imaging live cells is how to assess phototoxicity in a given sample. Different approaches have been used and greatly vary in their sensitivity. Readouts range from viability (live/dead cells) and cellular morphology on the rather blunt end of the assessment criteria spectrum to the dynamics of a biological process and gene expression on the sensitive readout end.

In this study, we use a sensitive and straight-forward method to establish a dose-response curve for phototoxicity in mammalian cell line models. Specifically, we assess the effect of blue light, as commonly used for GFP and YFP excitation, on a motile mammalian cell line. Phototoxic effects are measured using a sensitive dynamic process, showing that motility can be used to reliably assess subtle positive and negative effects of illumination. For highly sensitive detection of the effect of blue light, we analysed the expression of genes involved in oxidative stress.

RESULTS

Blue Light has Intensity-Dependent Positive and Negative Effects on PC3 Motility

We acquired images of motile, fluorescent PC3-GFP cells (the prostate cancer cell line PC3, stably transfected with a GFP expression vector) in large fields-of-view (FOVs) over 24 h (**Figure 2A**) at different excitation light intensities and exposure times. Within a given condition, cell motility varied considerably between measured cells; an example is shown in **Figure 2B**, with median speeds ranging from 0.67 nm/s (blue

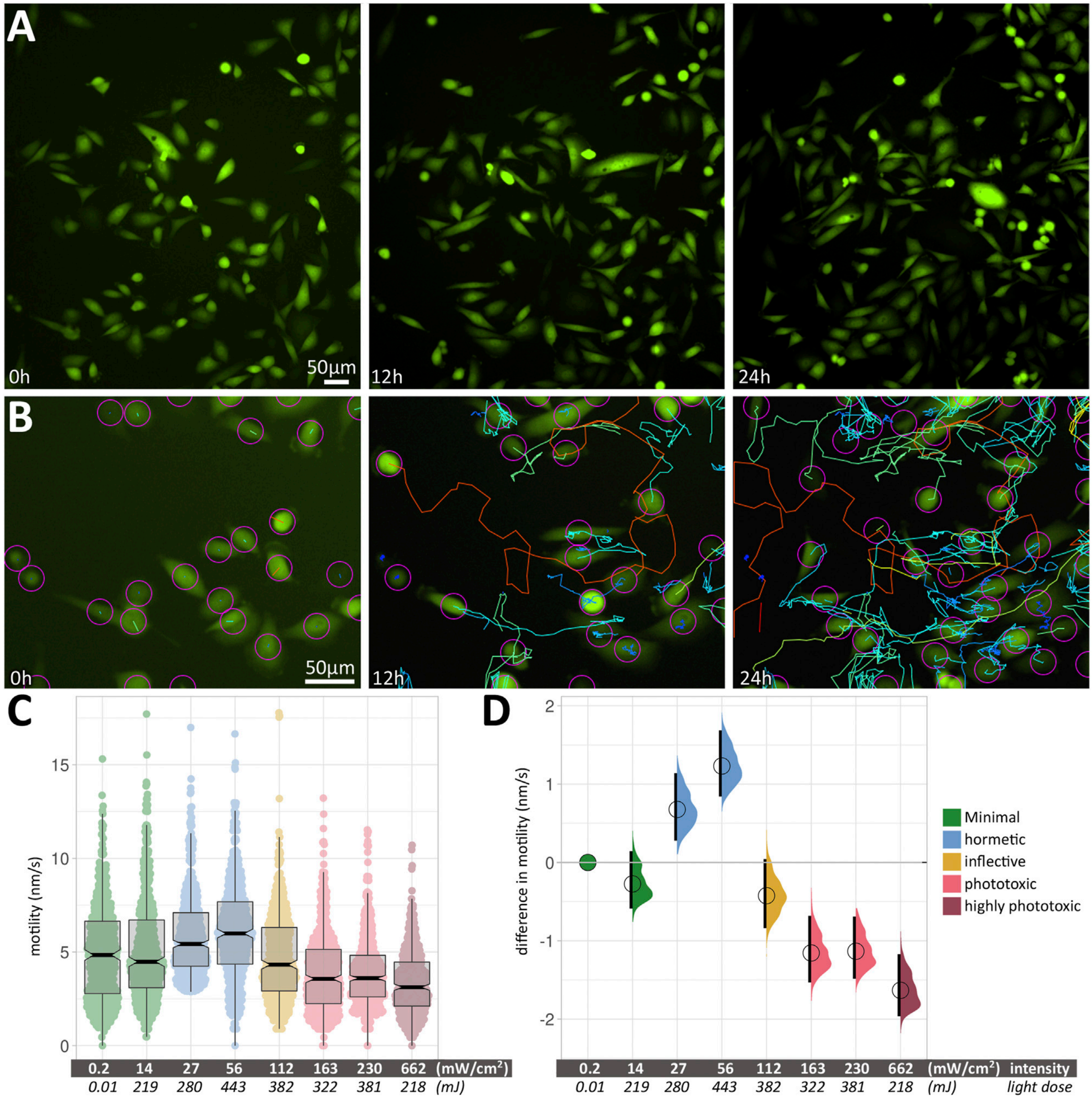

FIGURE 2 | (A) Large field-of-view of fluorescent PC3 cells from a 24 h time-lapse movie. Three images from timepoints 0, 12 and 24 h change the appearance due to the displacement of motile cells. **(B)** An example of the automated cell tracking used to determine cell speeds. As in **(A)**, three images from timepoints 0, 12 and 24 h are shown, along with colour-coded tracks. Blue and green tracks show low speeds around 1–5 nm/s, while orange to red tracks shows fast-moving cells at around 12–15 nm/s. **(C)** Box plots of cell motility at different intensities. The *Y* axis shows cell motility, measured in nm/s. Within each box (interquartile range), the thick black line shows the median speed for each condition, and indentations depict its 95% compatibility interval. The data points used to produce the box plots are overlaid in colour. **(D)** Relative differences in motility between conditions are shown as relative effect sizes. Data points and effect sizes share the same colour-coding depicted in the legend inset in **Figure 2C**. The difference between median values is determined relative to the green minimal-intensity conditions and indicated with a circle. The compatibility interval is derived from the bootstrap distribution and indicated with the black vertical bars. See **Supplementary Table S1** for 95% CI and *p*-values.

tracks) to 24.12 nm/s (red tracks). The median speeds of 500 cells were measured for each experimental condition. **Figure 2C** shows the box plots of cell motility at different intensities. Thick black lines show the median speed for each condition, and indentations in the box depict its 95% compatibility interval (CI). Green signifies minimal intensity conditions, where 0.2 mW/cm^2 was obtained using brightfield illumination without fluorescence excitation, providing a least-invasive base line speed. 14 mW/

cm^2 was used for minimally invasive fluorescence excitation with blue light (480 ± 30 nm). This intensity was doubled twice (27 and 56 mW/cm^2, respectively), leading to increased cell motility (blue). Further doubling (112 mW/cm^2) reduces the cell speed again (yellow) to a level close to the minimally invasive speed. Increasing intensities further (163, 230 and 662 mW/cm^2) lead to a significant reduction in median cell speeds (light red/dark red).

The corresponding relative differences in motility between conditions are shown in **Figure 2D** as relative effect sizes (Goedhart, 2019) and clearly show positive and negative effects of blue light excitation on PC3-GFP cell motility. Data points and effect sizes share the same colour-coding depicted in the legend inset in **Figure 2C** Experimental conditions and statistical parameters are summarised in **Supplementary Table S1**.

Intensity, Not Total Light Dose, Determines the Effect of Blue Light on Cell Motility

A pivotal finding was that the effect of blue light on cell motility scales with intensity (mW/cm^2), not total light dose (mJ). Grouping median speeds according to intensity showed a clear biphasic response (**Figures 2C,D**), with an initial positive effect (increased cell motility) followed by a negative one (reduced cell motility). Conversely, total light dose cannot be used to explain the observed patterns, as nearly identical light doses of 219 and 218 mJ had drastically different effects on cell motility. A similar difference in response can be seen at nearly identical light doses of 382 and 381 mJ, where the lower intensity has a hormetic effect, while the higher intensity leads to a significantly reduced speed.

We used non-fluorescent brightfield microscopy (with differential interference contrast (DIC) for optical contrast). Since no fluorescence, and hence no blue light illumination, was used in this condition, it provided a non-invasive baseline for all following experiments. For the first fluorescence condition, we used very low intensity (14 mW/cm^2). Long exposure times were needed to collect sufficient light for acceptable image contrast. This condition led to a slight, but non-significant decrease in cell motility compared to the non-invasive baseline. Doubling that initial low blue light intensity twice (i.e., 27 and 56 mW/cm^2, respectively) led to a significant increase in cell motility. This positive effect was surprising, since hormesis has not been attributed to the short wavelengths used here (465–495 nm).

The Intensity-Dependent Effect on Motility Increases With the Duration of the Observation

We grouped the effect of blue light on cell motility scales according to the duration of the time-lapse recording of PC3-GFP cells with blue light at different intensities (**Figure 3**, **Supplementary Table S2**). The differences between 6, 12 and 24 h at low intensity (14 mW/cm^2) were not significant. At medium intensity (112 mW/cm^2), a small hormetic trend was visible with increasing exposure time. The two significant reductions in motility (after 12 and 24 h) were seen at high intensity (230 mW/cm^2).

Mitotic Delay Does Not Robustly Identify Phototoxic Effects

We next used mitotic delay as a biological readout to check for phototoxicity (**Figure 4**, **Supplementary Table S3**). The duration of mitoses was measured in multiple cells from start (the rounding of a cell) to end (cytokinesis of the two newly formed cells), with an image taken every 15 min for 24 h. Examples at low and high intensities are shown in **Figure 4A**. At low intensity (14 mW/cm^2), the PC3 cell shown here took 60 min from rounding up to cytokinesis (indicated by "mitosis" bracket). At high intensity (230 mW/cm^2), the process took 115 min in the cell shown. However, the statistical analysis used did not detect a significant increase in mitotic delay at higher intensities, as boxplots reveal (**Figure 4B**). Using effect sizes, the differences between the low intensity baseline **Figure 4C**, green circle and horizontal line) and subsequent median values (circles) show an increase with higher intensities. However, the 95% compatibility intervals (CI) (**Figure 4C**, black vertical bars) never rise above the low intensity baseline. Corresponding *p*-values are 0.299 or higher (**Supplementary Table S3**). Consequently, it can be neither concluded nor excluded that the higher intensities used here lead to mitotic delay.

PC3 Cell Motility Does Not Show an Effect of Short-Term Blue Light Illumination at Moderate Intensity

We next wanted to find out if short, continuous exposure to blue light at moderate intensity would result in an effect on cell motility. We subjected cells to 112 mW/cm^2 blue light intensity, continuously for 2 minutes. This had no measurable effect on cell motility in PC3-GFP cells measured non-invasively over the following 24 h (**Figure 5**, **Supplementary Table S4**).

Gene Expression Shows a Clear Effect of Short-Term Blue Light Illumination at Moderate Intensity

We wanted to examine whether short exposures to a moderate intensity of blue light (as used in **Figure 5**, **Supplementary Table S4**) were measurable using a more sensitive readout compared to cell motility. We used RT-qPCR to determine the effect of blue light illumination upon the transcription of a panel of genes known to be important in ROS signalling (SAB target list H384 (Leone et al., 2017)). Since the generation of H_2O_2 is a direct result of blue light illumination [see above, **Figure 1** (Alghamdi, 2017)], we chose genes that are important in the antioxidant response: *SOD3, CCS, DUSP1, PRDX1, PRDX2, NQO1*, and *GPX1*. These genes, their roles and the reference genes used are detailed in **Supplementary Table S5**. In these genes, a time- and dose-dependent response to illumination was evident (**Figure 6**). At the 1 h time point, SOD3 was the main

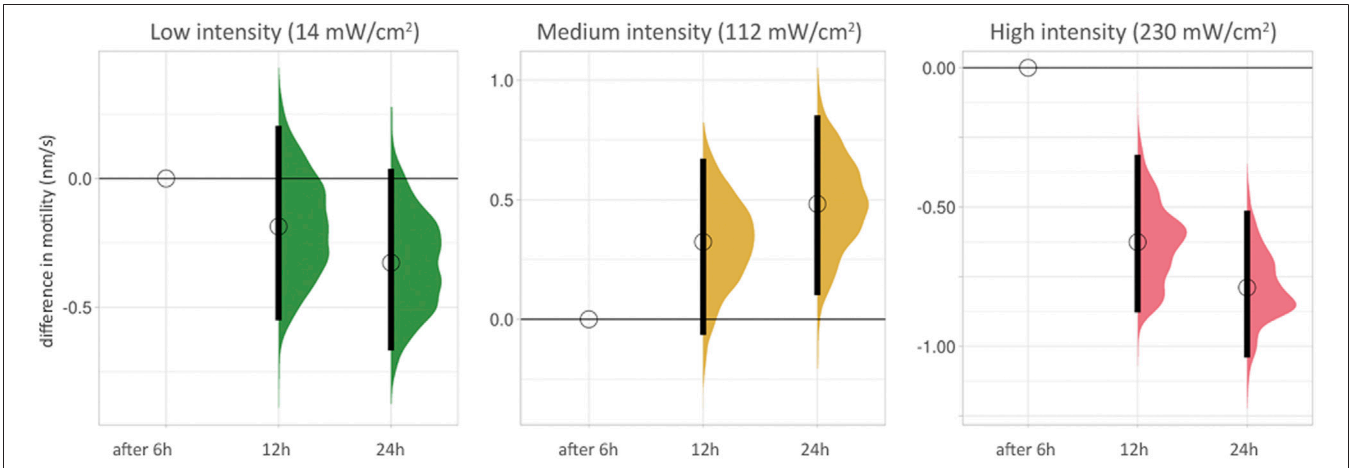

FIGURE 3 | Cell motility after increasing duration of time-lapse recordings for low, medium and high intensity blue light illumination. The lowest duration (6 h) is used as baseline for each condition. The difference between median values is determined relative to the 6 h value for each condition and indicated with a circle. 95% compatibility intervals are indicated by black vertical bars. The differences between 6, 12 and 24 h at low intensity (14 mW/cm^2, green, left side) are not significant (see also **Supplementary Table S2**). At medium intensity (112 mW/cm^2, yellow, middle), a small hormetic trend appears with increasing exposure time. The two significant reductions in motility (after 12 and 24 h) are seen at high intensity (230 mW/cm^2, red, right side).

up-regulated gene in response to illumination. At 6 h, all candidate genes were found to be up-regulated. In decreasing order of fold-changes, the expression of SOD3, CCS, DUSP1, PRDX2, PRDX1, NQO1, and GPX1 increased with higher light intensity. The transcription levels of all genes were subsequently lower 12 h post illumination.

DISCUSSION

Phototoxicity Scales With Intensity, Not Light Dose

Two different approaches have commonly been used to reduce the phototoxic effects of fluorescence excitation. The first consists of lowering exposure times and increasing excitation intensity (Swedlow et al., 2009; Ettinger and Wittmann, 2014; Douthwright and Sluder, 2016). The second, converse approach favours increasing exposure times while lowering excitation intensity (Dixit and Cyr, 2003; Magidson and Khodjakov, 2013; Icha et al., 2017; Kiepas et al., 2020). Our data presented here clearly agree with the latter approach.

Different Intensities of Blue Light Cause Hormetic or Negative Effects on PC3-GFP Cell Motility

Blue light is known to reduce motility in single cells (Mubaid and Brown, 2017; Kiepas et al., 2020). Knoll and coworkers showed that excitation at 540–585 nm, at a low intensity of 1.25 mW/cm^2 over 60 s (resulting in 75 mJ/cm^2), leads to rapid cytoskeletal force relaxation (Knoll et al., 2015). On the basis of these findings, we expected the blue light used in this study to have a purely negative effect on cell motility, leading to a decrease in their median speed. Here we show that the effect of blue light (480 ± 30 nm) on PC3 cell motility is biphasic (**Figure 2**, **Table 2**). Compared to a no-effect level at low intensity (14 mW/cm^2), an increase in intensity (27 and 56 mW/cm^2) leads to increased cell motility. An inflection point was found at moderate intensity (112 mW/cm^2), after which higher intensities (163, 230 and 662 mW/cm^2) cause a significant reduction in motility.

Hormetic effects have been described for longer wavelengths, e.g., in the case of low-level laser therapy in the 600–700 nm range (AlGhamdi et al., 2015), but not for the shorter wavelengths used here. Longer wavelengths in the visible range have consistently been shown to be less damaging than shorter blue ones (Schneckenburger et al., 2012; Wäldchen et al., 2015; Douthwright and Sluder, 2016; Icha et al., 2017; Kilian et al., 2018). However, blue light (which we here define as ranging from around 440–500 nm) is still widely used in fluorescence microscopy, and it is unrealistic to expect that, simply due to their potentially damaging effect, excitation wavelengths below 500 nm will be avoided in the future. Many GFP-derived labels exist and are being routinely used (Remington, 2011; Rodriguez et al., 2017), so it is important to understand the effect that blue light illumination can have on mammalian cell lines (Carlton et al., 2010; Wäldchen et al., 2015; Douthwright and Sluder, 2016; Icha et al., 2017; Laissue et al., 2017).

Mitotic Delay Is a Sparser and Less Sensitive Readout Compared to Motility

The timing of mitosis has been proposed as an ideal measure of imaging-related stress on cells (Cole, 2014). However, for the experimental setup presented here, it is a less reliable readout compared to cellular motility. While measurement of the latter was able to pick up subtle differences caused by small variations in intensity, these were missed using the timing of mitosis as a biological readout. The data are too dispersed to allow robust conclusions. More mitoses would need to be

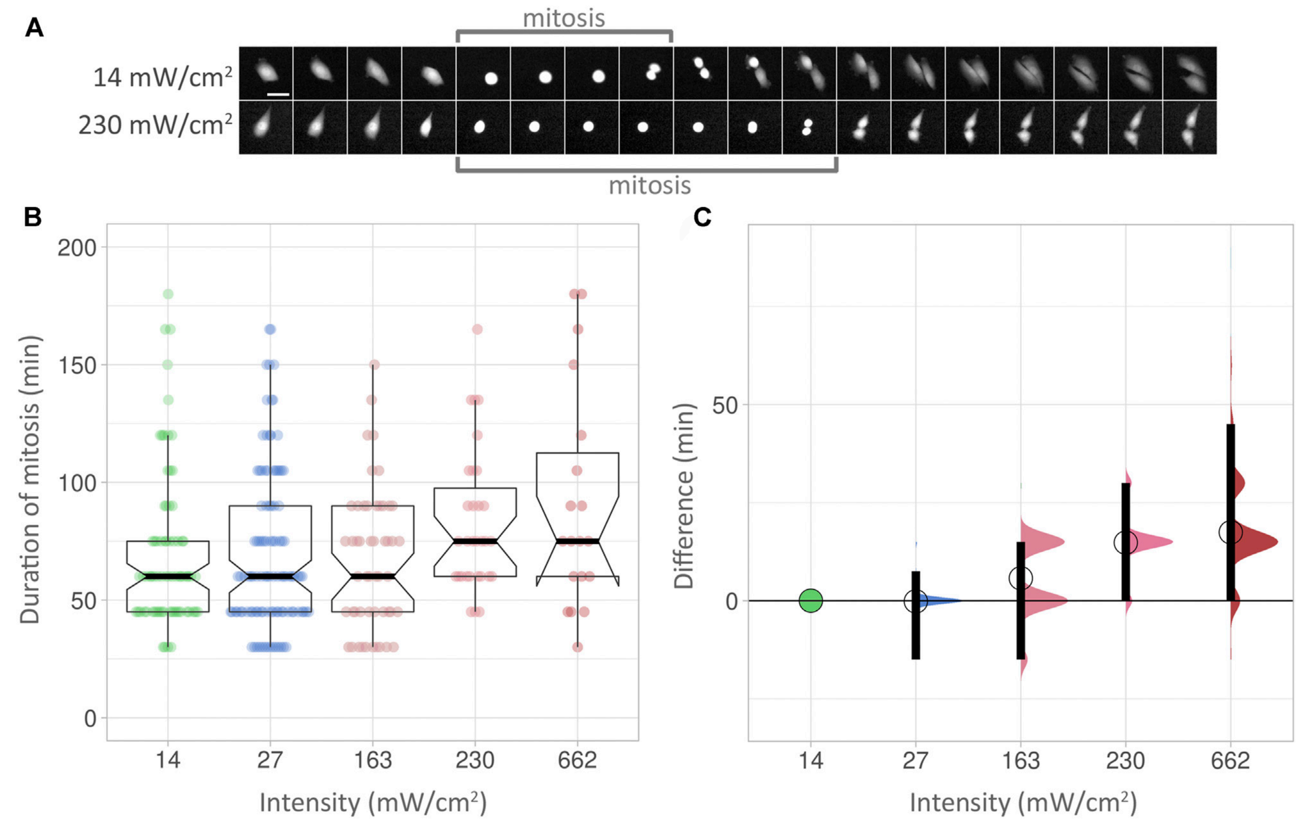

FIGURE 4 | (A) Top row: Duration of mitosis examples. Images were taken at 15 min intervals. Scalebar 50 µm. **(B)** Box plots showing the duration of mitoses at different intensities over 24 h. The *Y* axis shows the duration of mitoses, measured in minutes. Within each box (interquartile range), the thick black line shows the median speed for each condition, and indentations depict its 95% compatibility interval (CI). The data points used to produce the box plots are overlaid in colour. **(C)** Effect sizes of the conditions in **(B)**. The lowest intensity (14 mW/cm^2) is used as baseline. The differences between median values are indicated with a circle. 95% compatibility intervals are indicated by black vertical bars.

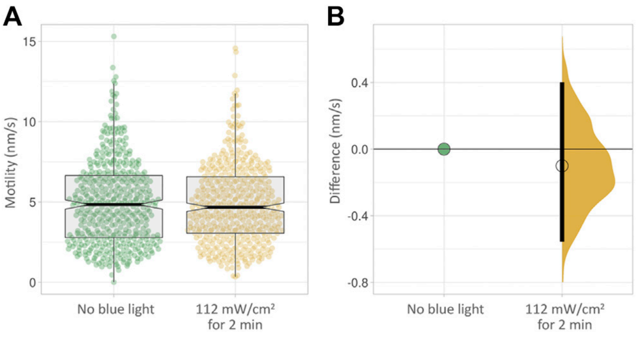

FIGURE 5 | (A) Box plots of PC3 cell motility over 24 h with no blue light exposure (green) and after 2 min at a moderate intensity of 112 mW/cm^2. **(B)** The effect size corresponding to **(A)**. No clear difference in motility is visible.

measured to decrease the uncertainty of the effect size in these examples. However, in our motile PC3 cells, movement can be assessed for the majority of cells within the field of view, whereas mitoses occur far less frequently; using the same number of fields of view, a total of 2,477 motility tracks were identified, compared to 280 mitoses. The frequency of a biological readout used to assess phototoxicity is hence an important consideration.

A Working Model for Phototoxicity

To find an acceptable imaging mode for a given sample, ensuring that valid conclusions are drawn from its live observation using fluorescence microscopy, we believe it is helpful to have a working model in mind. Based on our findings and previous studies (Carlton et al., 2010; Dixit and Cyr, 2003; Icha et al., 2017; Kiepas et al., 2020; Laissue et al., 2017; Tinevez et al., 2012), we propose a general, simplified model for phototoxicity using a “photodamage landscape” consisting of three axes: Excitation light intensity, exposure time and cellular health. The latter is defined by the minimal or absent perturbation of the sample based on the biological readout used to assess phototoxic effects (**Figure 7**). Note that we here use “the cell” in a *pars pro toto* sense, i.e., as a term for any living sample, be that single-celled or multicellular. In our model, fluorescence excitation light induces the production of ROS in the observed living cell. At low intensities and short observation periods, this can be dealt with by the cell using its native ROS scavenging abilities. With moderate stress, there

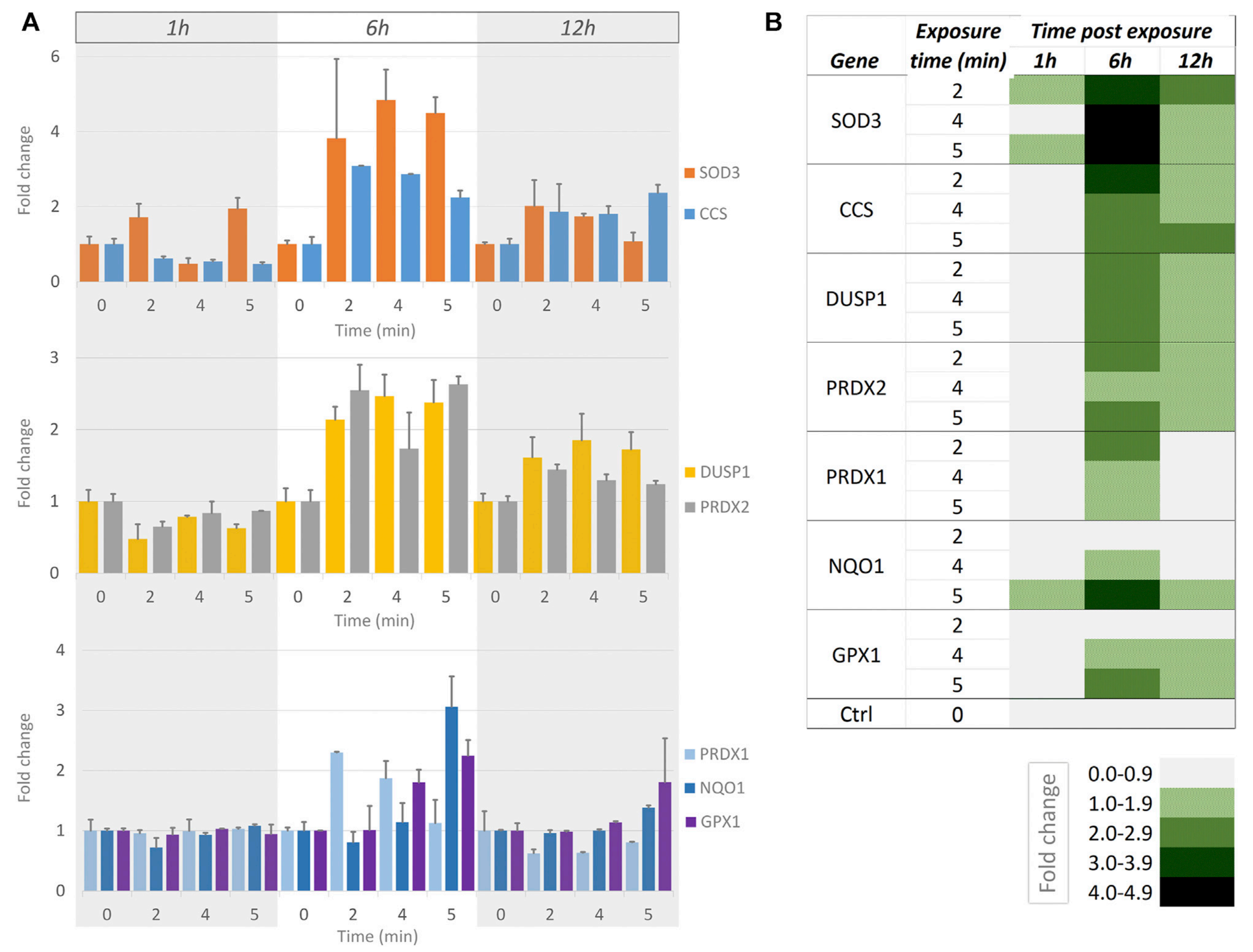

FIGURE 6 | Measurements of RT-qPCR-based gene expression at different times after short exposures to moderate-intensity blue light. **(A)** Bar graphs showing gene expression fold-changes at 1, 6 and 12 h (indicated by grey/white/grey columns underlying all bar graphs) after no illumination (0) and 2, 4 and 5 min continuous illumination with blue light at 112 mW/cm^{2}intensity. Top graph: SOD3 (orange) and CCS (blue). Middle graph: DUSP1 (yellow) and PRDX2 (grey). Bottom graph: PRDX1 (light blue), NQO1 (dark blue) and GPX1 (purple). Error bars indicate standard error in all graphs. **(B)** Heat map summarily visualising the responses [as shown in **(A)**]. The fold changes are indicated at the bottom of the heat map, with higher fold changes represented by darker shades of green.

is also an adaptive range, entailing upregulation of genes to deal with the oxidative stress. Phototoxicity occurs, primarily through oxidative stress, when ROS are not scavenged quickly enough: The rate of repair of damaged cell components fails to keep pace with the rate of damage. If this situation persists, the cell progresses past a hypothetical inflection point, beyond which irreversible damage occurs. This results in an impairment of numerous cellular functions, a concomitant loss of physiological competence, and eventual cell death. For this progression from a physiological or adaptive state to a pathophysiological one, we propose a bi-phasic, sigmoidal effect of phototoxicity that scales with illumination intensity—similar to the model proposed for high-light responses in plants and algae (Laloi and Havaux, 2015; Mullineaux et al., 2018). The biphasic nature of phototoxicity has been described in previous studies (Dixit and Cyr, 2003; Carlton et al., 2010; Schneckenburger et al., 2012; Tinevez et al., 2012). On a molecular level, it may be related to the supralinear photobleaching of fluorescent proteins at high intensity (Cranfill et al., 2016).

TABLE 1 | Terminology and units for the key parameters used in this study.

Physical parameters	Unit
Intensity (irradiance, surface power density)	mW/cm^2
Exposure time (illumination time)	sec
Power	mW
Light dose (power x exposure time)	mJ
Biological parameters	**Unit**
Cell motility	nm/s
Duration of mitosis	min
Gene copy number (RT-qPCR)	Fold-change

The model assumes that many other factors influencing phototoxicity are already set: excitation wavelength, fluorophores (both their concentration and their subcellular localization), dark intervals between images, oxygen

TABLE 2 | Primers for RT-qPCR used in this study. RG: reference gene.

Gene symbol	Oligo sequence forward/Reverse	
PRDX1	TTGCGCGTTTTGTTCTTCCC	GCTGTGGCTTTGAAATTGGG
CCS	AACAACTGCAACAGCTGTGG	AGCATCAGCATGGACATTGC
DUSP1	AACGTCTCAGCCAATTGTCC	TGAAGTCAATCGCCTCGTTG
GPX1	ACGATGTTGCCTGGAACTTC	ATGTCAATGGTCTGGAAGCG
NQO1	TTCCAGAGTAAGAAGGCAGTGC	TGGAAGCCACAGAAATGCAG
PRDX2	TTGATGGCGCCTTCAAAGAG	TGGGGCACACAAAAGTGAAG
SOD3	TCTCACCTTCGCCTTTGTTG	TACAAATGGAGGCCTTCAGACC
GAPDH (RG)	ATTCCACCCATGGCAAGTTC	ATCGCCCCACTTGATTTTGG
HPRT1 (RG)	AACGTCTTGCTCGAGATGTG	AATCCAGCAGGTCAGCAAAG
TUBA1A (RG)	TGCAAACAGTCTACGGATGC	TGCCAAAGACCACATGCTTG
PPIA (RG)	TGCTGGACCCAACACAAATG	TGCCAAAGACCACATGCTTG
TBP (RG)	CCACTCACAGACTCTCACAAC	CTGCGGTACAATCCCAGAACT

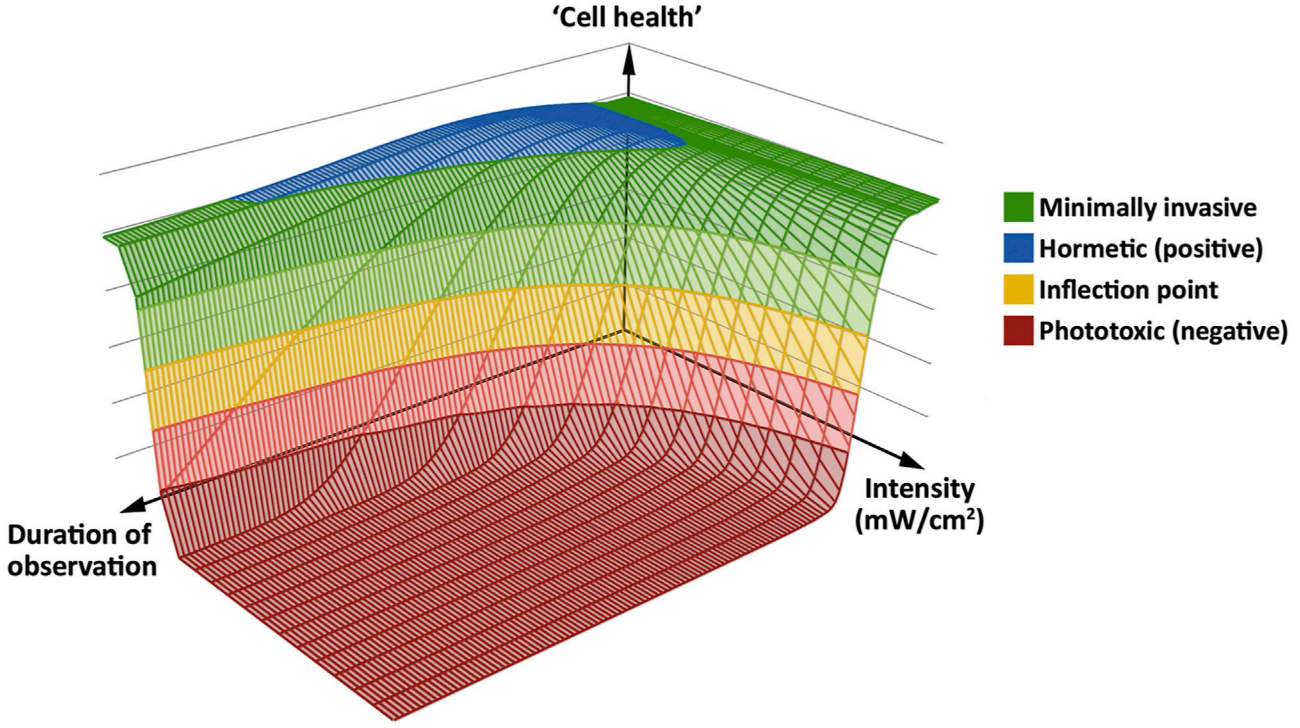

FIGURE 7 | A "phototoxicity landscape" as a working model, based on the three key parameters of excitation light intensity, duration of observation and "cell health." At low intensity, the effects of excitation light can be minimal (green) to positive (blue), with no negative effect on "cell health." However, if excitation at low intensity occurs over a long period of observation, negative effects may start to manifest. At higher intensities, negative effects take hold more quickly. At the inflection point (yellow band), phototoxicity can reach an irreversible level, which leads to immediate or delayed cell death (red floor). Adapted from (Alghamdi, 2017).

concentration, media, sample preparation, developmental (or cell cycle) stage, cell type and age, and synergistic effects of experimental perturbations all can affect a live sample under fluorescence microscopy observation. However, if these parameters are set, we expect any sample to qualitatively behave in a similar way.

Gauging Phototoxicity: How Low Should It Be in a Given Experiment?

In an ideal experiment using live fluorescence microscopy, the excitation illumination should have no measurable effect on the observed sample [i.e., the no-effect level (NOEL) (Schmidt et al., 2020)]. This will however depend on how phototoxicity is assessed. Readouts such as the ratio of living to dead cells (assessed right at the end of the experiment), or using purely morphological indicators such as blebbing, are not sensitive readouts and their use is increasingly discouraged (Icha et al., 2017). A biological process will provide a more sensitive readout, such as the timing of mitosis (Cole, 2014). Its use in this study however showed limited sensitivity, and cell motility proved a better readout for PC3 cells. Increasing sensitivity further, our RT-qPCR results show that even when no differences in cell motility are found, blue light illumination may have altered gene expression. RT-qPCR thus served as a relatively simple, early ROS-induced marker at transcriptional level, revealing an effect of blue light not measurable using morphological or dynamical readouts. Note however that verifying whether the upregulated transcription of mRNAs translates into corresponding mature and active proteins cannot be answered by RT-qPCR.

This leads to two conclusions: 1) Finding sensitive methods to quantify the effect of excitation light is key. To encourage the usage of such methods and lower the effort threshold for such experiments to be included in live imaging studies using fluorescence microscopy, it is also important that they be as simple, as robust and as widely applicable as possible. 2) While it is possible that in certain experimental setups, phototoxicity can be entirely avoided, this is unlikely to apply to many experiments where higher light intensities are used to achieve the requisite spatial and/or temporal resolution of the biological process of interest. However, it is in any case fundamentally important to identify how much the applied illumination affects the sample—and biological process—in question. In all cases, illumination should be lowered to produce the minimal amount of image contrast that allows quantification of the acquired datasets.

In practical terms, this means that two fundamental questions need to be addressed prior to acquiring images for a series of experiments based on fluorescence microscopy. We propose the following steps:

1. What is the temporal and spatial resolution you require to observe the biological process of interest?
2. What is the minimal contrast required to quantify this? Consult existing literature to find initial values, then run tests to determine a narrow range for these fundamental parameters.
3. Choosing the most sensitive biological readout possible, establish a dose-response curve: At first, an intensity that produces obvious signs of phototoxicity can be used to determine the damaging end of the excitation intensity range. Now continuously reduce the excitation intensity until arriving at a minimally (or ideally non-) invasive level while still acquiring images with sufficient contrast for quantification. A reduced excitation intensity has the advantages of reducing phototoxicity and photobleaching, and may allow extending the duration of observation.

MATERIALS AND METHODS

PC3 Cell Preparation and Image Acquisition

We used the human prostate cancer cell line PC3 (ATCC CRL-1435, Manassas, VA), stably transfected with an empty GFP plasmid for cytoplasmic expression of GFP. The cells were grown in RPMI-1640, supplemented with 10% FBS, 1% penicillin/streptomycin and 1% L-glutamine. 80–90% monolayer confluence was reached 24 h before imaging. Cells were detached from the flask with Tryp LE™, and 2×10^4 cells were seeded in 96 microwell plates (ibidi GmbH, Munich, Germany). Samples were imaged at 37°C and 5% CO_2 in a stage-top incubator (Model H301, OkoLab, Italy), with each imaged well surrounded by empty wells to avoid "splash damage" of light. Multi-location time lapse images were taken using widefield fluorescence microscopy. A Nikon Eclipse Ti-E main body was used with an automated stage for multipoint acquisition and NIS-Elements (version 3.21.03, build 705 LO) for control. Microscope objectives were a Nikon CFI PlanFluor 10x (NA 0.3, WD 16 mm) or a Nikon S Fluor 20x (NA 0.75, WD 1 mm). The light source was a metal halide Nikon Intensilight. GFP was excited with a single band emission filter at 480 ± 15 nm and its emission collected with hard-coated interference filters, using a chromatic reflector at 505 nm and a single band emission filter at 535 ± 20 nm (Chroma Technology Corp., VT, United States). Differential interference contrast (DIC) images for cellular outlines were acquired using an incandescent tungsten white light source. Two-dimensional time-lapse series were acquired with an Andor camera (Luca-R DL-626, Andor Technology, United Kingdom), with an image being taken every 15 min for at least 24 h. Intensity (irradiance) was estimated using the power (measured with an ML9002A optical handy power meter (Anritsu Corp., Japan) at sample height) and the corresponding field of view's diagonal to calculate the circular area of illumination.

Image Analysis

Image analysis was done using Fiji v1.53c (Schindelin et al., 2012) with the TrackMate plugin (Tinevez et al., 2017). A blob diameter of 28′000 nm and noise threshold of 0.8 were used with a Laplacian of Gaussian detector using sub-pixel localisation accuracy. Next, we selected the Linear Assignment Problem (LAP) tracker using frame-to-frame linking of 15’000 nm, track segment gap closing of 40’000 nm with a maximum frame gap of 2, and finally a track segment splitting of 15,000 nm. Median velocity was used as the measure of cell motility.

Between 56 and 131 tracks per single well in a 96-well plate were measured (average of 88 ± 22 tracks per well). We found that at a low count (60 tracks), a clear difference (1.05 nm/s) was found between two randomly chosen wells acquired in identical imaging conditions. Increasing the number of tracks to 240 by determining the median speeds in three wells, this difference was roughly halved (0.59 nm/s). Doubling the number of imaged wells to six (increasing the readout to 480 tracks) resulted in almost identical values for median speeds (difference 0.12 nm/s). We settled on the measurement of 500 tracks for each imaging condition to ensure a reliable readout of median cell speeds.

Mitotic delay analysis was conducted by observing the number of frames each cell took to complete mitosis (**Figure 4A**). Frames were taken in 15-min intervals. The starting point was a rounded cell; the end point was arrived at once the mitotic cell had split it into two separate cells.

RNA Extraction and Quantitative Real-Time PCR

Cells for quantitative real-time PCR (RT-qPCR) were seeded on three 12 well plates. Each plate was exposed briefly (2, 4 and

5 min) to moderate-intensity blue light (112 mW/cm^2). Controls were not exposed to blue light. After blue light exposure, RNA extraction was carried out on separate multiwell plates after 1, 6 and 24 h, respectively. All RNA samples from each well were collected in separate Eppendorf tubes and stored at - 80°C. Total RNA was extracted from PC3 cells using CellAmp Direct RNA Prep kit for RT-qPCR and Protein Analysis Kit (Takara Bio Inc., Japan). RNA (1 μg) was treated with Ambion RNase-free DNase1 (Thermo Fisher Scientific, Waltham, Massachusetts, United States). The cDNA samples were synthesized using random nonamer primers and the First-Strand Synthesis System (Sigma-Aldrich, United States). Quantitative real-time PCR of the cDNA was performed using an EvaGreen fluorescence-based procedure with reagents purchased from Applied Biological Materials (Richmond, Canada). The primers used in this study for RT-qPCR are given in **Table 2**.

Relative and normalised fold expression values were calculated using the CFX Manager Software 3.1 (Bio-Rad, California, United States). A set of reference genes, glyceraldehyde-3-phosphate dehydrogenase (GAPDH), hypoxanthine guanine phosphoribosyl transferase (HPRT1A) peptidylprolyl isomerase (PPIA) and TATA box binding protein (TBP) were checked with the population of cDNA samples. The entire Ct dataset was analysed using qBASE+ (Biogazelle) implemented in CFX Manager Software 3.1 (Bio-Rad). The reference genes that showed higher expression stability were PPIA/TBP (CV = 0.20; M = 0.56) followed by HPRT1 (CV = 0.56; M = 0.94), TUB1A (CV = 0.66; M = 1.08) and GAPDH (CV = 0.72; M = 01.20) for the normalization purpose (Vandesompele et al., 2002). The expression stability values calculated for the pairs of reference genes PPIA/TBP are inside the ranges proposed by Hellemans and co-workers (Hellemans et al., 2007) as acceptable for heterogeneous ($M \leq 1$; $CV \leq 0.5$) and relatively homogeneous ($M \leq 0.5$ and $CV \leq 0.25$) sample panels. We consider a relative quantification (RQ) significant when there is a minimum two-fold change: RQ of more than 2 or less than 0.5.

Statistical Analysis With PlotsOfDifferences

Data analysis was done using PlotsOfDifferences (Goedhart, 2019). Data were visualised using box plots (with 95% compatibility intervals indicated by indentations) and a quasi-random distribution of data, along with displaying effect sizes. Corresponding *p*-values were produced using randomisation tests (Hooton, 1991; Nuzzo, 2017; Goedhart 2019).

CONCLUSION

Our study shows that 1) even very low intensity alters the experimental outcome in the case of PC3-GFP motility illuminated by blue light, 2) effects can be positive or negative, 3) effects scale with intensity, not light dose, and 4) changes in gene expression may long precede morphological or cell dynamical parameters. All of which underlines the crucial importance of assessing phototoxicity in live imaging studies to avoid drawing misleading conclusions.

DATA AVAILABILITY STATEMENT

The raw data supporting the conclusion of this article will be made available by the authors, without undue reservation.

AUTHOR CONTRIBUTIONS

PL, GB, PM, ME-R, and RA conceived, planned, carried out and analysed the experiments. All authors provided critical feedback and helped shape the research, analysis and manuscript.

FUNDING

This project was funded by the Deanship of Scientific Research (DSR) at King Abdulaziz University, Jeddah, Saudi Arabia, under grant no. G: 602-665-1439. The authors acknowledge the DSR with thanks for technical and financial support.

SUPPLEMENTARY MATERIAL

The Supplementary Material for this article can be found online at: https://www.frontiersin.org/articles/10.3389/fcell.2021.738786/full#supplementary-material

REFERENCES

AlGhamdi, K. M., Kumar, A., Ashour, A. E., and AlGhamdi, A. A. (2015). A Comparative Study of the Effects of Different Low-Level Lasers on the Proliferation, Viability, and Migration of Human Melanocytes *In Vitro*. *Lasers Med. Sci.* 30, 1541–1551. doi:10.1007/s10103-015-1758-x

Alghamdi, R. (2017). “Quantified Phenotype Analysis in a Cell Model for Autosomal Dominant Retinitis Pigmentosa,” (UK: University of Essex). PhD thesis.

Becker, A., Klapczynski, A., Kuch, N., Arpino, F., Simon-Keller, K., De La Torre, C., et al. (2016). Gene Expression Profiling Reveals Aryl Hydrocarbon Receptor as a Possible Target for Photobiomodulation when Using Blue Light. *Sci. Rep.* 6 (6), 33847–33911. doi:10.1038/srep33847

Belousov, V. V., Fradkov, A. F., Lukyanov, K. A., Staroverov, D. B., Shakhbazov, K. S., Terskikh, A. V., et al. (2006). Genetically Encoded Fluorescent Indicator for Intracellular Hydrogen Peroxide. *Nat. Methods* 3, 281–286. doi:10.1038/nmeth866

Cadenas, E., and Davies, K. J. A. (2000). Mitochondrial Free Radical Generation, Oxidative Stress, and Aging. *Free Radic. Biol. Med.* 29, 222–230. doi:10.1016/s0891-5849(00)00317-8

Carlton, P. M., Boulanger, J., Kervrann, C., Sibarita, J.-B., Salamero, J., Gordon-Messer, S., et al. (2010). Fast Live Simultaneous Multiwavelength Four-Dimensional Optical Microscopy. *Proc. Natl. Acad. Sci.* 107, 16016–16022. doi:10.1073/pnas.1004037107

Cole, R. (2014). Live-cell Imaging. *Cell Adhes. Migration* 8, 452–459. doi:10.4161/cam.28348

Cranfill, P. J., Sell, B. R., Baird, M. A., Allen, J. R., Lavagnino, Z., de Gruiter, H. M., et al. (2016). Quantitative Assessment of Fluorescent Proteins. *Nat. Methods* 13, 557–562. doi:10.1038/nmeth.3891

Diaspro, A., Chirico, G., Usai, C., Ramoino, P., and Dobrucki, J. (2006). "Photobleaching," in *Handbook of Biological Confocal Microscopy*. Editor J. Pawley (New York: Springer US), 690–702. doi:10.1007/978-0-387-45524-2_39

Dixit, R., and Cyr, R. (2003). Cell Damage and Reactive Oxygen Species Production Induced by Fluorescence Microscopy: Effect on Mitosis and Guidelines for Non-invasive Fluorescence Microscopy. *Plant J.* 36, 280–290. doi:10.1046/j.1365-313x.2003.01868.x

Douthwright, S., and Sluder, G. (2016). Live Cell Imaging: Assessing the Phototoxicity of 488 Nm and 546 Nm Light and Methods to Alleviate it. *J. Cel. Physiol.* 232, 2461–2468. doi:10.1002/jcp.25588

Dröge, W. (2002). Free Radicals in the Physiological Control of Cell Function. *Physiol. Rev.* 82, 47–95. doi:10.1152/physrev.00018.2001

Ettinger, A., and Wittmann, T. (2014). Fluorescence Live Cell Imaging. *Methods Cel. Biol.* 123, 77–94. doi:10.1016/b978-0-12-420138-5.00005-7

Goedhart, J. (2019). Plots Of Differences – a Web App for the Quantitative Comparison of Unpaired Data. *bioRxiv*. 578575. doi:10.1101/578575

Greenbaum, L., Rothmann, C., Lavie, R., and Malik, Z. (2000). Green Fluorescent Protein Photobleaching: a Model for Protein Damage by Endogenous and Exogenous Singlet Oxygen. *Biol. Chem.* 381, 1251–1258. doi:10.1515/BC.2000.153

Hancock, J. T., Desikan, R., and Neill, S. J. (2001). Role of Reactive Oxygen Species in Cell Signalling Pathways. *Biochem. Soc. Trans.* 29, 345–349. doi:10.1042/bst0290345

Hellemans, J., Mortier, G., De Paepe, A., Speleman, F., and Vandesompele, J. (2007). qBase Relative Quantification Framework and Software for Management and Automated Analysis of Real-Time Quantitative PCR Data. *Genome Biol.* 8 (8), R19–R14. doi:10.1186/gb-2007-8-2-r19

Hooton, J. W. L. (1991). Randomization Tests: Statistics for Experimenters. *Comput. Methods Programs Biomed.* 35, 43–51. doi:10.1016/0169-2607(91)90103-z

Icha, J., Weber, M., Waters, J. C., and Norden, C. (2017). Phototoxicity in Live Fluorescence Microscopy, and How to Avoid it. *BioEssays* 39, 1700003. doi:10.1002/bies.201700003

Kiepas, A., Voorand, E., Mubaid, F., Siegel, P. M., and Brown, C. M. (2020). Optimizing Live-Cell Fluorescence Imaging Conditions to Minimize Phototoxicity. *J. Cel. Sci.* 133, jcs242834. doi:10.1242/jcs.242834

Kilian, N., Goryaynov, A., Lessard, M. D., Hooker, G., Toomre, D., Rothman, J. E., et al. (2018). Assessing Photodamage in Live-Cell STED Microscopy. *Nat. Methods* 15, 755–756. doi:10.1038/s41592-018-0145-5

Knoll, S. G., Ahmed, W. W., and Saif, T. A. (2015). Contractile Dynamics Change before Morphological Cues during Fluorescence Illumination. *Sci. Rep.* 5, 18513. doi:10.1038/srep18513

Laissue, P. P., Alghamdi, R. A., Tomancak, P., Reynaud, E. G., and Shroff, H. (2017). Assessing Phototoxicity in Live Fluorescence Imaging. *Nat. Methods* 14, 657–661. doi:10.1038/nmeth.4344

Laloi, C., and Havaux, M. (2015). Key Players of Singlet Oxygen-Induced Cell Death in Plants. *Front. Plant Sci.* 6, 39. doi:10.3389/fpls.2015.00039

Leone, A., Roca, M. S., Ciardiello, C., Costantini, S., and Budillon, A. (2017). Oxidative Stress Gene Expression Profile Correlates with Cancer Patient Poor Prognosis: Identification of Crucial Pathways Might Select Novel Therapeutic Approaches. *Oxid. Med. Cel. Longev.* 2017, 2597581. doi:10.1155/2017/2597581

Magidson, V., and Khodjakov, A. (2013). Circumventing Photodamage in Live-Cell Microscopy. *Methods Cel. Biol.* 114, 545–560. doi:10.1016/b978-0-12-407761-4.00023-3

Markvicheva, K. N., Bilan, D. S., Mishina, N. M., Gorokhovatsky, A. Y., Vinokurov, L. M., Lukyanov, S., et al. (2011). A Genetically Encoded Sensor for H2O2 with Expanded Dynamic Range. *Bioorg. Med. Chem.* 19, 1079–1084. doi:10.1016/j.bmc.2010.07.014

Mubaid, F., and Brown, C. M. (2017). Less Is More: Longer Exposure Times with Low Light Intensity Is Less Photo-Toxic. *Micros. Today* 25, 26–35. doi:10.1017/s1551929517000980

Mullineaux, P. M., Exposito-Rodriguez, M., Laissue, P. P., and Smirnoff, N. (2018). ROS-dependent Signalling Pathways in Plants and Algae Exposed to High Light: Comparisons with Other Eukaryotes. *Free Radic. Biol. Med.* 122, 52–64. doi:10.1016/j.freeradbiomed.2018.01.033

Nuzzo, R. L. (2017). Randomization Test: An Alternative Analysis for the Difference of Two Means. *PM&R* 9, 306–310. doi:10.1016/j.pmrj.2017.02.001

Poli, G., Leonarduzzi, G., Biasi, F., and Chiarpotto, E. (2004). Oxidative Stress and Cell Signalling. *Curr. Med. Chem.* 11, 1163–1182. doi:10.2174/0929867043365323

Redmond, R. W., and Kochevar, I. E. (2006). Spatially Resolved Cellular Responses to Singlet Oxygen. *Photochem. Photobiol.* 82, 1178–1186. doi:10.1562/2006-04-14-IR-874

Remington, S. J. (2011). Green Fluorescent Protein: a Perspective. *Protein Sci.* 20, 1509–1519. doi:10.1002/pro.684

Riley, P. A. (1994). Free Radicals in Biology: Oxidative Stress and the Effects of Ionizing Radiation. *Int. J. Radiat. Biol.* 65, 27–33. doi:10.1080/09553009414550041

Rodriguez, E. A., Campbell, R. E., Lin, J. Y., Lin, M. Z., Miyawaki, A., Palmer, A. E., et al. (2017). The Growing and Glowing Toolbox of Fluorescent and Photoactive Proteins. *Trends Biochem. Sci.* 42, 111–129. doi:10.1016/j.tibs.2016.09.010

Schindelin, J., Arganda-Carreras, I., Frise, E., Kaynig, V., Longair, M., Pietzsch, T., et al. (2012). Fiji: an Open-Source Platform for Biological-Image Analysis. *Nat. Methods* 9, 676–682. doi:10.1038/nmeth.2019

Schmidt, G. W., Cuny, A. P., and Rudolf, F. (2020). Preventing Photomorbidity in Long-Term Multi-color Fluorescence Imaging of Saccharomyces cerevisiae and *S. pombe*. *G3 (Bethesda, Md.)*. 10 (12), 4373–4385. doi:10.1534/g3.120.401465

Schneckenburger, H., Weber, P., Wagner, M., Schickinger, S., Richter, V., Bruns, T., et al. (2012). Light Exposure and Cell Viability in Fluorescence Microscopy. *J. Microsc.* 245, 311–318. doi:10.1111/j.1365-2818.2011.03576.x

Seko, Y., Pang, J., Tokoro, T., Ichinose, S., and Mochizuki, M. (2001). Blue Light-Induced Apoptosis in Cultured Retinal Pigment Epithelium Cells of the Rat. *Graefe's Arch. Clin. Exp. Ophthalmol.* 239, 47–52. doi:10.1007/s004170000220

Swedlow, J. R., Porter, I. M., Posch, M., and Swift, S. (2009). "*In Vivo* Imaging of Mammalian Cells," in *Live Cell Imaging: A Laboratory Manual*. Editors R. Goldman, J. Swedlow, and D. Spector (New York, United States: Cold Spring Harbor Laboratory Press).

Tinevez, J.-Y., Dragavon, J., Baba-Aissa, L., Roux, P., Perret, E., Canivet, A., et al. (2012). A Quantitative Method for Measuring Phototoxicity of a Live Cell Imaging Microscope. *Methods Enzymol.* 506, 291–309. doi:10.1016/b978-0-12-391856-7.00039-1

Tinevez, J.-Y., Perry, N., Schindelin, J., Hoopes, G. M., Reynolds, G. D., Laplantine, E., et al. (2017). TrackMate: An Open and Extensible Platform for Single-Particle Tracking. *Methods* 115, 80–90. doi:10.1016/j.ymeth.2016.09.016

Vandesompele, J., De Preter, K., Pattyn, F., Poppe, B., Van Roy, N., De Paepe, A., et al. (2002). Accurate Normalization of Real-Time Quantitative RT-PCR Data by Geometric Averaging of Multiple Internal Control Genes. *Genome Biol.* 3 (3), RESEARCH0034–12. doi:10.1186/gb-2002-3-7-research0034

Wäldchen, S., Lehmann, J., Klein, T., van de Linde, S., and Sauer, M. (2015). Light-induced Cell Damage in Live-Cell Super-resolution Microscopy. *Sci. Rep.* 5, 15348. doi:10.1038/srep15348

Yuan, Y., Yan, G., Gong, R., Zhang, L., Liu, T., Feng, C., et al. (2017). Effects of Blue Light Emitting Diode Irradiation on the Proliferation, Apoptosis and Differentiation of Bone Marrow-Derived Mesenchymal Stem Cells. *Cell Physiol. Biochem.* 43, 237–246. doi:10.1159/000480344

Conflict of Interest: The authors declare that the research was conducted in the absence of any commercial or financial relationships that could be construed as a potential conflict of interest.

frontiers
in Cell and Developmental Biology

REVIEW
published: 18 January 2022
doi: 10.3389/fcell.2021.725114

Imaging Approaches for the Study of Metabolism in Real Time Using Genetically Encoded Reporters

Panagiotis Chandris[1]*, Christina C. Giannouli[2] and George Panayotou[1]

[1]Institute for Bioinnovation, Biomedical Sciences Research Center "Alexander Fleming", Vari, Greece, [2]Biomedical Research Foundation Academy of Athens, Athens, Greece

Metabolism comprises of two axes in order to serve homeostasis: anabolism and catabolism. Both axes are interbranched with the so-called bioenergetics aspect of metabolism. There is a plethora of analytical biochemical methods to monitor metabolites and reactions in lysates, yet there is a rising need to monitor, quantify and elucidate in real time the spatiotemporal orchestration of complex biochemical reactions in living systems and furthermore to analyze the metabolic effect of chemical compounds that are destined for the clinic. The ongoing technological burst in the field of imaging creates opportunities to establish new tools that will allow investigators to monitor dynamics of biochemical reactions and kinetics of metabolites at a resolution that ranges from subcellular organelle to whole system for some key metabolites. This article provides a mini review of available toolkits to achieve this goal but also presents a perspective on the open space that can be exploited to develop novel methodologies that will merge classic biochemistry of metabolism with advanced imaging. In other words, a perspective of "watching metabolism in real time."

Keywords: fluorescent sensor, fluorescence resonance energy transfer, Warburg effect, permuted fluorescent proteins, metabolism

Edited by:
Michelle S. Itano,
University of North Carolina at Chapel Hill, United States

Reviewed by:
Jian-Qiu Wu,
The Ohio State University, United States
Matthew Anderson,
National Cancer Institute at Frederick, United States

***Correspondence:**
Panagiotis Chandris
chandris@fleming.gr

Specialty section:
This article was submitted to Cell Growth and Division, a section of the journal Frontiers in Cell and Developmental Biology

Received: *14 June 2021*
Accepted: *13 December 2021*
Published: *18 January 2022*

Citation:
Chandris P, Giannouli CC and Panayotou G (2022) Imaging Approaches for the Study of Metabolism in Real Time Using Genetically Encoded Reporters. Front. Cell Dev. Biol. 9:725114. doi: 10.3389/fcell.2021.725114

INTRODUCTION

The term metabolism is used to describe a vast field which actually comprises anything involving synthesis, recycling and breakdown of biological molecules in tight balance with the energy budget (production and waste). As the term is rather generic, it practically involves every metabolic reaction and metabolite trafficking inside a cell or systemic circulation and trafficking of metabolites between tissues and organs of multicellular organisms. Regarding pathophysiology, cancer research has been leading in the past few years a renaissance of the study of metabolism (Pavlova and Thompson, 2016; Altea-Manzano et al., 2020). Researchers though tend to classify diseases as "chronic" (e.g., irritable bowel syndrome, Crohn's disease etc.), "degenerative" (for instance dementia) or "infectious." One might be caught by surprise to find out that relief or aggravation or even therapeutic approaches for these diverse diseases might be metabolism dependent (Kaser et al., 2010). Further afield, even stemness has been proven to be tightly intertwined with the presence of certain metabolites (Carey et al., 2015; Schell et al., 2017; Tsogtbaatar et al., 2020). In addition, what we perceive as metabolic status, or even hormonal regulation of the body as a network, appears to be influenced -not to say coordinated- by the gut microbiome and its metabolites (Zhao S. et al., 2020). This repositioning of metabolism as a key aspect of current biomedical research propelled the advancement of sophisticated quantitative metabolic profiling methodologies, such as NMR and mass spectrometry, using hybrid approaches to analyze metabolites in solution (Chen et al., 2020) or even *in situ*, in tissues (Andersen et al., 2021).

In the last two decades there has been an explosion in the field of light microscopy, which resulted in the breaking of the diffraction barrier using super resolution approaches—both deterministic (SIM, STED) and probabilistic (PALM, STORM, GSDIM)—with variants or even hybrids (MINFLUX) of those optical methods (Sahl et al., 2017). Furthermore we had the implementation and constant expansion of diffraction–limited but much gentler and faster microscope systems, such as light sheet microscopes at different setups that allow accommodation of diverse biological entities, ranging from cells to whole organisms (Wan et al., 2019). Collectively, although super resolution has a constantly expanding irrefutable role in our understanding of how cells organize their subcellular entities (Baddeley and Bewersdorf, 2018), its role in dissecting highly dynamic phenomena in living systems is rather limited so far due to the increased phototoxicity by high light intensities, but also due to long acquisition times needed to paint the structural landscape, not only with increased resolution but also with increased precision. In parallel, confocal systems have become faster and more light-efficient and even wide-field microscopy has benefited substantially from highly sensitive and much faster cameras (sCMOS and EMCCDs). Overall, combining optical hardware improvement with the development of new genetically encoded fluorescent toolkits allows us to observe in a quantitative manner dynamic phenomena of metabolic nature, thus complementing metabolomics analysis by disruptive approaches, such as NMR and mass spectrometry.

In this mini review we will present a set of metabolite sensors targeted to distinct subcellular compartments. Further, we propose re-targeting of some sensors to monitor metabolites in different compartments along with suggestions for a new set of sensors for metabolites with emerging roles in biomedical research for which there are no available quantitative tools in intact biological systems.

THE FIELD

The cell organizes its metabolism by compartmentalization. Sets of reactions take place in individual compartments and metabolites are exchanged either directly or indirectly by conversion to an intermediate metabolite that can pass a membrane barrier, (Lewis et al., 2014; Maddocks et al., 2014; Oeggl et al., 2018). It is also not uncommon that upon perturbation of a metabolic pathway cells will rewire their metabolic network to sustain viability and growth (Jiang et al., 2017) and this is always concerted with the balance of the redox potential of the cell (Hosios and Vander Heiden, 2018). Classic metabolic pathways include the uptake and metabolism of simple sugars such as glucose. The carbohydrate is imported into the cell with the action of transporters (Kayano et al., 1990; Chadt and Al-Hasani, 2020), gets phosphorylated and depending on the metabolic status of the cell, the hexose may be diverted to the pentose phosphate pathway to drive nucleotide synthesis or broken down to trioses. From that point on the cell may favor conversion to pyruvate and import it into mitochondria to support the Krebs cycle and oxidative phosphorylation (OXPHOS) along with energy production, or follow the anaerobic path and produce and secrete lactate (**Figure 1**). Glycolysis takes place in the cytosol while OXPHOS in the mitochondrial matrix. The pentose phosphate pathway occurs in the cytosol, yet the full path down to purine synthesis shuttles between cytosol and mitochondria.

In parallel to glucose metabolism, the cells may uptake other nutrients from the microenvironment including amino acids (Chantranupong et al., 2015; Efeyan et al., 2015). Glutamine for instance exerts a central role in metabolism, as it is regarded an "essential non-essential" amino acid. It is used in translation but it also serves to supply the cell with carbon and nitrogen. Glutamine may enter the cell and either get metabolized to glutamate in the cytosol or shunted to mitochondria where it is converted to glutamate and finally to a-ketoglutarate to feed the Krebs cycle (anaplerosis) (**Figure 1**). Alternatively, it can be diverted to non-essential amino acid (NEAA) synthesis *via* transamination reactions to support cell growth (Coloff et al., 2016). Elevated demand and metabolic rates for glutamine have been documented for many types of cancer (Zhang et al., 2017; Sniegowski et al., 2021) and evidence suggests that this nutrient's uptake and metabolic reprogramming is directly connected to the action of oncogenes in cancer (Wise et al., 2008). As a result, mitochondrial glutaminase isoforms (the enzymes that hydrolyze glutamine in mitochondria) are emerging as important therapeutic targets. Glutamine metabolism is directly related to glutamate, which also plays an essential role in intracellular metabolism but furthermore functions extracellularly as a major neurotransmitter.

Although much attention has been given to mitochondria (for obvious reasons) regarding their role in metabolism, other organelles also hold a central role in metabolism, particularly for certain classes of metabolites. In light of the finding that a major orchestrator of metabolism, the target of rapamycin complex (TORC), shuttles on and off the lysosomes, this organelle is no longer considered simply a trash bin of the cell, but a hub of major recycling pathways, ranging from amino acid to sphingolipid metabolism (Sancak et al., 2008; Sancak et al., 2010; Betz and Hall, 2013; Sabatini, 2017; Wyant et al., 2017). Just to name a few more key players, peroxisomes are also key constituents for fatty acid synthesis and oxidation (Wanders et al., 2020), while the endoplasmic reticulum synthesizes phospholipids cooperatively with mitochondria (Jacquemyn et al., 2017).

Metabolism is a vast field and it is not the scope of this mini review to cover all aspects of metabolism–related sensors. We will mostly focus on the variety of sensor tools that have been developed to monitor key aspects of carbon and to some extent nitrogen balance, due to their importance and topical interest.

THE DESIGN RATIONALE

FRET and B-RET Based Sensors

Forster (or Fluorescent) Resonance Energy Transfer, is a physical process where energy migrates from an excited fluorophore to an

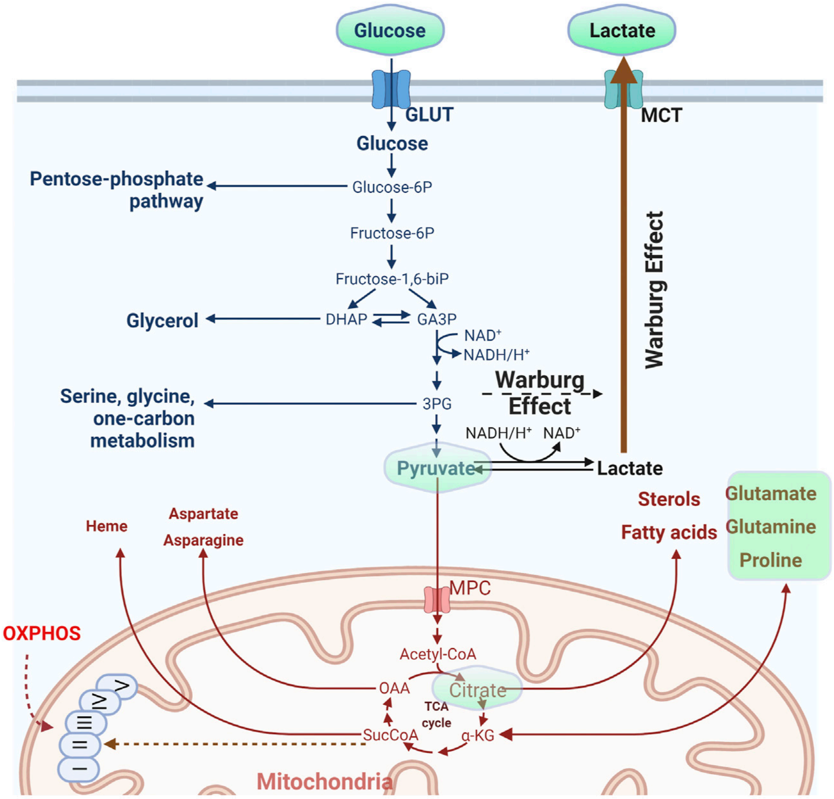

FIGURE 1 | Outline of the basic metabolic pathway of glucose. The molecule is imported inside the cells and depending on the metabolic status might be used either for the synthesis of nitrogen bases through the pentose phosphate pathway or converted to trioses and from there to pyruvate. The last metabolite may either feed mitochondria or be converted to lactate and secreted in the extracellular medium. High rate of pyruvate conversion to lactate despite the presence of oxygen is called the "Warburg effect." For some of the metabolites depicted in the figure, existing fluorescent reporters are described in the main text. Those metabolites are embedded in a light green frame. (Figure prepared by modifying a Biorender.com template).

adjacent one in a non-radiative manner. It is the result of long-range dipole-dipole coupling and it has a useful range between 10–100 Å (1–10 nm). The method has been extensively used to monitor protein-protein interactions, affinity and other dynamic parameters (Berney and Danuser, 2003; Bajar et al., 2016). FRET may occur between two different fluorophores (hetero-FRET) but also between two molecules of the same fluorophore (homo-FRET). Homo-FRET analysis is based on anisotropy measurements, requires specialized instrumentation and although it can be used for analyzing molecular dynamics and signaling events (Bader et al., 2009; Warren et al., 2015), it is not the method of choice when it comes to metabolite analysis.

Regarding fluorescent reporters for monitoring metabolic activity, "cameleon" type systems are mostly used (Miyawaki et al., 1997; Lindenburg and Merkx, 2014). In this case, donor and acceptor (usually two fluorescent proteins with overlapping spectra) are fused together (thus securing the 1:1 ratio) and in between them, a protein domain is placed that binds the metabolite of interest. Upon binding of the metabolite, a resulting conformational change of the linker domain results in a modified distance between the two fluorophores, thus tuning FRET efficiency, read as change in fluorescence intensity (**Figure 2A**). Cameleon-type systems bypass the fluctuating ratio between separated donor and acceptor, yet normalization of FRET intensity should be done carefully, taking into account artefactual readouts attributed to cross-excitation and bleedthrough (Bajar et al., 2016). In addition, although overlapping spectra is the primary criterion for efficient FRET readouts, pairs of proteins with markedly different maturation times should be avoided (Shaner et al., 2005). An alternative readout regarding FRET pairs is through the affected lifetime of the fluorophore of the donor molecule (lifetime FRET, LT-FRET). In this case, instead of measuring the drop of intensity of the donor and the increased intensity in the acceptor channel, the statistical distribution of the time required for the fluorophore to emit photons after a pulsed excitation is measured (Datta et al., 2020). These measurements can be conducted in time (time-correlated single photon counting-TCSPC) or frequency domain (FD). The advantage of LT-FRET over intensity–based is that it is to a large extent (but not completely) independent of the concentration of the fluorophores. It should however be taken into account that lifetime FRET (LT-FRET) is a very sensitive technique that is prone to errors attributed to violation of the sampling rate (especially for time correlated single photon counting approaches-TCSPC).

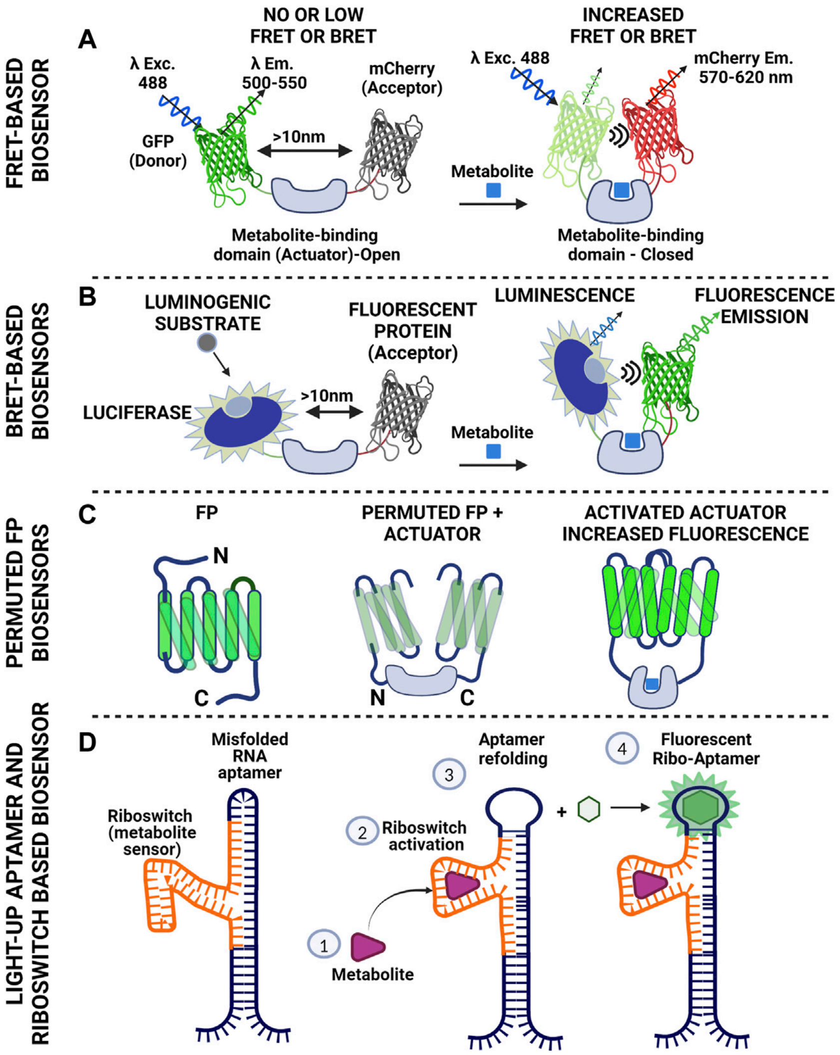

FIGURE 2 | Schematics of basic tools used to construct biosensors for metabolite monitoring. **(A)** Cameleon-like Förster Resonance Energy Transfer design using fluorescent donor and acceptor with overlapping spectra. The fluorescent molecules are bridged with a protein domain that serves as specific metabolite sensor. Binding of the metabolite to the actual sensor (Actuator) triggers conformational changes that result in reduced distance between the two fluorescent proteins. Proximity facilitates energy transfer to the acceptor resulting in its excitation and subsequent photon emission. Of note, there is no direct photon transfer between the two molecules (non-radiative). This scheme gives positive read out signal (increased FRET). Reciprocally, the actuator might cause the fluorescent proteins to come in proximity in the absence of the metabolite and loosen its conformation upon metabolite binding. In this case the readout will be negative (reduced FRET). **(B)**. Bioluminescence Resonance Energy Transfer is an approach similar to FRET. The energy donor here is luciferase. There is no excitation light for the donor. In the presence of oxygen the enzyme catalyzes oxidation of luciferin (or other suitable substrate) and the reaction emits photons. The wavelength of this emission falls within the excitation spectrum of the acceptor. In a manner similar to FRET, energy is transferred to the acceptor causing the molecule to fluoresce. This scheme allows control of the timing of the recording, as luciferase will produce light when the substrate is supplied. At the same time though the readout will fade with time due to substrate consumption. **(C)** Single color biosensors, based on permutation of fluorescent proteins. One can shuffle fragments of a fluorescent protein (notice the rearrangement of the C- and N- termini of the protein after permutation) and introduce an actuator within the FP sequence compromising fluorescence. Metabolite binding by the actuator increases proximity of the FP domains thus increasing fluorescence intensity **(D)** RNA-based strategy for metabolite detection. The scheme includes a type of RNA (aptamer) that binds a fluorogenic substrate and becomes fluorescent (light-up aptamer). This feature though depends on the conformation of the aptamer. Inserting a fragment of RNA in the aptamer sequence that can identify a metabolite (riboswitch) can cause suboptimal folding of the aptamer and loss of fluorescence. Metabolite binding to the riboswitch causes refolding of the aptamer, which thus gains the ability to fluoresce upon substrate binding. The system has been used with success for imaging S-Adenosylmethionine in bacteria and lately in mammalian systems. (Figure prepared using biorender.com).

B-RET (Bioluminescence resonance energy transfer) is a phenomenon similar to FRET, but in this case there is radiation coming from a luminescent molecule (luciferase activity in the presence of suitable substrate) and the photons emitted are in the excitation range of the acceptor. The readout is fluorescence that comes from the acceptor molecule and the useful distance is again within the 10 nm scale (**Figure 2B**). The method has been used to monitor protein-protein-interactions in living cells (Kobayashi et al., 2019; Kobayashi and Bouvier, 2021) but also for setting up biosensors.

Single–Protein Based Fluorescent Reporters

Fluorescent proteins can have major parts of their sequence rearranged and yet retain their fluorescent properties. This type of sequence shuffling is called permutation. Permutations can be circular or non-circular depending on the way the protein segments are rearranged. Permutation takes place in nature by gene duplications and truncations or partial gene duplications and insertions (Vogel and Morea, 2006). Permuted fluorescent proteins though, exhibit higher sensitivity to environmental factors, such as ions and pH, and furthermore spectral shifts usually arise. Permutation of fluorescent proteins has been used in a variety of applications, ranging from monitoring of calcium fluctuations, to estimation of redox levels (Shui et al., 2011; Kostyuk et al., 2019; Kostyuk et al., 2020). The rationale behind shuffling a fluorescent protein is simple: one may insert a fragment of interest that will work as an actuator within the structure of a permuted fluorescent protein. This inserted fragment (or fragments) has affinity for a molecule of interest. Upon binding of the ligand, a conformational change will be reflected upon the intensity of the signal coming from the fluorescent protein and/or ratiometric changes on their spectra (**Figure 2C**). The great advantage is of course the single molecule approach that alleviates the burdens of FRET-based sensors, yet shuffling a protein sequence and inserting sensory domains is far from trivial. One though may set off by using published efficient permuted variants and implement the actuator of interest.

RNA Aptamer-Based Sensors

RNA aptamers can bind to a fluorogenic molecule in a reversible manner and become fluorescent. They come in different "flavors," acting as monomers (e.g., Spinach2, Broccoli, Mango), but also as dimers (Corn) (Warner et al., 2014; Warner et al., 2017). The fluorogenic substrate defines excitation and emission spectrum (Trachman et al., 2017a; Trachman et al., 2017b; Warner et al., 2017; Truong and Ferre-D'Amare, 2019). RNA aptamers may be used as single fluorescent reporters or as FRET pairs (Trachman et al., 2020). So how do we get to use them as sensors? The answer lies in the "RNA world" and more precisely in the combinatorial use of riboswitches with RNA aptamers. Riboswitches are sequences of RNA that are found in the 3′ UTR of mRNAs and fold in three dimensions, exhibiting affinity for certain small molecules and metabolites. In bacteria for example, riboswitches are used to sense availability of certain nutrients (Barrick and Breaker, 2007; Henkin, 2008), or even control their levels (Ruff et al., 2016; Sherlock et al., 2018). The challenge lies in the proper combination of riboswitch and RNA aptamer so that the riboswitch-induced conformational change upon ligand binding will produce a read–out of fluorescent intensity of the aptamer (**Figure 2D**) (Hallberg et al., 2017).

THE TOOLKIT

Glucose Sensors

Glucose is one of the most fundamental metabolites, as it is used for energy production but also for the synthesis of metabolic intermediates ranging from complex carbohydrates to nucleotides that are used for RNA and DNA synthesis. Cells have specialized transporters to import the molecule (Navale and Paranjape, 2016). Glucose uptake has long been used in clinical practice for PET (Positron Emission Tomography) using for instance a radioactive isotope of FDG (fluorodeoxyglucose, a non-metabolizable analogue of the sugar) to trace tissues with supraphysiological metabolic activity, as is the case in cancer (Almuhaideb et al., 2011).

Given the central role of the metabolite, initial imaging efforts led to the creation of a CFP-YFP cameleon FRET based sensor with intervened bacterial glucose/galactose binding protein (GGBP) serving as the actuator of FRET response upon glucose fluctuations (Fehr et al., 2003). Improved versions of this system yielded a new set of reporters with dynamic range from micromolar to millimolar range (Takanaga et al., 2008; Bermejo et al., 2010). A new set of single fluorophore-based glucose sensors, the Green Glifons, have been raised by engineering previous versions that harbor the bacterial periplasmic glucose/galactose binding protein embedded into the Citrine variant of GFP core (Mita et al., 2019). These sensors cover a broad range of glucose concentrations, exhibiting a 5–8 fold increase in fluorescence intensity. They also show however significant affinity for galactose and this should be taken into account for those planning experiments using this carbohydrate to diminish ATP from glycolysis, increase lactate consumption and boost OXPHOS (Mot et al., 2016; Balsa et al., 2019).

A single–wavelength intensity–based glucose sensor with applicability in various systems, ranging from single cell to organismal applications, has also been reported (Keller et al., 2021). This sensor is based on permuted green fluorescent protein with a sensitivity range from 1 μM to 10 mM, practically spanning the largest part of concentration range for both *in vitro* and *in vivo* systems. The sensor exhibits significant response (up to 200% increase in fluorescence intensity) and flexible applicability, even allowing intravital imaging. Following similar strategies, sensors for mono (ribose) or di-saccharides (sucrose), have been developed and applied in non-mammalian systems or even in small animals such as *Drosophila* and *C. elegans* (Lager et al., 2006; Sadoine et al., 2020). Along with the above, a FLIM-based sensor has been reported (Diaz-Garcia et al., 2017; Diaz-Garcia et al., 2019) yielding a maximum lifetime change in the range of 0.38 ns, yet as with every FLIM measurement, special equipment is needed and read outs are not straightforward. A large number of photons is required for accurate assignment of the lifetime of a fluorophore, rendering the use of such sensors more cumbersome than anticipated.

Pyruvate and Lactate Sensors

We have grouped these substances for two reasons: 1) the interconversion of one to the other through combinatorial heterotetramerization of lactate dehydrogenase (LDH) isoforms (Gerich et al., 2001; George Cahill, 2006; Valvona et al., 2016; Parks et al., 2020) ties up their biochemistry in such a manner that their relative ratio depicts physiological status in a more accurate way and 2) a set of developed sensors are ratiometric for the two molecules.

Pyruvate plays a crucial role for cellular metabolism, as it is imported in mitochondria and converted to acetyl-CoA to fuel the Krebs cycle, is used in transamination reactions, while also serving as a ROS scavenger, and in particular for H_2O_2 (Gray et al., 2014; Liu et al., 2018). Lactate is produced from pyruvate through the action of lactate dehydrogenase and is mostly released in the extracellular space. Systemically, the metabolite traffics through the bloodstream, reaches the liver and is converted back to glucose in a process known as gluconeogenesis. Conversion of pyruvate to lactate occurs at high rates when oxygen availability is limited (anaerobic conditions). It may however follow this route under normal oxygen conditions in a process called “aerobic glycolysis” or Warburg effect (**Figure 1**), named after the Nobel laurate Otto Warburg who described this phenomenon as a fingerprint of tumor physiology (Warburg, 1956). Although demonized because of its elevated levels in cancer, aerobic glycolysis also takes place in normal cells and tissues under conditions where a high proliferation rate is required, as it is also used to provide the cell with metabolic intermediates (Hume and Weidemann, 1979; Lunt and Vander Heiden, 2011; Liberti and Locasale, 2016; Prochownik and Wang, 2021).

Given that pyruvate is converted to lactate in the cytosol and then excreted, most efforts have centered on sensors that record cytosolic lactate or those that record lactate fluctuations in the extracellular milieu. An initial effort was with a mTFP1-Venus based FRET nanosensor harboring the lactate binding domain of the *E. coli* protein LldR, termed Laconic (LACtate Optical Nano Indicator from CECs), where upon lactate binding a decrease in FRET efficiency is recorded (San Martin et al., 2013). The sensor gave a low to modest response yet it was tested at a high concentration range (up to 10 mM); it was however pH sensitive, necessitating read out normalization. It is of particular importance for lactate sensors to validate their pH dependence since the extracellular concentration of lactate can be in the millimolar range (from 1 up to 20 mM or even higher in some cases) both *in vitro* and *in vivo* (Kuhr and Korf, 1988; Grist et al., 2018), pushing the limits of the sensor regarding its dynamic range but also its response in acidic environments. As a proof of principle, Barros and others used a nuclear–targeted version of this sensor in combination with the FRET–based glucose sensor FLII12Pglu700μδ6 (Takanaga et al., 2008) to monitor simultaneous glucose and lactate fluctuations in HEK cells after pharmacological inhibition of lactate export (Barros et al., 2013). The same sensor, along with the FRET–based pyruvate sensor Pyronic (San Martin et al., 2014) with a negative readout (reduced FRET upon pyruvate binding), has been applied to *in vivo* experiments using 2-photon and intravital imaging to monitor intracellular lactate levels in astrocytes and neurons after intravenous lactate administration. Adenoviral vectors carrying the sensors under the control of cell–type specific promoters, were injected in the primary somatosensory cortex of mice, with the data supporting a model of higher lactate uptake by neurons compared to astrocytes (Machler et al., 2016).

More recently, new lactate sensors have been developed based on a single permuted protein for lactate (termed Green Lindoblum) and pyruvate (termed Green Pegassos) (Harada et al., 2020), introducing part of the LldR protein (amino acids 86–260) for lactate or PdhR (1–260) for pyruvate between amino acids N145 and S146 of the GFP molecule that was used in the G-GECO calcium indicator (Zhao et al., 2011). These sensors exhibit increased specificity and good dynamic range of metabolite concentration (pyruvate saturation close to 1 mM and lactate exhibiting plateau close to 2 mM), with an increase in brightness that can reach up to 5-fold for Lindoblum at the highest concentration and 3-fold for Pegassos. Robert Campbell’s group recently reported a single protein fluorescent reporter named eLACCO1.1, created by inserting circularly permuted GFP (cpGFP) into the bacterial L-lactate binding protein TTHA0766 and improving the best candidate (out of 70 constructs) by directed evolution. The sensor appears to function as a dimer and requires Ca^{2+} concentration above 0.6 μM to function. The sensor exhibits a 5-fold increase in fluorescence in the presence of 10 mM lactate and was used for monitoring extracellular lactate in cells in culture but also in the brain (Nasu et al., 2021).

As mentioned before, pyruvate is a crucial metabolite that bridges carbohydrate metabolism to mitochondrial function and OXPHOS but even more, glycolysis and ROS scavenging. After the first FRET based reporter for pyruvate (San Martin et al., 2014), Bulusu and others created another one harboring the bacterial Pyruvate dehydrogenase complex repressor (PdhR) between mTurqoise and cpVenus 173 (Bulusu et al., 2017). Upon pyruvate binding the sensor exhibits negative read out (reduced FRET). Although a weak responder (maximum $\Delta R/R_0$ in the range of −15%), the construct was used to generate a transgenic mouse with ubiquitous expression of the reporter, called the PYRATES (PYRuvATE Sensor) mouse, attempting to link presomitic mesoderm (PSM) development with glycolytic activity. They used 2D cell culture models to record the pyruvate gradient within the expanding culture, finding a maximum reduction of FRET in the range of 16%. It should be noted though that the pyruvate concentration used to achieve such difference was supraphysiological (20 mM).

A BRET (Bioluminescence Resonance Energy Transfer) approach was undertaken to investigate the activity of the mitochondrial pyruvate carrier (MPC) (Bricker et al., 2012; Herzig et al., 2012) and its role in modulating the Warburg effect. The investigators tagged the MPC isoforms 1 and 2 with either luciferace (luc8) or Venus and titrated BRET efficiency in transfected cells under various conditions of exogenously added pyruvate in permeabilized cells (Compan et al., 2015). They named this sensor RESPYR and used it in HEK and INS-1 cells to investigate the Warburg effect using pharmacological approaches to control metabolite fluxes. A single protein fluorescent sensor (PyronicSF) was recently reported, using the same regulatory bacterial protein as in Pyronic, with greater dynamic range and sensitivity (almost 20-fold more sensitive than the initial FRET–based Pyronic sensor) and high selectivity (Arce-Molina et al., 2020). The investigators targeted the sensor to astrocyte mitochondria and used it to first estimate the concentration of pyruvate in mitochondria, reporting a concentration in the range of 30 μM (variable between cell types) and then extended their studies to monolayers of *Drosophila* perineurial glial cells, to investigate the role of the mitochondrial pyruvate carrier (MPC) in metabolism.

As mentioned at the beginning of this section, lactate and pyruvate have a tight relationship. Given that pyruvate stands at the crossroads of OXPHOS and glycolysis, it is advisable to measure *ratios* of lactate to pyruvate in every biochemical application. This is far from being trivial on the microscope stand. Recently though, a FRET based lactate to pyruvate sensor was reported from the same team that launched the Pyronic FRET sensor. The investigators used the *Bacillus subtillis* LutR transcriptional regulator that appears to bind pyruvate and lactate, and placed it between mTFP1 and cpVenus173. The Lapronic sensor (LActate/Pyruvate Ratio Optical Nano-Indicator from CECs) exhibits positive FRET values at increasing lactate concentration and negative readouts upon pyruvate increase (Galaz et al., 2020).

Citrate Sensor

Citrate is a product of the Krebs cycle, which bridges carbohydrate with lipid metabolism (**Figure 1**) (Zhao et al., 2016; Haferkamp et al., 2020). Soon after the finding that citrate lyase activity actually links the Krebs cycle with histone acetylation and gene expression (Wellen et al., 2009), a set of FRET–based (CFP/Venus) sensors for the metabolite were reported, using part of the histidine kinase CitA from *Klebsiella pneumoniae* that harbors a citrate sensing domain (Ewald et al., 2011). The sensors were initially tested *in vitro* and in bacteria, but the system was later used to measure cytosolic citrate fluctuation in pancreatic beta-cells as a function of CDK1 signaling (Gregg et al., 2019). Honda and Kirimura (Honda and Kirimura, 2013) created a different set of fluorescent indicators for citrate based on circular permutation, yet utilizing the citrate binding domain of CitA. These sensors (CF98) exhibit a high dynamic range (from 0.1 to 50 mM), yet their response is pH dependent, and normalization should be carried out. Following the single fluorescent protein strategy and based on circular permutation, Robert Campbell's group created a new set of citrate sensors by swapping the calmodulin (CaM)-RS20 domain from their previously reported Ca^{2+} indicator ncpGCaMP6s (Qian et al., 2019) with residues 4–133 of the CitAP domain of *Klebsiella pneumoniae*. Following directed evolution, they created two citrate sensors, one with increased signal upon citrate binding (Citron1) with a $\Delta F/Fmin \approx 9$ and one with inverse-response (reduced signal upon citrate binding), named Citroff1, with a $\Delta F/Fmin \approx 18$, compared to $\Delta F/Fmin \approx 1.1$ for the CF98 sensor (measurements done in isolated proteins in solution) (Zhao Y. et al., 2020).

Glutamine and a-Ketoglutarate

Glutamine is the most abundant amino acid in the blood stream and serves a central role in metabolism (Yoo et al., 2020). It can be converted intracellularly to glutamate by the action of glutaminase and then glutamate may be converted to a-ketoglutarate or used for transamination reactions (Coloff et al., 2016). Despite the increasing interest in investigating glutamine metabolism and one of its main derivatives (a-ketoglutarate), the palette of genetically encoded sensors remains poor. Regarding glutamine, there is one FRET-based sensor (Gruenwald et al., 2012), with Teal (mTFP) and Venus proteins as the FRET pair (FLIPQ-TV sensors), using GlnH (periplasmic glutamine binding) as actuator. These sensors exhibit fair stability within the physiological pH range, but their readout response falls below 10%, with glutamine concentration in the nano- to micro-molar range. The response was negligible in most cell lines tested, despite the increased extracellular glutamine concentration (up to 5 mM). An alternative FRET–based sensor harbors the bacterial GlnBP as cameleon with GFP. GlnBP is incorporating the unnatural fluorescent amino acid L-(7-hydroxycoumarin-4-yl)ethylglycine (CouA) by replacing the N138 codon with an amber codon (TAG) and co-transforming the *E. coli* strain C321.ΔA with the pEvol-CouRS tRNA ligase. The fluorescent amino acid serves as a donor and GFP as the acceptor. The sensor was tested *in vitro* and exhibited a maximum 1.9-fold FRET ratio increase, with a response curve titrated for glutamine concentration from 0 to 50 μM. As mentioned above, this type of sensor requires coexpression of the appropriate tRNA ligase and is a system that has to overcome various technical and biological obstacles before it can be applied successfully (Elia, 2021).

Regarding a-ketoglutarate, there are no valid reporters for mammalian or invertebrate systems at present. There have been efforts though to generate FRET based reporters that harbor either the NifA transcriptional regulator from *Azotobacter*, which is involved in the nitrogen fixation process and has a ketoglutarate binding domain (GAF) (Zhang et al., 2013) or the monomeric PII or NtcA proteins, both of which are involved in nitrogen metabolism and carry ketoglutarate binding domains in-between CFP and YFP (Luddecke et al., 2017; Chen et al., 2018). These sensors have been tested *in vitro* and in bacteria only, usually have a modest negative readout (FRET reduction) and may require additional factors, such as ATP, in order to operate, thus hampering their potential as tools for *in vivo* imaging in higher eukaryotes.

Glutamate

Glutamate has long been at the center of neuroscientists' attention, given that this is the most abundant amino acid in the brain and has a central role as a neurotransmitter. A number of glutamate transporters (EEAT1-3) have been characterized that exhibit cell–type preference for their expression. Glutamate is crucial for balanced brain function, as low levels of the molecule have been linked to serious pathological conditions, such as dementia, schizophrenia, and epileptic seizures amongst others (Zhou and Danbolt, 2014; Volk et al., 2015). As such, the molecule has attracted scientific interest for the development of genetically encoded biosensors to monitor extracellular levels. In fact, all available sensors for this amino acid were developed for neuroscience research with no particular emphasis regarding the intracellular effect of glutamate on amino acid balance and bioenergetics. A major problem though in the redesigning of the sensors is that glutamate concentration is compartment–specific, varying by orders of magnitude (Featherstone, 2010).

A series of FRET–based sensors have been developed making use of the glutamate/aspartate binding protein Ybej from *E. coli* and ECFP/Venus (or Citrine) molecules (Okumoto et al., 2005; Tsien, 2005). A follow-up resulted in a version of a glutamate–sensing fluorescent reporter (GluSnFR) improved by a factor of 6.2 over the initial version, and was used to monitor glutamate release in cultured hippocampal neurons with the sensor being targeted to the plasma membrane (Hires et al., 2008). Subsequently, Looger's lab created a single–protein fluorescent sensor based on permuted GFP intensity-based glutamate-sensing fluorescent reporter (iGluSnFR) again using the same YbeJ (or GltI periplasmic glutamate binding protein from bacteria as actual sensor), achieving a 6-fold increase in fluorescence upon addition of extracellular glutamate (Marvin et al., 2013). This was further improved by replacing eGFP with circularly permuted superfolded GFP, creating a series of SFiGluSnFR sensors that expand the concentration range and include chromatic variants. The iGluSnFR sensors were further improved [termed fast (iGluf) and ultrafast (iGluu)] so as to monitor the waves of glutamate release in synapses (Helassa et al., 2018), with speed of data recording in the range of 10 Hz. Robert Campbell's group have also reported a set of single–protein glutamate sensors, introducing red variants from circularly permuted mApple (R-iGluSnFR1) in the palette, but also with different topology, including non-circular permuted variants (Wu et al., 2018). These sensors were used to monitor extracellular glutamate in HEK cells with affinities in the micromolar range.

Sensors for Other Amino Acids

During the last few years, demand has increased for sensors monitoring the intracellular amino acid pool upon metabolic fluctuations. To this end, a set of single fluorophore histidine sensors was developed by embedding the bacterial periplasmic histidine sensing protein HisJ in the cpYFP, and exhibited a broad concentration range (up to 1 mM) and a response ranging from 2- to 5-fold (Hu et al., 2017). The sensors were also tested for measuring mitochondrial concentration of histidine, albeit in this case a careful pH titration had to be performed given the more alkaline environment of the mitochondrial matrix.

A sensor for L-methionine has recently been reported (Ko Wooseok, 2019). This tool is based on a methionine binding protein (MetQ) from *E. coli*, mutagenized to harbor four residues of the fluorescent unnatural amino acid CouA, which acts as a FRET donor. A fusion protein between the mutant MetQ and YFP results in a cameleon-type system that responds to the presence of methionine in the micromolar concentration range. The reporter was used to report the metabolite levels in FBS. Its capabilities though were demonstrated only *in vitro*, in a buffer system with an alkaline pH (9.0). Furthermore, the use of unnatural amino acids as FRET partners necessitates the use of wavelengths close to the UV range, which poses extra stress to cells.

A set of FRET–based (CFP/Venus) cysteine sensors has also been reported, based on the Cj0982 protein as the actual cysteine sensor, with a modest response at high cysteine concentrations (up to 20% increase in FRET efficiency upon binding of 1 mM cysteine) (Singh et al., 2020). Furthermore, Ameen and others created a lysine sensor with the lysine binding periplasmic protein (LAO) from *Salmonella* sandwiched between CFP and YFP (Ameen et al., 2016). The sensors exhibited a concentration range from micro- to milli-molar but their performance was tested in bacteria and yeast only. Recently a FRET–based sensor (CFP/YFP) was developed for BCAA (branched chain amino acids) that was named optical biosensor for leucine–isoleucine–valine (OLIVe) (Yoshida et al., 2019) using a leucine/isoleucine/valine-binding protein from *E. coli*. The sensor exhibited a good response in the presence of BCAAs, yet it also exhibited a modest response in the presence of cysteine or threonine and was affected by redox conditions. In general, setting up sensors for amino acids is not trivial given the common structural backbone. Most importantly, assessing the total pool of amino acids by cytoplasmic targeting of the sensor will probably give erroneous results, in particular under nutrient challenging conditions. The main hub of amino acid turnover and sensing is the lysosome, on the surface of which natural amino acid sensors are residing along with the main regulator of metabolism, mTORC1 (Rebsamen et al., 2015).

RNA-Based Sensors for S-Adenosylmethionine

S-Adenosylmethionine (SAM) is a widely studied metabolite that is a universal donor for methylation reactions and is also directly linked to methionine metabolism and ATP levels, thus impacting physiology and the epigenetic landscape (Lu and Mato, 2012; Janke et al., 2015). Sensors for SAM exhibit a particular interest and were the first to use riboswitches from the bacterial world (Batey, 2011) and implement RNA aptamers with fluorogenic substrates for visualization. Fluorogenic compounds are non-fluorescent (or dim) when in solution. Upon binding to the aptamer they become fluorescent with their spectra resembling those of fluorescent proteins (Bouhedda et al., 2017). One of the main problems in using RNA aptamers and riboswitches to construct sensors, is their low levels in mammalian systems, either due to low expression or to misfolding and rapid degradation. Samie Jaffrey's group from Cornell initially developed a sensor for SAM (Paige et al., 2012) using a stem sequence that acted as actuator along with the metabolite binding sequence, and the Spinach aptamer as a fluorescent reporter emitting in the green region upon binding of the DFHBI (3,5-difluoro-4-hydroxybenzylidene imidazolinone) fluorogenic substrate (Paige et al., 2011). This tool was initially used in bacteria, however, the same group recently introduced additional tools that have been implemented in mammalian cell culture systems. The first one is based on the SAM-III riboswitch and a Corn aptamer that forms dimers. Corn was engineered to be conditionally dimeric upon binding of S-Adenosylmethionine into its SAM-III riboswitch, causing binding of its fluorogenic substrate DFHO (3,5-difluoro-4-hydroxybenzylidene imidazolinone-2-oxime), which fluoresces in the yellow region (Kim and Jaffrey, 2019). The second tool

TABLE 1 | Listing of available biosensors for key metabolites.

Metabolite	Name	Sensor type	Biological system	Dynamic range	Reference
Glucose	FlipGlu	FRET	Cos-7 cells	Micromolar to millimolar	Fehr et al. (2003)
Glucose	Modified FlipGlu	FRET	HepG2 cells	Micromolar to millimolar	Takanaga et al. (2008)
Glucose	Green Glifons (various)	Single fluorescent protein	MIN pancreatic cells	Micromolar to millimolar	Mita et al. (2019)
Glucose	iGlucoSnFR	Circularly permuted GFP	Neuronal cells, *Drosophila*, Zebrafish	Micromolar to millimolar	Keller et al. (2021)
Glucose	iGlucoSnFR-TS	Fluorescence lifetime (FLIM)	Neuronal cells	Micromolar to millimolar	(Diaz-Garcia et al., 2017; Diaz-Garcia et al., 2019)
Sucrose/Trehalose/ Glucose	FLIPsuc-90µ (various)	FRET	*In vitro only*	Micromolar to millimolar	(Lager et al., 2006; Sadoine et al., 2020)
Pyruvate	Green Pegassos	Single permuted fluorescent protein	HEK293, Hela cells	Micromolar (higher end) to millimolar	Harada et al. (2020)
Pyruvate	Pyronic	FRET	Astrocytes, HEK293, T98G glioma cells	Micromolar to millimolar	San Martin et al. (2014)
Pyruvate	PYRATES	FRET	*Ex vivo* Presomitic cell culture model	Micromolar to millimolar	Bulusu et al. (2017)
Lactate	LACONIC	FRET	Astrocytes, HEK293, T98G glioma cells	Micromolar to millimolar	San Martin et al. (2013)
Lactate	Green Lindoblum	Single permuted fluorescent protein	HEK293, Hela cells	Micromolar (higher end) to millimolar	Harada et al. (2020)
Lactate	eLACCO1.1	Circularly permuted GFP	T98G cells and *ex vivo* mouse brain tissue imaging	Micromolar to millimolar	Nasu et al. (2021)
Pyruvate Carrier activity	RESPYR	BRET	HEK293 cell culture	Micromolar (higher end) to millimolar	Compan et al. (2015)
Pyruvate	PyronicSF	Circularly permuted GFP	Mouse astrocyte cell culture and *Drosophila* dissected brain	Micromolar (lower end) to millimolar	Arce-Molina et al. (2020)
Lactate/Pyruvate ratio	Lapronic	FRET	HEK293 cell culture	Micromolar (from lower end) to millimolar (lower end)	Galaz et al. (2020)
Citrate	Cit96µ	FRET	Islet β-cells in culture	Micromolar (from lower end) to millimolar (lower end	Gregg et al. (2019)
Citrate	CF98	Circularly permuted fluorescent protein	*In vitro*	Millimolar	Honda and Kirimura, (2013)
Citrate	Citron and Citroff	Circularly permuted fluorescent protein	*In vitro* and Hela cells	Micromolar (lower end) to high millimolar	Zhao et al. (2020b)
Glutamine	FLIPQ-TV	FRET	Cos-7 cells	Nanomolar to micromolar	Gruenwald et al. (2012)
Glutamate	GluSnFR	FRET	HEK, Hela, Neuronal cells	Micromolar	Hires et al. (2008)
Glutamate	iGluSnFR	Permuted fluorescent protein	Mouse retina and neural cells and zebrafish	Micromolar	Marvin et al. (2013)
Glutamate	iGluf and iGluu	Circularly permuted GFP	HEK293 and neuronal cells	Micromolar	Helassa et al. (2018)
Glutamate	R-iGluSnFR1 and G-iGluSnFR	Circularly permuted fluorescent proteins	HEK293 and hippocampal neurons	Nanomolar to micromolar	Wu et al. (2018)
Histidine	HisJ	Circularly permuted YFP	Hela cells	Nanomolar to micromolar	Hu et al. (2017)
Methionine	YFPMetQ-R189CouA	FRET	*In vitro* (Serum)	Micromolar	Ko Wooseok, (2019)
Cysteine	Cys-FS	FRET	Yeast, HEK293	Micromolar	Singh et al. (2020)
Lysine	FLIPK	FRET	*In vitro,* Yeast	Micromolar	Ameen et al. (2016)
leucine–isoleucine–valine	OLIVe	FRET	Hela	Micromolar to millimolar	Yoshida et al. (2019)
S-Adenosyl methionine (SAM)	Corn-SAM	Corn RNA aptamer/SAM Riboswitch	HEK293T	Micromolar to millimolar	Kim and Jaffrey, (2019)
S-Adenosyl methionine (SAM)	Red Broccoli-SAM sensor	Broccoli RNA aptamer/ SAM Riboswitch	HEK293	Micromolar to millimolar	Li et al. (2020)
S-Adenosyl methionine (SAM)	Tornado-Broccoli-SAM	Circularized RNA/Broccoli aptamer/SAM riboswitch	HEK293T	Micromolar to millimolar	Litke and Jaffrey, (2019)

The table includes mostly those biosensors that have been tested in higher eukaryotes. A brief description of the dynamic range is given. In many cases the reported biosensor includes a set of variants that cover the whole dynamic range with a complete description in the accompanying reference.

involves the Red Broccoli aptamer, which is a monomer and along with a SAM riboswitch can glow into the red region upon binding to its substrate, OBI (3,5-difluoro-4-hydroxybenzylidene-imidazolinone-2-oxime-1-benzoimidazole), which is cell permeable and can be used in cell culture systems (Li et al., 2020). The same group has also implemented a system termed "Tornado," based on circular RNAs. In this case, the RNA of interest is flanked by Twister ribozymes. Upon expression,

TABLE 2 | Basic requirements and features for the construction and use of a metabolite sensor.

Guidelines for the use of a metabolic sensor

Critical parameter	Important feature
Compartmentalization of metabolites	Concentration differences may exist for the same metabolite in different compartments (cytosol, mitochondria, nucleus, endoplasmic reticulum etc.).
Toolkit selection	Start by trying existing ones first! Permuted FP-based reporters are single molecule (read out as intensity difference) while FRET and BRET require 2 molecules. RNA aptamers may be used as single color readout (intensity) or as FRET pairs.
Sensitivity of the reporter	Always check if the dynamic range of the reporter falls within the physiological range of the system under study!
Specificity/selectivity of the reporter	One of the most essential features. Promiscuity (cross-reactivity with similar metabolites) must be kept at a minimum. A new reporter should first be tested *in vitro* regarding dynamic range and specificity.
Neutrality of the reporter	A reporter should be as "neutral" as possible (should not affect the metabolite levels, which is not always the case though!).
Reversibility of read out	It goes with affinity. The reporter should follow metabolite fluctuations with a minimum lag phase.
Environmental effect on the stability of the reporter	In most cases it is environment-dependent (pH, redox). Subcellular organelles exhibit major pH differences. Peroxisomes and mitochondrial matrix are on the highest end (pH ~8–8.5). Lysosomes and secretory vesicles are on the lowest pH range (pH~5.5 or lower), while Golgi is slightly acidic and cytosol and nucleus exhibit more neutral pH
Time scale of reporter maturation	This is of particular importance, especially when setting up "cameleon" type FRET reporters. Donor and acceptor should have comparable maturation lifetimes.
Photostability	Fluorescent proteins/tags prone to bleaching can give erroneous readouts especially for FRET based applications
Brightness	Permuted fluorescent proteins > FRET/BRET > RNA light-up aptamers (for mammalian systems).
Difficulty of read out/need for special equipment	Reporter tools are listed in descending order regarding "difficulty of read out": Lifetime-FRET > Intensity FRET > BRET > RNA light-up aptamers > Permuted fluorescent proteins.

ribozymes self-catalyze their cleavage, followed by ligation from the ubiquitously expressed RNA ligase RtcB, thus resulting in circularization of the RNA and increased stability. The system can harbor monomeric (Broccoli) but also dimeric aptamers (Corn) and was used with success in various cell lines to demonstrate detection of S-Adenosylmethionine (Litke and Jaffrey, 2019). The flexibility on the selection of the RNA aptamer and fluorogenic substrate also provides the benefit of multicolor imaging.

CONCLUSION AND PERSPECTIVE

Being able to "watch biochemistry in real time" is essential in order to integrate knowledge from diverse areas of higher eukaryote metabolism and mammals in particular. Delving into complex biochemical pathways requires an interdisciplinary effort to develop novel tools that can address the spatiotemporal organization of biochemistry. In other words, where are things happening and in what order? Sensors for monitoring metabolites in real time have therefore attracted much attention and although technology has allowed us the expansion of available tools in particular for higher eukaryotes (see **Table 1**), further development is essential. Although metabolism is a huge field, if we were to pinpoint some aspects of "immediate need" we would first retarget some of the existing sensors in other subcellular compartments, such as mitochondria and the nucleus. This however is not as trivial as it sounds, since metabolite concentrations may change drastically, as for instance in the case of glutamate, which exists at low concentration extracellularly (micromolar range) but it jumps to the millimolar range intracellularly (Moussawi et al., 2011). Hence, not only one has to pick the right sensor but chances are that the tool will have to be rebuilt, taking into consideration rules and limitations that escort the designing of the reporter system (Deuschle et al., 2005; Fehr et al., 2005) (see also **Table 2**). In addition, and despite the fact that some metabolites, such as glutamine and a-ketoglutarate and the enzymes involved in their metabolism are targets of intensive research, we are still lacking toolkits for *in vivo* monitoring, at least in cell culture systems. Although fluorescent proteins have been the major tool to setup reporters, RNA-based reporters incorporating tools from the bacterial world are rapidly coming to the fore. One of the main challenges with the RNA probes has been their proper folding and stability, as well as the availability of cell permeable substrates. Recent implementation of a combinatorial use of ribozyme, riboswitch and aptamer resulting in circular RNA with significant stability is expected to broaden our palette of available tools for metabolite sensing. Last but not least is the question regarding "which microscope to use"? Is there any space for super resolution in metabolite sensing? Super resolution has provided significant insight regarding, for instance, mitochondria structure overall, with recent data from live imaging with Airyscan further supporting the notion that the organelle is not uniform (Wolf et al., 2019) and a metabolic gradient may appear within the same mitochondrion. It seems likely that super resolution modalities will be the optical tools of choice in cases where we need to monitor the interactions and nanoclustering of enzymes involved in metabolic pathways. On the other hand, confocal, wide field and variants of selective plane illumination (SPIM) microscopy, will be the primary choice for monitoring metabolites, in particular for small animal imaging. Finally, for those cases where we need to image long term or a wider field of view is required, light sheet microscopy which exhibits fast imaging with reduced phototoxicity looks set to become the standard.

AUTHOR CONTRIBUTIONS

PC wrote the manuscript with input from CG and GP. All authors have reviewed and approved the manuscript.

REFERENCES

Almuhaideb, A., Papathanasiou, N., and Bomanji, J. (2011). 18F-FDG PET/CT Imaging in Oncology. *Ann. Saudi Med.* 31, 3–13. doi:10.5144/0256-4947.2011.3

Altea-Manzano, P., Cuadros, A. M., Broadfield, L. A., and Fendt, S. M. (2020). Nutrient Metabolism and Cancer in the *In Vivo* Context: a Metabolic Game of Give and Take. *EMBO Rep.* 21, e50635. doi:10.15252/embr.202050635

Ameen, S., Ahmad, M., Mohsin, M., Qureshi, M. I., Ibrahim, M. M., Abdin, M. Z., et al. (2016). Designing, Construction and Characterization of Genetically Encoded FRET-Based Nanosensor for Real Time Monitoring of Lysine Flux in Living Cells. *J. Nanobiotechnol* 14, 49. doi:10.1186/s12951-016-0204-y

Andersen, M. K., Høiem, T. S., Claes, B. S. R., Balluff, B., Martin-Lorenzo, M., Richardsen, E., et al. (2021). Spatial Differentiation of Metabolism in Prostate Cancer Tissue by MALDI-TOF MSI. *Cancer Metab.* 9, 9. doi:10.1186/s40170-021-00242-z

Arce-Molina, R., Cortés-Molina, F., Sandoval, P. Y., Galaz, A., Alegría, K., Schirmeier, S., et al. (2020). A Highly Responsive Pyruvate Sensor Reveals Pathway-Regulatory Role of the Mitochondrial Pyruvate Carrier MPC. *Elife* 9. doi:10.7554/eLife.53917

Baddeley, D., and Bewersdorf, J. (2018). Biological Insight from Super-resolution Microscopy: What We Can Learn from Localization-Based Images. *Annu. Rev. Biochem.* 87, 965–989. doi:10.1146/annurev-biochem-060815-014801

Bader, A. N., Hofman, E. G., Voortman, J., van Bergen en Henegouwen, P. M. P., and Gerritsen, H. C. (2009). Homo-FRET Imaging Enables Quantification of Protein Cluster Sizes with Subcellular Resolution. *Biophysical J.* 97, 2613–2622. doi:10.1016/j.bpj.2009.07.059

Bajar, B. T., Wang, E. S., Zhang, S., Lin, M. Z., and Chu, J. (2016). A Guide to Fluorescent Protein FRET Pairs. *Sensors (Basel)* 16. doi:10.3390/s16091488

Balsa, E., Soustek, M. S., Thomas, A., Cogliati, S., García-Poyatos, C., Martín-García, E., et al. (2019). ER and Nutrient Stress Promote Assembly of Respiratory Chain Supercomplexes through the PERK-eIF2α Axis. *Mol. Cel* 74, 877–890. doi:10.1016/j.molcel.2019.03.031

Barrick, J. E., and Breaker, R. R. (2007). The Distributions, Mechanisms, and Structures of Metabolite-Binding Riboswitches. *Genome Biol.* 8, R239. doi:10.1186/gb-2007-8-11-r239

Barros, L. F., San Martín, A., Sotelo-Hitschfeld, T., Lerchundi, R., Fernández-Moncada, I., Ruminot, I., et al. (2013). Small Is Fast: Astrocytic Glucose and Lactate Metabolism at Cellular Resolution. *Front. Cel. Neurosci.* 7, 27. doi:10.3389/fncel.2013.00027

Batey, R. T. (2011). Recognition of S -adenosylmethionine by Riboswitches. *WIREs RNA* 2, 299–311. doi:10.1002/wrna.63

Bermejo, C., Haerizadeh, F., Takanaga, H., Chermak, D., and Frommer, W. B. (2010). Dynamic Analysis of Cytosolic Glucose and ATP Levels in Yeast Using Optical Sensors. *Biochem. J.* 432, 399–406. doi:10.1042/bj20100946

Berney, C., and Danuser, G. (2003). FRET or No FRET: a Quantitative Comparison. *Biophysical J.* 84, 3992–4010. doi:10.1016/s0006-3495(03)75126-1

Betz, C., and Hall, M. N. (2013). Where Is mTOR and what Is it Doing There? *J. Cel Biol* 203, 563–574. doi:10.1083/jcb.201306041

Bouhedda, F., Autour, A., and Ryckelynck, M. (2017). Light-Up RNA Aptamers and Their Cognate Fluorogens: From Their Development to Their Applications. *Int. J. Mol. Sci.* 19. doi:10.3390/ijms19010044

Bricker, D. K., Taylor, E. B., Schell, J. C., Orsak, T., Boutron, A., Chen, Y.-C., et al. (2012). A Mitochondrial Pyruvate Carrier Required for Pyruvate Uptake in Yeast, Drosophila , and Humans. *Science* 337, 96–100. doi:10.1126/science.1218099

Bulusu, V., Prior, N., Snaebjornsson, M. T., Kuehne, A., Sonnen, K. F., Kress, J., et al. (2017). Spatiotemporal Analysis of a Glycolytic Activity Gradient Linked to Mouse Embryo Mesoderm Development. *Developmental Cel* 40, 331–341. doi:10.1016/j.devcel.2017.01.015

CahillCahill, G. F. J. (2006). Fuel Metabolism in Starvation. *Annu. Rev. Nutr.* 26, 1–22. doi:10.1146/annurev.nutr.26.061505.111258

Carey, B. W., Finley, L. W. S., Cross, J. R., Allis, C. D., and Thompson, C. B. (2015). Intracellular α-ketoglutarate Maintains the Pluripotency of Embryonic Stem Cells. *Nature* 518, 413–416. doi:10.1038/nature13981

Chadt, A., and Al-Hasani, H. (2020). Glucose Transporters in Adipose Tissue, Liver, and Skeletal Muscle in Metabolic Health and Disease. *Pflugers Arch. - Eur. J. Physiol.* 472, 1273–1298. doi:10.1007/s00424-020-02417-x

Chantranupong, L., Wolfson, R. L., and Sabatini, D. M. (2015). Nutrient-sensing Mechanisms across Evolution. *Cell* 161, 67–83. doi:10.1016/j.cell.2015.02.041

Chen, H. L., Latifi, A., Zhang, C. C., and Bernard, C. S. (2018). Biosensors-Based *In Vivo* Quantification of 2-Oxoglutarate in Cyanobacteria and Proteobacteria. *Life (Basel)* 8. doi:10.3390/life8040051

Chen, L., Zhong, F., and Zhu, J. (2020). Bridging Targeted and Untargeted Mass Spectrometry-Based Metabolomics via Hybrid Approaches. *Metabolites* 10. doi:10.3390/metabo10090348

Coloff, J. L., Murphy, J. P., Braun, C. R., Harris, I. S., Shelton, L. M., Kami, K., et al. (2016). Differential Glutamate Metabolism in Proliferating and Quiescent Mammary Epithelial Cells. *Cel Metab.* 23, 867–880. doi:10.1016/j.cmet.2016.03.016

Compan, V., Pierredon, S., Vanderperre, B., Krznar, P., Marchiq, I., Zamboni, N., et al. (2015). Monitoring Mitochondrial Pyruvate Carrier Activity in Real Time Using a BRET-Based Biosensor: Investigation of the Warburg Effect. *Mol. Cel* 59, 491–501. doi:10.1016/j.molcel.2015.06.035

Datta, R., Heaster, T. M., Sharick, J. T., Gillette, A. A., and Skala, M. C. (2020). Fluorescence Lifetime Imaging Microscopy: Fundamentals and Advances in Instrumentation, Analysis, and Applications. *J. Biomed. Opt.* 25, 1–43. doi:10.1117/1.jbo.25.7.071203

Deuschle, K., Fehr, M., Hilpert, M., Lager, I., Lalonde, S., Looger, L. L., et al. (2005). Genetically Encoded Sensors for Metabolites. *Cytometry* 64A, 3–9. doi:10.1002/cyto.a.20119

Díaz-García, C. M., Lahmann, C., Martínez-François, J. R., Li, B., Koveal, D., Nathwani, N., et al. (2019). Quantitative *In Vivo* Imaging of Neuronal Glucose Concentrations with a Genetically Encoded Fluorescence Lifetime Sensor. *J. Neurosci. Res.* 97, 946–960. doi:10.1002/jnr.24433

Díaz-García, C. M., Mongeon, R., Lahmann, C., Koveal, D., Zucker, H., and Yellen, G. (2017). Neuronal Stimulation Triggers Neuronal Glycolysis and Not Lactate Uptake. *Cel Metab.* 26, 361–374. doi:10.1016/j.cmet.2017.06.021

Efeyan, A., Comb, W. C., and Sabatini, D. M. (2015). Nutrient-sensing Mechanisms and Pathways. *Nature* 517, 302–310. doi:10.1038/nature14190

Elia, N. (2021). Using Unnatural Amino Acids to Selectively Label Proteins for Cellular Imaging: a Cell Biologist Viewpoint. *Febs J.* 288, 1107–1117. doi:10.1111/febs.15477

Ewald, J. C., Reich, S., Baumann, S., Frommer, W. B., and Zamboni, N. (2011). Engineering Genetically Encoded Nanosensors for Real-Time *In Vivo* Measurements of Citrate Concentrations. *PLoS One* 6, e28245. doi:10.1371/journal.pone.0028245

Featherstone, D. E. (2010). Intercellular Glutamate Signaling in the Nervous System and beyond. *ACS Chem. Neurosci.* 1, 4–12. doi:10.1021/cn900006n

Fehr, M., Lalonde, S., Lager, I., Wolff, M. W., and Frommer, W. B. (2003). Imaging of the Dynamics of Glucose Uptake in the Cytosol of COS-7 Cells by Fluorescent Nanosensors. *J. Biol. Chem.* 278, 19127–19133. doi:10.1074/jbc.m301333200

Fehr, M., Okumoto, S., Deuschle, K., Lager, I., Looger, L. L., Persson, J., et al. (2005). Development and Use of Fluorescent Nanosensors for Metabolite Imaging in Living Cells. *Biochem. Soc. Trans.* 33, 287–290. doi:10.1042/bst0330287

Galaz, A., Cortés-Molina, F., Arce-Molina, R., Romero-Gómez, I., Mardones, G. A., Felipe Barros, L., et al. (2020). Imaging of the Lactate/Pyruvate Ratio Using a Genetically Encoded Förster Resonance Energy Transfer Indicator. *Anal. Chem.* 92, 10643–10650. doi:10.1021/acs.analchem.0c01741

Gerich, J. E., Meyer, C., Woerle, H. J., and Stumvoll, M. (2001). Renal Gluconeogenesis: its Importance in Human Glucose Homeostasis. *Diabetes Care* 24, 382–391. doi:10.2337/diacare.24.2.382

Gray, L. R., Tompkins, S. C., and Taylor, E. B. (2014). Regulation of Pyruvate Metabolism and Human Disease. *Cell. Mol. Life Sci.* 71, 2577–2604. doi:10.1007/s00018-013-1539-2

Gregg, T., Sdao, S. M., Dhillon, R. S., Rensvold, J. W., Lewandowski, S. L., Pagliarini, D. J., et al. (2019). Obesity-dependent CDK1 Signaling Stimulates Mitochondrial Respiration at Complex I in Pancreatic β-cells. *J. Biol. Chem.* 294, 4656–4666. doi:10.1074/jbc.ra118.006085

Grist, J. T., Jarvis, L. B., Georgieva, Z., Thompson, S., Kaur Sandhu, H., Burling, K., et al. (2018). Extracellular Lactate: A Novel Measure of T Cell Proliferation. *J.I.* 200, 1220–1226. doi:10.4049/jimmunol.1700886

Gruenwald, K., Holland, J. T., Stromberg, V., Ahmad, A., Watcharakichkorn, D., and Okumoto, S. (2012). Visualization of Glutamine Transporter Activities in

Living Cells Using Genetically Encoded Glutamine Sensors. *PLoS One* 7, e38591. doi:10.1371/journal.pone.0038591

Haferkamp, S., Drexler, K., Federlin, M., Schlitt, H. J., Berneburg, M., Adamski, J., et al. (2020). Extracellular Citrate Fuels Cancer Cell Metabolism and Growth. *Front. Cel Dev. Biol.* 8, 602476. doi:10.3389/fcell.2020.602476

Hallberg, Z. F., Su, Y., Kitto, R. Z., and Hammond, M. C. (2017). Engineering and *In Vivo* Applications of Riboswitches. *Annu. Rev. Biochem.* 86, 515–539. doi:10.1146/annurev-biochem-060815-014628

Harada, K., Chihara, T., Hayasaka, Y., Mita, M., Takizawa, M., Ishida, K., et al. (2020). Green Fluorescent Protein-Based Lactate and Pyruvate Indicators Suitable for Biochemical Assays and Live Cell Imaging. *Sci. Rep.* 10, 19562. doi:10.1038/s41598-020-76440-4

Helassa, N., Dürst, C. D., Coates, C., Kerruth, S., Arif, U., Schulze, C., et al. (2018). Ultrafast Glutamate Sensors Resolve High-Frequency Release at Schaffer Collateral Synapses. *Proc. Natl. Acad. Sci. USA* 115, 5594–5599. doi:10.1073/pnas.1720648115

Henkin, T. M. (2008). Riboswitch RNAs: Using RNA to Sense Cellular Metabolism. *Genes Dev.* 22, 3383–3390. doi:10.1101/gad.1747308

Herzig, S., Raemy, E., Montessuit, S., Veuthey, J.-L., Zamboni, N., Westermann, B., et al. (2012). Identification and Functional Expression of the Mitochondrial Pyruvate Carrier. *Science* 337, 93–96. doi:10.1126/science.1218530

Hires, S. A., Zhu, Y., and Tsien, R. Y. (2008). Optical Measurement of Synaptic Glutamate Spillover and Reuptake by Linker Optimized Glutamate-Sensitive Fluorescent Reporters. *Proc. Natl. Acad. Sci.* 105, 4411–4416. doi:10.1073/pnas.0712008105

Honda, Y., and Kirimura, K. (2013). Generation of Circularly Permuted Fluorescent-Protein-Based Indicators for *In Vitro* and *In Vivo* Detection of Citrate. *PLoS One* 8, e64597. doi:10.1371/journal.pone.0064597

Hosios, A. M., and Vander Heiden, M. G. (2018). The Redox Requirements of Proliferating Mammalian Cells. *J. Biol. Chem.* 293, 7490–7498. doi:10.1074/jbc.tm117.000239

Hu, H., Gu, Y., Xu, L., Zou, Y., Wang, A., Tao, R., et al. (2017). A Genetically Encoded Toolkit for Tracking Live-Cell Histidine Dynamics in Space and Time. *Sci. Rep.* 7, 43479. doi:10.1038/srep43479

Hume, D. A., and Weidemann, M. J. (1979). Role and Regulation of Glucose Metabolism in Proliferating Cells. *J. Natl. Cancer Inst.* 62, 3–8.

Jacquemyn, J., Cascalho, A., and Goodchild, R. E. (2017). The Ins and Outs of Endoplasmic Reticulum-controlled Lipid Biosynthesis. *EMBO Rep.* 18, 1905–1921. doi:10.15252/embr.201643426

Janke, R., Dodson, A. E., and Rine, J. (2015). Metabolism and Epigenetics. *Annu. Rev. Cel Dev. Biol.* 31, 473–496. doi:10.1146/annurev-cellbio-100814-125544

Jiang, L., Boufersaoui, A., Yang, C., Ko, B., Rakheja, D., Guevara, G., et al. (2017). Quantitative Metabolic Flux Analysis Reveals an Unconventional Pathway of Fatty Acid Synthesis in Cancer Cells Deficient for the Mitochondrial Citrate Transport Protein. *Metab. Eng.* 43, 198–207. doi:10.1016/j.ymben.2016.11.004

Kaser, A., Zeissig, S., and Blumberg, R. S. (2010). Inflammatory Bowel Disease. *Annu. Rev. Immunol.* 28, 573–621. doi:10.1146/annurev-immunol-030409-101225

Kayano, T., Burant, C. F., Fukumoto, H., Gould, G. W., Fan, Y. S., Eddy, R. L., et al. (1990). Human Facilitative Glucose Transporters. Isolation, Functional Characterization, and Gene Localization of cDNAs Encoding an Isoform (GLUT5) Expressed in Small Intestine, Kidney, Muscle, and Adipose Tissue and an Unusual Glucose Transporter Pseudogene-like Sequence (GLUT6). *J. Biol. Chem.* 265, 13276–13282. doi:10.1016/s0021-9258(19)38295-x

Keller, J. P., Marvin, J. S., Lacin, H., Lemon, W. C., Shea, J., Kim, S., et al. (2021). *In Vivo* glucose Imaging in Multiple Model Organisms with an Engineered Single-Wavelength Sensor. *Cel Rep.* 35, 109284. doi:10.1016/j.celrep.2021.109284

Kim, H., and Jaffrey, S. R. (2019). A Fluorogenic RNA-Based Sensor Activated by Metabolite-Induced RNA Dimerization. *Cel Chem. Biol.* 26, 1725–1731. doi:10.1016/j.chembiol.2019.09.013

Ko, W., and Lee, H. S. (2019). Development of Specificl-Methionine Sensors by FRET-Based Protein Engineering. *RSC Adv.* 9, 15648–15656. doi:10.1039/c9ra01317b

Kobayashi, H., and Bouvier, M. (2021). Bioluminescence Resonance Energy Transfer (BRET) Imaging in Living Cells: Image Acquisition and Quantification. *Methods Mol. Biol.* 2274, 305–314. doi:10.1007/978-1-0716-1258-3_26

Kobayashi, H., Picard, L.-P., Schönegge, A.-M., and Bouvier, M. (2019). Bioluminescence Resonance Energy Transfer-Based Imaging of Protein-Protein Interactions in Living Cells. *Nat. Protoc.* 14, 1084–1107. doi:10.1038/s41596-019-0129-7

Kostyuk, A. I., Demidovich, A. D., Kotova, D. A., Belousov, V. V., and Bilan, D. S. (2019). Circularly Permuted Fluorescent Protein-Based Indicators: History, Principles, and Classification. *Int. J. Mol. Sci.* 20. doi:10.3390/ijms20174200

Kostyuk, A. I., Panova, A. S., Kokova, A. D., Kotova, D. A., Maltsev, D. I., Podgorny, O. V., et al. (2020). *In Vivo* Imaging with Genetically Encoded Redox Biosensors. *Int. J. Mol. Sci.* 21. doi:10.3390/ijms21218164

Kuhr, W. G., and Korf, J. (1988). Extracellular Lactic Acid as an Indicator of Brain Metabolism: Continuous On-Line Measurement in Conscious, Freely Moving Rats with Intrastriatal Dialysis. *J. Cereb. Blood Flow Metab.* 8, 130–137. doi:10.1038/jcbfm.1988.17

Lager, I., Looger, L. L., Hilpert, M., Lalonde, S., and Frommer, W. B. (2006). Conversion of a Putative Agrobacterium Sugar-Binding Protein into a FRET Sensor with High Selectivity for Sucrose. *J. Biol. Chem.* 281, 30875–30883. doi:10.1074/jbc.m605257200

Lewis, C. A., Parker, S. J., Fiske, B. P., Mccloskey, D., Gui, D. Y., Green, C. R., et al. (2014). Tracing Compartmentalized NADPH Metabolism in the Cytosol and Mitochondria of Mammalian Cells. *Mol. Cel* 55, 253–263. doi:10.1016/j.molcel.2014.05.008

Li, X., Mo, L., Litke, J. L., Dey, S. K., Suter, S. R., and Jaffrey, S. R. (2020). Imaging Intracellular S-Adenosyl Methionine Dynamics in Live Mammalian Cells with a Genetically Encoded Red Fluorescent RNA-Based Sensor. *J. Am. Chem. Soc.* 142, 14117–14124. doi:10.1021/jacs.0c02931

Liberti, M. V., and Locasale, J. W. (2016). The Warburg Effect: How Does it Benefit Cancer Cells? *Trends Biochem. Sci.* 41, 211–218. doi:10.1016/j.tibs.2015.12.001

Lindenburg, L., and Merkx, M. (2014). Engineering Genetically Encoded FRET Sensors. *Sensors* 14, 11691–11713. doi:10.3390/s140711691

Litke, J. L., and Jaffrey, S. R. (2019). Highly Efficient Expression of Circular RNA Aptamers in Cells Using Autocatalytic Transcripts. *Nat. Biotechnol.* 37, 667–675. doi:10.1038/s41587-019-0090-6

Liu, X., Cooper, D. E., Cluntun, A. A., Warmoes, M. O., Zhao, S., Reid, M. A., et al. (2018). Acetate Production from Glucose and Coupling to Mitochondrial Metabolism in Mammals. *Cell* 175, 502–513. doi:10.1016/j.cell.2018.08.040

Lu, S. C., and Mato, J. M. (2012). S-adenosylmethionine in Liver Health, Injury, and Cancer. *Physiol. Rev.* 92, 1515–1542. doi:10.1152/physrev.00047.2011

Lüddecke, J., Francois, L., Spät, P., Watzer, B., Chilczuk, T., Poschet, G., et al. (2017). PII Protein-Derived FRET Sensors for Quantification and Live-Cell Imaging of 2-Oxoglutarate. *Sci. Rep.* 7, 1437. doi:10.1038/s41598-017-01440-w

Lunt, S. Y., and Vander Heiden, M. G. (2011). Aerobic Glycolysis: Meeting the Metabolic Requirements of Cell Proliferation. *Annu. Rev. Cel Dev. Biol.* 27, 441–464. doi:10.1146/annurev-cellbio-092910-154237

Mächler, P., Wyss, M. T., Elsayed, M., Stobart, J., Gutierrez, R., von Faber-Castell, A., et al. (2016). *In Vivo* Evidence for a Lactate Gradient from Astrocytes to Neurons. *Cel Metab.* 23, 94–102. doi:10.1016/j.cmet.2015.10.010

Maddocks, O. D. K., Labuschagne, C. F., and Vousden, K. H. (2014). Localization of NADPH Production: a Wheel within a Wheel. *Mol. Cel* 55, 158–160. doi:10.1016/j.molcel.2014.07.001

Marvin, J. S., Borghuis, B. G., Tian, L., Cichon, J., Harnett, M. T., Akerboom, J., et al. (2013). An Optimized Fluorescent Probe for Visualizing Glutamate Neurotransmission. *Nat. Methods* 10, 162–170. doi:10.1038/nmeth.2333

Mita, M., Ito, M., Harada, K., Sugawara, I., Ueda, H., Tsuboi, T., et al. (2019). Green Fluorescent Protein-Based Glucose Indicators Report Glucose Dynamics in Living Cells. *Anal. Chem.* 91, 4821–4830. doi:10.1021/acs.analchem.9b00447

Miyawaki, A., Llopis, J., Heim, R., Mccaffery, J. M., Adams, J. A., Ikura, M., et al. (1997). Fluorescent Indicators for Ca2+based on green Fluorescent Proteins and Calmodulin. *Nature* 388, 882–887. doi:10.1038/42264

Mot, A. I., Liddell, J. R., White, A. R., and Crouch, P. J. (2016). Circumventing the Crabtree Effect: A Method to Induce Lactate Consumption and Increase Oxidative Phosphorylation in Cell Culture. *Int. J. Biochem. Cel Biol.* 79, 128–138. doi:10.1016/j.biocel.2016.08.029

Moussawi, K., Riegel, A., Nair, S., and Kalivas, P. W. (2011). Extracellular Glutamate: Functional Compartments Operate in Different Concentration Ranges. *Front. Syst. Neurosci.* 5, 94. doi:10.3389/fnsys.2011.00094

Nasu, Y., Murphy-Royal, C., Wen, Y., Haidey, J., Molina, M. R. S., Aggarwal, A., et al. (2021). A Genetically Encoded Fluorescent Biosensor for Extracellular L-Lactate. *Nat. Commun.* 12, 7058. doi:10.1038/s41467-021-27332-2

Navale, A. M., and Paranjape, A. N. (2016). Glucose Transporters: Physiological and Pathological Roles. *Biophys. Rev.* 8, 5–9. doi:10.1007/s12551-015-0186-2

Oeggl, R., Neumann, T., Gätgens, J., Romano, D., Noack, S., and Rother, D. (2018). Citrate as Cost-Efficient NADPH Regenerating Agent. *Front. Bioeng. Biotechnol.* 6, 196. doi:10.3389/fbioe.2018.00196

Okumoto, S., Looger, L. L., Micheva, K. D., Reimer, R. J., Smith, S. J., and Frommer, W. B. (2005). Detection of Glutamate Release from Neurons by Genetically Encoded Surface-Displayed FRET Nanosensors. *Proc. Natl. Acad. Sci.* 102, 8740–8745. doi:10.1073/pnas.0503274102

Paige, J. S., Nguyen-Duc, T., Song, W., and Jaffrey, S. R. (2012). Fluorescence Imaging of Cellular Metabolites with RNA. *Science* 335, 1194. doi:10.1126/science.1218298

Paige, J. S., Wu, K. Y., and Jaffrey, S. R. (2011). RNA Mimics of green Fluorescent Protein. *Science* 333, 642–646. doi:10.1126/science.1207339

Parks, S. K., Mueller-Klieser, W., and Pouysségur, J. (2020). Lactate and Acidity in the Cancer Microenvironment. *Annu. Rev. Cancer Biol.* 4, 141–158. doi:10.1146/annurev-cancerbio-030419-033556

Pavlova, N. N., and Thompson, C. B. (2016). The Emerging Hallmarks of Cancer Metabolism. *Cel Metab.* 23, 27–47. doi:10.1016/j.cmet.2015.12.006

Prochownik, E. V., and Wang, H. (2021). The Metabolic Fates of Pyruvate in Normal and Neoplastic Cells. *Cells* 10. doi:10.3390/cells10040762

Qian, Y., Rancic, V., Wu, J., Ballanyi, K., and Campbell, R. E. (2019). A Bioluminescent Ca 2+ Indicator Based on a Topological Variant of GCaMP6s. *Chembiochem* 20, 516–520. doi:10.1002/cbic.201800255

Rebsamen, M., Pochini, L., Stasyk, T., de Araújo, M. E. G., Galluccio, M., Kandasamy, R. K., et al. (2015). SLC38A9 Is a Component of the Lysosomal Amino Acid Sensing Machinery that Controls mTORC1. *Nature* 519, 477–481. doi:10.1038/nature14107

Ruff, K. M., Muhammad, A., Mccown, P. J., Breaker, R. R., and Strobel, S. A. (2016). Singlet glycine Riboswitches Bind Ligand as Well as Tandem Riboswitches. *RNA* 22, 1728–1738. doi:10.1261/rna.057935.116

Sabatini, D. M. (2017). Twenty-five Years of mTOR: Uncovering the Link from Nutrients to Growth. *Proc. Natl. Acad. Sci. USA* 114, 11818–11825. doi:10.1073/pnas.1716173114

Sadoine, M., Reger, M., Wong, K. M., and Frommer, W. B. (2020). Affinity Series of Genetically Encoded High Sensitivity Förster Resonance Energy Transfer Sensors for Sucrose. *ACS Sens.* 6, 1779–1784. doi:10.1021/acssensors.0c02495

Sahl, S. J., Hell, S. W., and Jakobs, S. (2017). Fluorescence Nanoscopy in Cell Biology. *Nat. Rev. Mol. Cel Biol* 18, 685–701. doi:10.1038/nrm.2017.71

San Martín, A., Ceballo, S., Baeza-Lehnert, F., Lerchundi, R., Valdebenito, R., Contreras-Baeza, Y., et al. (2014). Imaging Mitochondrial Flux in Single Cells with a FRET Sensor for Pyruvate. *PLoS One* 9, e85780. doi:10.1371/journal.pone.0085780

San Martín, A., Ceballo, S., Ruminot, I., Lerchundi, R., Frommer, W. B., and Barros, L. F. (2013). A Genetically Encoded FRET Lactate Sensor and its Use to Detect the Warburg Effect in Single Cancer Cells. *PLoS One* 8, e57712. doi:10.1371/journal.pone.0057712

Sancak, Y., Bar-Peled, L., Zoncu, R., Markhard, A. L., Nada, S., and Sabatini, D. M. (2010). Ragulator-Rag Complex Targets mTORC1 to the Lysosomal Surface and Is Necessary for its Activation by Amino Acids. *Cell* 141, 290–303. doi:10.1016/j.cell.2010.02.024

Sancak, Y., Peterson, T. R., Shaul, Y. D., Lindquist, R. A., Thoreen, C. C., Bar-Peled, L., et al. (2008). The Rag GTPases Bind Raptor and Mediate Amino Acid Signaling to mTORC1. *Science* 320, 1496–1501. doi:10.1126/science.1157535

Schell, J. C., Wisidagama, D. R., Bensard, C., Zhao, H., Wei, P., Tanner, J., et al. (2017). Control of Intestinal Stem Cell Function and Proliferation by Mitochondrial Pyruvate Metabolism. *Nat. Cel Biol* 19, 1027–1036. doi:10.1038/ncb3593

Shaner, N. C., Steinbach, P. A., and Tsien, R. Y. (2005). A Guide to Choosing Fluorescent Proteins. *Nat. Methods* 2, 905–909. doi:10.1038/nmeth819

Sherlock, M. E., Sudarsan, N., Stav, S., and Breaker, R. R. (2018). Tandem Riboswitches Form a Natural Boolean Logic Gate to Control Purine Metabolism in Bacteria. *Elife* 7. doi:10.7554/eLife.33908

Shui, B., Wang, Q., Lee, F., Byrnes, L. J., Chudakov, D. M., Lukyanov, S. A., et al. (2011). Circular Permutation of Red Fluorescent Proteins. *PLoS One* 6, e20505. doi:10.1371/journal.pone.0020505

Singh, S., Sharma, M. P., and Ahmad, A. (2020). Construction and Characterization of Protein-Based Cysteine Nanosensor for the Real Time Measurement of Cysteine Level in Living Cells. *Int. J. Biol. Macromolecules* 143, 273–284. doi:10.1016/j.ijbiomac.2019.12.025

Sniegowski, T., Korac, K., Bhutia, Y. D., and Ganapathy, V. (2021). SLC6A14 and SLC38A5 Drive the Glutaminolysis and Serine-Glycine-One-Carbon Pathways in Cancer. *Pharmaceuticals (Basel)* 14. doi:10.3390/ph14030216

Takanaga, H., Chaudhuri, B., and Frommer, W. B. (2008). GLUT1 and GLUT9 as Major Contributors to Glucose Influx in HepG2 Cells Identified by a High Sensitivity Intramolecular FRET Glucose Sensor. *Biochim. Biophys. Acta (Bba) - Biomembranes* 1778, 1091–1099. doi:10.1016/j.bbamem.2007.11.015

Trachman, R. J., 3rd, Cojocaru, R., Wu, D., Piszczek, G., Ryckelynck, M., Unrau, P. J., et al. (2020). Structure-Guided Engineering of the Homodimeric Mango-IV Fluorescence Turn-On Aptamer Yields an RNA FRET Pair. *Structure* 28, 776–785. doi:10.1016/j.str.2020.04.007

Trachman, R. J., 3rd, Demeshkina, N. A., Lau, M. W. L., Panchapakesan, S. S. S., Jeng, S. C. Y., Unrau, P. J., et al. (2017a). Structural Basis for High-Affinity Fluorophore Binding and Activation by RNA Mango. *Nat. Chem. Biol.* 13, 807–813. doi:10.1038/nchembio.2392

Trachman, R. J., 3rd, Truong, L., and Ferré-D'Amaré, A. R. (2017b). Structural Principles of Fluorescent RNA Aptamers. *Trends Pharmacol. Sci.* 38, 928–939. doi:10.1016/j.tips.2017.06.007

Truong, L., and Ferré-D'Amaré, A. R. (2019). From Fluorescent Proteins to Fluorogenic RNAs: Tools for Imaging Cellular Macromolecules. *Protein Sci.* 28, 1374–1386. doi:10.1002/pro.3632

Tsien, R. Y. (2005). Building and Breeding Molecules to Spy on Cells and Tumors. *FEBS Lett.* 579, 927–932. doi:10.1016/j.febslet.2004.11.025

Tsogtbaatar, E., Landin, C., Minter-Dykhouse, K., and Folmes, C. D. L. (2020). Energy Metabolism Regulates Stem Cell Pluripotency. *Front. Cel Dev. Biol.* 8, 87. doi:10.3389/fcell.2020.00087

Valvona, C. J., Fillmore, H. L., Nunn, P. B., and Pilkington, G. J. (2016). The Regulation and Function of Lactate Dehydrogenase A: Therapeutic Potential in Brain Tumor. *Brain Pathol.* 26, 3–17. doi:10.1111/bpa.12299

Vogel, C., and Morea, V. (2006). Duplication, Divergence and Formation of Novel Protein Topologies. *Bioessays* 28, 973–978. doi:10.1002/bies.20474

Volk, L., Chiu, S.-L., Sharma, K., and Huganir, R. L. (2015). Glutamate Synapses in Human Cognitive Disorders. *Annu. Rev. Neurosci.* 38, 127–149. doi:10.1146/annurev-neuro-071714-033821

Wan, Y., Mcdole, K., and Keller, P. J. (2019). Light-Sheet Microscopy and its Potential for Understanding Developmental Processes. *Annu. Rev. Cel Dev. Biol.* 35, 655–681. doi:10.1146/annurev-cellbio-100818-125311

Wanders, R. J. A., Vaz, F. M., Waterham, H. R., and Ferdinandusse, S. (2020). Fatty Acid Oxidation in Peroxisomes: Enzymology, Metabolic Crosstalk with Other Organelles and Peroxisomal Disorders. *Adv. Exp. Med. Biol.* 1299, 55–70. doi:10.1007/978-3-030-60204-8_5

Warburg, O. (1956). On the Origin of Cancer Cells. *Science* 123, 309–314. doi:10.1126/science.123.3191.309

Warner, K. D., Chen, M. C., Song, W., Strack, R. L., Thorn, A., Jaffrey, S. R., et al. (2014). Structural Basis for Activity of Highly Efficient RNA Mimics of green Fluorescent Protein. *Nat. Struct. Mol. Biol.* 21, 658–663. doi:10.1038/nsmb.2865

Warner, K. D., Sjekloća, L., Song, W., Filonov, G. S., Jaffrey, S. R., and Ferré-D'Amaré, A. R. (2017). A Homodimer Interface without Base Pairs in an RNA Mimic of Red Fluorescent Protein. *Nat. Chem. Biol.* 13, 1195–1201. doi:10.1038/nchembio.2475

Warren, S., Margineanu, A., Katan, M., Dunsby, C., and French, P. (2015). Homo-FRET Based Biosensors and Their Application to Multiplexed Imaging of Signalling Events in Live Cells. *Ijms* 16, 14695–14716. doi:10.3390/ijms160714695

Wellen, K. E., Hatzivassiliou, G., Sachdeva, U. M., Bui, T. V., Cross, J. R., and Thompson, C. B. (2009). ATP-citrate Lyase Links Cellular Metabolism to Histone Acetylation. *Science* 324, 1076–1080. doi:10.1126/science.1164097

Wise, D. R., Deberardinis, R. J., Mancuso, A., Sayed, N., Zhang, X.-Y., Pfeiffer, H. K., et al. (2008). Myc Regulates a Transcriptional Program that Stimulates Mitochondrial Glutaminolysis and Leads to Glutamine Addiction. *Proc. Natl. Acad. Sci.* 105, 18782–18787. doi:10.1073/pnas.0810199105

Wolf, D. M., Segawa, M., Kondadi, A. K., Anand, R., Bailey, S. T., Reichert, A. S., et al. (2019). Individual Cristae within the Same Mitochondrion Display Different Membrane Potentials and Are Functionally Independent. *EMBO J.* 38, e101056. doi:10.15252/embj.2018101056

Wu, J., Abdelfattah, A. S., Zhou, H., Ruangkittisakul, A., Qian, Y., Ballanyi, K., et al. (2018). Genetically Encoded Glutamate Indicators with Altered Color and Topology. *ACS Chem. Biol.* 13, 1832–1837. doi:10.1021/acschembio.7b01085

Wyant, G. A., Abu-Remaileh, M., Wolfson, R. L., Chen, W. W., Freinkman, E., Danai, L. V., et al. (2017). mTORC1 Activator SLC38A9 Is Required to Efflux Essential Amino Acids from Lysosomes and Use Protein as a Nutrient. *Cell* 171, 642–654. doi:10.1016/j.cell.2017.09.046

Yoo, H. C., Yu, Y. C., Sung, Y., and Han, J. M. (2020). Glutamine reliance in Cell Metabolism. *Exp. Mol. Med.* 52, 1496–1516. doi:10.1038/s12276-020-00504-8

Yoshida, T., Nakajima, H., Takahashi, S., Kakizuka, A., and Imamura, H. (2019). OLIVe: A Genetically Encoded Fluorescent Biosensor for Quantitative Imaging of Branched-Chain Amino Acid Levels inside Single Living Cells. *ACS Sens.* 4, 3333–3342. doi:10.1021/acssensors.9b02067

Zhang, C., Wei, Z.-H., and Ye, B.-C. (2013). Quantitative Monitoring of 2-oxoglutarate in *Escherichia coli* Cells by a Fluorescence Resonance Energy Transfer-Based Biosensor. *Appl. Microbiol. Biotechnol.* 97, 8307–8316. doi:10.1007/s00253-013-5121-5

Zhang, J., Pavlova, N. N., and Thompson, C. B. (2017). Cancer Cell Metabolism: the Essential Role of the Nonessential Amino Acid, Glutamine. *EMBO J.* 36, 1302–1315. doi:10.15252/embj.201696151

Zhao, S., Jang, C., Liu, J., Uehara, K., Gilbert, M., Izzo, L., et al. (2020a). Dietary Fructose Feeds Hepatic Lipogenesis via Microbiota-Derived Acetate. *Nature* 579, 586–591. doi:10.1038/s41586-020-2101-7

Zhao, S., Torres, A., Henry, R. A., Trefely, S., Wallace, M., Lee, J. V., et al. (2016). ATP-citrate Lyase Controls a Glucose-To-Acetate Metabolic Switch. *Cel Rep.* 17, 1037–1052. doi:10.1016/j.celrep.2016.09.069

Zhao, Y., Araki, S., Wu, J., Teramoto, T., Chang, Y.-F., Nakano, M., et al. (2011). An Expanded Palette of Genetically Encoded Ca 2+ Indicators. *Science* 333, 1888–1891. doi:10.1126/science.1208592

Zhao, Y., Shen, Y., Wen, Y., and Campbell, R. E. (2020b). High-Performance Intensiometric Direct- and Inverse-Response Genetically Encoded Biosensors for Citrate. *ACS Cent. Sci.* 6, 1441–1450. doi:10.1021/acscentsci.0c00518

Zhou, Y., and Danbolt, N. C. (2014). Glutamate as a Neurotransmitter in the Healthy Brain. *J. Neural Transm.* 121, 799–817. doi:10.1007/s00702-014-1180-8

Conflict of Interest: The authors declare that the research was conducted in the absence of any commercial or financial relationships that could be construed as a potential conflict of interest.

frontiers | Frontiers in Cell and Developmental Biology

TYPE Methods
PUBLISHED 07 October 2022
DOI 10.3389/fcell.2022.1012820

OPEN ACCESS

EDITED BY
Konstantinos Palikaras,
National and Kapodistrian University of Athens, Greece

REVIEWED BY
Matthias Rieckher,
University of Cologne, Germany
Myeongwoo Lee,
Baylor University, United States

*CORRESPONDENCE
David R. Sherwood,
david.sherwood@duke.edu
David Q. Matus,
david.matus@stonybrook.edu

†These authors have contributed equally to this work and share first authorship

‡Paid employee of: Arcadia Science

SPECIALTY SECTION
This article was submitted to Cell Growth and Division,
a section of the journal
Frontiers in Cell and Developmental Biology

RECEIVED 05 August 2022
ACCEPTED 20 September 2022
PUBLISHED 07 October 2022

CITATION
Smith JJ, Kenny IW, Wolff C, Cray R, Kumar A, Sherwood DR and Matus DQ (2022), A light sheet fluorescence microscopy protocol for Caenorhabditis elegans larvae and adults.
Front. Cell Dev. Biol. 10:1012820.
doi: 10.3389/fcell.2022.1012820

A light sheet fluorescence microscopy protocol for *Caenorhabditis elegans* larvae and adults

Jayson J. Smith[1,2,3†], Isabel W. Kenny[3,4†], Carsten Wolff[3,5], Rachel Cray[5], Abhishek Kumar[3,5], David R. Sherwood[3,4]* and David Q. Matus[3,6*‡]

[1]Department of Neurobiology, University of Chicago, Chicago, IL, United States, [2]University of Chicago Neuroscience Institute, Chicago, IL, United States, [3]Embryology: Modern Concepts and Techniques, Marine Biological Laboratory, Woods Hole, MA, United States, [4]Department of Biology, Duke University, Durham, NC, United States, [5]Marine Biological Laboratory, Woods Hole, MA, United States, [6]Department of Biochemistry and Cell Biology, Stony Brook University, Stony Brook, NY, United States

Light sheet fluorescence microscopy (LSFM) has become a method of choice for live imaging because of its fast acquisition and reduced photobleaching and phototoxicity. Despite the strengths and growing availability of LSFM systems, no generalized LSFM mounting protocol has been adapted for live imaging of post-embryonic stages of *C. elegans*. A major challenge has been to develop methods to limit animal movement using a mounting media that matches the refractive index of the optical system. Here, we describe a simple mounting and immobilization protocol using a refractive-index matched UV-curable hydrogel within fluorinated ethylene propylene (FEP) tubes for efficient and reliable imaging of larval and adult *C. elegans* stages.

KEYWORDS

***C. elegans*, light sheet fluorescence microscopy, BIO-133, postembryonic development, timelapse**

Introduction

Light sheet fluorescence microscopy (LSFM) affords several advantages for live imaging of biological samples over standard epifluorescence or confocal microscopy. Whereas wide-field microscopy illuminates an entire specimen for imaging, LSFM achieves reduced phototoxicity, photobleaching, and background signal by restricting the proportion of the sample that is illuminated during acquisition. Relative to wide-field imaging, point-scanning confocal methods reduce out of focus sample illumination in the X-Y dimension by only exciting a single point in the sample at a time. To cover the whole region of interest the laser repeatedly sweeps across the sample and for each point scanned the entire Z depth is illuminated. Thus, out of focus photobleaching and phototoxicity occurs in the Z-dimension (Fischer et al., 2011). In contrast to a confocal point-scanning microscope where out of focus light is rejected by discarding unwanted emitted photons, LSFM systems generate a light sheet that selectively illuminates a narrow z-range of the sample in the desired focal plane at a given time (Fischer et al., 2011;

Albert-Smet et al., 2019). This eliminates out of focus photobleaching and permits the collection of the entire fluorescence signal of a section of the sample at one time point, dramatically increasing acquisition speeds (Fischer et al., 2011). Another advantage of LSFM is the ability to acquire multi-view image data *via* multidirectional illumination, sample rotation, or a combination of both techniques (Huisken and Stainier 2009; Schmid and Huisken 2015). To overcome loss of resolution at increased tissue depths, many LSFMs are equipped with the ability to simultaneously image an individual sample from multiple sides, which can then be computationally deconvolved and reconstructed to render a single image of isotropic resolution. These technical advantages have made LSFM a popular imaging method for visualization of complex three-dimensional cells and tissues over developmental time (Keller et al., 2008; Liu et al., 2018).

Most LSFMs are equipped with two or more perpendicular illumination and detection objectives with the sample centered under or between the objectives. This unique orientation of objectives relative to the sample impedes the use of traditional flat microscopy slide mounts for the majority of LSFM systems. Samples for LSFMs are thus often embedded in a cylinder of low-melt agarose that hangs vertically between the objectives. In cases where the agarose is not dense enough to maintain its form, rigid fluorinated ethylene propylene (FEP) tubes can be used to surround the agarose cylinder to stabilize and support the agar (Kaufmann et al., 2012; Girstmair et al., 2016; Steuwe et al., 2020). The refractive indices of low-melt agarose (1.33) and FEP tubes (1.34) are well matched to the refractive index of water (1.33) and this sample mounting method works well for many organisms.

The *C. elegans* embryo has been particularly helpful in advancing the use of LSFM. For example, *C. elegans* embryogenesis was used to demonstrate the enhanced spatiotemporal resolution that is achieved using lattice light-sheet microscopy (Chen et al., 2014). Similarly, the *C. elegans* embryo facilitated showing the effectiveness of four-dimensional (4D) live imaging with the Dual Inverted Selective Plane Illumination Microscope (diSPIM) system (Kumar et al., 2014). LSFM has also advanced our understanding *C. elegans* embryogenesis (Chardès et al., 2014; Duncan et al., 2019), such as helping to reveal how the rigid egg shell contributes to asymmetrical cell divisions (Fickentscher and Weiss 2017), how circuit structures are organized within the nerve ring (the *C. elegans* brain) (Moyle et al., 2021), and how the zinc finger protein PIE-1 concentration gradient is established and maintained in the zygote (Benelli et al., 2020).

Although LSFM can also be used to capture embryogenesis in mice (Ichikawa et al., 2014; Udan et al., 2014) and zebrafish (Keller et al., 2008; Kaufmann et al., 2012; Icha et al., 2016; Pang et al., 2020), the increased tissue size and thickness, tissue pigmentation, and lack of transparency limits post-embryonic imaging in these animal models. In contrast, the small size and transparency of *C. elegans* larvae and adults makes them ideal to examine post-embryonic developmental and physiological processes. *C. elegans* is also amenable to high-resolution live imaging of genetically encoded fluorophores fused to proteins to follow protein dynamics and assess gene expression levels and patterns (Tsuyama et al., 2013; Yoshida et al., 2017; Heppert et al., 2018; Mita et al., 2019; Keeley et al., 2020). Genetically encoded fluorophores can also be conjugated to biosensors, which have been used to quantitatively monitor cell cycle state (Adikes et al., 2020) and ATP in *C. elegans* larvae (Garde et al., 2022). *C. elegans* can also be easily stained with vital dyes (Hermann et al., 2005; Schultz and Gumienny 2012; Kelley et al., 2019).

Despite the advantages of LSFM in *C. elegans* for live imaging, LSFM use in larvae and adults has been limited by the difficulty of sample mounting. Because of its ease of use and good optical properties, low melt agar has been used extensively to mount larger organisms such as zebrafish for LSFM (Kaufmann et al., 2012; Icha et al., 2016; Pang et al., 2020). More recently, it has been reported to work as a mounting media for *C. elegans* (Rieckher et al., 2018). However, small organisms such as *C. elegans* are capable of burrowing into soft agar (Burnett et al., 2018), which might be one reason that the longest time lapse reported for this method was 20 min. In addition, the 2% low-melt agarose required to immobilize worms has a gelling temperature of 24–28°C (Icha et al., 2016; Hirsinger and Steventon 2017), which extends beyond the 25°C thermal tolerance of *C. elegans* (Stiernagle 2006). To avoid high temperatures, photo-activated polyethylene glycol (PEG) hydrogels have been used to physically immobilize *C. elegans* for live imaging (Burnett et al., 2018). Yet, the refractive indices of these hydrogels are often not well-matched for the imaging media or the organism. Here we present a simple protocol for preparing and mounting post-embryonic *C. elegans* for LSFM imaging using a combination of the refractive index matched, ultraviolet (UV)-activated adhesive hydrogel BIO-133 (Han et al., 2021) and FEP tube encasement. This approach has the advantage of much longer imaging sessions (several hours) and avoids potential negative physiological effects on the worm due to heat stress. We show how this protocol can be used to time-lapse image PVD neuron dendritic branching and pruning. We also demonstrate how this protocol is applicable to imaging a variety of proteins and structures, including extracellular matrix proteins (type IV collagen and laminin), the nuclear envelope, and the distal tip cell (DTC). We expect the adoption of these methods will enable better live-imaging studies of important dynamic cell and developmental processes, such as germ stem cell biology, cell migration, cell division, and cell invasion (Sherwood and Plastino, 2018; Gordon et al., 2020; Smith et al., 2022). Furthermore, this protocol is generalizable and applicable to other organisms with little or no modifications.

Methods

Objectives and validation

Our objective was to develop a procedure for immobilizing larvae and adult *C. elegans* for two-to-three-hour long LSFM time lapse imaging sessions. To accomplish this, we developed a mounting strategy that combines anesthesia, the recently developed BIO-133 UV-activated adhesive hydrogel (Han et al., 2021) and animal encasement in an FEP tube (Figure 1). This mounting method allows liquid perfusion of the worms for long term live imaging (upper limit of 3 h to avoid physiological changes that occur from starvation) and is refractive index-matched to water to minimize the light interface resulting in optimal resolution during imaging. Furthermore, this mounting protocol can be adapted to work with LSFM systems equipped with either universal stage sample mounts (Figures 1A,B) or vertical mounts (Figures 1A–C). To validate our mounting protocol, we used the diSPIM (Kumar et al., 2014) to time-lapse image the PVD neurons using a strain harboring endogenously yellow fluorescent protein (YFP) tagged RAB-10 (strain *wy1001[zf1::yfp::rab-10]*) and a membrane tethered GFP expressed in the PVD and OLL neurons (*wyIs592* [*ser-2prom3p::myr-GFP*]). *Rab-10* is a small GTPase involved in post-Golgi vesicle trafficking and is a reporter for the Golgi and early endosome vesicles in the PVD neurons (Figure 2A) (Zou et al., 2015). The multi-dendritic mechanosensory PVD neurons exist as a pair, PVDL and PVDR. Each PVD neuron sits on one side of the animal and has a single axon that extends ventrally to the nerve cord (Figure 2A, bottom). PVD dendritic branching is predictable and developmentally regulated. Specifically, early in the L2 larval stage, the PVD extends three processes—one ventrally, one anteriorly, and one posteriorly. Beginning in late L2, the anterior and posterior processes send out short extensions that will elaborate into dendritic trees that compose the non-overlapping, anteroposterior repeating structural units of the PVDs referred to as “menorahs” (Figure 2B, top) (Oren-Suissa et al., 2010). The branches of these menorah structures cover most of the body, except for the neck and head, and are labeled in the proximal-distal and chronological order in which they occur: primary (1°), secondary (2°), tertiary (3°), or quaternary (4°) (Figure 2B**, bottom**) (Smith et al., 2010). Focusing on the PVDs allowed us to validate the efficacy of this protocol with respect to anterior, midbody, and posterior immobilization as well as imaging clarity throughout LSFM-based live cell imaging. Additionally, PVD development has been the subject of previous confocal-based time lapse studies (Zou et al., 2015) and thus provided us with a point of comparison in the validation of this protocol with respect to stereotyped subcellular dynamics and structural development in a two-to-three-hour timeframe (Chen and Pan 2021; Wang et al., 2021).

We first performed time-lapse imaging of the posterior region of the PVD neuron in an L4 larval stage animal using 2-min acquisition intervals, a z-step size of 1 µm and z-range of 23 µm (Supplementary Movie S1). This allowed examination of PVD dendritic morphogenesis. We observed tertiary dendritic branch elongation (Figure 2C, bracket) as well as the growth of a quaternary branch (Figure 2C, arrow) (Smith et al., 2010; Albeg et al., 2011).

To further test the compatibility of this mounting protocol with other LSFMs, we imaged multiple fluorescently tagged strains on the Zeiss Lightsheet seven from two different acquisition angles. Compared to the diSPIM, which is equipped with a universal stage, the Lightsheet 7 has a vertical tube mount, which enables sample rotation during the acquisition for multi-view imaging. Using tiling and a small step size (0.30 µm), we imaged endogenously tagged type IV collagen (EMB-9:mRuby2, Figure 3A), endogenously tagged laminin (LAM-2:mNG, Figure 3B), endogenously tagged nucleoporin (NDC-1:mNG, Figure 3C), and a cell-specific transgene expressing membrane bound GFP in the somatic distal tip cells of the germline (*lag-2p*:GFP, Figure 3D). Using a 20X, 1.0 NA objective, we observed fine morphological and cellular structures. For example, we resolved the ring of type IV collagen at the edge of the spermatheca in young adult animals (Figure 3A′′), the laminin network surrounding the epithelial cells of the L4 stage spermatheca (Figure 3B′), the distribution of nucleoporin in L4 stage germ cells (Figure 3C′), and the elaborations of the distal tip cell in the young adult stage that enwrap the germ stem cell niche (Figure 3D′). Applying Multiview-registration [Fiji plugin BigStitcher (Hörl et al., 2019)] during image processing, we were also able to create an isotropic image of type IV collagen by combining two different 180° images of the same worm (Supplementary Movie S2).

Materials and equipment

Key resources
M9 buffer.
Nematode growth medium (NGM) agar plates.

Levamisole stock solution (anesthetic)

1. Prepare 200 mM levamisole stock solution in sterile water.
2. Aliquot 150 µL anesthetic stock solution into 1.5 ml Eppendorf tubes and store at -20°C.

4% (weight/volume) noble agar

1. Microwave 4% (weight/volume) noble agar in water to dissolve.
2. Aliquot 1 ml of the melted noble agar into disposable glass tubes and cover with foil or plastic cap. Store at room temperature for up to 3 months.
3. To use, melt noble agar in the glass tube over a Bunsen burner and add to heat block at 70°C to prevent solidification.

Stepwise procedures

Steps 1–14 described below are shown in Figure 1A and Supplementary Video S1. Video tutorials for agar pad

Reagent or resource	Source	Identifier
Bacterial strain		
E. coli OP50 standard food	*Caenorhabditis* Genetics Center (CGC)	OP50
Chemicals and Peptides		
NaCl	Millipore Sigma	Cat #S9888
Agar A	Bio Basic	Cat # FB0010
Peptone	Gibco	Cat # 211,677
5 mg/ml cholesterol in EtOH		
KH_2PO_4		
NA_2HPO_4		
K_2HPO_4		
H_2O		
$MgSO_4$		
(4) Levamisole hydrochloride	Millipore Sigma	Cat #L9756
DIFCO™ Noble agar	VWR	Cat # 90,000–774
TetraSpeck Microspheres 0.5um	Invitrogen	Cat #T7281
Experimental models: Strain		
TV19023	(rab-10 (wy1001 [*zf1::yfp::rab-10*]); wyIs592 [*ser-2prom-3p::myr-GFP*]	Zou et al. (2015)
NK2585	qy152 [*emb-9::mRuby2*]	Jayadev et al. (2022)
NK2335	qy20 [*lam-2::LL::mNG*]	Keeley et al. (2020)
SBW244	sbw8 [*ndc-1::mNG*]	Mauro et al. (2021)
NK1770	qyIs353 [*lag-2p::GFP::CAAX*]; naSi2 [*mex-5p::H2B::mCherry::nos-2 3′ UTR*]	Gordon et al. (2019)
Software and algorithms		
Fiji Version 2.3.0	Fiji	
Imaris 9.6.0	Oxford Instruments/Bitplane	
Microscopes and Imaging		
Stereo microscope		
MicroManager Imaging Software	For diSPIM control and data acquisition we used the ASI diSPIM plugin within the micro-manager	https://micro-manager.org/ASIdiSPIM_Plugin: http://dispim.org/(Ardiel et al., 2017)
DiSPIM	A fiber-coupled diSPIM	http://dispim.org/(Kumar et al., 2014
DiSPIM Objective 1	40x, 0.8 NA, Water dipping	Cat # MRD07420;Nikon; Melville, NY
DiSPIM Objective 2	40x, 0.8 NA, Water dipping	Cat # MRD07420;Nikon; Melville, NY
DiSPIM Filter set	Quad band notch filter	Part # Semrock NF03-405/488/561/635E-25
ZEISS Lightsheet 7	Illumination: 10×, NA 0.2 foc (400,900–9000): Detection: Clr Plan-Apochromat 20×, 1.0 NA (421,452–9700)	Zeiss.com
Other		
(13) 15″ Aspirator Tube Assembly (for mouth pipette)	VWR®	Cat # 53,507–278
(9) Bunsen Burner		
(3) Eppendorf Research Plus Adjustable Vol., Single Channel Pipette (20–200 µL)	Eppendorf®	Cat #Z683817
(2) BIO-133	My Polymers Ltd	N/A
(6) Disposable Scalpel (for trimming FEP tubes)	Fisher Scientific	Cat #12–000-133
(12) Disposable glass culture tubes	VWR®	Cat # 47,729–572
Plastic glass culture tube caps	Port City Diagnostics	Cat #T3600CAP
(5) Pyrex® Depression Spot Plate (85 × 100 mm)	Corning®	Cat # 89,090–482
(14) Open ended melted capillary (for mouth pipette)	KIMBLE® KIMAX®	Cat # 34,500 99

(Continued on following page)

(*Continued*)

Reagent or resource	Source	Identifier
(15) Kimberly-Clark Professional™ Kimtech Science™ Delicate Task Wipers	Fisher Scientific	Cat # 06–666
(10) Glass slides (25 × 75 × 1 mm)	Globe Scientific Inc	Cat # 1301
Heat block		
Cover glass (22 × 22 mm No. 1.5)	Fisher Brand	Cat # 12541 B
(1) Fluidon FEP tube (0.8/1.2 mm, 0.2 mm wall thickness)	ProLiquid, Germany	Cart # 2,001,048
(11) General-Purpose lab labeling tape	VWR®	Cat # 89097-COLOR
(19) Petri Dish 100 mm × 15 mm	Fisher Scientific (Falcon™)	Cat # 08–757-100D
Petri Dish 60 mm	[Worm culturing]	
(8) Platinum Wire (for worm pick)	SPI Supplies	Cat # 01703-AC
(18) UV light source (40 W)	LKE - Amazon	ASIN: B07G31SQZ7
(16) Specimen Forceps (serrated) [203 mm]	VWR®	Cat # 82,027–442
(7) Dissecting Stereoscope	Zeiss	Cat # Stemi 2000
(17a) Syringe Needle (1 in., 21 G)	BD™	Cat # 305,165
(17b) Syringe PP/PE (1 ml, luer slip tip)	Millipore Sigma	Cat #Z683531

M9 buffer

Reagent	Final concentration	Amount
NA_2HPO_4	42.2 mM	6 g
KH_2PO_4	22 mM	3 g
NaCl	85.5 mM	5 g
1 M $MgSO_4$	1 mM	1 ml
Deionized water	-	999 ml
Total	-	**1 L**

*Autoclave to sterilize. Aliquot 50 ml into 50 ml falcon tubes. One aliquot will provide enough imaging buffer for one timelapse imaging session.

Nematode growth medium (NGM) agar plates

Reagent	Final concentration	Amount
Agar A	17 g/L	34 g
Peptone	2.5 g/L	5 g
NaCl	25.66 mM	3 g
Cholesterol (5 mg/ml)	12.92 µM	2 ml
Deionized water	-	1.95 L
Total	-	**2 L**

*Sterilize with autoclave (60 min). Cool to 55°C in a water bath and then add 50 ml 1 M KPO_4 buffer (pH 6.0), 2 ml 1 M $MgSO_4$, and 2 ml 1 M $CaCl_2$. Add 8 ml of warm NGM to each sterile plastic Petri dish using sterile technique and allow to cool. For storage, plates are inverted (NGM side up) at 4°C. NGM plates are warmed to room temperature before seeding with OP50 bacteria for feeding and culturing *C. elegans* strains.

construction, worm anesthetization, and worm transfer can also be found elsewhere (Kelley et al., 2017). All necessary materials required to perform this procedure following preparation of M9 and NGM plates are shown in Supplementary Figure S1.

Total time: 45–65 min

C. elegans stage selection and anesthesia (timing: ~30 min)

1. Synchronize worm cultures (Porta-de-la-Riva et al., 2012) (**Time:** 15 min) or pick appropriate staged animals for imaging. (**Time:** 2–3 min)
2. Add 50 µl anesthesia solution (5 mM Levamisole in M9) to a clean well in a glass depression dish.

   Alternative to anesthesia: In addition to immobilization, the anesthetic relaxes the animals into a straight conformation, which facilitates consistent tissue geometry during imaging and permits Multiview registration. However, the use of anesthetic is not suitable for all experiments as levamisole is an acetylcholine receptor agonist that results in muscle contraction (Manjarrez and Mailler 2020). As an alternative, we found animals can be immobilized with cold temperatures by treatment at 5–7°C for ~15 min prior BIO-133 UV-crosslinking.
3. Add 100 µl of BIO-133 to a clean well of the glass depression dish.

   Detail for precision: BIO-133 is very viscous. Use a scalpel to trim the end of a pipette tip to transfer the hydrogel more easily.

   (For Multiview registration) In an Eppendorf tube combine 80 µl BIO-133 and 20 µl of TetraSpeck Microspheres (1: 2,000 dilution), vortex thoroughly to ensure beads are evenly dispersed in BIO-133. Once mixed, add 50–100 µl of BIO-133 to a clean well.

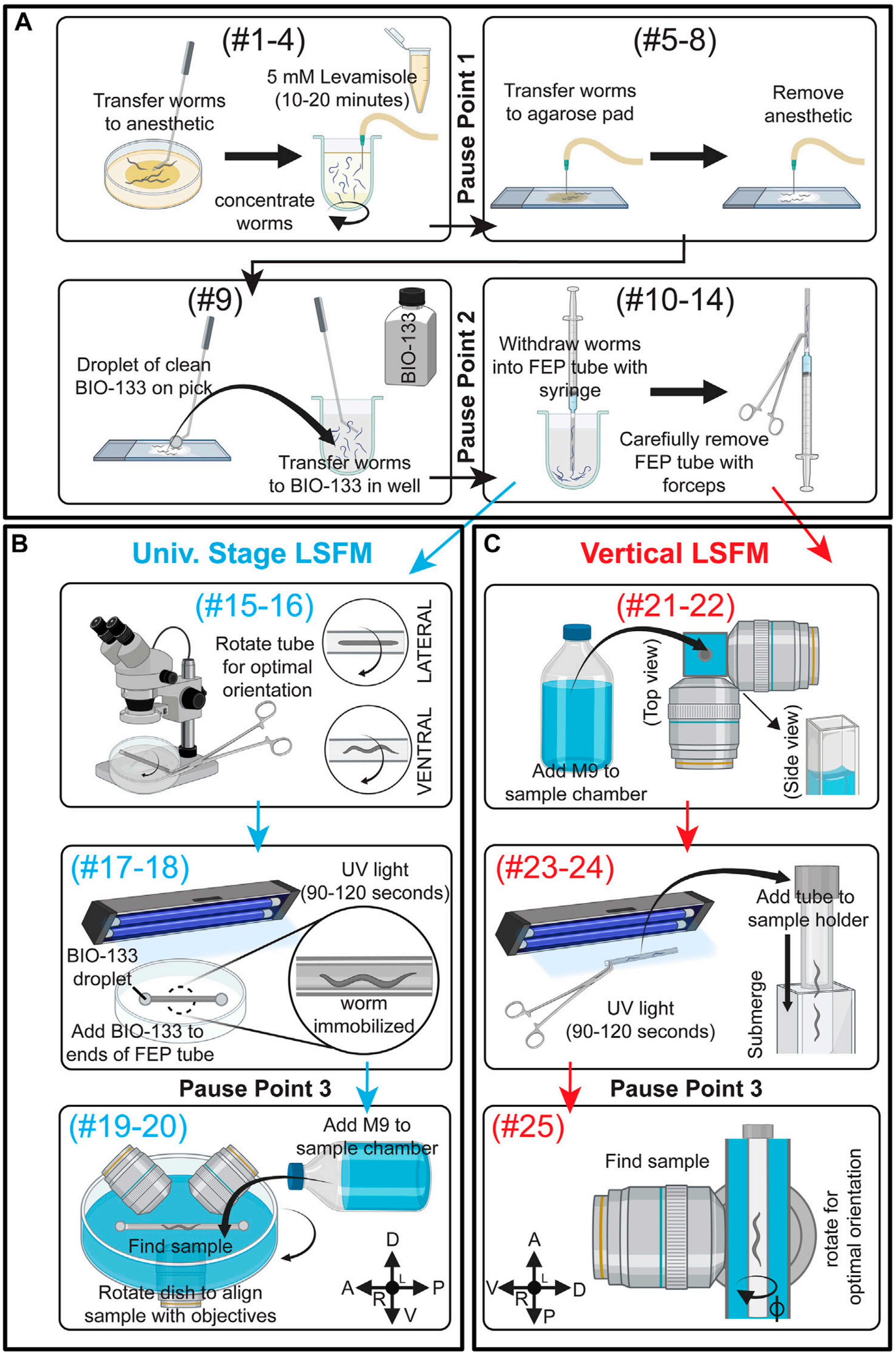

FIGURE 1
Schematic summary of *C. elegans* post-embryonic BIO-133 mounting strategies for LSFM imaging. **(A)** A schematic summary of steps #1–14 of the FEP-BIO-133 mounting protocol for time-lapse imaging of post-embryonic *C. elegans* on light sheet fluorescence microscopes, including animal anesthesia (top left, *steps #1–4*), transfer to BIO-133 (top right, *steps #5–8*), BIO-133 encapsulation (bottom left, *step #9*), and sample withdrawal into the FEP tube (bottom right, *steps #10–14*). Protocol steps #1–14 can be used for mounting samples on LSFMs configured with either a universal stage mount or a vertically-mounted sample. Pause points #1-2 in the procedure are indicated where they occur in the protocol. **(B)** A schematic summary of FEP tube-sample orientation (top, *steps #15–16*), UV-curation and bonding of FEP tube to Petri dish sample imaging chamber (middle, *steps #17–18*) and sample mounting (bottom, *Steps #19–20*) for LSFM systems equipped with a universal stage mount. After steps #1–14 **(A)**, proceed to steps #15–20. Pause point #3 is indicated. **(C)** A schematic depicting preparation for a vertically-mounted sample, including sample chamber flooding (top, *steps #21–22*), UV-curation and loading of the FEP tube into the sample holder (middle, *steps #23–24*) and rotating the FEP tube to achieve optimal sample orientation (bottom, *step #25*). After steps #1–14 **(A)**, skip steps #15–20 and proceed to steps #21–25. Pause point #3 is indicated. Created with BioRender.com.

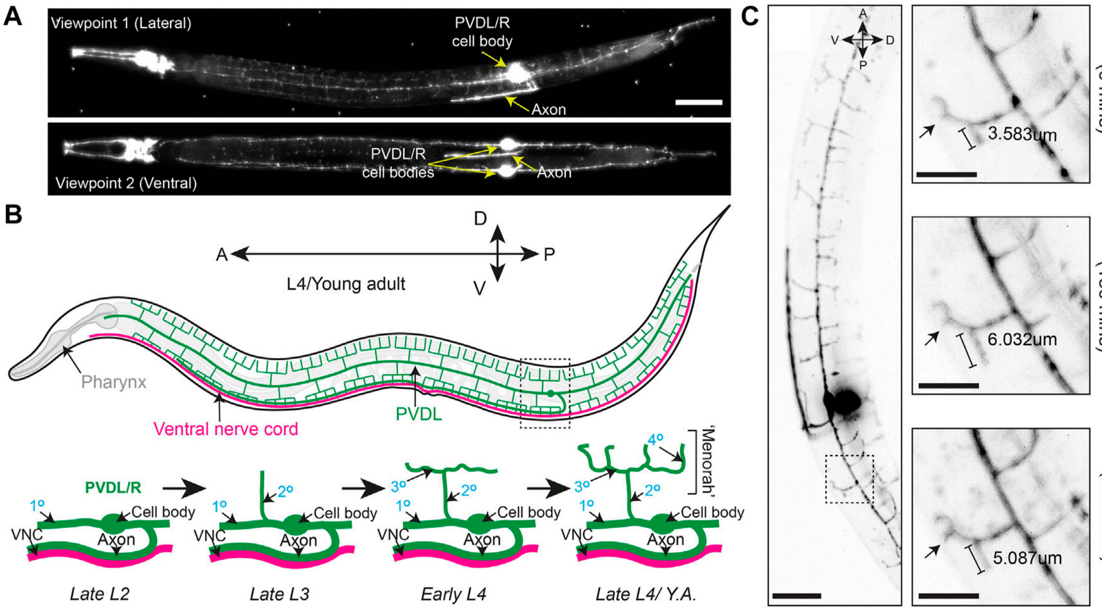

FIGURE 2
Branching and elongation of PVD neuron dendrites during a 5 h time-lapse on a DiSPIM. **(A)** LSFM Z-projections of an L4 hermaphrodite expressing *yfp::rab-10* (acquired with 40x NA 0.8 water-dipping lenses, z-step = 1 μm, $200uW/cm^2$ 488 nm laser power and 20 ms exposure) mounted using protocol Steps #1–20 on a diSPIM configured with a universal stage mount. Viewpoints were captured with imaging objectives oriented at 90° to simultaneously view the lateral and ventral aspects of the animal. Scale bar is 25 μm **(B)** (Top) A depiction of the fully elaborated PVD neurons in a young adult hermaphrodite animal. (Bottom) The developmental progression of PVD arborization focusing on the region indicated by the dashed box above. By late L2, the PVD neurons have extended their axons ventrally to contact the nerve cord and the primary (1°) dendrites have elongated along the anterior-posterior axis of the animal. The secondary (2°) dendrites branch dorsally and ventrally from the 1° dendrites by late L3. In early L4, the tertiary (3°) dendrites branch anteroposteriorly from the 2° dendrites, which is followed by the emergence of quaternary (4°) dendrites beginning in the late L4. **(C)** (Left) Timestamp from the beginning of a LSFM time-lapse in an L4 hermaphrodite expressing *yfp:rab-10* as in **(A)** (Right) Time series of 3° and 4° dendritic dynamics over the course of a 300 min LSFM timelapse (acquired with the same parameters described in A). Scale bar 25 μm, 10 μm for inset.

4. Transfer 20–50 animals to the anesthesia solution and wait for 12 min or until most of the animals have ceased moving. Larvae or adults should be straight and rod-like before proceeding to the next step. (**Time**: 15–20 min)

[Pause point 1]
Transferring *C. elegans* from anesthetic to BIO-133 (Timing: ~15 min)

5. First swirl the glass depression dish to concentrate the anesthetized animals in the center of the well and then use the mouth pipette to remove most of the liquid anesthetic from the well to further concentrate the worm bodies. (**Time:** 1–3 min).
6. Prepare an agar pad on a glass slide (See Kelley et al., 2017 for details on agar pad construction) and allow to cool for 1 min (**Time:** 1–2 min)
7. Use a mouth pipette to transfer anesthetized animals from the well in the glass depression dish to the agar pad. (**Time:** 1 min)
8. Use a mouth pipette to remove anesthetic liquid from the agar pad until animals appear nearly dry (Supplementary Figure S2). Avoid removing anesthetized animals with the anesthetic solution. (**Time:** 1–3 min)
9. Using a worm pick, gather a droplet of BIO-133 at the end of the pick. Use the BIO-133 droplet to pick and then transfer worms from the nearly dry agar pad to the well of the glass depression dish that contains the BIO-133. Carefully and vigorously swirl the worms in the BIO-133 to separate individual animals and break up any liquid droplets or bubbles that form from the worm transfer. (**Time:** 2–5 min)
Detail for precision: Any transfer of the anesthetic or water to the BIO-133 solution will result in droplets forming in the adhesive, which will trap the animals, removing them from the hydrogel.
Detail for precision: Transferring individual animals rather than many larvae or adults on the pick at the same time will reduce the chances of aggregation.

[Pause point 2]
Loading BIO-133-encased C. elegans into FEP tube and polymerizing the mount (Timing: ~20 min)

10. Attach the 21-G syringe needle to the 1 ml syringe barrel.
11. Use serrated forceps to slide the FEP tube onto the 21-G syringe needle.

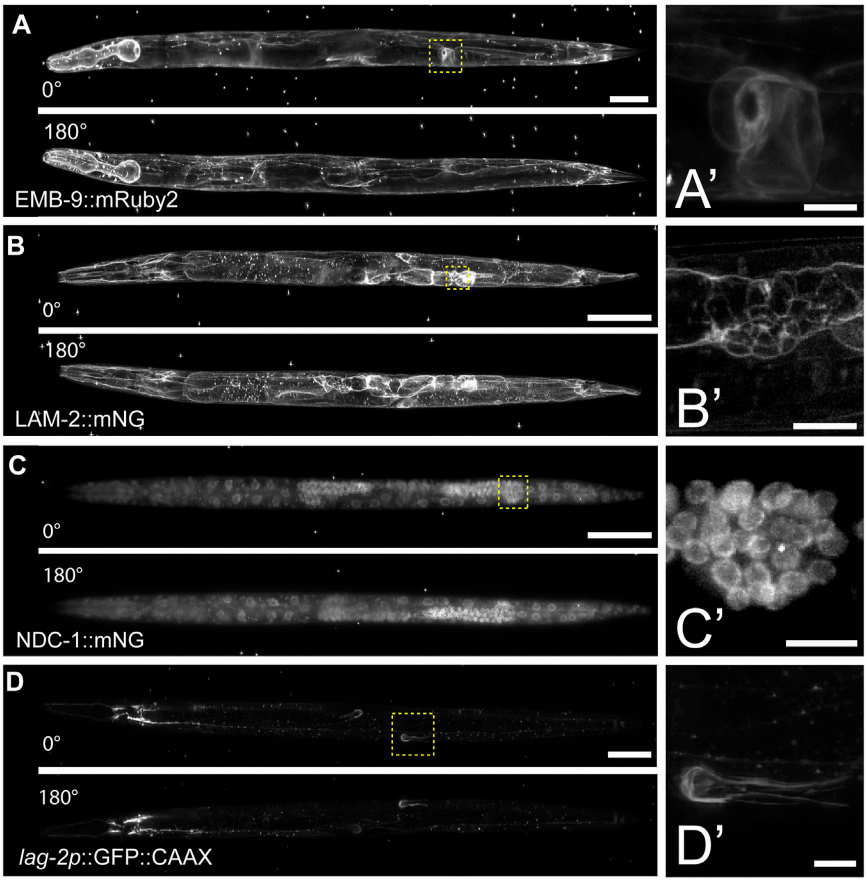

FIGURE 3
Multiview imaging of endogenously-tagged proteins in *C. elegans* young adults and larvae on a Zeiss Lightsheet 7 with a vertical mount. **(A)** Projected fluorescent images from two viewpoints on the Zeiss L7 showing endogenously-tagged type IV collagen (EMB-9:mRuby2) in a young adult hermaphrodite. The images were acquired from two angles 180° apart using a 20x NA 1.0 water dipping lens (z-step = 0.30 µm, 561 nm laser 2% power and 30 ms exposure). **(B)** Two projected images from LSFM sectioning of endogenously-tagged laminin (LAM-2:mNG) in an L4 hermaphrodite. The images were acquired from two angles 180° apart using a 20x NA 1.0 water dipping lens (z-step = 0.30 µm, 488 nm laser 1.5% power and 30 ms exposure). **(C)** Two projected images showing endogenously-tagged nucleoporin (NDC-1:mNG) in an L4 hermaphrodite. The images were acquired from two angles 180° apart using a 20x NA 1.0 water dipping lens (z-step = 0.30 µm, 488 nm laser 2% power and 50 ms exposure). **(D)** Two projected images showing distal tip cell (DTC) specific expression of membrane-tethered GFP in an adult hermaphrodite. The images were acquired from two angles 180° apart using a 20x NA 1.0 water dipping lens (z-step = 0.30 µm, 488 nm laser 7% power and 40 ms exposure). Scale bar for all images is 50 µm, 10 µm for inset. **(A'–D')** Magnified insets of regions in the yellow dashed boxes in **(A–D)**.

Detail for precision: FEP tubes need to be rinsed and stored in double-distilled water prior to use (reference https://huiskenlab.com/sample-mounting/). Dry the outside of the tube with a Kimwipe and push air through the tube using the syringe plunger to dry the inside of the tube (**Time:** 1–3 min). Removing all water will reduce the number of droplets in the BIO-133.

Detail for precision: Depending on the length of the FEP tube, it may be necessary to use a disposable scalpel or razor blade to trim the tube into 2–5 cm lengths. Having a shorter segment of FEP tube reduces the time required to find the sample on a LSFM system by minimizing the area containing the sample. Shorter segments of FEP tubes also bond more easily to the bottom of the plastic Petri dish that will become the imaging chamber (See steps 14–16).

12. Place the open end of the FEP tube that is attached to the syringe into the BIO-133 adhesive solution. Using the syringe plunger, draw BIO-133 into the FEP tube until the tube is ¼ full. This primes the tube and ensures that *C. elegans* larvae and adults are positioned centrally, away from the edge of the FEP tube (Step 17). (**Time:** 1–3 min)
Detail for precision: Due to the high viscosity of the BIO-133 adhesive solution, there will be a delay between when you stop pulling the syringe plunger and when BIO-133 stops flowing into the FEP tube. If more than ¼ of the tube is filled with BIO-133 by the time the pressure is equalized, carefully

expel the excess BIO-133 back into the well of the glass depression dish.

Detail for precision: To avoid introducing air bubbles into the FEP tube, do not remove the end of the tube from the BIO-133 until you have filled the final ¾ with anesthetized animals and BIO-133 (Step 14).

13. Slowly pull the plunger to draw 5–10 anesthetized animals into the primed FEP tube. (**Time:** 2–5 min)

    Detail for precision: Due to the high viscosity of the BIO-133 adhesive solution, there will be a delay between pulling the syringe plunger and drawing anesthetized animals into the FEP tube. To avoid drawing BIO-133 and animals into the syringe barrel, stop pulling the syringe plunger when the FEP tube is ¾ full. Wait until the pressure equalizes, the FEP tube is full, and the worms stop flowing before removing the end of the FEP tube from the BIO-133 to avoid introducing air bubbles to the FEP tube.

    Detail for precision: Position the opening of the FEP tube so that the animals will be drawn into the tube longitudinally. Draw one animal up at a time and avoid overlapping animals in the tube.

    Detail for precision: Ensure that larvae and adults occupy the middle of the FEP tube since LSFM systems equipped with dip lenses will not be able to image animals that are too close to the ends of the FEP tube.
14. Remove the FEP tube from the BIO-133 and check the open end of the FEP tube and the end connected to the needle for air bubbles. The FEP tube should be filled with the adhesive solution, *C. elegans* larvae and adults, and free of air bubbles. Detach the FEP tube from the syringe with serrated forceps. (**Time:** 1–2 min)

IF USING A VERTICAL MOUNT, SKIP TO STEPS 21–25

(Steps 15–20 described below are shown in Figure 1B and Supplementary Video S2)

15. Place the FEP tube in the middle of the Petri dish. Add 2-3 drops of BIO-133 hydrogel to the FEP tube using a worm pick or pipette tip. BIO-133 will stabilize the FEP tube during and following UV-treatment. (**Time:** 1–2 min)
16. Use a stereo microscope to find the optimal orientation of the FEP tube such that your sample is as close as possible to the imaging objective. If multiple animals are mounted, roll the FEP tube in the uncured BIO-133 to achieve the orientation in which most animals are oriented properly (Figure 1B). (**Time:** 1–3 min)
17. Cure the mount with UV light for 2 min to crosslink the BIO-133 around the anesthetized animals and bond the sample-containing FEP tube to the plastic Petri dish imaging chamber. (**Time:** 2 min)

Installing the mount on an LSFM equipped with a universal stage and dipping lenses (Timing: ~2 min)

18. After UV curing, the FEP tube should be stably attached to the surface of the plastic Petri dish and the sample should be encased in a rigid hydrogel in the FEP tube. Ensure that the FEP tube is securely attached to the Petri dish by lightly tapping it with forceps or a pipette tip. The tube should not budge or move at all before proceeding. (**Time:** 1 min)
19. Add mount to the universal stage on the LSFM system. Once the mount is resting on the universal stage, rotate the dish until your sample is optimally aligned with the imaging objectives (Figures 1B). Fasten the specimen clips to secure the Petri dish imaging chamber. (**Time:** 1 min)
20. Slowly fill the Petri dish imaging chamber with 45–50 ml room temperature M9 buffer (imaging medium), after which the dipping lens objectives can be lowered into the M9 for sample finding and subsequent imaging.

END OF PROCEDURE FOR LSFM WITH UNIVERSAL STAGE MOUNT

Installing the mount on an LSFM which requires a vertically mounted sample (Timing: ~5 min)

(Steps 21–25 described below are shown in Figure 1C and step 23 (UV-curing) is shown in Supplementary Video S3)

21. Fill the LSFM media chamber with M9. (**Time:** 1 min)

    Detail for Precision: M9 can be added to the media chamber prior to starting the protocol and does not need to be replaced between samples.
22. Wipe the FEP tube containing animals in BIO-133 with a Kimwipe to remove any BIO-133 from the outside of the tube. (**Time:** 1 min)

    Detail for Precision: When possible, use forceps to handle the tube to keep the tube as clean as possible, as any smudges on the outside of the tube might impede the clarity of the imaging
23. Cure the mount with UV light for 2 min to crosslink the BIO-133 around the anesthetized animals; this can be done before or after detaching the FEP tube from the syringe needle. (**Time:** 2 min)

    Detail for Precision: Use a stereomicroscope to locate the straight, centered, and non-overlapping animals within the FEP tube. (**Time:** 1 min)
24. Attach the tube in the sample holder, keeping in mind the positions of the animals as identified in step 24. If the animals are close to the end of the tube, place the opposite end of the tube in the sample holder. (**Time:** 1 min)
25. Place the sample holder with FEP tube back into the mount so that the FEP tube is submerged in M9 and ready for sample finding and imaging. (**Time:** 1 min)

Anticipated results

This work introduces the advantages of LSFM live imaging to long term postembryonic *C. elegans* development, including faster acquisition speed and reduced phototoxicity and photobleaching. Prior to the development of this protocol, light-sheeting imaging of *C. elegans* had been limited to embryos, very short time-lapse imaging of larvae and adults, and fixed samples (Chardès et al., 2014; Chen et al., 2014; Liu et al., 2018; Rieckher et al., 2018; Breimann et al., 2019; Duncan et al., 2019). We anticipate that adult or larval encasement in BIO-133 within an FEP tube will enable continuous LSFM imaging for at least 2 h, a time span that is comparable to that typical of confocal time lapses (Kelley et al., 2017) and which approaches the physiological limit imposed by starvation (Schindler and Sherwood 2014). Unlike the confocal time-lapse mount, this protocol exposes animals to minimal amounts (up to 2 min) of direct UV light or low temperatures (7°C for the thermal immobilization method).

In addition to the extended time of imaging and optical properties of BIO-133, other major advantages of this protocol are the low material cost, accessibility of reagents and equipment (See Materials and Equipment table), and a similarity to established low-melt agarose-based LSFM mounting protocols currently used for *C. elegans*. The mounting strategy can be easily performed with resources already present in most *C. elegans* labs, except for a UV-light source, BIO-133, and FEP tubes. Compared to a previous method which uses low-melt agarose and a glass capillary tube to immobilize larvae and adults for LSFM imaging (Rieckher et al., 2018), this mounting strategy relies on similar procedural steps but avoids exposing animals to potentially harmful temperatures and provides a submersible mount that is compatible with most LSFM configurations. A minor drawback is that there are additional steps in the BIO-133 protocol relative to the low-melt agarose-based procedure. Namely, transfer of anesthetized animals to BIO-133 requires a drying process (steps 5–9) and the mount must be UV-cured (steps 15–18 or 21–23).

Compared to the short amount of time between preparing a traditional time lapse slide and imaging a sample on a point-scanning confocal system (Kelley et al., 2017), an additional limitation of this protocol is the length of time it takes to compose and cure the mount (~30 min) before imaging. In this protocol animals are removed from food for a longer period before imaging, which reduces the time available for timelapse before starvation by ~30 min compared to a slide-based time-lapse mount (Kelley et al., 2017). Furthermore, since the orientation of animals within the FEP tube is fixed after UV curing, it can take multiple mounting attempts to achieve optimal animal orientation. This protocol is therefore comparatively low throughput. This is a significant drawback to the investigation of developmental processes with sensitive timing, or if there is limited time available to use an LSFM system. To shorten the time to imaging, multiple LSFM time lapse mounts can be assembled in parallel.

Another potential limitation of this protocol is that BIO-133 must be cured with light of 300–400 nm in wavelength (Han et al., 2021) Animals must thus be exposed to UV-A light, which, while less damaging to DNA than UV-B or UV-C irradiation, is known to have a photoaging effect in *C. elegans* following prolonged exposure (more than 2 h) (Prasanth et al., 2016). Importantly, in this protocol we used a UV lamp which exposed the samples to UV-A light of 365 nm and 405 nm at an irradiance of approximately 6 mW/cm^2 (Ford et al., 2021). At 2 minutes of exposure, animals received an estimated dose of UV-A light of 720 mJ/cm^2, well-below the 15 J/cm^2 that leads to *C. elegans* lethality (Ward et al., 2008). Although we did not monitor signs of UV-induced damage in animals treated with UV light, such as germ cell death, much higher doses of UV-A light are required to induce aging in the nematode (Prasanth et al., 2016) and all animals were viable following exposure and encapsulation in BIO-133.

Finally, we have not tested the diffusion mechanics of the activated BIO-133 hydrogel. It is possible that this protocol cannot be adapted for use in combination with diffusible cues and hormones (e.g., auxin for degron-based protein depletion) (Zhang et al., 2015; Martinez et al., 2020; Martinez and Matus 2020) or mitogens (Monsalve et al., 2019). However, pre-treatment with drugs or hormones prior to mounting animals may be sufficient to capture the desired effects, depending on the mechanics of the biological process or technique of interest. Since the ends of the FEP tubes are left open in the mount, the BIO-133 hydrogel matrix and sample should also be exposed to oxygen and media.

Discussion

Here we describe a simple protocol for collecting high-quality post-embryonic LSFM time-lapse imaging data of larval and adult *C. elegans*. It is likely that this protocol can be adapted for the purposes of imaging other animal models, as the BIO-133 adhesive is biocompatible and FEP tubes are available in a variety of lengths and diameters. Though this method of immobilization and sample mounting provides novel opportunities for *in vivo* imaging of post-embryonic *C. elegans*, such as germ cell divisions, DTC migrations, sex myoblast migration, and anchor cell invasion, there remain a few shortcomings, such as the extended time it takes to prepare samples as discussed in the anticipated results section (Sherwood and Plastino 2018; Adikes et al., 2020; Gordon et al., 2020).

Among the many advantages to light-sheet microscopy mentioned above, this protocol enables multi-view image data *via* multidirectional illumination or sample rotation by providing access to the input image data necessary for 4D image reconstruction (Huisken and Stainier 2009; Schmid and Huisken 2015). Using 4D image reconstruction, we were able to discern the ring structure of type IV collagen in the spermathecal valve that opens to the uterus and laminin tightly covering the individual epithelial cells of the spermatheca. The BIO-133 can also be seeded with fluorescent beads (microspheres) as fiduciary markers (Preibisch et al., 2010; Wu et al., 2013) to improve multi-view image processing with greater temporal and spatial registration (Supplementary Movie S2). This protocol for *C. elegans* post-embryonic time-lapse imaging should be adaptable to any light sheet or confocal microscope that contains water dipping lenses and a universal stage mount or vertically mounted samples submerged in a sample chamber.

Data availability statement

The original contributions presented in the study are included in the article/Supplementary Material, further inquiries can be directed to the corresponding authors.

Author contributions

JS, IK, and DM conceptualized the project. JS and IK designed the protocol, collected all data (with microscopy and image processing help from CW and AK), and wrote the manuscript. DM, DS edited and revised the manuscript. CW and AK provided additional comments on the manuscript. RC independently tested the protocol and provided helpful feedback.

Funding

IK and DS are supported by R35GM118049-06, R21OD028766, and R21OD032430. Some strains were provided by the *Caenorhabditis* Genetics Center, which is funded by National Institutes of Health Office of Research Infrastructure Programs (P40 OD010440). DM is supported by grant R01GM121597. The Embryology course was funded by NIH/NICHD grant R25HD094666, Burroughs Wellcome Fund 1021168 and the Company of Biologists. AK and RC are supported by the Chan Zuckerberg Initiative (CZI) Imaging Scientists Program, The Arnold and Mabel Beckman Foundation Lightsheet and Data Science Program, and startup funds provided to AK from the MBL. The ZEISS Lightsheet seven system at MBL was supported by the Howard Hughes Medical Institute.

Acknowledgments

The authors would like to thank J. Henry for help recording the videos and the Marine Biological Laboratory (MBL), the MBL Central Microscopy Facility, and the MBL Embryology course directors, staff, and students for providing the lab space and environment within which this protocol was developed. Michael Weber from the Flamingo team is greatly acknowledged for providing FEP tubes and support during preliminary imaging experiments.

Conflict of interest

The authors declare that the research was conducted in the absence of any commercial or financial relationships that could be construed as a potential conflict of interest.

Publisher's note

Supplementary material

The Supplementary Material for this article can be found online at: https://www.frontiersin.org/articles/10.3389/fcell.2022.1012820/full#supplementary-material

SUPPLEMENTARY MOVIE S1
Elaboration of the PVD neuron in the L4 midbody. A 5 h time-lapse of an L4 hermaphrodite expressing *yfp::rab-10*. The time-lapse was acquired on diSPIM with 40x NA 0.8 water-dipping objective lenses and images were collected every 2 min.

SUPPLEMENTARY MOVIE S2
Using microspheres for enhanced spatiotemporal resolution. An isotropic image of endogenously-tagged type IV collagen (EMB-9: mRuby2) derived from the Multiview registration of images in Figure 3A.

SUPPLEMENTARY VIDEO S1
Step 1 to step 14.

SUPPLEMENTARY VIDEO S2
Step 15 to step 17.

SUPPLEMENTARY VIDEO S3
Step 23 (UV-curing mount for LSFMs which require vertically-mounted sample).

References

Adikes, R. C., Kohrman, A. Q., Martinez, M. A. Q., Palmisano, N. J., Smith, J. J., Medwig-Kinney, T. N., et al. (2020). Visualizing the metazoan proliferation-quiescence decision *in vivo*. *eLife* 9, e63265. doi:10.7554/eLife.63265

Albeg, A., Smith, C. J., Chatzigeorgiou, M., Feitelson, D. G., Hall, D. H., Schafer, W. R., et al. (2011). *C. elegans* multi-dendritic sensory neurons: Morphology and function. *Mol. Cell. Neurosci.* 46 (1), 308–317. doi:10.1016/j.mcn.2010.10.001

Albert-Smet, I., Marcos-Vidal, A., Vaquero, J. J., Desco, M., Muñoz-Barrutia, A., and Ripoll, J. (2019). Applications of light-sheet microscopy in microdevices. *Front. Neuroanat.* 13, 1. doi:10.3389/fnana.2019.00001

Ardiel, E. L., Kumar, A., Marbach, J., Christensen, R., Gupta, R., Duncan, W., et al. (2017). Visualizing calcium flux in freely moving nematode embryos. *Biophys. J.* 112 (9), 1975–1983. doi:10.1016/j.bpj.2017.02.035

Benelli, R., Struntz, P., Hofmann, D., and Weiss, M. (2020). Quantifying spatiotemporal gradient formation in early *Caenorhabditis elegans* embryos with lightsheet microscopy. *J. Phys. D. Appl. Phys.* 53 (29), 295401. doi:10.1088/1361-6463/ab8597

Breimann, L., Preusser, F., and Preibisch, S. (2019). Light-microscopy methods in *C. elegans* research. *Curr. Opin. Syst. Biol.* 13, 82–92. doi:10.1016/j.coisb.2018.11.004

Burnett, K., Edsinger, E., and Albrecht, D. R. (2018). Rapid and gentle hydrogel encapsulation of living organisms enables long-term microscopy over multiple hours. *Commun. Biol.* 1, 73. doi:10.1038/s42003-018-0079-6

Chardès, C., Mélénec, P., Bertrand, V., and Lenne, P.-F. (2014). Setting up a simple light sheet microscope for *in toto* imaging of *C. elegans* development. *J. Vis. Exp.* 87. doi:10.3791/51342

Chen, B.-C., Legant, W. R., Wang, K., Shao, L., Milkie, D. E., Davidson, M. W., et al. (2014). Lattice light-sheet microscopy: Imaging molecules to embryos at high spatiotemporal resolution. *Science* 346 (6208), 1257998. doi:10.1126/science.1257998

Chen, C.-H., and Pan, C.-L. (2021). Live-cell imaging of PVD dendritic growth cone in post-embryonic *C. elegans*. *Star. Protoc.* 2 (2), 100402. doi:10.1016/j.xpro.2021.100402

Duncan, L. H., Moyle, M. W., Shao, L., Sengupta, T., Ikegami, R., Kumar, A., et al. (2019). Isotropic light-sheet microscopy and automated cell lineage analyses to catalogue *Caenorhabditis elegans* embryogenesis with subcellular resolution. *J. Vis. Exp.* 148. doi:10.3791/59533

Fickentscher, R., and Weiss, M. (2017). Physical determinants of asymmetric cell divisions in the early development of *Caenorhabditis elegans*. *Sci. Rep.* 7 (1), 9369. doi:10.1038/s41598-017-09690-4

Fischer, R. S., Wu, Y., Kanchanawong, P., Shroff, H., and Waterman, C. M. (2011). Microscopy in 3D: A biologist's toolbox. *Trends Cell Biol.* 21 (12), 682–691. doi:10.1016/j.tcb.2011.09.008

Ford, H., Horsham, C., Urban, D., Tinker, R., and Hacker, E. (2021). Quantifying the ultraviolet radiation emitted by nail curing devices: A descriptive study. *Australas. J. Dermatol.* 62, e311–e313. doi:10.1111/ajd.13539

Garde, A., Kenny, I. W., Kelley, L. C., Chi, Q., Mutlu, A. S., Wang, M. C., et al. (2022). Localized glucose import, glycolytic processing, and mitochondria generate a focused ATP burst to power basement-membrane invasion. *Dev. Cell* 57 (6), 732–749. e7. doi:10.1016/j.devcel.2022.02.019

Girstmair, J., Zakrzewski, A., Lapraz, F., Handberg-Thorsager, M., Tomancak, P., Pitrone, P. G., et al. (2016). Light-sheet microscopy for everyone? Experience of building an OpenSPIM to study flatworm development. *BMC Dev. Biol.* 16 (1), 22. doi:10.1186/s12861-016-0122-0

Gordon, K. L., Payne, S. G., Linden-High, L. M., Pani, A. M., Goldstein, B., Hubbard, E. J. A., et al. (2019). Ectopic germ cells can induce niche-like enwrapment by neighboring body wall muscle. *Curr. Biol.* 29 (5), 823–833. e5. doi:10.1016/j.cub.2019.01.056

Gordon, K. L., Zussman, J. W., Li, X., Miller, C., and Sherwood, D. R. (2020). Stem cell niche exit in *C. elegans* via orientation and segregation of daughter cells by a cryptic cell outside the niche. *eLife* 9, e56383. doi:10.7554/eLife.56383

Han, X., Su, Y., White, H., O'Neill, K. M., Morgan, N. Y., Christensen, R., et al. (2021). A polymer index-matched to water enables diverse applications in fluorescence microscopy. *Lab. Chip* 21 (8), 1549–1562. doi:10.1039/d0lc01233e

Heppert, J. K., Pani, A. M., Roberts, A. M., Dickinson, D. J., and Goldstein, B. (2018). A CRISPR tagging-based screen reveals localized players in wnt-directed asymmetric cell division. *Genetics* 208 (3), 1147–1164. doi:10.1534/genetics.117.300487

Hermann, G. J., Schroeder, L. K., Hieb, C. A., Kershner, A. M., Rabbitts, B. M., Fonarev, P., et al. (2005). Genetic analysis of lysosomal trafficking in *Caenorhabditis elegans*. *Mol. Biol. Cell* 16 (7), 3273–3288. doi:10.1091/mbc.e05-01-0060

Hirsinger, E., and Steventon, B. (2017). A versatile mounting method for long term imaging of zebrafish development. *J. Vis. Exp.* 119. doi:10.3791/55210

Hörl, D., Rojas Rusak, F., Preusser, F., Tillberg, P., Randel, N., Chhetri, R. K., et al. (2019). BigStitcher: Reconstructing high-resolution image datasets of cleared and expanded samples. *Nat. Methods* 16 (9), 870–874. doi:10.1038/s41592-019-0501-0

Huisken, J., and Stainier, D. Y. R. (2009). Selective plane illumination microscopy techniques in developmental biology. *Development* 136 (12), 1963–1975. doi:10.1242/dev.022426

Icha, J., Schmied, C., Sidhaye, J., Tomancak, P., Preibisch, S., and Norden, C. (2016). Using light sheet fluorescence microscopy to image zebrafish eye development. *J. Vis. Exp.* (110), e53966. doi:10.3791/53966

Ichikawa, T., Nakazato, K., Keller, P. J., Kajiura-Kobayashi, H., Stelzer, E. H. K., Mochizuki, A., et al. (2014). Live imaging and quantitative analysis of gastrulation in mouse embryos using light-sheet microscopy and 3D tracking tools. *Nat. Protoc.* 9 (3), 575–585. doi:10.1038/nprot.2014.035

Jayadev, R., Morais, M. R. P. T., Ellingford, J. M., Srinivasan, S., Naylor, R. W., Lawless, C., et al. (2022). A basement membrane discovery pipeline uncovers network complexity, regulators, and human disease associations. *Sci. Adv.* 8 (20), eabn2265. doi:10.1126/sciadv.abn2265

Kaufmann, A., Mickoleit, M., Weber, M., and Huisken, J. (2012). Multilayer mounting enables long-term imaging of zebrafish development in a light sheet microscope. *Development* 139 (17), 3242–3247. doi:10.1242/dev.082586

Keeley, D. P., Hastie, E., Jayadev, R., Kelley, L. C., Chi, Q., Payne, S. G., et al. (2020). Comprehensive endogenous tagging of basement membrane components reveals dynamic movement within the matrix scaffolding. *Dev. Cell* 54 (1), 60–74. e7. doi:10.1016/j.devcel.2020.05.022

Keller, P. J., Schmidt, A. D., Wittbrodt, J., and Stelzer, E. H. K. (2008). Reconstruction of zebrafish early embryonic development by scanned light sheet microscopy. *Science* 322 (5904), 1065–1069. doi:10.1126/science.1162493

Kelley, L. C., Chi, Q., Cáceres, R., Hastie, E., Schindler, A. J., Jiang, Y., et al. (2019). Adaptive F-actin polymerization and localized ATP production drive basement membrane invasion in the absence of MMPs. *Dev. Cell* 48 (3), 313–328. e8. doi:10.1016/j.devcel.2018.12.018

Kelley, L. C., Wang, Z., Hagedorn, E. J., Shen, W., and Lei, S. (2017). Live-cell confocal microscopy and quantitative 4D image analysis of anchor-cell invasion through the basement membrane in *Caenorhabditis elegans*. *Nat. Protoc.* 12 (10), 2081–2096. doi:10.1038/nprot.2017.093

Kumar, A., Wu, Y., Christensen, R., Chandris, P., Gandler, W., McCreedy, E., et al. (2014). Dual-view plane illumination microscopy for rapid and spatially isotropic imaging. *Nat. Protoc.* 9 (11), 2555–2573. doi:10.1038/nprot.2014.172

Liu, T.-L., Upadhyayula, S., Milkie, D. E., Singh, V., Wang, K., Swinburne, I. A., et al. (2018). Observing the cell in its native state: Imaging subcellular dynamics in multicellular organisms. *Science* 360 (6386), eaaq1392. doi:10.1126/science.aaq1392

Manjarrez, J. R., and Mailler, R. (2020). Stress and timing associated with *Caenorhabditis elegans* immobilization methods. *Heliyon* 6 (7), e04263. doi:10.1016/j.heliyon.2020.e04263

Martinez, M. A. Q., Kinney, B. A., Medwig-Kinney, T. N., Ashley, G., Ragle, J. M., Johnson, L., et al. (2020). Rapid degradation of *Caenorhabditis elegans* proteins at single-cell resolution with a synthetic auxin. *G3* 10, 267–280. doi:10.1534/g3.119.400781

Martinez, M. A. Q., and Matus, D. Q. (2020). Auxin-mediated protein degradation in *Caenorhabditis elegans*. *Bio. Protoc.* 10 (8), e3589. doi:10.21769/BioProtoc.3589

Mauro, M. S., Celma, G., Zimyanin, V., Gibson, K. H., Redemann, S., and Bahmanyar, S. (2021). Ndc1 drives nuclear pore complex assembly independent of membrane biogenesis to promote nuclear formation and growth. *eLife* 11 e75513. doi:10.7554/eLife.75513

Mita, M., Ito, M., Harada, K., Sugawara, I., Ueda, H., Tsuboi, T., et al. (2019). Green fluorescent protein-based glucose indicators report glucose dynamics in living cells. *Anal. Chem.* 91 (7), 4821–4830. doi:10.1021/acs.analchem.9b00447

Monsalve, G. C., Yamamoto, K. R., and Ward, J. D. (2019). A new tool for inducible gene expression in *Caenorhabditis elegans*. *Genetics* 211 (2), 419–430. doi:10.1534/genetics.118.301705

Moyle, M. W., Barnes, K. M., Kuchroo, M., Gonopolskiy, A., Duncan, L. H., Sengupta, T., et al. (2021). Structural and developmental principles of neuropil assembly in *C. elegans*. *Nature* 591 (7848), 99–104. doi:10.1038/s41586-020-03169-5

Oren-Suissa, M., Hall, D. H., Treinin, M., Shemer, G., and Podbilewicz, B. (2010). The fusogen EFF-1 controls sculpting of mechanosensory dendrites. *Science* 328 (5983), 1285–1285. doi:10.1126/science.1189095

Pang, M., Bai, L., Zong, W., Wang, X., Bu, Y., Xiong, C., et al. (2020). Light-sheet fluorescence imaging charts the gastrula origin of vascular endothelial cells in early zebrafish embryos. *Cell Discov.* 6, 74. doi:10.1038/s41421-020-00204-7

Porta-de-la-Riva, M., Fontrodona, L., Villanueva, A., and Cerón, J. (2012). Basic *Caenorhabditis elegans* methods: Synchronization and observation. *J. Vis. Exp.* (64), e4019. doi:10.3791/4019

Prasanth, M. I., Santoshram, G. S., Bhaskar, J. P., and Balamurugan, K. (2016). Ultraviolet-A triggers photoaging in model nematode *Caenorhabditis elegans* in a DAF-16 dependent pathway. *AGE* 38 (27). doi:10.1007/s11357-016-9889-y

Preibisch, S., Saalfeld, S., Schindelin, J., and Tomancak, P. (2010). Software for bead-based registration of selective plane illumination microscopy data. *Nat. Methods* 7 (6), 418–419. doi:10.1038/nmeth0610-418

Rieckher, M., Psycharakis, S. E., Ancora, D., Zacharopoulos, A., Ripoll, J., Tavernarakis, N., et al. (2018). Demonstrating improved multiple transport-mean-free-path imaging capabilities of light sheet microscopy in the quantification of fluorescence dynamics. *Biotechnol. J.* 13 (1), 1700419. doi:10.1002/biot.201700419

Schindler, A. J., and Sherwood, D. R. (2014). Should I stay or should I go? Identification of novel nutritionally regulated developmental checkpoints in *C. elegans*. *Worm* 3 (4), e979658. doi:10.4161/21624054.2014.979658

Schmid, B., and Huisken, J. (2015). Real-time multi-view deconvolution. *Bioinformatics* 31 (20), 3398–3400. doi:10.1093/bioinformatics/btv387

Schultz, R. D., and Gumienny, T. L. (2012). Visualization of Caenorhabditis elegans cuticle structures using the lipophilic vital dye, DiI. *J. Vis. Exp.* (59), e3362. doi:10.3791/3362

Sherwood, D. R., and Plastino, J. (2018). Invading, leading and navigating cells in *Caenorhabditis elegans*: Insights into cell movement *in vivo*. *Genetics* 208 (1), 53–78. doi:10.1534/genetics.117.300082

Smith, C. J., Watson, J. D., Spencer, W. C., O'Brien, T., Cha, B., Albeg, A., et al. (2010). Time-lapse imaging and cell-specific expression profiling reveal dynamic branching and molecular determinants of a multi-dendritic nociceptor in *C. elegans*. *Dev. Biol.* 345 (1), 18–33. doi:10.1016/j.ydbio.2010.05.502

Smith, J. J., Xiao, Y., Parsan, N., Medwig-Kinney, T. N., Martinez, M. A. Q., Moore, F. E. Q., et al. (2022). The SWI/SNF chromatin remodeling assemblies BAF and PBAF differentially regulate cell cycle exit and cellular invasion *in vivo*. *PLoS Genet.* 18 (1), e1009981. doi:10.1371/journal.pgen.1009981

Steuwe, C., Vaeyens, M.-M., Jorge-Peñas, A., Cokelaere, C., Hofkens, J., Roeffaers, M. B. J., et al. (2020). Fast quantitative time lapse displacement imaging of endothelial cell invasion. *Plos One* 15 (1), e0227286. doi:10.1371/journal.pone.0227286

Stiernagle, T. (2006). *Maintenance of* C. elegans. Wormbook: The online Review of C. Elegans biology, 1–11.

Tsuyama, T., Kishikawa, J., Han, Y.-W., Harada, Y., Tsubouchi, A., Noji, H., et al. (2013). *In vivo* fluorescent adenosine 5'-triphosphate (ATP) imaging of *Drosophila melanogaster* and *Caenorhabditis elegans* by using a genetically encoded fluorescent ATP biosensor optimized for low temperatures. *Anal. Chem.* 85 (16), 7889–7896. doi:10.1021/ac4015325

Udan, R. S., Piazza, V. G., Hsu, C.-W., Hadjantonakis, A.-K., and Dickinson, M. E. (2014). Quantitative imaging of cell dynamics in mouse embryos using light-sheet microscopy. *Development* 141 (22), 4406–4414. doi:10.1242/dev.111021

Wang, X., Li, T., Hu, J., Feng, Z., Zhong, R., Nie, W., et al. (2021). *In vivo* imaging of a PVD neuron in *Caenorhabditis elegans*. *Star. Protoc.* 2 (1), 100309. doi:10.1016/j.xpro.2021.100309

Ward, A., Liu, J., Feng, Z., and Xu, X. Z. S. (2008). Light-sensitive neurons and channels mediate phototaxis in *C. elegans*. *Nat. Neurosci.* 11, 916–922. doi:10.1038/nn.2155

Wu, Y., Wawrzusin, P., Senseney, J., Fischer, R. S., Christensen, R., Santella, A., et al. (2013). Spatially isotropic four-dimensional imaging with dual-view plane illumination microscopy. *Nat. Biotechnol.* 31 (11), 1032–1038. doi:10.1038/nbt.2713

Yoshida, T., Alfaqaan, S., Sasaoka, N., and Imamura, H. (2017). Application of FRET-based biosensor "ATeam" for visualization of ATP levels in the mitochondrial matrix of living mammalian cells. *Methods Mol. Biol.* 1567, 231–243. doi:10.1007/978-1-4939-6824-4_14

Zhang, L., Ward, J. D., Cheng, Z., and Dernburg, A. F. (2015). The auxin-inducible degradation (AID) system enables versatile conditional protein depletion in *C. elegans*. *Development* 142 (24), 4374–4384. doi:10.1242/dev.129635

Zou, W., Yadav, S., DeVault, L., Nung Jan, Y., and Sherwood, D. R. (2015). RAB-10-Dependent membrane transport is required for dendrite arborization. *PLoS Genet.* 11 (9), e1005484. doi:10.1371/journal.pgen.1005484

Frontiers in
Cell and Developmental Biology

Explores the fundamental biological processes of life, covering intracellular and extracellular dynamics.

The world's most cited developmental biology journal, advancing our understanding of the fundamental processes of life. It explores a wide spectrum of cell and developmental biology, covering intracellular and extracellular dynamics.

Discover the latest Research Topics

See more →

frontiers

Frontiers in
Cell and Developmental
Biology

Frontiers

Avenue du Tribunal-Fédéral 34
1005 Lausanne, Switzerland
frontiersin.org

Contact us

+41 (0)21 510 17 00
frontiersin.org/about/contact